

# The Assembly Histories of Nearby Galaxies

By

**Adriano Poci**

A thesis submitted to Macquarie University  
for the degree of Doctor of Philosophy  
Department of Astronomy, Astrophysics, and Astrophotonics  
July 2021



Except where acknowledged in the customary manner, the material presented in this thesis is, to the best of my knowledge, original and has not been submitted in whole or part for a degree in any university.

---

Adriano Poci

# Acknowledgements

This has been a long journey, with a correspondingly long list of people I need to thank.

To the Fornax3D team; the in-person meetings were especially fun, informative, and really welcoming, often having just flown to the other side of the world alone. It's been greatly instructive being a part of this team, and I hope to work with you all long into the future. Thanks as well for the collaboration on mine and other's works - it's been great to be involved. A special shout-out to Katja for driving me around, and without whom I'd probably still be stumbling around Germany asking if anyone spoke English. A super special thanks to Glenn and Ling for devoting so much extra time to showing me the Schwarzschild code, and hospitality during my many disruptive visits. Those intense few weeks catapulted my progress every time.

To the Cool Garching Kids, and the rest of the Garching kids; thanks for keeping my year in Garching fun, interesting, bizarre, chaotic, and hilarious. All the beach volleyball (though a distinct lack of football), the days at the lake, the beer gardens, and just generally hanging out, was awesome. Thanks for making me feel self-conscious about my German, Italian, and English. It's actually impressive that you could make me, one of the few native speakers, start to question my English. A special shout-out to Frau Genau. Seriously though, it was a great culture-rich experience, and I'll see you all at Jockys Treff again for a beer.

To the Macquarie folks; it seems like ages since we were all in the office. Thanks for the futsal, pouring rain or 40° weather, full of sand either way. Tom, thanks for not playing Showdown despite my pestering. You said you were busy, but I guess it was so I didn't keep winning. Thanks to the many ExGal people over the years – all the way back to the original group circa 2014 – for the fruitful discussions, cake days, and all-round friendly meetings.

To Mariya, my ESO supervisor; thanks for all the time put into my stay in Garching. For driving my project forward, and especially for the advice – scientific, professional, and general. Thanks for seeing me through the job application season, which was *not at all stressful*. To more projects in the future.

To all the boys; Vartuli, Vuko, Dooley, Mihaljek, Paul, Angelo; and Michael, Steve, Al, Adj, Roy. It's been a busy few years for everyone, but thanks for sticking around with my constant departures and messy schedule. Thanks for getting me out of the house when I probably needed to. The futsal, football, tag, and associated beers, is always good fun. The FIFA nights, World Cup games at odd hours, and everything else that shall remain off record; thanks for reminding me of everything outside study. I'll probably see you this week anyway.

To my family; for asking what I actually do, if the world is flat, if aliens exist, if there is a thirteenth star sign, and when I'm going to space. For the video calls, trips to the airport, and send-offs. I'll make the tomatoes and wine remotely. Thanks to my grandmother for acting like I was never coming back every time I got on a flight. To my mother; thanks for giving me a place to live while I'm 'in-between countries'. Thanks for putting up with my 'almost finished' for 4+ years, for driving me to and from the airport countless times, the food – both locally and internationally, and of course everything else that wouldn't fit on the

page. Thanks.

To my partner Frana; thanks for putting up with me for a long time. For driving me insane so that I don't go insane from my thesis – genius plan. For dealing with my ‘habits’. For coming to visit me in various locations. For keeping on top of which concerts we should go to. You don't even like Thornhill. For proof-reading most things (but not this small 184-page document?!). For “basically writing your thesis” by correcting one grammar mistake. As always, you're alright. I love you.

Richard. It's been quite some time, but there isn't much left to say. I am hugely grateful for everything over all these years. I've probably learnt a bit about galaxies, but you've certainly made me into the semi-competent scientist I am today, and probably a less judgemental person in general. Thanks for having my back, always having my best interests in mind, and being incredibly understanding about everything. Cheers.

# Abstract

Galaxy formation and evolution is a collection of complex physical processes. Different processes can affect galaxies in vastly different ways, and so the final state of a galaxy depends on the delicate interplay between them. While evolution is a continuous process over many billions of years, galaxies are only observed at a single instance in time. From single-epoch data of external galaxies, star-formation histories provide constraints on when the stars formed, but not their actual history - namely where they came from and when they entered their present-day host (if formed externally). These histories are instead encoded in the orbits which the stars inhabit within their host. For resolved galaxies such as the Milky Way and other Local-Group members, orbital, chemical, and chronological information can be measured for individual stars, and such studies have clearly shown that this combination of properties reveals distinct events in a galaxy's history. Due to the inherent limitations of projected data, however, this has not yet been achieved for unresolved galaxies.

In this work we develop a new methodology in order to access intrinsic (de-projected) properties from the projected measurements of external galaxies. We build upon Schwarzschild orbit-superposition dynamical models, which allow for general shapes of the velocity ellipsoid and matter distribution. Using numerically-integrated orbits within a self-consistent model for the gravitational potential, we are able to reproduce all available stellar properties in projection, which we show is able to recover the true underlying distributions. In doing so, we are able to investigate the chemistry (metallicity), ages, and kinematics of the stars simultaneously, analogous to resolved studies. We develop diagnostics that enable the derivation of unique assembly histories constrained by the observational data. Intrinsic chemo-dynamical correlations are measured from these models, showing that stars which formed in the early Universe exhibit less ordered rotation compared to those which formed later. We find that for the massive field galaxy NGC 3115, the accretion of external material is the dominant driver of its evolution.

These models are applied to a small sample of galaxies in a nearby ( $z = 0$ ) cluster with high-quality spatially-resolved spectroscopy. We find evidence that the dense environment suppresses the accretion of external material, while also inducing mild kinematic perturbations. Using the increased sample size, we uncover additional intrinsic chemo-dynamical correlations which were previously only accessible to Local-Group galaxies, indicating that stars with higher heavy-element abundances exhibit stronger rotational support, irrespective of their age.

This methodology is finally extended to include new spatially-resolved measurements of the stellar Initial Mass Function (IMF). These models provide further evidence of significant variation of the IMF between galaxies. They also provide tentative evidence that it is approximately consistent for all the stars formed within a given galaxy, but that those which were brought in externally were formed with distinct IMF. This result, together with the other correlations studied by this work, show that the local conditions of star-formation across cosmic time can be analysed even with single-epoch, projected data of external galaxies.



# Contents

<b>Acknowledgements</b>	<b>iii</b>
<b>Abstract</b>	<b>v</b>
<b>Contents</b>	<b>vii</b>
<b>List of Figures</b>	<b>xi</b>
<b>List of Tables</b>	<b>xix</b>
<b>1 Introduction</b>	<b>1</b>
1.1 Cosmological Model . . . . .	2
1.2 The Formation of Galaxies in $\Lambda$ CDM . . . . .	4
1.3 <i>In-Situ</i> Star Formation in Galaxies . . . . .	7
1.3.1 Initial Mass Function . . . . .	8
1.3.2 Population Synthesis . . . . .	13
1.4 <i>Ex-Situ</i> Processes in Galaxies . . . . .	17
1.4.1 Accretion . . . . .	17
1.4.2 Environment . . . . .	18
1.5 Stellar Kinematics . . . . .	19
1.5.1 Kinematic Properties . . . . .	19
1.5.2 Observations of Stellar Kinematics . . . . .	20
1.5.3 Dynamical Models . . . . .	22
1.6 Motivation and Aims . . . . .	26
<b>2 Combining Stellar Populations with Orbit-Superposition Dynamical Modelling – the Formation History of the Lenticular Galaxy NGC 3115</b>	<b>57</b>
2.1 Introduction . . . . .	59
2.2 Observational Data and Kinematic Extraction . . . . .	60
2.3 Spatially-Resolved Star-Formation History . . . . .	61
2.4 Dynamical Model . . . . .	63
2.4.1 Mass Model . . . . .	63
2.4.2 Orbit Solution . . . . .	66
2.4.3 Model Free Parameters . . . . .	67
2.4.4 Intrinsic Angular Momentum . . . . .	68
2.4.5 Applying Stellar Populations to the Orbital Structures . . . . .	70
2.5 Results . . . . .	74
2.5.1 Constraining the Required Number of Dynamical Components . . .	75
2.5.2 Recovering the Dynamical SFH . . . . .	76

2.5.3	Intrinsic Stellar Velocity Dispersion and Stellar Populations . . . . .	78
2.5.4	Modelling Systematics . . . . .	79
2.6	Discussion . . . . .	81
2.6.1	Galactic Components of NGC 3115 . . . . .	81
2.6.2	Implications for the Formation History of NGC 3115 . . . . .	81
2.6.3	Comparison to Previous Inferences . . . . .	83
2.6.4	Resolved Studies and Galaxy Formation Simulations . . . . .	83
2.6.5	Non-Axisymmetric Structures . . . . .	85
2.7	Conclusions . . . . .	86
<b>Appendices</b>		<b>97</b>
2.A	Mass Surface Density MGE . . . . .	98
2.B	Regularisation in the Dynamical Star-Formation History . . . . .	98
2.C	Marginalised Intrinsic Velocity Dispersion Profiles . . . . .	99
<b>3</b>	<b>The Fornax3D project: Assembly Histories of Lenticular Galaxies from a Combined Dynamical and Population Orbital Analysis</b>	<b>103</b>
3.1	Introduction . . . . .	105
3.2	Data and Targets . . . . .	107
3.2.1	Photometry . . . . .	107
3.2.2	Spectroscopy . . . . .	107
3.2.3	Targets . . . . .	109
3.3	Stellar Content of Galaxies . . . . .	110
3.3.1	Stellar Mass Model . . . . .	110
3.3.2	Schwarzschild Dynamical Models . . . . .	111
3.3.3	Dynamical Decomposition . . . . .	113
3.3.4	Adding Stellar Populations . . . . .	114
3.4	Combined Dynamical and Stellar Populations . . . . .	116
3.4.1	FCC 153 . . . . .	120
3.4.2	FCC 170 . . . . .	121
3.4.3	FCC 177 . . . . .	122
3.5	Mass Assembly Histories in Context . . . . .	123
3.5.1	The Stellar Age–Velocity-Dispersion Relation . . . . .	124
3.5.2	S0 Formation . . . . .	129
3.5.3	The Fornax Galaxy Cluster Population . . . . .	130
3.6	Conclusions . . . . .	130
<b>Appendices</b>		<b>143</b>
3.A	Mass Density MGE . . . . .	144
3.B	Dynamical Modelling . . . . .	144
3.C	Validation on Mock Data . . . . .	147
<b>4</b>	<b>An Orbital Model of the Local Stellar Initial Mass Function in Nearby Galaxies</b>	<b>159</b>
4.1	Introduction . . . . .	159
4.2	Full-Index Fitting . . . . .	161
4.3	The IMF in Orbital-Population Dynamical Models . . . . .	162
4.4	Results . . . . .	163
4.4.1	Fits to Observational Data . . . . .	163
4.4.2	The IMF in the Circularity Plane . . . . .	165

4.4.3	The IMF of Principle Galactic Orbital Components . . . . .	166
4.5	Discussion . . . . .	169
4.5.1	The Local Variations of the Galactic IMF . . . . .	169
4.5.2	Further Developments . . . . .	170
<b>5</b>	<b>Conclusion</b>	<b>177</b>
5.1	Findings of this Thesis . . . . .	177
5.2	The Current State of Galaxy Evolution . . . . .	179
5.3	The Future of Galaxy Formation Models . . . . .	179



# List of Figures

1.1	The Emu in the Sky, reproduced with permission from Norris (2009). The band of lights in what we understand to be the baryonic component of the Milky Way Galaxy ( <i>upper</i> ) and its stone carving representation by the local First Nations people ( <i>lower</i> ). . . . .	2
1.2	The rotation curve of the spiral galaxy NGC 3198, reproduced with permission from Freeman (2003), with the original data from Begeman (1989). The observed stellar rotation is shown as black data points with error bars. The solid curves show the predictions for rotation of the stars and gas ( <i>orange</i> ) and gas alone ( <i>pink</i> ) assuming that the mass density in the galaxy approximately follows the observed luminosity density. There is a clear discrepancy between what is measured, and what is predicted from the luminous component of the galaxy. . . . .	3
1.3	Various literature IMF functions. The single power-law from Salpeter (1955) is in dotted blue, the broken power-law from Kroupa (2001) is in dot-dashed orange, the log-normal from Chabrier (2003) is in dashed green, and the smooth broken power-law ‘bimodal’ from Vazdekis et al. (1996) is in solid red. The IMF from Vazdekis et al. (1996) is an explicit function of the high-mass slope $\Gamma_b$ , so is presented here with a slope $\Gamma_b = 1.35$ for illustration. Curves are offset for presentations. . . . .	9
2.1	The fit in PPXF to the highest (left) and lowest (right) $S/N$ spectra in the dataset, with $S/N = 119$ and $67$ , respectively. In each panel, the top row shows the data and model in black and red, respectively. The residuals are shown as green diamonds, and have been arbitrarily offset for presentation. The grey bands are masked during the fit. The outer-most pixels on either extremity have also been excluded to avoid edge effects. The bottom panels show the associated luminosity-weighted SFH, which illustrates the contributions from each age/metallicity bin to the corresponding spectrum. . . . .	62
2.2	The reconstructed image from the 3D data cube in arbitrary flux units, and the surface-brightness MGE contours overplotted in 1 mag intervals. . . . .	64
2.3	A map of $M_\star/L$ in $V$ -band inferred from full spectral fitting with variable age and metallicity, and assuming a Kroupa IMF. . . . .	64
2.4	The fit in red to the iso-mass contours of the scaled mass image in black (top). The surface-brightness MGE is shown for reference in dashed blue. The panel shows the FOV of the IFU, while the zoom-in shows only the disk region between $0$ and $40''$ . The fractional residuals between the mass ‘image’ and $MGE_\Sigma$ are shown in the bottom panel. . . . .	65

2.5	The grid search over the free parameters of the Schwarzschild model. Each panel shows the marginalised $\Delta\chi^2$ contour surface in colour. The black solid lines show, from bold to thin, the $1-$ , $2-$ , and $3-\sigma$ ranges, respectively. The grey ‘+’ symbols show the underlying grid of models that were generated, and the magenta lines indicate the final best-fitting values. . . . .	69
2.6	The data (left), model (center), and residuals (right) for the best-fitting Schwarzschild model of NGC 3115. From top to bottom (labelled in the top-left corner of each model panel) is the surface brightness, followed by all kinematic moments. The model is fit to the surface brightness MGЕ, rather than the surface brightness directly. The residuals for the surface brightness have been offset such that 0 is the black end of its corresponding colourbar. All other residual panels have been offset such that 0 corresponds to the green (centre) of their corresponding colourbars. . . . .	70
2.7	The $\lambda_z - r$ phase-space of the best-fitting Schwarzschild model of NGC 3115. The density map is the orbital probability distribution (circularity; § 2.4.4), with the dynamical component selections of Sample III shown in white boxes. The vertical dashed line marks $R_e$ . Highlighted and numbered are components representative of different regions of the circularity phase-space; see Fig. 2.8. . . . .	72
2.8	The surface brightness (left), mean velocity (middle), and velocity dispersion (right) of four characteristic dynamical components. Each component is presented on the same binning and FOV as the data for consistency. The FOV is outlined by the brown dashed line, and the component labels are on the far right of each row (refer to Fig. 2.7). Note that each of these components does <i>not</i> contribute equal mass to the dynamical model, but were selected to illustrate different regions in circularity phase-space. . . . .	73
2.9	The LOSVD in a single aperture, for the dynamical components of Sample I (coloured histograms), their sum (black), and from the original Schwarzschild model (grey filled). . . . .	73
2.10	The luminosity-weighted age (left) and metallicity (right) maps. The first four rows are for the different dynamical selection criteria (§ 2.4.5), labelled on the far right. The number of dynamical components resulting from each sample is inset in the top right of each metallicity panel. The bottom row shows the maps derived from the SFH (§ 2.3). . . . .	75
2.11	The surface brightness (left), mean velocity (middle) and velocity dispersion (right) of the dynamically-selected components, binned into their corresponding mean stellar age from young (top) to old (bottom). The bin ranges and corresponding stellar masses of each bin are inset in the upper right and left of each surface brightness panel, respectively. . . . .	77
2.12	As Fig. 2.11, but for the stellar metallicity. . . . .	77

2.13 <i>Main</i> : The radial profiles of the $z$ -component of the <i>intrinsic</i> velocity dispersion for the dynamical components grouped by their mean stellar-population properties. Each curve is coloured by its $\sigma_z$ values to allow an easier quantitative comparison between panels. The variance within the annuli (see text) are shown as errorbars. The grey curves are Monte Carlo simulations of the stellar-population fits. They are computed by randomly perturbing the stellar-population maps from the spectral SFH (§ 2.3) within their measurement uncertainties, and re-fitting to the dynamical components. Each trial is plotted with high transparency, such that only the regions with high density of curves are visible. We note that, in a few instances, the Monte Carlo simulation has populated distinct panels from the best-fit model. <i>Inset</i> : The surface-brightness of each age/metallicity bin, observed at the best-fitting projection of the Schwarzschild model ( $\sim 85^\circ$ ) on the same FOV as the MUSE observations. All surface-brightness panels are on the same colour-scale. The absolute stellar masses are inset in cyan. . . . .	79
2.14 The vertical component of the intrinsic velocity dispersion of the orbits associated with the disk region (see text) of NGC 3115 (data points) as a function of redshift. These data are computed as the average of the radial profiles for the components with $\lambda_z > 0.5$ and high metallicity. The data points are the centres of the age bins, vertical errorbars show the magnitude of the variation of each profile with radius, while horizontal errorbars show the widths of the age bins. The formation redshifts are approximated from the stellar ages assuming standard $\Lambda$ CDM cosmology. The size of each point is proportional to the mass contained in that bin. Literature measurements are shown as box and whiskers according to the legend, and the red dashed line shows the $18 \cdot (1 + z)$ evolution from Wisnioski et al. (2015) – though we note that these measurements are of <i>star-forming, gaseous</i> disks. . . . .	84
2.B.1 The circularity phase-space, as shown in Fig. 2.7, but where the components are additionally coloured by their assigned mean stellar age. The top panel shows an unregularised fit, while the bottom panel shows the regularisation that was used throughout this work. . . . .	100
2.C.1 Radial profiles of the intrinsic vertical velocity dispersion for dynamical components binned by their mean stellar age (averaged over metallicities). The absolute stellar mass of each bin is given in Fig. 2.11. As with Fig. 2.13, the variance within the annuli are shown as errorbars. . . . .	101
2.C.2 As Fig. 2.C.1, but binned by mean stellar metallicity (averaged over ages). The absolute stellar mass of each bin is given in Fig. 2.12. . . . .	101
3.1 Fits ( <i>red</i> ) to spectra ( <i>black</i> ) from the centre and outer regions ( <i>top</i> and <i>bottom</i> of each pair of spectra, respectively) for our galaxy sample, as labelled on the right. Residuals are shown in green, offset for presentation. The grey bands show regions which are masked during the fit. All spectra are normalised, but vertically offset for presentation. It can be seen that the outer spectra are more noisy, as expected, but that in all cases the data are reproduced well by the fit. . . . .	108
3.2 Full $r$ -band images from FDS, overlaid with the MUSE FOV in dashed brown for FCC 153 ( <i>left</i> ), FCC 170 ( <i>middle</i> ), and FCC 177 ( <i>right</i> ). . . . .	109

3.3 Enclosed-mass profiles of the total (dynamical) mass ( <i>solid line</i> ), stellar mass ( <i>dashed line</i> ), and DM ( <i>dot-dashed line</i> ) for the three galaxies. The effective radii are denoted by the small arrows, and the radial extent of each spectroscopic FOV is shown by the vertical dotted line. The lower radial bound of the figure is set to half the width of the point-spread function from the spectroscopic observations. . . . .	113
3.4 Phase-space of circularity $\lambda_z$ as a function of cylindrical radius $R$ for the best-fit model of FCC 153. The colour represents the orbital weight from the Schwarzschild model, which has been normalised to an integral of unity. The dynamical decomposition is overlaid in black, where only those components which have non-zero contribution to the original model are defined. The figure is shown on the radial extent of the spectroscopy for clarity, but the decomposition is conducted over the full Schwarzschild model. The black dashed line is the half-mass radius, derived from $MGE_\Sigma$ , shown for scale. The distribution indicates the prevalence of high-angular-momentum (cold disk-like) co-rotating orbits in this galaxy, with very little contribution from hot ( $\lambda_z \sim 0$ ) or counter-rotating ( $\lambda_z < 0$ ) orbits. . . . .	115
3.5 Same as Fig. 3.4, but for FCC 170. This galaxy has a large contribution from hot central orbits, with most of the cold orbits appearing at larger radius. . . . .	115
3.6 Same as Fig. 3.4, but for FCC 177. Similarly to FCC 153, this galaxy is dominated by co-rotating cold orbits. . . . .	116
3.7 Best-fitting Schwarzschild model for FCC 153. The data ( <i>left</i> ), fits ( <i>middle</i> ), and residuals ( <i>right</i> ) of, from top to bottom, the dynamical model (surface brightness, velocity, velocity dispersion, and $h3 - h6$ ), and the subsequent stellar-population fitting (age and metallicity). The outline of the MUSE mosaic is shown in dashed brown. All residual panels show the absolute differences (data - model), but are offset such that green is zero. The stellar-population maps share a common colour-bar between galaxies for comparison. We note that for FCC 153, since the observed metallicity map reaches 0.4 dex along the major axis, and is itself an average through the LOS, we extend the upper bound for the individual components during the stellar-population fitting to 1.0 dex. . . . .	117
3.8 Same as Fig. 3.7, but for FCC 170. . . . .	118
3.9 Same as Fig. 3.7, but for FCC 177. . . . .	119

3.10 Mass assembly history for FCC 153. The panels are ordered by increasing mean stellar age ( <i>left to right</i> ) and decreasing mean stellar metallicity ( <i>top to bottom</i> ). The value given at the top and right of each column and row, respectively, denotes its upper bound (inclusive). Each panel is composed of a radial profile of the vertical stellar velocity dispersion $\sigma_z$ ( <i>black/white curve</i> ), the surface brightness distribution at the best-fitting projection ( <i>top-right</i> ) with the outline of the MUSE mosaic shown in dashed brown, and the total stellar mass within the FOV for that panel. The $\sigma_z(R)$ profiles are coloured according to the stellar mass in that panel at that radius (sampled within the logarithmic radial bins). This indicates the spatial region in which each curve contributes most (white regions), and which regions may be impacted by numerical noise (black regions). The grey shaded regions show the spread of velocity dispersion profiles for 100 Monte Carlo fits to the stellar-population maps. This galaxy exhibits a dominant disk-like, metal-rich component that has steadily formed over the last $\sim 10$ Gyr. . . . .	120
3.11 Same as Fig. 3.10, but for FCC 170. This galaxy is dominated by an old central pressure-supported spheroidal component spanning $\sim 1$ dex in metallicity. It has a secondary contribution from a progressively thinner and younger disk-like component, and a potential minor contribution from a warm metal-poor halo-like component. . . . .	121
3.12 Same as Fig. 3.10, but for FCC 177. This galaxy appears to have begun forming late. It is dominated by a young, thin disk, with contributions from dynamically-warmer and slightly older stars. . . . .	122
3.13 Stellar disk AVR as derived from our models. The coloured stars are the galaxies modelled in this work (and Poci et al., 2019, for NGC 3115). The symbol size is proportional to the fractional stellar mass in each age bin, for each galaxy independently. The horizontal error-bars denote the width of the age bin. The vertical error bars are computed as the weighted standard deviation within each age bin, for the best-fit model. The shaded regions show the spread in $\sigma_z$ for 100 Monte Carlo fits to the stellar-population maps. The dashed curves show the stellar AVR of the four S0 galaxies when all orbits are included (no selection on orbital circularity). The box-whisker plots are literature measurements of cold gas disks, from HERACLES (Leroy et al., 2009), DYNAMO (Green et al., 2014), GHASP (Epinat et al., 2010), PHIBBS (Tacconi et al., 2013), MASSIV (Epinat et al., 2012), OSIRIS (Law et al., 2009), AMAZE-LSD (Gnerucci et al., 2011), SINS (Schreiber et al., 2009) and zC-SINF (Schreiber et al., 2014), KMOS <sup>3D</sup> (Wisnioski et al., 2015), and KDS (Turner et al., 2017). The black dots and crosses are Milky-Way stellar measurements (Yu and Liu, 2018) for stars on ( $ z  < 270$ pc) and off ( $ z  > 270$ pc) the plane, respectively. Galaxy disks become dynamically colder towards the present day. The cluster S0 galaxies have a higher contribution from warmer orbits at more recent times compared to the field galaxy (comparing the full and disk-only $\sigma_z$ ). The Milky-Way, despite its higher stellar mass, is dynamically colder than the S0 galaxies studied here. . . . .	125

3.14 Correlations of $\sigma_z$ with stellar age at fixed metallicity ( <i>left</i> ), and stellar metallicity at fixed age ( <i>right</i> ) for, from top to bottom, the three galaxies studied in this work, and the field S0 NGC 3115 (Poci et al., 2019). The curves are coloured by their age/metallicity bin corresponding to those of Figures 3.10 to 3.12. The Spearman rank coefficient $r$ and the associated $p$ -value, computed for all curves collectively in a given panel, are inset. The shaded regions correspond to the variations derived from 100 Monte Carlo fits to the stellar population maps. The stellar AVR at fixed metallicity exhibits lower significance than the $[Z/H] - \sigma_z$ at fixed age. . . . .	127
3.A.1 Mass-density MGE for FCC 153. <i>Top</i> : Contours of the projected mass density (black), the mass density $MGE_\Sigma$ (red), and the surface brightness $MGE_\mu$ (blue). <i>Bottom</i> : The ratio between the mass and surface-brightness models, showing the structural differences. This panel is normalised by the average $M_\star/L$ such that values of 1.0 (white) are consistent with the assumption of a spatially-constant $M_\star/L$ , and any deviations are percentages in stellar mass. The outline of the MUSE mosaic is shown in dashed brown.	144
3.A.2 Same as Tab. 3.A.1, but for FCC 170. . . . .	145
3.A.3 Same as Fig. 3.A.1, but for FCC 177. . . . .	146
3.B.1 Optimisation over the 5D parameter-space for FCC 153. The grey points indicate the exploration of the parameter-space with the smaller orbit sampling, while the coloured points show the $\chi^2_r$ of the models with the high orbit sampling (see § 3.3.2). The best-fit parameters are indicated by the brown lines. . . . .	148
3.B.2 Same as Fig. 3.B.1, but for FCC 170. . . . .	149
3.B.3 Same as Fig. 3.B.1, but for FCC 177. . . . .	150
3.B.4 Un-symmetrised kinematics extracted for FCC 153 ( <i>left</i> ), and associated errors computed through Monte Carlo simulations ( <i>right</i> ). The outline of the MUSE mosaic is shown in dashed brown. . . . .	151
3.B.5 Same as Fig. 3.B.4, but for FCC 170. . . . .	152
3.B.6 Same as Fig. 3.B.4, but for FCC 177. . . . .	153
3.C.1 Stellar-population Schwarzschild model fits to the mock data. Mean stellar age ( <i>left</i> ) and metallicity ( <i>right</i> ) are shown for Auriga halos 5 ( <i>top</i> ) and 6 ( <i>bottom</i> ). From top to bottom, the rows represent the true means, models fits, and residuals. . . . .	154
3.C.2 Intrinsic $t - Z$ distribution ( <i>left</i> ) and that retrieved from our model ( <i>right</i> ) for halos 5 ( <i>top</i> ) and 6 ( <i>bottom</i> ). The 1D distributions are also shown for each simulation, as kernel density estimates of the underlying data. The intrinsic distributions are black dashed curves, and the model distributions are the blue solid curves. . . . .	155
3.C.3 Similar to Fig. 3.10, showing the assembly history for halo 5 ( <i>top</i> ) and halo 6 ( <i>bottom</i> ). In addition to the $\sigma_z$ radial profile ( <i>black/white line</i> ) and surface brightness distribution ( <i>upper right</i> ) from the Schwarzschild model, the shaded regions correspond to the variations derived from 100 Monte Carlo fits to the stellar population maps. Each panel also contains the intrinsic $\sigma_z$ radial profile ( <i>red line</i> ) and surface brightness distribution ( <i>upper left</i> ) from the simulations. . . . .	156
3.C.4 Similar to Fig. 3.13, showing the recovered ( <i>blue</i> ) and intrinsic ( <i>red</i> ) AVR for halos 5 and 6. . . . .	157

4.1	The IMF parametrisations $m_{0.5}$ ( <i>left</i> ), $m_{1.0}$ ( <i>middle</i> ), and $\xi$ ( <i>right</i> ) for FCC 153. The rows show the data ( <i>top</i> ), model ( <i>middle</i> ), and residual ( <i>bottom</i> ). The outline of the MUSE mosaic is shown in dashed brown. Maps of $\xi$ are presented on a common colour scale across all galaxies for comparison. . . . .	164
4.2	As Fig. 4.1, but for FCC 170. . . . .	164
4.3	As Fig. 4.1, but for FCC 177. . . . .	165
4.4	The circularity phase-space coloured by IMF, for FCC 153 ( <i>top left</i> ), FCC 170 ( <i>top right</i> ), and FCC 177 ( <i>bottom left</i> ). The colour bar, common to all three galaxies, shows the luminosity-weighted average $\xi$ in each region, which is computed as the ratio of the luminosity-weighted average $m_{0.5}$ and $m_{1.0}$ . The original weight distribution of the underlying orbits (from Figures 3.4 to 3.6) is depicted by transparency, where opaque represents high weight and transparent represents zero weight. The brown dashed lines illustrate the dynamical selection of the three broad components explored in § 4.4.3. . . . .	166
4.5	The spatial distribution of the IMF parametrisations in FCC 153 for the ‘disk’ ( <i>top</i> ), ‘bulge’ ( <i>middle</i> ), and ‘warm’ ( <i>bottom</i> ) components. The outline of the MUSE mosaic is shown in dashed brown. From left to right are the projected maps of $m_{0.5}$ , $m_{1.0}$ , and $\xi$ , as well as the fractional weight for all orbits in a given component ( $\tilde{\omega}$ ). Each component is necessarily re-normalised, but this means that the relative contribution to the same spatial region between the three rows is not captured. This is instead shown explicitly in the $\tilde{\omega}$ panels, such that the values of the mass integrals and $\xi$ for a given component contribute most to the observed maps (Fig. 4.1) in the regions where the respective weight is high. FCC 153 exhibits elevated $\xi$ (increasing dwarf-richness) in the high-angular-momentum component concentrated in a disk-like geometry (but not exactly in the disk plane). . . . .	167
4.6	As Fig. 4.5, but for FCC 170. Like FCC 153, but to a lesser degree, FCC 170 exhibits increased $\xi$ in the high-angular-momentum component in a disk-like geometry (except for the central region). Even the ‘warm’ component exhibits elevated $\xi$ along the disk plane at larger radii. . . . .	167
4.7	As Fig. 4.5, but for FCC 177. As with the other projections, FCC 177 exhibits globally lower values of $\xi$ , yet a peak still exists in the ‘disk’ component. . . . .	168
4.8	The luminosity-weighted average IMF as a function of the luminosity-weighted average orbital circularity for the three dynamical components ( <i>symbols</i> , defined in text) of the three Fornax3D galaxies. Horizontal lines mark literature IMF values for reference. Only those orbits with time-averaged radii within the spectroscopic data are included during the averaging. The dynamically-cold components exhibit comparable richness of dwarf stars to the hot central spheroids, which are more dwarf-rich compared to the extended warm component. . . . .	169



# List of Tables

2.1	The free parameters of the Schwarzschild model, their corresponding step sizes, $\Delta$ , and the final best-fitting values. $u$ is fixed in our model, while $\theta, \phi, \psi$ are derived from $q, p, u$ . These parameters therefore have no $\Delta$ . * Note that the black-hole mass is sampled logarithmically, and so its $\Delta$ is multiplicative rather than additive. . . . .	68
2.A.1	The counts, widths, and axis ratios of the Gaussians in our $MGE_{\Sigma}$ model. . . . .	98
3.1	Physical properties of the galaxy sample. (1) galaxy name (2) distance to the galaxy measured by Blakeslee et al. (2009) using surface-brightness fluctuations (3) $r$ -band effective radius taken from Iodice et al. (2019a) and converted into physical units at our adopted distances (3) – (4) stellar and DM masses enclosed within $R_e$ , respectively (5) radius which encloses 98% of the stellar mass (6) – (7) stellar and DM masses enclosed within $R_{\text{enc}}$ , respectively. . . . .	114
3.A.1	$MGE_{\Sigma}$ for FCC 153. The columns represent, from left to right, the projected mass surface density, the width (peak location), and axis ratio, respectively.	145
3.A.2	Same as Tab. 3.A.1, but for FCC 170. . . . .	145
3.A.3	Same as Tab. 3.A.1, but for FCC 177. . . . .	146
3.B.1	Best-fit parameters for the Schwarzschild models. Columns marked with * are fixed to the values given here. . . . .	147



---

# CHAPTER 1

---

## INTRODUCTION

In the outback of Australia on a clear moonless night, a spectacular band of lights stretches across the sky (Fig. 1.1). It is understood by the Ku-ring-gai people, a tribe of the Indigenous First Nations people, to be a giant ‘Emu in the Sky’. The emu is a large, native, flightless bird, part of Australia’s diverse and unique fauna. The carving shown at the bottom of Fig. 1.1 was made by First Nations people, in what is known today as the Ku-ring-gai Chase National Park, just north of Sydney, Australia. The collection of purely-oral stories which ‘The Emu in the Sky’ belongs to is known as the Dreaming (or Dreamtime); a foundational pillar of Indigenous culture. The Dreaming explains and records all things of the natural world (including its creation), with emphasis on the people, flora, and fauna. The night sky, however, plays a key role. So much so, in fact, that there have been a number of references to the Indigenous Australians as the “world’s first astronomers” (for example, Haynes, 1995, 2000). Among the stories of The Dreaming are records of many astrophysical phenomena such as what Western astronomers understand to be meteors, variable stars, and lunar-induced ocean tides (Hamacher, 2012).

The sophisticated network of stories of the Indigenous people is simultaneously philosophical and pragmatic. Consider the emu in the sky, for instance. While the aesthetic connection between the dark sky and the carving in Fig. 1.1 is clear, Norris (2009) explains that the alignment of the depictions in the sky and carving coincides with the time of year when emus lay their eggs (a valuable food source for the Indigenous people) highlighting the practical applications of the Dreamtime. Moreover, The Emu in the Sky, like most of the Dreamtime stories, explains *how* this emu came to be and *why* it is now in the sky. This highlights the Dreaming’s role in explaining the natural world on a philosophical level, and ultimately the relationship of the Indigenous people with everything in it. The Emu in the Sky is but one small facet illustrating the cultural significance of the natural world to the Indigenous people. A comprehensive review of the connection between the Dreaming and astronomy is presented in Norris (2016).

Modern astrophysics parallels many of the aspects of this Indigenous culture – primarily, the endeavour to observe and explain natural phenomena, and the significance of our existence. Moreover, the Milky-Way galaxy is central to this endeavour in both cultures. As may be guessed, the Emu in the Sky is what we understand to be the baryonic component of our Galaxy; specifically, its dust lanes (dark patches), stellar body (diffuse orange glow), and nebulae (bright pink point-sources). The shear size and visibility of the Milky-Way explains its significance, and are why it is an anchor to the vast majority of fields in modern astrophysics and ancient cultures alike. However it eventually emerged that the Milky-Way galaxy is one of *many* other galaxies. Estimates for the total number of galaxies in the observable Universe were at first hundreds of thousands (Slipher, 1917; Hubble, 1929), later billions (Williams et al., 1996; Beckwith et al., 2006), then trillions (Conselice et al., 2016), and by a recent estimate



FIGURE 1.1: The Emu in the Sky, reproduced with permission from Norris (2009). The band of lights in what we understand to be the baryonic component of the Milky Way Galaxy (*upper*) and its stone carving representation by the local First Nations people (*lower*).

has now settled back down to billions (Lauer et al., 2021). Thus, while our perspective of the Milky Way is unique and this is why it is crucial for the *philosophy* of astronomy, the Galaxy itself is by no means atypical and it is in fact the study of the broader population of *external* galaxies that will ultimately illuminate the physical nature and evolution of our Universe. The observable characteristics of these galaxies show extraordinary constraining power across all scales of the Universe, from cosmological concepts regarding the structure of the Universe itself (for instance, see Peacock et al., 2001; Colless et al., 2001) including its earliest phases (for example, Trenti et al., 2010; Bouwens et al., 2015), through the formation and evolution of those galaxies, to even the local processes and conditions for the formation of stars.

## 1.1 Cosmological Model

The study of how galaxies form and evolve has been a rapidly-progressing field of research over the last century. This has historically been coupled to progress in a number of other sub-fields in astronomy and astrophysics, including cosmology in particular. The discovery that the vast majority of observed ‘nebulae’ were actually external galaxies (Hubble, 1929) simultaneously showed that these galaxies are receding from Earth (the observer), and those which are further are travelling at faster velocities along the line-of-sight (LOS). The implication of this is that the Universe itself is expanding – which is clearly important for cosmology. It was hypothesised that if the Universe is expanding in the present-day, it must have been much smaller in the past. In fact, theory predicted that the Universe originated from a singularity, in an explosive ‘Big Bang’. The density of matter within this early Universe was high due to its small volume, leading to the efficient retention of radiation. Thus the early Universe was opaque. After the formation of radiating sources, the constituent matter became ionised, causing the transition to a transparent Universe. This transition, though very

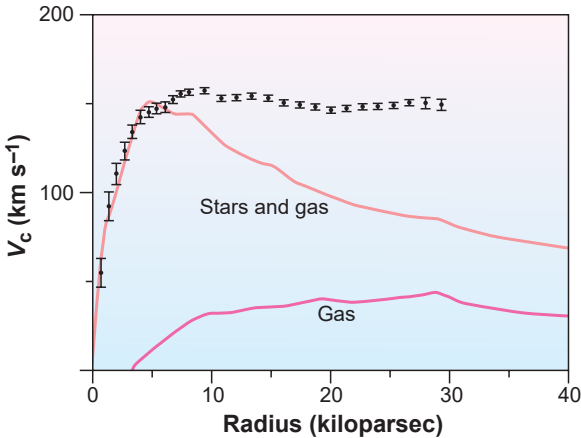


FIGURE 1.2: The rotation curve of the spiral galaxy NGC 3198, reproduced with permission from Freeman (2003), with the original data from Begeman (1989). The observed stellar rotation is shown as black data points with error bars. The solid curves show the predictions for rotation of the stars and gas (orange) and gas alone (pink) assuming that the mass density in the galaxy approximately follows the observed luminosity density. There is a clear discrepancy between what is measured, and what is predicted from the luminous component of the galaxy.

early in the history of the Universe, can still be observed in the present-day in the microwave region of the electromagnetic spectrum. The accidental discovery of the Cosmic Microwave Background (CMB; Penzias and Wilson, 1965), the near-uniform ‘screen’ of radiation which is the remnant of this transition from opaque to transparent as predicted by Dicke et al., 1965, provided experimental validation for the Big Bang hypothesis. Through the study of this cosmological phenomenon with sequentially higher-resolution instruments (Smoot et al., 1992; Bennett et al., 2003; Ade et al., 2014), the non-uniformities of the CMB emerged. It is believed these non-uniformities, though tiny at the epoch of the CMB, grew to provide the initial over-densities in which galaxies formed. In fact, galaxies themselves are believed to have contributed ionising radiation during this transition period (Ota et al., 2010; Ouchi et al., 2010; Trenti et al., 2012).

Later still, the discovery of plateauing rotational velocities as a function of galactocentric radius for stars in external galaxies (Rubin and Ford, 1970; Ostriker et al., 1974; Einasto et al., 1974) dramatically changed the paradigm of galaxy formation. The stark difference between the observed and expected (from simple Keplerian motion) rotational velocities is exemplified in Fig. 1.2. Observations such as these led to the implication that a significant portion of the mass in galaxies, and by extension the Universe itself, is invisible to all electromagnetic radiation: the so-called dark matter (DM). Retrospectively, similar conclusions could be drawn from much earlier work on clusters of galaxies (Zwicky, 1933). Galaxies, then, are believed to be composed of luminous baryons which dominate their central regions, embedded within a larger ‘halo’ of DM (see for instance White and Rees, 1978 or the complete reviews of DM in galaxies from Wechsler and Tinker, 2018; Salucci, 2019; de Martino et al., 2020). Despite the current uncertainties surrounding the nature of DM, it is believed to be a collisionless non-relativistic particle which interacts solely (or at least predominantly) through gravity (Porter et al., 2011). Therefore, while it can not currently be observed directly, DM affects the kinematics of the galactic material interior to it, and can therefore be studied indirectly by modelling these kinematics.

Following the initial outward ‘push’ from the Big Bang, the rate of expansion of the Universe could logically be expected to steadily decrease as a result of gravity if sufficient matter is present. To measure this deceleration, velocity measurements were required for objects at larger distances compared to the sample used by Hubble (1929). Owing to the inherent difficulty of measuring distances to astronomical objects, this was only possible by using observations of Type Ia supernovae. These have relatively secure, and often quite large, distances compared to galaxies alone. The results of systematic measurements of Type Ia supernovae (Riess et al., 1998; Perlmutter et al., 1999) resulted in another dramatic shift

in paradigm, as they showed that the Universe is not only expanding, but that the rate of expansion is *increasing* with time – that is, accelerating. This acceleration is characterised by an energy tensor with negative pressure,  $\Lambda$ , originally proposed by Einstein (1916). Such expansion alludes to another as-yet unseen component of the Universe, the so-called dark energy (see review of, for instance, Binétruy, 2013).

Finally, built upon Einstein’s geometric theory of gravity (Einstein, 1905, 1916), and in combination with the aforementioned landmark discoveries of the past century, the current paradigm of galaxy formation and evolution is established. This paradigm, the  $\Lambda$ -Cold Dark Matter ( $\Lambda$ CDM) model, describes a geometrically-quasi-flat Universe. In this model, the Universe grew via expansion from an initial ‘singularity’ – the Big Bang – and left its in-print in the CMB shortly thereafter. The density of matter ( $\Omega_M$ ), energy ( $\Omega_\Lambda$ ), and radiation ( $\Omega_r$ ) in the current  $\Lambda$ CDM model satisfy  $\Omega_M + \Omega_\Lambda + \Omega_r + \Omega_K = 1$ , with any curvature of the Universe arising from  $\Omega_K \neq 0$ . The most recent experiment resulted in a measurement of  $\Omega_K = 0.001 \pm 0.002$  (Aghanim et al., 2020). Moreover, the baryonic matter, dark matter, and dark energy contribute  $\sim 5$ ,  $\sim 25$ , and  $\sim 70$  per cent, respectively, to the total energy budget (with the precise relative contributions varying among different experiments; Kofman et al., 1993; Bennett et al., 2003, for instance). Where applicable, this work assumes the cosmology of the *Planck* 2015 experiment (Ade et al., 2016), which measured  $\Omega_M = 0.307$ , and a rate of expansion of the Universe of  $H_0 = 67.8 \pm 0.9 \text{ km s}^{-1} \text{ Mpc}^{-1}$ . It is possible to estimate the age of the Universe by tracing this expansion rate back in time. For the cosmological model assumed here, this results in a present-day age for the Universe of 13.80 Gyr.

## 1.2 The Formation of Galaxies in $\Lambda$ CDM

The  $\Lambda$ CDM cosmology describes a hierarchical self-similar Universe in which the initial ‘primordial’ inhomogeneities in the CMB gave rise to many small over-densities which allowed DM to gradually coalesce through gravity. These growing DM halos attracted baryons in the form of gas which could sink to their centres to form stars and the seeds of galaxies. Galaxies are not the end-point of hierarchical merging, however. Collections of galaxies in close proximity result in the merging of their DM halos. These gravitationally-bound collections of galaxies are termed groups and clusters, categorised according to the total mass in the system;  $\log_{10}(M/M_\odot) = 12.5 - 14$  for groups, and  $\log_{10}(M/M_\odot) > 14$  for clusters. Additionally, separate groups and clusters may become gravitationally-bound, leading to the formation of ‘super-clusters’ (Oort, 1983). The relative over- and under-density of galaxy groups, clusters, and super-clusters results in the large-scale structure of the Universe itself, which had been predicted by simulations (Davis et al., 1985) and later seen in observations (Peacock et al., 2001; Colless et al., 2001, though with early hints from de Lapparent et al., 1986). The clusters and super-clusters form ‘nodes’ which are believed to be connected by ‘filaments’ of primordial gas. This leaves regions of under-densities, known as ‘voids’. Together, this structure constitutes the so-called ‘cosmic web’. Hierarchical structure thus sets the basic framework and environment in which galaxies began to form, and is a direct consequence of the  $\Lambda$ CDM paradigm.

What follows is billions of years of evolution dictated by many gravitational and thermodynamic processes. It is believed that galaxy formation occurs from these initial seeds via the ‘two-phase’ scenario. This scenario was primarily borne out of complex simulations set within the  $\Lambda$ CDM cosmology (White and Rees, 1978; Blumenthal et al., 1984; Zhao et al., 2003; Naab et al., 2007; Oser et al., 2010), but has also been supported by data-model

comparisons (Driver et al., 2013). It dictates the formation of galaxies broadly through two main serial processes; galaxies experience a rapid initial burst of stars formed internally (*in-situ* star formation), followed later by a period of less-intense internal star formation, continued evolution of existing stars, and the smooth (gradual) accretion of material from external sources (*ex-situ* stellar and gas accretion).

Yet there exists an immense diversity of galaxies in the present-day Universe. The classification of this diversity was originally purely morphological, and there have been a number of such schemes (Hubble, 1926; de Vaucouleurs, 1959; van den Bergh, 1976; Kormendy and Bender, 1996, 2011; Cappellari et al., 2011b). From these schemes, galaxies are broadly separated into two main morphological categories; those containing spiral arms (S) and those which exhibit smooth elliptical morphologies (E). These classification schemes then further separate on the number and visibility of spiral arms (Sa-Sd), the presence of a central stellar bar (SBa-SBd), and how spheroidal elliptical galaxies are (E0-E5). Galaxies with a smooth but disk-like morphology with no detectable spiral arms are indicated by the intermediate classification S0. There remains a final class of morphologically-irregular (Irr) galaxies which defy simple classification. Hubble (1926) proposed the terms “early”- and “late”-type galaxies to categorise the galaxies along this sequence of morphology. These terms were intended to capture the increasing morphological complexity, not necessarily any evolutionary behaviour (Hubble, 1926, 1927). Modern evidence indicates that any evolution between these morphologies is likely to proceed from late- to early-type (for example, Moore et al., 1998; Bekki et al., 2002; Kovač et al., 2010; Peng et al., 2010b; Cappellari et al., 2011a; Bremer et al., 2018; Mamon et al., 2019) – spiral to elliptical. Interestingly, even the modern interpretation is inconclusive (Springel and Hernquist, 2005; Governato et al., 2009; Mapelli, 2015; Sparre and Springel, 2017; Pak et al., 2019), as there appears to be no single evolutionary track for galaxies owing to the diversity of histories they can experience.

The ‘shapes’ of galaxies are typically characterised by the lengths of their three spatial axes; the ‘major’ (longest), intermediate, and ‘minor’ (shortest) axes, with intrinsic lengths  $A$ ,  $B$ , and  $C$ , respectively. Thus, a system is spherical if  $A = B = C$ , axisymmetric if  $A = B > C$ , or triaxial if  $A > B > C$ . Observationally these lengths are rarely available, but it is instead straight-forward to measure the ratio of the two space dimensions of a projected image. This ratio is the observed ellipticity  $\varepsilon = 1 - C'/A'$ , for the projected major and minor axes  $A'$  and  $C'$ , respectively. It is possible to derive the *statistical* distribution of intrinsic shapes from these projected measurements over an entire galaxy population (Hubble, 1926; Sandage et al., 1970; Lambas et al., 1992; Tremblay and Merritt, 1996; Ryden, 2004, 2006; Vincent and Ryden, 2005; Kimm and Yi, 2007; Padilla and Strauss, 2008; Méndez-Abreu et al., 2010; Yuma et al., 2012; Weijmans et al., 2014; Foster et al., 2017; Li et al., 2018b). To measure the intrinsic shape of an individual galaxy, more sophisticated analyses are required (see § 1.5).

Meanwhile, the projected surface brightness has played a key role in understanding galaxy formation and evolution, in particular through its radial profile. In addition to his pioneering morphological classifications, Hubble (1930) provided an analytic framework to represent these profiles as a simple power-law in projected radius  $r$ . An alternative power-law formalism, tailored to ETG, was later introduced (de Vaucouleurs, 1948, 1959), which had a fixed 1/4 slope, and was normalised to the projected radius containing half of the total light; the half-light (‘effective’) radius  $R_e$ . This relation was later generalised by Sérsic (1963) into

a universal ‘Sérsic’ profile given in Eq. (1.1), parametrised by the shape  $n$ ,

$$I(R) = I_e \exp \left\{ -b_n \left[ \left( \frac{R}{R_e} \right)^{\frac{1}{n}} - 1 \right] \right\} \quad (1.1)$$

where  $I_e$  is the projected intensity at  $R_e$ .  $b_n$  is a  $n$ -dependent coefficient which can be evaluated numerically according to  $\gamma(2n; b_n) = \frac{1}{2}\Gamma(2n)$  for the lower incomplete, and complete, Gamma functions  $\gamma$  and  $\Gamma$ , respectively. With  $n = 4$ , the relation reverts to that of de Vaucouleurs (1948), while  $n = 1$  results in a standard exponential profile. The more general ‘Nuker’ law was proposed as an alternative for the central regions of ETG (Lauer et al., 1995, and independently proposed for the intrinsic, rather than projected, density; Zhao, 1996, 1997).

Another quantitative way of characterising galaxy morphology is to model the projected surface brightness through the identification of structural components; morphologically-distinct regions within individual galaxies. These analyses were initially conducted on radial surface brightness profiles, which appeared to be the superposition of at least two distinct components (Kormendy, 1977; Burstein, 1979; Boroson, 1981; Kent, 1985; Lauer, 1986; Aguerri et al., 2005; Yoshino and Ichikawa, 2008; Reis et al., 2020). Such one-dimensional studies have been found to introduce systematic errors (Baggett et al., 1998), and so a similar approach can be applied to the photometric images themselves, rather than radial profiles (Shaw and Gilmore, 1989; Byun and Freeman, 1995; Jong, 1996; Moriondo et al., 1998; Scorza et al., 1998; Souza et al., 2004; Wadadekar et al., 1999; Khosroshahi et al., 2000; Peng et al., 2002; Gadotti, 2009; Méndez-Abreu et al., 2017; Argyle et al., 2018; Bottrell et al., 2019; Cook et al., 2019; Barsanti et al., 2021). Such works established the paradigm in which the diversity of galaxies is explained by the relative contribution of a central elliptical bulge and an outer flattened disk. These techniques usually define the disk as the (outer) portion of the light which has a Sérsic index  $n = 1$ , and, somewhat arbitrarily, the bulge as the (central) portion with  $n \gtrsim 1$  (though with much more general approaches available, such as GALFIT; Peng et al., 2010a). This interpretation has been complicated by finding ‘bulges’ with  $n \lesssim 1$  (Salo et al., 2015), and those with significant rotation which can have  $n \sim 1$  (Krajnović et al., 2013). At the same time, embedded disks have been found within bulge-like components (for instance, Scorza et al., 1998), meaning that neither Sérsic index nor location within the galaxy can necessarily discriminate between these photometric components. Nevertheless, on account of the breadth of applications of such techniques, the established paradigm seemingly ratifies the two-phase scenario of galaxy formation; the central bulge forms in the initial rapid burst, while the disk forms later and more gradually in the second phase. More recently, and motivated by the increasingly detailed data of the Milky-Way, additional stellar components are being included, including multiple stellar disks (‘thin’ and ‘thick’), bars, and/or stellar halos (for example, Janz et al., 2012; Huang et al., 2013; Salo et al., 2015; Méndez-Abreu et al., 2017).

While the two-phase scenario has been successful in its aim of describing the broad population of galaxies observed in the Universe, the history of any given galaxy may deviate significantly from this paradigm. There are many often-competing processes which dictate the formation, evolution, and present-day state of a galaxy on an individual basis. A given galaxy may experience multiple episodes of internal star formation over its lifetime (for instance, if it acquires more gas at later times through the cosmic web and undergoes ‘rejuvenation’), may experience multiple distinct accretion/merger events, or could for instance have had little/no early bulge formation (Weinzirl et al., 2009). This is further complicated

by the observations of twists in the angle of the major axis (position angle) within a galaxy, implying an underlying distribution which is triaxial (Bertola and Galletta, 1979; Leach, 1981; Mizuno and Hamajima, 1987), which needs to be accounted for by this scenario of galaxy formation. Thus, the order and rate of occurrence of these two phases of galaxy evolution is not necessarily as straight-forward as a simple serial progression. Nevertheless, whether a galaxy's history is simple or complex, it is clear that the ways in which galaxies assemble their mass can be divided into those two main categories; *in-situ* and *ex-situ*.

### 1.3 *In-Situ* Star Formation in Galaxies

Star formation is a complex process involving all of the fundamental forces of physics; gravitation, electromagnetism, and the strong and weak nuclear forces. It is subsequently difficult to accurately explain from both a theoretical and observational perspective (see review of Kennicutt and Evans, 2012, for both Galactic and extragalactic perspectives). Nevertheless, through our unparalleled perspective into the Milky-Way, it has emerged that star formation typically occurs via the coalescence of relatively cool molecular gas into dense clouds which are clumpy on small scales. The over-densities in these clouds can then collapse to form stars. A single Giant Molecular Cloud (GMC) can form in excess of hundreds of individual stars (see Lada and Lada, 2003, and references therein), with some distribution in the resulting stellar masses (see § 1.3.1). At the earliest cosmological epochs, the gas from which these stars were to be created would be predominantly composed of Hydrogen, with a non-negligible Helium fraction, and trace amounts of Lithium, as this is believed to be the primordial composition of the Universe (Fumagalli et al., 2011; Coc and Vangioni, 2017, and the review of Zyla et al., 2020). The exact proportion of Lithium, however, remains contentious as the observed abundance is lower than predicted by Big Bang nucleosynthesis at  $> 5\sigma$  significance (Tanabashi et al., 2018). The stars that formed in a given GMC would inherit this primordial chemical composition, and would all be of the same age (from a cosmological perspective). Through stellar evolutionary processes, elements heavier than Helium ('metals' hereafter) would be generated internally in stars, then deposited into the surrounding environment as gas at the end of each star's life. GMC could form once again from this expunged gas, forming new stars with higher proportions of these metals – higher metallicity. This cycle is described in, for instance, Hopkins et al. (2011). Metallicity in this work is always measured relative to the Solar abundance, and is given in the form

$$[\text{S}/\text{T}] = \log_{10} \left( \frac{\text{S}}{\text{T}} \right)_{\text{obs}} - \log_{10} \left( \frac{\text{S}}{\text{T}} \right)_{\odot} \quad (1.2)$$

for some atomic species S and T. In this notation, the abundance of all metals – that is, the total metallicity – is denoted as [Z/H] for heavy-element and hydrogen abundances, Z and H, respectively.

The metal content of the Universe is gradually built up via this continual process. Therefore, from this argument alone (see, for instance, Portinari et al., 1998), there should exist a relationship between when a star is created (its present-day age) and its inherited metallicity, which would on average increase with cosmic time. Such an age-metallicity relation has indeed been observed for the Milky-Way and other local resolved systems (Twarog, 1980; Meusinger et al., 1991; Edvardsson et al., 1993; Ng et al., 1997; Piatti, 2012; Dobbie et al., 2014; Haggi et al., 2017; Feuillet et al., 2019). However, there is a significant degree of scatter (for example, Bergemann et al., 2014; Villanova et al., 2014), which can be caused by, for

instance, the accretion of stars, or the accretion of gas which will go on to form stars, both with distinct chemistry to the original populations (discussed further in § 1.4.1). Moreover, star formation can not continue indefinitely even in the presence of gas. Energy can be re-injected into a galaxy which prevents the unabated cooling of gas and subsequent star formation. This energy, known as feedback, can originate from a number of sources. Stellar feedback arises from the process of star formation itself, whereby newly-formed stars emit winds which disperse their surroundings and massive stars undergo supernova explosions soon thereafter (for example, see Hopkins et al., 2014). The super-massive black holes (SMBH) residing in the centres of galaxies can temporarily accrete vast amounts of material, transforming into active galactic nuclei (AGN). AGN feedback is also suspected of impeding star formation (for example, see Beckmann et al., 2017). Once again, the diversity of assembly histories within the galaxy population – including the diversity in the accreted stars and gas – complicates the interpretation of observations of external galaxies.

### 1.3.1 Initial Mass Function

Each cluster of stars that forms from a GMC will exhibit a particular distribution of stellar masses. This distribution of masses at the time of formation is known as the stellar Initial Mass Function (IMF; Salpeter, 1955). The IMF is of critical importance for just about any deduction from observational data of galaxies. It is also one of the most poorly defined quantities in astrophysics. In this section, all relevant concepts are defined explicitly to avoid ambiguities and misnomers.

The stellar IMF is a count per unit stellar mass for a given star-formation event. It has two typical forms; as a function of linear and logarithmic stellar mass, as

$$\frac{dN}{dm} \propto \left(\frac{m}{M_\odot}\right)^\alpha \quad \text{and} \quad (1.3)$$

$$\frac{dN}{d \log_{10}(m)} \propto \left(\frac{m}{M_\odot}\right)^\Gamma \quad (1.4)$$

respectively, for the mass of an individual star,  $m$ . In these representations, the indices are related as  $\Gamma = \alpha + 1$ . Through copious observations of Milky-Way stars, there have been a number of iterations of this functional form. The original proposition by Salpeter (1955) was that over the stellar mass range  $m \in [0.4, 10.0] M_\odot$ , the data were reasonably represented by a single power-law with a slope of  $\alpha = -2.35$ . Miller and Scalo (1979) introduced a log-normal distribution, or “half-Gaussian”, which they state is consistent with the data for  $m \in [0.1, 50] M_\odot$ . This was later adapted by Chabrier (2003), who find that the IMF is a power-law for  $m \gtrsim 1 M_\odot$ , and a log-normal distribution below. A dual power-law function has also been proposed from a theoretical perspective (Hoffmann et al., 2018). Another approach is to consider the slope of the power-law function to depend on stellar mass in a piece-wise manner. One such example is that of Kroupa (2001), whose resulting IMF is of the form

$$\alpha = \begin{cases} 0.7 & \text{for } 0.01 < m/M_\odot < 0.08 \\ -0.3 & \text{for } 0.08 \leq m/M_\odot < 0.50 \\ -1.3 & \text{for } m/M_\odot \geq 0.50 \end{cases} \quad (1.5)$$

A version of the piece-wise power-law has been proposed where the mass regimes transition smoothly rather than discontinuously (Vazdekis et al., 1996). These examples are compared in Fig. 1.3. The broken power-law form has become the functional form for modern IMF

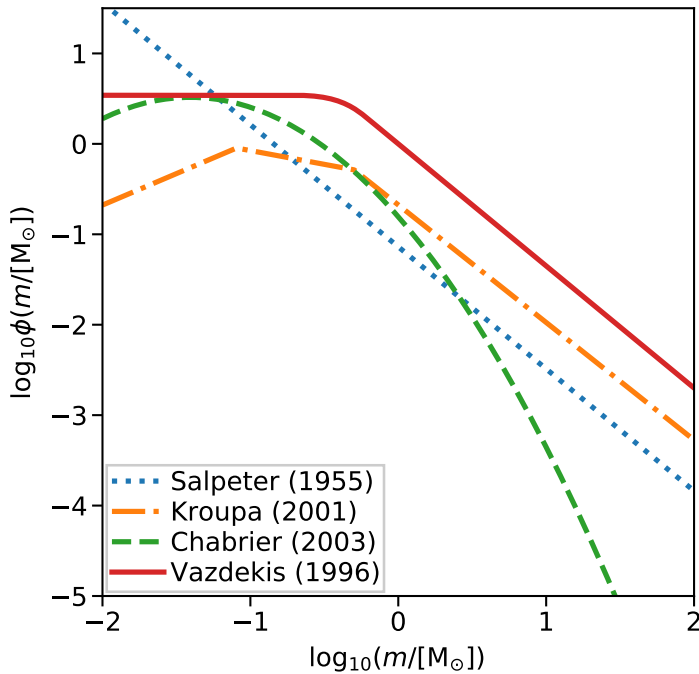


FIGURE 1.3: Various literature IMF functions. The single power-law from Salpeter (1955) is in dotted blue, the broken power-law from Kroupa (2001) is in dot-dashed orange, the log-normal from Chabrier (2003) is in dashed green, and the smooth broken power-law ‘bimodal’ from Vazdekis et al. (1996) is in solid red. The IMF from Vazdekis et al. (1996) is an explicit function of the high-mass slope  $\Gamma_b$ , so is presented here with a slope  $\Gamma_b = 1.35$  for illustration. Curves are offset for presentations.

studies, but with flexible slopes and stellar mass regimes (as used in Conroy et al., 2017; van Dokkum et al., 2017; Vaughan et al., 2018b; Martín-Navarro et al., 2019).

In the original derivation in Salpeter (1955) and a number of works following, two major assumptions defined the stellar IMF; that it is universal in space and time, and that the IMF conceptually describes a probability distribution function from which the masses of stars are drawn with some inherent degree of stochasticity. These assumptions were based on the available data at the time, and whether or not either of them are valid has profound implications for the physics of star formation (McKee and Ostriker, 2007; Zinnecker and Yorke, 2007) and by extension (the *in-situ* portion of) galaxy formation. This is because, especially for integrated-light observations, almost all measurable quantities require the consideration of an IMF. This includes stellar masses, ages, and chemistry, as well as the rate of star-formation, which have all subsequently been used in the vast majority of pivotal results on galaxy evolution. Whether, therefore, these assumptions hold is of considerable importance. Although this interpretation has persisted since those defining works (for instance Padoan et al., 1997), there has been mounting evidence recently that indicates that possibly neither of those assumptions are valid.

The universality of the IMF is the proposition that its shape is constant across star-formation sites, galaxy environments, and cosmic time. This in retrospect appears to be in spite of the evidence, as will become clear below. The very possibility of a non-universal IMF first necessitates further disambiguation regarding this concept, as proposed in Hopkins (2018).

## Stellar IMF

The *stellar* IMF defined above refers specifically to the mass function from individual GMC-scale star-formation events. As a result, measurements of the stellar IMF are typically limited to the Milky-Way and the close members of the Local Group for which these regions and/or individual stars can be resolved. The stellar IMF is typically measured for resolved stellar populations through one of two methods; direct star counts (Miller and Scalo, 1979; Scalo,

1986; Massey, 2002; Reid et al., 2002), or fitting theoretical isochrones to colour-magnitude diagrams (Selman et al., 1999; Espinoza et al., 2009; Geha et al., 2013; Bruzzese et al., 2020; Hosek Jr et al., 2019). Through various observations of resolved stellar populations, evidence against a universal IMF has been amassing almost since its inception (Schmidt, 1963; Scalo, 1998; Bartko et al., 2009; Elmegreen, 2009). Importantly, these works report variations in the *stellar* IMF, and this variation acts on the scale of local star-formation locations. The evidence for and against variation of the IMF on Galactic scales and beyond is reviewed in detail in Bastian et al. (2010).

## Galactic IMF

Studies of external galaxies through integrated-light observations where the physical scales of the stellar IMF are not resolved, are sensitive to the average over the many star-formation sites (and their respective IMF). This is the *galactic* IMF, and is in fact the most important IMF concept for this work. The Integrated Galactic IMF (IGIMF; Weidner and Kroupa, 2005; Kroupa et al., 2013) is a special case of this, under the assumption that the most massive star which can be formed depends on the mass of its parent cluster/GMC (which is not the case for a probabilistic IMF). In this work no specific assumption about the physics of star formation on those scales is made, and hence the general galactic IMF is the default paradigm.

Studies of the galactic IMF have come from a variety of techniques and data. Some studies target spectral features that are sensitive to the surface gravity of stars, most notably the absorption features of the NaI doublet at  $\lambda \sim 8190$  Å, the ‘Wing-Ford’ FeH (Wing and Ford, 1969) at  $\lambda = 9910$  Å, as well as the many TiO and TiO<sub>2</sub> features including  $\lambda \sim 5965, 6231, 8430, 8880$  Å (such as in Trager et al., 1998). These spectral features are present in observations of dwarf or low-mass stars ( $m \lesssim 0.3 M_{\odot}$ ), and weak or absent in more massive stars. Thus, measuring these features for different populations will result in the relative fraction of low- to high-mass stars (for a given age), which is in turn a proxy for how steep the IMF slope is. Works using such techniques are overwhelmingly in favour of a non-universal IMF (Whitford, 1977; Matteucci, 1994; Smith et al., 2012; Spiniello et al., 2012; Spiniello et al., 2014; van Dokkum and Conroy, 2012; La Barbera et al., 2013; La Barbera et al., 2016; La Barbera et al., 2019; Martín-Navarro et al., 2015; Cañameras et al., 2017; Lagattuta et al., 2017; Rosani et al., 2018; Sonnenfeld et al., 2018). These results imply variation of the galactic IMF *between* galaxies.

Another popular approach to the galactic IMF is through gravitational mass-to-light ratio ( $M/L$ ) measurements. This technique relies on the measurements of the total mass of galaxies (stars, gas, dust, DM), typically through the stellar kinematics and/or strong gravitational lensing. This total mass can then be compared with the stellar mass inferred from the luminous component of the galaxy (which requires a choice of IMF). Any discrepancy, and its magnitude, provides an estimate for how accurate the choice of IMF is, in terms of its mass normalisation. However, discrepancies between gravitational and stellar masses will also arise due to the presence of DM (§ 1.1), and therefore accurately taking into account its mass and distribution is critical if such an approach is to constrain the IMF. Another possible source of discrepancy between gravitational and stellar masses is through the contribution of gas and dust not accounted for when measuring the stellar mass. This can mostly be avoided by studying galaxies which have undetectable quantities of such material. ETG are usually assumed to be such galaxies. Dabringhausen et al. (2009) also discusses these sources of discrepancy for  $M_{\text{grav}}/L$  studies of the IMF. Many works have found evidence that the degree of discrepancy between the dynamical and stellar masses – interpreted as

variation of the galactic IMF – correlates with other galaxy properties. Numerous studies using dynamical modelling (Cappellari et al., 2012; McDermid et al., 2014; Tortora et al., 2014; Lyubenova et al., 2016; Davis and McDermid, 2017; Li et al., 2017; Mendel et al., 2020) and strong gravitational lensing (Treu et al., 2010; Posacki et al., 2015; Leier et al., 2016; Newman et al., 2017; Collier et al., 2020) have all found evidence in favour of variation in the galactic IMF, with varying assumptions between these works regarding – among other things – the stellar-population and DM distributions. The study of Thomas et al. (2011) found good agreement between the general trends derived from dynamical-modelling and lensing approaches for the same sample. Interestingly, Smith (2014) found that while the general trends agree, the interpretations of the variation in the IMF are incompatible between these two approaches on a galaxy-by-galaxy basis. So while there exists an apparent tension regarding the interpretation of *why* it varies, there remains strong evidence for variation of the galactic IMF. In this case also, the scale for variation is between galaxies. A comprehensive review of evidence in favour of IMF variation for ETG, using the techniques described here, is presented in Smith (2020).

It has recently been possible, through developments in data quality, theoretical modelling, and computational techniques, to undertake the aforementioned studies at various locations across a single galaxy. This leads to constraints on the galactic IMF, but in a spatially-resolved manner. Once again, works on spectral features (Alton et al., 2017; van Dokkum et al., 2017; Parikh et al., 2018; Sarzi et al., 2018; Vaughan et al., 2018a; Martín-Navarro et al., 2019; Zhou et al., 2019) and  $M_{\text{grav}}/L$  techniques (Davis and McDermid, 2017; Oldham and Auger, 2018b,a) find evidence for variation of the galactic IMF, in this case *within* individual galaxies. Spatial variations in spectral features have been seen for quite some time (Delisle and Hardy, 1992), however that work was (perhaps justifiably) hesitant to interpret those results as spatial variation of the IMF. Using a spatially-resolved spectral approach on one galaxy, Mentz et al. (2016) find results consistent with the Kroupa (2001) IMF or one with a slightly higher relative abundance of high-mass stars (more shallow slope). Their data suggest a tentative increase in steepness of the IMF slope towards the very centre, but with large errors. Models of the IMF also predict variations depending on local galactic properties (for example Fontanot et al., 2018).

Conversely, there are a number of works which conclude that the measured mass for external galaxies is consistent with the mass derived with a given IMF. This would imply that those results are consistent with a universal IMF. However, the reference IMF are often different, with some works consistent with the Salpeter (1955) IMF (Spinelli et al., 2011), the Kroupa (2001) IMF (Smith and Lucey, 2013; Smith et al., 2020; Alton et al., 2018), or the Chabrier (2003) IMF (Zieleniewski et al., 2017). Therefore, even in these cases, the combined evidence favours a varying galactic IMF. Finally, it is important to note that even in a universe where the stellar IMF is universal, this could still lead to observed variations of the galactic IMF due to differences in the assembly processes between galaxies (and in different regions within individual galaxies).

## Cosmic IMF

Finally, the average stellar mass distribution over the observable galaxy population is known as the cosmic IMF. There are various methods to study the cosmic IMF, with constraints coming from the density of star formation over cosmic time (Baldry and Glazebrook, 2003; Hopkins and Beacom, 2006; Fardal et al., 2007; Nanayakkara et al., 2017), colour-equivalent-width planes (Hoversten and Glazebrook, 2008), the ratios of specific sub-millimetre emission lines

for high-redshift galaxies (Zhang et al., 2018; Cai et al., 2020), the density of stellar mass over cosmic time (Wilkins et al., 2008),  $M_{\text{grav}}/L$  arguments (van Dokkum, 2008), targeted theoretical models (Narayanan and Davé, 2013), as well as cosmological considerations based on the evolving conditions in the very early Universe (Smith et al., 2009; Trenti and Shull, 2010). While the cosmic IMF is substantially less studied than either the stellar or galactic IMF, the majority of evidence provided here posits a variable cosmic IMF. This variation acts not only on cosmological volumes, but also on cosmological time-scales.

## Correlations of the IMF

Across these different definitions of IMF, the breadth of physical scales on which they act, the specific shape and functional form, and whether it is universal or not, the actual *meaning* of the IMF is also to be contended. The formation of stars has been believed to be an inherently stochastic process resulting from turbulence-driven gravitational collapse (McKee and Ostriker, 2007). In this scenario, the IMF dictates the probability for stars to form with a given stellar mass (for instance Andrews et al., 2014). Recent studies, however, show that perhaps this turbulence is not necessary for star formation (Li et al., 2020). Observations of filamentary fragmentation on local star-formation scales find that the resulting stellar mass distribution depends on the number of intersecting filaments at the site of star formation (Hacar et al., 2018). Finally, by studying resolved star-formation sites, a  $m_{\star,\text{max}} - M_{\text{ecl}}$  correlation was found, which relates the most massive star formed  $m_{\star,\text{max}}$  to the total mass of its parent cluster  $M_{\text{ecl}}$ , and which is approximately linear over five decades of cluster mass (Stephens et al., 2017; Yan et al., 2017). These works indicate that the turbulence-driven stochastic process of star formation, and hence interpretation of the IMF, may be incomplete. The scenario in which the IMF depends on some physical process or other in a deterministic way, raises the question of just which processes and/or properties it depends on.

The IMF (or some parametrisation thereof) has been observed to correlate with a number of local or global (galactic) properties. A growing body of work has shown trends of the galactic IMF with the central stellar velocity dispersion  $\sigma_e$  (Treu et al., 2010; Cappellari et al., 2012; Wegner et al., 2012; Conroy et al., 2013; Ferreras et al., 2013; Geha et al., 2013; Tortora et al., 2013; Shetty and Cappellari, 2014; Spiniello et al., 2015) – as a proxy for the stellar mass in virialised systems (see § 1.5). This indicates that galaxies with higher velocity dispersion contain more unaccounted mass with respect to standard IMF parametrisations, and this can originate from either low-mass stars which are very dim, or remnants of high-mass stars which radiate no light at all. Incidentally, these indistinguishable origins – dim stars, or stellar remnants – result from opposite ends on the IMF, making the interpretation of these results particularly precarious. The correlation with photometric colours (van Dokkum and Conroy, 2012) may indicate an underlying trend with the stellar populations which give rise to those colours. Indeed, correlations have been found with the [Mg/Fe] abundance (Conroy and Dokkum, 2012, though with conflicting results from Smith, 2014; La Barbera et al., 2015), the abundance of all the elements produced through  $\alpha$ -processes of nuclear fusion ([ $\alpha$ /Fe]; McDermid et al., 2014), the total metallicity (McDermid et al., 2014; Martín-Navarro et al., 2015; Gennaro et al., 2018), and stellar age (McDermid et al., 2014). A higher abundance of high-mass stars has been found for galaxies with higher star-formation rate (Gunawardhana et al., 2011). A number of independent techniques have found evidence that the IMF varies with galactocentric radius (Alton et al., 2017; Davis and McDermid, 2017; van Dokkum et al., 2017; Zieleniewski et al., 2017; Parikh et al., 2018; Vaughan et al., 2018a), where an excess of low-mass stars is observed at smaller radii – although in this case, the physical

cause of the correlation is almost certainly some other parameter which also happens to vary with galactocentric radius. It has recently been suggested that the spatially-resolved galactic IMF is somehow tied to the orbits which those stars follow (Martín-Navarro et al., 2019). A dependence on time (redshift) has been proposed for both the cosmic (van Dokkum, 2008; Narayanan and Davé, 2013) and galactic (Ferreras et al., 2015; De Masi et al., 2019) IMF, where more massive stars formed at earlier times. Constraining these correlations will shed light on the fundamental physical processes driven by the IMF, and will consequently also illuminate how exactly the IMF should be interpreted.

It has become apparent from the discussion above, which does not even recount all of its subtleties and observational difficulties, that the IMF itself may be a problematic concept. The large dynamic range of physical scales that is traversed by the ‘IMF’ poses interesting challenges for star and galaxy formation. Understanding the IMF will require a model which explains the variation on local through to cosmological scales. Thus, constraining the IMF to meet this requirement remains a crucial aspect of modern astrophysics.

### 1.3.2 Population Synthesis

The stellar populations of a galaxy reveal a great deal about its assembly. In the two-phase scenario of galaxy formation, each phase should leave a distinct signature in these populations. The initial violent burst of star formation should result in stars that are old (in the present-day) and have low metallicity (metal-poor) due to their formation from primordial gas. Any star formation that occurs during the second phase will result in younger stars which are typically more metal-rich, since they likely formed from the gas expelled from the first generation of stars.

Different stellar populations will manifest themselves observationally through the relative strength of the flux coming from the galaxy as a function of wavelength. These measurements constitute a Spectral Energy Distribution (SED) or spectrum, for coarse and fine sampling of wavelength, respectively. Therefore, decoding the populations in a galaxy from their SED and spectra is of critical importance to understanding how galaxies have formed.

A common tool to do this is through population synthesis models. The goal of population synthesis models is to predict the SED or spectrum of a population of stars that has a given age, chemical composition, and was formed with a given IMF. Each of these constitutes a Single Stellar Population (SSP), and many such populations are explored by varying the age, metallicity and IMF. To do this, individual stars are first modelled through stellar evolution theory, or observed directly typically in the Solar vicinity. The theoretical models can often explore a wide range of stellar population parameters, but are forced to make specific assumptions in lieu of a complete theory of stellar evolution. Models derived from the empirical spectra are limited in range to the stellar populations which are near our Sun, but do not suffer from any systematics and uncertainties associated with stellar evolution theory. In either case, in order to convert a series of stellar parameters into the properties of the integrated population, these stellar spectra/models must ‘evolve’ from their formation to their given age. This is done through isochrones; the track a population of a single age will form in the intrinsic  $T_{\text{eff}} - \log g$  plane (Hertzsprung-Russell diagram; Hertzsprung, 1911; Russell, 1914, or the observational equivalent, the colour-magnitude diagram). There have been a number of isochrone models, such as the ‘Yonsei-Yale’ (Yi et al., 2001), ‘Padova’ (Girardi et al., 2000, 2002), BaSTI (Pietrinferni et al., 2004; Hidalgo et al., 2018), ‘Dartmouth’ (Dotter et al., 2007) and MIST (Dotter, 2016; Paxton et al., 2010, 2013, 2015; Choi et al., 2016), with differences including the treatment of stellar evolution physics and unresolved populations

(including the fraction of stars in multiple systems).

There has also been a large set of work on developing the predictions and SSP models for given stellar populations (Tinsley, 1978; Bruzual, 1983; Bruzual and Charlot, 1993; Bruzual and Charlot, 2003; Bressan et al., 1994; Fioc and Rocca-Volmerange, 1997; Maraston, 2005; Maraston et al., 2020, fSPS from Conroy et al., 2009; Conroy and Gunn, 2010, (E)MILES/MUISCAT from Vazdekis et al., 2010, 2012, 2016; Falcón-Barroso et al., 2011). Differences between these models include (for those that utilise them) those inherent to the isochrone models, and also in the choice of which empirical ('Pickles' from Fanelli et al., 1992; Pickles, 1998, ELodie from Prugniel and Soubiran, 2001, STELIB from Borgne et al., 2003, MILES from Sánchez-Blázquez et al., 2006, XSL from Chen et al., 2014; Gonneau et al., 2020, MUSE from Ivanov et al., 2019, or MaSTAR from Chen et al., 2020), semi-empirical (Lejeune et al., 1997; Lejeune et al., 1998; Westera et al., 2002), or theoretical (Martins et al., 2005, UVBLUE from Rodríguez-Merino et al., 2005, MARCS from Gustafsson et al., 2008, or Coelho, 2014) stellar spectra are used. In fact, Maraston and Strömbäck (2011) tested the SSP models generated from a number of different empirical stellar spectral libraries on the same data and found significant differences among them. Ge et al. (2019) performed similar tests but with known (mock) input spectra, and also found differences in each models' ability to recover the parameters. In addition, Baldwin et al. (2018) showed that while some of these models agree reasonably well in the optical regime, they differ even more substantially in the infrared (IR) regime. This is particularly concerning for the IMF studies since many of the gravity-sensitive spectral features (§ 1.3.1) are in the IR. Finally, there are a number of tools available which fit observations for this purpose, including pPXF (Cappellari and Emsellem, 2004; Cappellari, 2017), STARLIGHT (Fernandes et al., 2005), STECKMAP (Ocvirk et al., 2006), GANDALF (Sarzi et al., 2006; Falcón-Barroso et al., 2006), SINOPSIS (Fritz et al., 2007), VESPA (Tojeiro et al., 2007), ULySS (Koleva et al., 2009), FIT3D (Sanchez et al., 2016), PROSPECTOR (Leja et al., 2017), FADO (Gomes and Papaderos, 2017), FIREFLY (Wilkinson et al., 2017) for spectra, or (x-)CIGALE (Burgarella et al., 2005; Noll et al., 2009; Boquien et al., 2019; Yang et al., 2019), BAYESED (Han and Han, 2012, 2018), BEAGLE (Chevallard and Charlot, 2016), BAGPIPES (Carnall et al., 2018), PROSPECT (Robotham et al., 2020) for photometric SED.

These differences aside, the application of SSP to real data is conceptually straightforward. Since the observed flux of galaxies is integrated over the many co-existing stellar populations in a galaxy, it stands to reason that these data can be represented as a combination of many individual SSP that represent a range of stellar ages, chemistry, and IMF. The relative contribution between these models is tuned in order to match each observed spectrum/SED. In practice, there are a number of issues that prevent a direct comparison of models to data. For instance, dust in our Galaxy and the galaxy of interest will affect the observations but not the models. This can be taken into account by correcting the observations for Galactic extinction using comprehensive observations of the Milky-Way's dust content (Schlegel et al., 1998; Schlafly and Finkbeiner, 2011). For the galaxy of interest, this can be mitigated by studying galaxies which have little dust content and/or include dust models as part of the SSP fit. Another caveat is that in practise the model spectrum is computed as a weighted linear combination of the various pre-computed SSP models, and so sensible solutions are obtained only if the varied parameters are linear. As a counter-example, the typical parametrisation of the IMF is the slope over some range of stellar mass. The slope of the integrated IMF for a composite stellar population is *not* the weighted combination of the IMF slopes that generated each population. By extension, the response of the model spectrum to changes in the IMF will also be non-linear. For this reason, many applications of SSP fitting keep the IMF fixed to one choice. An avenue which does not suffer from this particular issue is to generate SSP

models in real-time, during the fitting, such that the resulting spectrum takes into account the non-linear response of the IMF (or any other such parameter). These approaches have recently been implemented, but at considerably greater computational cost (Conroy et al., 2017; van Dokkum et al., 2017; Vaughan et al., 2018b; Martín-Navarro et al., 2019).

Despite these caveats, population synthesis techniques have allowed the extensive surveying of the galaxy population’s chemical and chronological distributions (for example Scott et al., 2017; Li et al., 2018a; Lacerna et al., 2020). By analysing the relative weighting between the SSP models for a given observed spectrum, its present-day chemistry can be inferred. In addition, the chronology of this chemistry is granted by sampling the SSP models over a range of stellar ages. In combination, the relative abundance of different chemical populations as a function of stellar age produces a Star-Formation History (SFH). For well-calibrated data of galaxies with known distances (and assumed IMF), the SSP models can be used to compute absolute stellar mass measurements, and in combination with the SFH, allows for the measurement of the star-formation rate (SFR).

One of the key issues with the derivation of SFH is the accuracy with which they can be recovered from observational data. SFH from full-spectral-fitting approaches are typically ‘non-parametric’ since they result from the flexible combination of individual models constrained solely by the data. Given this flexibility, there usually exists a number of different combinations of models which re-produce the data equally well (within observational uncertainties), but can lead to significantly different physical interpretations for the same observed spectrum. There are now a number of ways in which this issue can be mitigated. The specific spectral features which provide the most information have been studied (Asa’d and Goudfrooij, 2020; Goudfrooij and Asa’d, 2020), resulting in optimal ranges in wavelength which the observed spectra should cover. This is typically dependent on the signal-to-noise ( $S/N$ ), however. Higher  $S/N$  spectra have repeatedly been shown to result in more stable and accurate constraints, based on tests with known input spectra (Boecker et al., 2020; Asa’d and Goudfrooij, 2020; Goudfrooij and Asa’d, 2020). Finally, additional assumptions can be imposed to limit the flexibility of the solution, which is most often that the SFH of galaxies should vary relatively smoothly. Mathematically, this is implemented as a regularisation term during the fitting. Regularisation penalises solutions which vary rapidly in the phase-space being studied (in typical cases, this is stellar age and metallicity), which would *otherwise* be indistinguishable from a more smoothly-varying solution. Physically, this implies that there are no sudden bursts of star-formation across cosmic time or contributions from dramatically different metallicities in a single spectrum, unless such variations are required to fit it well. Regularisation is used in a number of physical problems in astrophysics, not limited to the recovery of SFH, but there is rarely a rigorous method of implementation, in particular regarding the quantitative tolerance on “indistinguishable solutions”. An alternative approach, and another avenue to mitigate degeneracies, is to use parametric SFH, where their variations are assumed to be described by smooth analytic functions of one or a few parameters. With the reduced flexibility imposed by the functional form, the solutions can not vary as much as in the non-parametric case, but are subject to the accuracy of their assumptions. Parametric SFH are typically reserved for SED fitting, where the information content in specific absorption features can not be exploited. Overall, such methods are reliable at making inferences about the chemical history of galaxies especially in their relative behaviour.

Stellar populations, stellar masses, and SFR measurements have opened vast areas of galactic parameter-space to constrain their formation and evolution. Using spectral-fitting techniques, it was found that the vast majority of local galaxies have not formed any significant fraction of their stellar mass in the last 2 Gyr (Kauffmann et al., 2003). It was later found

that the epoch at which galaxies stop forming stars depends on their present-day stellar mass, with more massive galaxies assembling earlier (Thomas et al., 2005; Gallazzi et al., 2008). Similarly, over many galaxy surveys which targeted different epochs, it has been possible to survey the cosmic SFR, which plays a critical role for evaluating the cosmic IMF. More than this, it was found that the average SFR of the Universe increased smoothly for  $\sim 3.5$  Gyr after the Big Bang, peaked at what is now redshift  $z \sim 1.9$ , and has been declining smoothly since (see Madau and Dickinson, 2014, for a recent review). Just like the population-average two-phase scenario of galaxy formation, though, an individual galaxy SFH can be markedly different from this cosmic behaviour.

Concerning galaxy evolution more directly, SED- and spectral-fitting techniques have shown that a galaxy's stellar mass is correlated with the average metallicity of its gas (Tremonti et al., 2004; Lee et al., 2006; Kewley and Ellison, 2008; Zahid et al., 2012; Andrews and Martini, 2013) and stars (Gallazzi et al., 2005 or higher-dimensional correlation between stellar mass, stellar metallicity, and SFR; Mannucci et al., 2010). A *luminosity*-metallicity relation had been seen previously (McClure and van den Bergh, 1968; Lequeux et al., 1979), but it was only through the combined improvements in SSP models and SED- and spectral-fitting techniques that permitted the observation of the more physically-meaningful mass-metallicity relation. It has recently been proposed, however, that both gas-phase (D'Eugenio et al., 2018) and stellar (Barone et al., 2018) metallicity more closely track the gravitational potential rather than stellar mass, reflective of galaxies being able to retain more heavy elements in deeper gravitational potentials. Moreover, there is a clear correlation between SFR and stellar mass for the population of galaxies which have measurable SFR (Brinchmann et al., 2004; Noeske et al., 2007; Peng et al., 2010b; Speagle et al., 2014; Renzini and Peng, 2015), known as the Star-Formation Main Sequence (SFMS).

The natural result of combining these spectral-fitting analyses with spatially-resolved data is the investigation of the stellar-population variations within galaxies. Most often, this is characterised by the radial profiles of each parameter and/or its gradient, which have been thoroughly studied in their connection to plausible assembly histories (Mehlert et al., 2003; McDermid et al., 2006a, 2014; Spolaor et al., 2009; Rawle et al., 2010; Pastorello et al., 2014; Hirschmann et al., 2015; Goddard et al., 2017; Molaeinezhad et al., 2017; Corsini et al., 2018; Ferreras et al., 2019; Fraser-McKelvie et al., 2019; Breda et al., 2020; Coenda et al., 2020; D'Eugenio et al., 2020; Grossi et al., 2020; Santucci et al., 2020). These have shown that age and metallicity, for instance, are typically characterised by radially declining profiles. Crucially, departures from these gradients can constrain diverse assembly histories, although atypical assembly histories can still give rise to typical radial gradients. Therefore, while gradients can provide key constraints on particular events formation pathways, a more general approach is still needed to overcome the observational degeneracies with measuring distinct assembly histories.

The techniques described here often fall under the umbrella term of ‘galactic archaeology’. They attempt to recover a galaxy’s history based on its present-day state. These techniques have evidently been able to uncover many interesting results, however they can not constrain the entire evolutionary history of a galaxy. For instance, stars that are formed externally, then later accreted (§ 1.4), may appear indistinguishable from stars of the same age which formed *in-situ*, thus masking an important event in the history of that galaxy. The stellar populations alone are insufficient to fully characterise such histories from observational data.

## 1.4 *Ex-Situ* Processes in Galaxies

By some estimates, present-day galaxies are predicted to have obtained  $\sim 60 - 80\%$  of their stellar mass from external sources (Oser et al., 2010). With such a significant contribution to the mass budget of galaxies, it is clear why the processes which assemble galaxies need to be understood. If such mass fractions do indeed originate from external sources, understanding this fraction and its spatial distribution will have dramatic subsequent effects on, among other things, many of the archaeological results described above.

### 1.4.1 Accretion

The merging of galaxies is believed to play a significant role in galaxy assembly (Larson, 1990), and to trigger substantial transformations in many of their observable properties (Barnes, 1992). This is because the merging process has a two-fold effect on the resulting galaxy; not only is the process itself typically violent and can dramatically re-organise the pre-existing stars, but the merging of both the baryonic and DM components of the constituent galaxies results in a deeper gravitational potential, which therefore changes the equilibrium state of that galaxy (although all of the mass of the merging galaxies does not necessarily remain bound to the resulting system; Valluri et al., 2007). Additionally, merging can include significant quantities of gas, which can cool efficiently, being collisional unlike the stars. Cool gas can then go on to form new generations of stars, which is another avenue by which mergers facilitate transformations.

Mergers are typically characterised by the relative mass of the two (or more) galaxies involved. ‘Major’ mergers typically refer to those with a mass ratio of 1 : 4 or larger, ‘minor’ mergers are between 1 : 4 and 1 : 10, and ‘mini’ mergers are up to 1 : 100. Most of the inferences about merging and its impact on galaxy evolution arise from sophisticated numerical simulations, where the merger can be tracked through time (see for instance Barnes, 1992; Valluri et al., 2007; Bournaud et al., 2008; Stewart et al., 2009; Chilingarian et al., 2010; Athanassoula et al., 2016 while Somerville and Davé, 2015; Naab and Ostriker, 2017 review these simulations in general), because their signatures are difficult to detect through observations (Mihos, 1995). Observations instead have to rely on cataloguing different systems at various stages of the merging process, owing to the long ( $\sim$  Gyr) time-scales involved. Interacting galaxies, or those which will soon interact, can be identified by proximity to one another in photometry, but should be confirmed spectroscopically to mitigate projection effects (Ventou et al., 2017). The presently-interacting systems are straight-forward to identify even through photometry (for instance Schweizer, 1996; Allam et al., 2004) owing to the visual disruptions caused by the interaction. Systems believed to be post-mergers can be identified using especially deep photometry to resolve remnants of past interactions which typically reside in the faint outskirts of galaxies (Iodice et al., 2016, 2017, 2019; Bílek et al., 2020). However, the systems observed at different stages of merging likely differ in their evolutionary histories and other physical properties, so the impact of the merging process is observationally difficult to isolate.

Mergers have been invoked to explain a number of observed properties of galaxies. Structural transformations are believed to be caused by major mergers, and minor mergers have been seen to result in larger galaxies (Chan et al., 2018). Star formation can be either suppressed (Croton et al., 2006; Hopkins et al., 2006; Khalatyan et al., 2008; Faisst et al., 2017) or induced (Mihos and Hernquist, 1996; Kannan et al., 2015; Cortijo-Ferrero et al., 2017; Weaver et al., 2018) by mergers. The net angular momentum of galaxies has also

been observed to change after a merger (Bournaud et al., 2004; D’Onghia et al., 2006; Romanowsky and Fall, 2012; Stewart et al., 2013; Zavala et al., 2016; Sparre and Springel, 2017; Tsatsi et al., 2017; Greene et al., 2018; Lagos et al., 2018), where the resulting angular momentum depends on the orbital trajectories of the merging galaxies (rather than the internal kinematics of each galaxy). Additionally, if the impacting galaxies contain large reservoirs of gas – or if gas is accreted from cosmic filaments – star-formation can subsequently occur in a thin-disk-like geometry, increasing both angular momentum and average SFR (Ellison et al., 2018). Conversely, if all other correlations are accounted for, no environmental dependence of the IMF has been observed (Rosani et al., 2018; Eftekhari et al., 2019). Finally, the most direct impact of mergers is the transformation of galaxy morphology. This is in fact the primary channel for the evolution of late- to early-type galaxies (Naab et al., 1999; Naab and Burkert, 2003; Bendo and Barnes, 2000; Cretton et al., 2001; Ciotti et al., 2007), except in the case where LTG can form from gas-rich mergers (Governato et al., 2009; Sparre and Springel, 2017).

### 1.4.2 Environment

Galaxies do not have to experience direct mergers to undergo transformations. Owing to the vast scales involved, individual galaxies may experience dramatically different local environments, depending on their position within the cosmic web. ‘Field’ galaxies exist (at least in the present-day) in isolation, in voids. Increasing in local density, galaxies may exist in pairs or multiples, as satellites of groups or clusters, or finally as the central systems of those groups and clusters. The presence of, or interaction with, other galaxies in dense environments is believed to be sufficient to cause changes to a galaxy’s physical properties. Moreover, the space between galaxies in clusters contains significantly more material compared to the field. Hot gas usually permeates the central regions of clusters, forming the intra-cluster medium (ICM). The ICM will exert non-gravitational forces on galaxies moving through it, and it has been suggested that this removes the outer, weakly-bound material from such galaxies (Gunn and Gott, 1972). In fact, many of the observational differences between central and satellite galaxies are seen predominantly in their outer regions (Spindler and Wake, 2017). Similarly, interactions between galaxies are believed to cause many of the observed asymmetric features such as ‘tidal arms’ (Toomre and Toomre, 1972), but are not strong enough to significantly alter, for instance, the disks in disk galaxies which are more tightly bound (Gerhard and Michael Fall, 1983). Thus, the local environment in which a galaxy resides has been observed to correlate with a number of observational characteristics of galaxies.

Both the projected and intrinsic morphologies of galaxies have been observed to depend on the local environment (Dressler, 1980; Postman and Geller, 1984; Ryden et al., 1993; Mayer et al., 2001; Fasano et al., 2010; Cappellari et al., 2011b; Rodríguez et al., 2016; Oh et al., 2018), where the presence of spiral features dramatically decreases for denser environments. It has been seen that galaxies in more dense local environments are larger (Huang et al., 2018; Gargiulo et al., 2019), even at fixed stellar mass. Galaxy colours (Peng et al., 2010b; Cibinel et al., 2013), SFR (Barton et al., 2000; Balogh et al., 2004; Poggianti et al., 2006; Allen et al., 2016; Wang et al., 2018; Barsanti et al., 2018; Davies et al., 2019; Owers et al., 2019), their constituent stellar populations (Thomas et al., 2005; Smith et al., 2012; McDermid et al., 2015; Schaefer et al., 2019), and the available gas content (Valluri and Jog, 1990; Zabel et al., 2019) have all been observed to correlate with environment, such that galaxies in denser environments are more red, have suppressed star-formation,

older average ages, and lower available gas. The incidence of merging has been shown to decrease for more massive galaxy groups (Pipino et al., 2014). Field galaxies may acquire angular momentum from the cosmic filaments they are connected to (Libeskind et al., 2012; Stewart et al., 2013; Tempel and Libeskind, 2013; Welker et al., 2020), while galaxy-galaxy interactions can increase the contribution of random motions within galaxies, resulting in lower net angular momentum in dense environments (Lee et al., 2018).

## 1.5 Stellar Kinematics

The kinematics of the baryonic content of galaxies provide insight into their most fundamental properties. Primarily, kinematics accurately characterise the gravitational (dynamical) mass, which is insensitive to the precise relative contributions of baryonic and dark matter. This renders kinematics a powerful tool in galaxy formation and evolution that is not subject to the same assumptions and uncertainties of most other galactic measurements. Beyond dynamical masses, stellar kinematics retain information of a galaxy’s history (even following a significant merger event; Valluri et al., 2007) owing to the fact that stars in galaxies can be considered collisionless\*. Unlocking this information provides an independent archaeological avenue to recover galactic assembly histories from observations.

### 1.5.1 Kinematic Properties

For unresolved observations, kinematics are measured by fitting absorption or emission lines of spectra, for stellar and gas kinematics, respectively. Analogous to the stellar population analyses (§ 1.3.2), the spectra of external galaxies can be modelled as a combination of many individual dynamical populations. For each spectrum, every population along an observed LOS has its own intrinsic kinematics. The resulting distribution of kinematics is the LOS velocity distribution (LOSVD). LOSVDs are typically parametrised using the Gauss-Hermite series (van der Marel and Franx, 1993; Gerhard, 1993; Binney et al., 1998), which is the extension of a Gaussian function with the Hermite polynomials. For practical reasons, this series is typically truncated to between 2 and 6 moments, with the first two terms approximating the true mean velocity  $V$  and velocity dispersion  $\sigma$ , respectively. Higher-order moments,  $h3$  and  $h4$ , describe departures of the LOSVD from a Gaussian shape due to skewness (asymmetry) and kurtosis (peakiness), respectively. The internal motions within a galaxy will shift absorption and emission features away from their laboratory (rest-frame) wavelengths through the Doppler shift (in addition to the global cosmological redshift caused by the galaxy’s motion as a whole), and so the location and shape of these features in observed spectra thus depend critically on the LOSVD. Using a series of rest-frame stellar spectra, it is then possible to derive an LOSVD which reproduces the observed absorption/emission lines, and in this way measure kinematics (such as the early implementation by Kuijken and Merrifield, 1993).

The dynamics of stars in galaxies sample the underlying stellar velocity ellipsoid (originally proposed by Schwarzschild, 1907), which is the distribution of stellar velocity dispersions – the magnitude of the random motions of stars – along all three principle axes.

---

\*In this context, ‘collisionless’ refers to the fact that the mean stellar density is a sufficient approximation in order to predict the motions of individual stars within that density. This is the case in galaxies, where there are many millions of stars which can be considered point-sources with respect to the distances between them.

Historically, the velocity ellipsoid for external galaxies is assumed to align with the cylindrical coordinate system, and so it is described by the radial, tangential, and vertical velocity dispersions,  $\sigma_R$ ,  $\sigma_\phi$ , and  $\sigma_z$ , respectively. The shape of this ellipsoid can then be characterised by its axis ratios, much like galaxy morphologies. For a general velocity ellipsoid, these are defined as (Binney and Tremaine, 1987; Cappellari et al., 2007)

$$\beta = 1 - \frac{\Pi_z}{\Pi_R} \quad (1.6)$$

$$\gamma = 1 - \frac{\Pi_\phi}{\Pi_R} \quad (1.7)$$

$$\delta = \frac{2\beta - \gamma}{2 - \gamma} \quad (1.8)$$

where  $\Pi_k$  is the contribution from the local  $\sigma_k$  at each location in the galaxy. A common simplifying assumption is that the velocity ellipsoid has a constant shape for a given galaxy, in which case  $\Pi_k = \bar{\sigma}_k$ , the average global velocity dispersion along that axis. A system has orbital isotropy if with  $\beta = \gamma = \delta = 0$ , and anisotropy otherwise. Since these measures are sensitive to the particular orbits on which the stars reside, they can therefore provide insight into possible violent disruptions (mergers) or internal instabilities that have shaped a galaxy over its history. However once again these intrinsic quantities can not be measured directly from observations due primarily to projection effects.

### 1.5.2 Observations of Stellar Kinematics

Galaxy kinematics are measured through one of three main observational utilities, each with their advantages and disadvantages. Early works utilised long-slit spectrographs, which collect a small number of spectra along one spatial dimension. The axis of the slit is typically aligned with the photometric major axis of the target galaxy, providing spectra – and therefore kinematic measurements – as a function of position from its centre. Long-slit data have been used in a vast body of work on galactic kinematics, including the DM results discussed above. Early mass census measurements used long-slit data to measure the asymptotic rotational velocities for a large number of nearby galaxies, via ionised gas (emission-line) kinematics (for example, Burbidge and Burbidge, 1959; Bertola, 1966; Bertola and Bernacca, 1967; Bertola and Capaccioli, 1977, 1978; Comte et al., 1979; Schweizer, 1980; Blackman, 1980, 1981; Blackman and Pence, 1982; Blackman, 1982; Danziger et al., 1981) or stellar (absorption-line) kinematics (for example, Walker, 1962; King and Minkowski, 1966; Demoulin, 1970; Morton and Chevalier, 1972; Morton and Chevalier, 1973; Bertola and Capaccioli, 1975; Sargent et al., 1978; Davies et al., 1983). Long-slit data were used for the first observations of both prolate rotation (where the kinematic major axis is the morphological minor axis; Bertola and Capaccioli, 1978), and counter-rotating components (see for example Franx and Illingworth, 1988; Bender, 1988; Jedrzejewski and Schechter, 1988; Jarvis and Peletier, 1991; Sarzi et al., 2000), which are hidden by the visual morphology. However in general long-slit data necessitated strong assumptions about the intrinsic geometry and observed inclinations of galaxies.

Exploiting the advances in multi-mode optical fibre technology for astronomical purposes, galaxy surveys were undertaken in which individual fibres targeted individual galaxies. This allowed many galaxies to be observed simultaneously, and facilitated the collection of spectra for truly large samples (millions) of galaxies. Pioneering surveys of this kind include the Sloan Digital Sky Survey (SDSS; York et al., 2000), the Two-Degree-Field Galaxy Redshift

Survey (2dFGRS; Colless et al., 2001) and its six-degree extension (6dFGRS; Jones et al., 2009), as well as upcoming programmes such as TAIPAN (da Cunha et al., 2017/ed). Data such as these can be used to, relatively straight-forwardly, derive ‘aperture’ velocity dispersion measurements for a large portion of the galaxy population (for instance, Sheth et al., 2003). Compared to long-slit spectra, measurements on aperture spectra lack any spatial information and focus solely on the central regions of galaxies. However they can be obtained in vastly greater numbers, and the derived velocity dispersions provide estimates of the dynamical mass over these large samples (albeit under specific assumptions about the light distribution and orbital anisotropy).

More recently, the implementation of Integral-Field Units (IFU) has revolutionised galaxy evolution research, including kinematic measurements. IFU collect spectra at many locations within a single galaxy. These instruments allow the investigation of galaxies over a near-contiguous area of the sky, and as a function of wavelength, producing 3D ‘data-cubes’. The growing array of IFUs have been built from one of a number of distinct design schemes. Lenslet IFUs use a regular grid of glass ‘lenslets’ to create the contiguous array of images which are fed to dispersive elements to produce a spectrum per lenslet. Such instruments include TIGER (Bacon et al., 1995), OASIS (Bacon et al., 2000), SAURON (Bacon et al., 2001), and OSIRIS Larkin et al. (2006). Fibre-bundle IFUs use many fibres (often in combination with lenslets) for a single galaxy, typically ordered in a hexagonal fashion to minimise the inter-fibre space. Such instruments include FLAMES (Pasquini et al., 2002), GMOS (Allington-Smith et al., 2002), VIMOS (LeFevre et al., 2003), PPAK (Kelz et al., 2006), KOALA (Ellis et al., 2012), VIRUS (Hill et al., 2014), SAMI (Bryant et al., 2015), and MANGA (Drory et al., 2015), as well as planned facilities such as ULTIMATE (Ellis et al., 2016). ‘Image slicer’ IFUs slice the two-dimensional image plane along one axis using a series of small staggered mirrors. Each slice can then be redirected, to be dispersed and imaged by a different region of the spectrograph. Such instruments include NIFS (McGregor et al., 2003), SINFONI (Eisenhauer et al., 2003) and now upgraded to ERIS (Davies et al., 2018), SWIFT (Tecza et al., 2006), MUSE (Bacon et al., 2010), KMOS (Sharples et al., 2013), FOCAS (Ozaki et al., 2014), and KCWI (Morrissey et al., 2018), and upcoming facilities such as GMTIFS (McGregor et al., 2012; Sharp et al., 2016), HARMONI (Thatte et al., 2016), and MAVIS (McDermid et al., 2020).

IFU kinematic data have begun to unravel the complexity of galaxy kinematics that was revealed by earlier long-slit data, providing unprecedented views of individual galaxies. IFU data have drastically improved the characterisation of Kinematically-Decoupled Cores (KDC), where different stellar populations rotate about different axes (not just counter-rotate about the same axis) and/or where the gas and stellar rotation axes do not align (e.g. Franx et al., 1991; Davies et al., 2001; Emsellem et al., 2007; McDermid et al., 2006b,a). Such data also facilitated more quantitative kinematic classification such as that of Krajnović et al. (2011). Overall, these analyses showed that simple photometric morphologies can harbour complex kinematics, and illustrated that morphology provides an incomplete categorisation of galaxies. However, IFU observations are difficult to scale to the numbers of galaxies achieved by aperture spectra surveys. Recently, such attempts have been made using fibre-bundle IFU, which typically permit of order tens of fibres per galaxy, and have achieved galaxy samples in the order of thousands. Such surveys include the Sydney-AAO Multi-object Integral-field spectrograph (SAMI; Croom et al., 2012) and the Mapping Nearby Galaxies at Apache point observatory (MaNGA; Bundy et al., 2015) surveys, as well as upcoming programmes such as HECTOR (Bryant et al., 2016, 2018).

Through these large and/or detailed surveys of the galaxy population, it has thus been possible to undertake kinematic classifications of galaxies, analogous to the morphological

classifications discussed above. In lieu of access to the shape of the intrinsic stellar velocity ellipsoid, observational alternatives were sought using these data sets. One of the first kinematic classification criteria was to establish the dominant mode of dynamical support via the straight-forward  $V/\sigma$  ratio, where galaxies are pressure- and rotation-supported for  $V < \sigma$  and  $V > \sigma$ , respectively. Such a classification is powerful because it could be measured straight-forwardly from widely available long-slit data. It was recognised observationally that this ratio correlates with the projected ellipticity  $\varepsilon$  (Illingworth, 1977; Schechter and Gunn, 1979; Davies, 1981), which could be compared to direct predictions from the tensor virial theorem (Binney, 1978, 2005). However, it later emerged that the interpretation of this ratio can be hindered by projection effects (e.g. Dehnen and Gerhard, 1994). A modern revision, exploiting the spatial resolution of IFU data, is the ‘stellar spin’  $\lambda_R \equiv \langle R |V| \rangle / \sqrt{V^2 + \sigma^2}$  (Emsellem et al., 2007). This quantity also reflects changes in the dominant mode of dynamical support, but does so in a spatially-resolved manner; that is, tracing the local angular momentum rather than global.

Galactic kinematics have been observed to correlate strongly with a number of other galactic properties, and these are believed to be driven by fundamental galaxy-formation processes. The total luminosity of elliptical galaxies was found to follow a tight power-law correlation with the central velocity dispersion, of the form  $L \propto \sigma^4$ ; the ‘Faber-Jackson’ relation (Faber and Jackson, 1976). In the three-dimensional space of half-light (‘effective’) radius  $R_e$ , central velocity dispersion  $\sigma_e$ , and central stellar surface brightness  $I_e$  (where ‘central’ is within  $R_e$ ), galaxies form a thin plane – the ‘Fundamental Plane’ – implying an intrinsic connection between these parameters (Djorgovski and Davis, 1987; Dressler et al., 1987). In fact, the Faber-Jackson relation is believed to be a re-projection of this plane from one set of parameters to the other, indicating that they are manifested by the same underlying physical processes. A relation analogous to the Faber-Jackson was found for disk galaxies, which relates their asymptotic rotational velocity  $V_{\text{rot}}$  (see Fig. 1.2) to their absolute magnitude (Tully and Fisher, 1977). It was then proposed that these relations are actually two manifestations of a universal connection between global kinematics and galactic properties, through the parameter  $S_K = \sqrt{KV_{\text{rot}}^2 + \sigma^2}$  (Weiner et al., 2006). Disk and elliptical galaxies have been found to simultaneously follow the  $S_K - M_\star$  relation with smaller scatter (Cortese et al., 2014; Aquino-Ortíz et al., 2018; Barat et al., 2019). This is likely to be a reflection of the virial theorem, which establishes the equilibrium condition between the kinetic energy and gravitational potential energy of self-gravitating systems, in this case approximated by  $S_K$  and  $M_\star$  (for the central region of galaxies, where DM is typically sub-dominant), respectively. In this respect then, such a connection is expected for a population of galaxies in which the majority are in virial equilibrium. Thus it can be seen how such kinematic properties provide a basis for the physical interpretation of the suite of observed galaxy properties. However, there remains sources of scatter and uncertainty in these relations that are yet to be understood, which could indicate that they too are projections of a more fundamental set of parameters.

### 1.5.3 Dynamical Models

Purely observational approaches to interpreting the measured kinematics of galaxies are limited in their applicability. This is driven by a number of causes. A major intrinsic limitation in extragalactic studies is the range of 3D geometries which are consistent with the observed 2D projection of a galaxy. For flattened observed geometries, the range of suitable deprojections is relatively small. Conversely, for increasingly circular projections, it becomes

difficult to distinguish intrinsically spherical galaxies from disk galaxies which happen to be viewed face-on (conventionally indicated with an inclination  $i = 0$ ). Furthermore, many different physical regions of the galaxy which lie on the same LOS are integrated into some unknown combination, necessarily dominated by the regions which contribute the most light (which is also *a priori* unknown). Thus, the direct interpretation of observed kinematics is inherently hindered by these issues. Instead, by confronting kinematic data with dynamical models, intrinsic properties of galaxies can be uncovered which are otherwise inaccessible. High-quality data and subsequent analyses thereof are required to access the information contained in the fine structures of the LOSVD, which assists in controlling for the inclination and projection effects.

Analogous to photometric decompositions of surface brightness profiles (§ 1.2), the rotation curves of galaxies were also subjected to structural analyses, corresponding to some of the earliest ‘dynamical models’. This was initially conducted on the kinematics of bright emission-line sources (tracing the gas) within disks of galaxies (Rubin and Ford, 1970; Casertano, 1983; Carignan and Freeman, 1985; van Albada et al., 1985; van Albada and Sancisi, 1986; Kent, 1986; Persic and Salucci, 1995; Martinsson et al., 2013; Lelli et al., 2016), as it was one of the few techniques which could probe sufficiently far from the galaxy centre to measure the velocity plateau. It was later also applied heavily to stellar kinematics (Persic and Salucci, 1988; Persic et al., 1996; Swaters et al., 2000; Noordermeer et al., 2007; Martinsson et al., 2013), especially so for the Milky-Way (see Sofue, 2020, for a review). This technique and its broad applications to the galaxy population are reviewed in Sofue and Rubin (2001). Typically rotation curves are decomposed into the mass contributions from the baryons and DM, which can thus quantify (at least in an average radial sense) their respective mass distributions. In more detailed implementations, the baryonic component can be further separated into stellar and gaseous contributions (Gentile et al., 2007). Finally, the modern implementation includes more than one stellar contribution, typically coming from the structural components found in photometry such as bulges, disks, and bars (Sofue, 2016). Such techniques provide insight into the mass composition of galaxies, and subsequently into how they may have formed. Yet they provide little constraints on the intrinsic shapes and mass distributions, since they require strong assumptions in these regards *a priori*. The suggestion was also made from these works that the earlier fundamental relations of galactic kinematics (Tully-Fisher, Faber-Jackson, Fundamental Plane) are actually driven by the local structural components within galaxies. That is, the Faber-Jackson relation should hold for all elliptical bodies, including the bulge components of disk galaxies, while disks in elliptical galaxies should follow the Tully-Fisher relation. This implies that it is simply the relative ratio between bulges and disks within individual galaxies that drives these correlations (Oh et al., 2020), rather than distinct morphological types following distinct relations. Yet the ambiguity in the definitions of these components (photometric, chemical, or kinematic definitions; classical or ‘pseudo’ bulges; thick and/or thin disks) has hampered their subsequent physical interpretation.

Dynamical models are derived using analytic formalisms (or numerical integrations thereof) in order to predict the intrinsic stellar kinematics of an observed galaxy. The principle goal of such an endeavour is to constrain a galaxy’s distribution function (DF), denoted as the six-dimensional function  $f(\mathbf{x}, \mathbf{v})$ , for 3D space vector  $\mathbf{x}$  and 3D velocity vector  $\mathbf{v}^\dagger$ . This function completely describes the probability of finding a star at a given

---

<sup>†</sup>In the most general case,  $f = f(\mathbf{x}, \mathbf{v}, t)$ , which can vary with time  $t$ . However, the vast majority of dynamical models, including those used in this work, are ‘equilibrium’ or ‘steady-state’ models in which the gravitational potential does not change with time, such that  $df/dt = 0$ .

location in the galaxy, and with a given velocity. It is, however, not feasible to constrain for all but the very nearest (resolved) galaxies. While the DF is a function of six unknown parameters, kinematic observations of external galaxies can provide only scalar quantities like the LOS velocity  $V_{\text{los}}$  with no spatial information from aperture spectra, one spatial and one velocity dimensions from long-slit data, or at-best two spatial and one velocity dimensions from IFU data. In addition, the DF is linked to the mass density,  $\rho(\mathbf{x})$ , in which it resides since  $\int f(\mathbf{x}, \mathbf{v}) d\mathbf{v} = \rho(\mathbf{x})$ . Yet these three- and six-dimensional functions can not be constrained simultaneously by the lower-dimensional observational data, so one must be assumed when the other is to be fit for. While the mass density distribution is not directly accessible via observations, it is often approximated from surface photometry by assuming a (typically-constant) conversion from stellar luminosity to stellar mass,  $M_\star/L$ . In this case, an additional assumption regarding the intrinsic shape is required to translate the observed surface density into an intrinsic 3D density, which is often that this shape can be described by one or more ellipsoids. Measuring or assuming a mass surface density allows the kinematic data to constrain the DF to some degree, but the deprojection into an intrinsic mass density is formally degenerate (Rybicki, 1987). This problem is compounded by the fact that the frames of reference of the observations (projections onto the sky) do not in most cases align with that of the target galaxy (its three intrinsic axes), meaning that the few orthogonal observational data do not correspond to even a subset of the orthogonal axes of the DF but rather some unknown combination thereof. Finally, there exists another fundamental degeneracy with attempting to constrain both the mass distribution of a galaxy and the anisotropy of that distribution's tracer population, when only the mean velocity and velocity dispersion are available (Binney and Mamon, 1982; Dejonghe and Merritt, 1992 though this can be mitigated to some degree by using higher-order kinematic information; Gerhard, 1993; Read and Steger, 2017). Consequently, the modelling of dynamical systems suffers from inherent degeneracies, where a range of intrinsic properties will match the observations in projection (as shown, for instance, in Gerhard and Binney, 1996; Krajnović et al., 2005).

A number of physical phenomena can be exploited to extract information from stellar kinematic data, with varying degrees of assumptions to break the aforementioned degeneracies. The scalar Virial Theorem provides one of the simplest methods for characterising the system giving rise to some observed kinematic data, most often by way of estimating the total system mass. This can be approximated using the mean central LOS velocity dispersion, and can therefore be applied to large galaxy samples with aperture kinematics. However, this only strictly holds for systems which are spherically-distributed and have isotropic stellar orbits.

The Jeans equations (Jeans, 1915) offer a more general avenue to study galactic kinematics. These equations describe a steady-state collisionless stellar system in terms of velocity moments of the collisionless Boltzmann equation for a given DF. The Jeans equations do not require the assumption of spherical mass distributions or isotropic stellar orbits. These equations are explored by exploiting Jeans' theorem. Jeans' theorem states that the  $\mathbf{x}$  and  $\mathbf{v}$  dependence of the DF is only via a number of separable ‘isolating’ integrals of motion which themselves explicitly depend on  $\mathbf{x}$  and  $\mathbf{v}$ ;  $I_1(\mathbf{x}, \mathbf{v}), \dots, I_N(\mathbf{x}, \mathbf{v})$  – where an integral of motion is any function  $I$  which has  $\frac{d}{dt} I[\mathbf{x}(t), \mathbf{v}(t)] = 0$ . Moreover, it states that any integral of motion is a solution to the collisionless Boltzmann equations. For the spherical and isotropic systems discussed above, they are fully described by  $\rho = \rho(r)$  and  $f = f(E)$ , where the density depends only on spherical radius  $r$  and the DF depends only on the orbital binding energy  $E$ . In spherical non-isotropic cases, orbits also conserve a second integral of motion, the magnitude of the angular momentum,  $L^2$ , giving  $f = f(E, L^2)$ . Such models have been

explored both theoretically (Richstone, 1987/ed; Cuddeford, 1991; Saha, 1992) and empirically in the case of unresolved (Read and Steger, 2017; Wasserman et al., 2018) and discrete (Wu and Tremaine, 2006; Massari et al., 2020, where each tracer – either individual stars or globular clusters – is resolved) kinematic data.

For an axisymmetric mass distribution,  $I_2(\mathbf{x}, \mathbf{v}) = L_z$ , the intrinsic angular momentum along the symmetry axis. In this ‘two-integral’  $f(E, L_z)$  family of dynamical models, the intrinsic velocity ellipsoid has  $\sigma_R = \sigma_z$ . With these constraints, the Jeans equations can be solved to predict the kinematics of the system. Two-integral models have been heavily studied theoretically (Nagai and Miyamoto, 1976; Batsleer and Dejonghe, 1993; Hunter and Qian, 1993; Magorrian, 1995; Jiang and Ossipkov, 2007) as they can be treated analytically. They have also been explored for real systems under a variety of assumptions: anisotropic axisymmetric models of both unresolved (e.g. Magorrian et al., 1998; Cappellari, 2008) and discrete (Watkins et al., 2013) kinematic data; and anisotropic triaxial models (in the case where the potential is separable; van de Ven et al., 2003).

A number of other methods have been implemented which avoid the limitation of having an analytic DF, and thus mitigate some of these assumptions. Some alternative approaches model the DF directly, such as the structural-component-based models of Taranu et al. (2017), and the statistical models of Gration and Wilkinson (2019), which have the added advantage of observational errors being treated robustly. Another approach, the so-called Made-to-Measure (M2M) model, computes  $N$ -body realisations of a given system while iteratively adjusting the masses of the particles until its projected time-averaged properties match the observations (Syer and Tremaine, 1996; De Lorenzi et al., 2007), resulting in a flexible approach applicable to general DF and intrinsic mass distributions. Another highly-general approach is a novel method first proposed by Schwarzschild (1979), in which ‘test’ orbits are numerically integrated within a given gravitational potential, and the projected time-averaged properties of the orbits are compared to observations. The Schwarzschild method does not impose any assumptions on the intrinsic density distribution or stellar velocity ellipsoid shape. Moreover, with a mass density constrained through photometry as described above, a specific DF does not need to be assumed, only that it can be described by its isolating integrals. Applications of this technique with a two-integral DF have provided measurements of, for instance, the intrinsic shapes and dominant dynamical support (Satoh, 1980; Dehnen and Gerhard, 1994; van der Marel et al., 1990; van der Marel et al., 1994) including for low-mass galaxies (Kowalczyk et al., 2019), and the kinematic properties of embedded stellar disks (van den Bosch and de Zeeuw, 1996).

Once again owing to our privileged perspective of the Milky-Way and the additional axes of the DF which can be measured for stars within it, numerical considerations found that the orbits of stars in the Galaxy conserve a third isolating integral  $I_3$  (Contopoulos, 1960; Ollongren, 1962; Saaf, 1968), a so-called ‘non-classical’ integral.  $I_3$  does not have an analytic representation for all but special cases of the gravitational potential, such as the Stäckel family (Kuzmin, 1956; de Zeeuw, 1985; Dejonghe and de Zeeuw, 1988) which are separable (An, 2013). Three-integral models in such potentials were subsequently explored (Famaey et al., 2002; van de Ven et al., 2008), including for alternative theories of gravity (Ciotti et al., 2012). The observations of the third conserved integral within the Milky-Way, as well as the observed deficiency of two-integral models (for example, see Binney et al., 1990; van der Marel et al., 1998; Cretton and van den Bosch, 1999; Emsellem et al., 1999; Verolme and de Zeeuw, 2002), necessitated three-integral implementations. To this end, theoretical experiments of three-integral models were explored (Petrou, 1983a,b; Dehnen and Gerhard, 1993; Stiavelli and Bertin, 1985, 1987; Robijn and de Zeeuw, 1996). For a

DF like  $f = f(E, I_2, I_3)$  in an arbitrary gravitational potential, the Jeans equations become intractable analytically and numerical approaches such as the Schwarzschild method are required. This motivated the extension of the Schwarzschild method to three-integral DF for axisymmetric mass distributions, which was then also applied to real data (van der Marel et al., 1998; Cretton and van den Bosch, 1999). Based on the considerations which motivated the three-integral models, and their resulting generality, they were applied to a variety of cases even where two-integral models existed already (e.g. Cretton et al., 1999; Gebhardt et al., 2000).

Finally, there was a growing observational need to model triaxial morphologies (Stark, 1977; Binney, 1978, 1985; Gerhard and Binney, 1985) on account of the twists observed in the photometry (Bertola and Galletta, 1979; Bertola et al., 1991; Wagner et al., 1988; Rix and Zaritsky, 1995; Schoenmakers et al., 1997; Naab and Burkert, 2003; Sil’chenko, 2016, and discussed in § 1.2), as well as from the observations of offsets between the photometric and kinematic major axes (Franx and de Zeeuw, 1992; Davies et al., 2001; Ene et al., 2018, 2020). In triaxial potentials,  $I_2$  is not strictly equivalent to the short-axis angular momentum, but must also be evaluated numerically as with  $I_3$ . The Schwarzschild method was once again extended to be able to model triaxial potentials with a three-integral DF (van den Bosch et al., 2008). At present, three-integral models are among the most general dynamical models available, but require high-quality data in order to sufficiently constrain them. There have now been a number of implementations of the Schwarzschild approach, including from Richstone and Tremaine (1984), Cretton (1997) and Rix et al. (1997), Verolme and de Zeeuw (2002), Valluri et al. (2004), van den Bosch et al. (2008), Vasiliev (2013), implementations for discrete (resolved) kinematic information (Chanamé et al., 2008), and the recent projects of FORSTAND (Vasiliev and Valluri, 2020) and SMART (Neureiter et al., 2021).

## 1.6 Motivation and Aims

What has emerged from this discussion so far is not only the remarkable advances made over the last century, but also the many defining properties of galaxies in the modern interpretation of galaxy formation. From their morphologies, to their stellar populations and dynamics, to their position with respect to other galaxies and in the cosmos in general – each with a variety of parametrisations – this abundance of galactic observables has lead to countless interesting and informative results. More broadly, it has become apparent that many of these ‘categories’ are rather continua, and their interpretation moving forward should reflect this.

One front which illuminates this clearly is the plethora of new correlations between these galactic properties that have emerged, in particular through large galaxy survey and simulation volumes. For instance, the stellar angular momentum (through various parametrisations) has been found to correlate with the visual morphology (Sweet et al., 2020), and local density (Cappellari et al., 2011b; D’Eugenio et al., 2013; Houghton et al., 2013; Fogarty et al., 2014). Yet it is already known that visual morphology correlates with local environment (§ 1.4.2). Similarly, some works find that at fixed stellar mass there is no longer a correlation between angular momentum and environment (Veale et al., 2017; Greene et al., 2018). Similar trends have been found for stellar populations, whereby younger galaxies have flatter intrinsic shapes (van de Sande et al., 2018). These results make it difficult to isolate the underlying physical driver of these trends, when the galactic parameters are all connected in some way.

As described in § 1.5.3, dynamical models are crucially dependent on the derivation of a prescription for the mass density distribution, which is necessarily based on the observed

luminosity density. However, there are different intrinsic stellar mass distributions which can result in the same observed luminosity distribution. For instance, at fixed observed luminosity, a galaxy (or region therein) can be composed of a large number of long-lived (typically low-mass and dim) stars, or a small number of young (typically high-mass and bright) stars. The old population will contain more mass owing to the significantly larger number of old stars required to produce the same luminosity. The result is that any mass densities derived from photometry are intricately coupled to the underlying stellar populations within each galaxy, and this subsequently also applies to dynamical models built from the inferred mass densities.

While this illuminates ‘self-consistency’ issues in the technical implementations of dynamical models if this dependence is not taken into account, the connections between stellar dynamics and populations are more physical still. Through studies of resolved populations within the Milky-Way and galaxies in the Local Group, it was found that younger stars in disks exhibit less random motion out of the disk plane (lower vertical velocity dispersion  $\sigma_z$ ) compared to older stars (Wielen, 1977; Nordström et al., 2004; Rocha-Pinto et al., 2004; Seabroke and Gilmore, 2007; Martig et al., 2014; Sharma et al., 2014; Beasley et al., 2015; Hayden et al., 2017; Leaman et al., 2017; Grieves et al., 2018; Yu and Liu, 2018; Bhattacharya et al., 2019; Mackereth et al., 2019). Similar correlations have been found between  $\sigma_z$  and the stellar metallicity, again for Local Group galaxies (Meusinger et al., 1991; Ness et al., 2013; Minchev et al., 2014; Dorman et al., 2015; Grieves et al., 2018; Arentsen et al., 2020), further highlighting the importance of connecting the stellar dynamics and populations.

Overall, the intrinsic correlations between stellar dynamics and populations uncovered from studies of the nearest (resolved) systems have motivated seeking similar correlations in more distant (unresolved) systems. In the unresolved regime, however, projection effects dramatically hinder this endeavour, since any given measurement through the LOS necessarily contains contributions from many different kinematic and stellar populations. What is required therefore is an analysis which can explore deprojected intrinsic properties of external galaxies in a high level of detail.

The work presented in this thesis aims to develop a method for modelling galaxy formation and evolution which is highly detailed, can access intrinsic properties, and is sufficiently general to account for the expected diversity of properties within the galaxy population. It also specifically aims to avoid many of the assumptions prevalent in previous works. To this end, assumptions regarding the specific shape and orientation of the DF and stellar velocity ellipsoid are avoided, the structural composition of galaxies is not assumed *a priori*, the self-consistency issues of the mass models caused by varying stellar populations ( $M_\star/L$ ) is explicitly taken into account, and any intrinsic correlations between stellar dynamics and populations, including the galactic IMF when possible, are borne directly out of the data rather than imposed by prior expectations. This thesis investigates how galaxy formation proceeds through the lens of high-accuracy, high-precision, self-consistent models of the observable data. By considering all available information simultaneously, these models circumvent the issues presented in this section concerning the interpretation of observed correlations. These models are designed to facilitate the exploration of correlations between *intrinsic* properties which are at every stage driven by the data, yet are agnostic to and independent of those in the literature. This thesis seeks to evaluate just how much information can be reliably extracted from current and future observations by pushing these model analyses beyond what has previously been sought.

With such a technique, this work aims to address many of the issues exposed in recent times, such as whether the intrinsic chemo-dynamical correlations uncovered in nearby

systems can also be recovered in more distant galaxies, if such correlations exist systematically within the galaxy population, and whether archaeological techniques for recovering galaxy assembly histories benefit from the combination of kinematics and stellar populations within a self-consistent orbital framework.

# Bibliography

- Ade, P. a. R. et al. (2014). *Astronomy & Astrophysics* 571, A16. issn: 0004-6361, 1432-0746. doi: 10.1051/0004-6361/201321591.
- Ade, P. a. R. et al. (2016). *Astronomy & Astrophysics* 594, A13. issn: 0004-6361, 1432-0746. doi: 10.1051/0004-6361/201525830.
- Aghanim, N. et al. (2020). *Astronomy & Astrophysics* 641, A6. issn: 0004-6361, 1432-0746. doi: 10.1051/0004-6361/201833910.
- Aguerri, J. a. L. et al. (2005). *Astronomy & Astrophysics* 434(1), pages 109–122. issn: 0004-6361, 1432-0746. doi: 10.1051/0004-6361:20041743.
- Allam, S. S. et al. (2004). *The Astronomical Journal* 127(4), page 1883. issn: 1538-3881. doi: 10.1086/381954.
- Allen, R. J. et al. (2016). *The Astrophysical Journal* 826(1), page 60. issn: 0004-637X. doi: 10.3847/0004-637X/826/1/60.
- Allington-Smith, J. et al. (2002). *Publications of the Astronomical Society of the Pacific* 114(798), page 892. issn: 1538-3873. doi: 10.1086/341712.
- Alton, P. D., Smith, R. J., and Lucey, J. R. (2018). *Monthly Notices of the Royal Astronomical Society* 478(4), pages 4464–4486. issn: 0035-8711. doi: 10.1093/mnras/sty1242.
- Alton, P. D., Smith, R. J., and Lucey, J. R. (2017). *Monthly Notices of the Royal Astronomical Society, Volume 468, Issue 2, p.1594-1615* 468, pages 1594–1615. doi: 10.1093/mnras/stx464.
- An, J. (2013). *Monthly Notices of the Royal Astronomical Society* 435(4), pages 3045–3057. issn: 0035-8711. doi: 10.1093/mnras/stt1498.
- Andrews, B. H. and Martini, P. (2013). *The Astrophysical Journal* 765(2), page 140. issn: 0004-637X. doi: 10.1088/0004-637X/765/2/140.
- Andrews, J. E. et al. (2014). *The Astrophysical Journal* 793(1), page 4. issn: 0004-637X. doi: 10.1088/0004-637X/793/1/4.
- Aquino-Ortíz, E. et al. (2018). *Monthly Notices of the Royal Astronomical Society* 479(2), pages 2133–2146. issn: 0035-8711. doi: 10.1093/mnras/sty1522.
- Arentsen, A. et al. (2020). *Monthly Notices of the Royal Astronomical Society: Letters* 491(1), pages L11–L16. issn: 1745-3925. doi: 10.1093/mnrasl/slz156.
- Argyle, J. J. et al. (2018). *Monthly Notices of the Royal Astronomical Society* 479(3), pages 3076–3093. issn: 0035-8711. doi: 10.1093/mnras/sty1691.
- Asa'd, R. and Goudfrooij, P. (2020). *Monthly Notices of the Royal Astronomical Society* 498(2), pages 2814–2832. issn: 0035-8711. doi: 10.1093/mnras/staa2515.
- Athanassoula, E. et al. (2016). *The Astrophysical Journal, Volume 821, Issue 2, article id. 90, 17 pp.* (2016). 821, page 90. doi: 10.3847/0004-637X/821/2/90.
- Bacon, R. et al. (1995). *Astronomy and Astrophysics Supplement Series* 113, page 347. issn: 0365-0138. URL: <http://adsabs.harvard.edu/abs/1995A%26AS..113..347B>.
- Bacon, R. et al. (2000). *Imaging the Universe in Three Dimensions*. Volume 195, page 173. isbn: 9781583810224. URL: <http://adsabs.harvard.edu/abs/2000ASPC..195..173B>.

- Bacon, R. et al. (2001). *Monthly Notices of the Royal Astronomical Society*, Volume 326, Issue 1, pp. 23–35. 326, pages 23–35. doi: 10.1046/j.1365-8711.2001.04612.x.
- Bacon, R. et al. (2010). *Ground-Based and Airborne Instrumentation for Astronomy III*. Volume 7735. International Society for Optics and Photonics, page 773508. doi: 10.1117/12.856027.
- Baggett, W. E., Baggett, S. M., and Anderson, K. S. J. (1998). *The Astronomical Journal* 116(4), page 1626. issn: 1538-3881. doi: 10.1086/300525.
- Baldry, I. K. and Glazebrook, K. (2003). *The Astrophysical Journal* 593(1), pages 258–271. issn: 0004-637X. doi: 10.1086/376502.
- Baldwin, C. et al. (2018). *Monthly Notices of the Royal Astronomical Society* 473(4), pages 4698–4721. issn: 0035-8711. doi: 10.1093/mnras/stx2502.
- Balogh, M. et al. (2004). *Monthly Notices of the Royal Astronomical Society* 348(4), pages 1355–1372. issn: 0035-8711. doi: 10.1111/j.1365-2966.2004.07453.x.
- Barat, D. et al. (2019). *Monthly Notices of the Royal Astronomical Society* 487(2), pages 2924–2936. issn: 0035-8711. doi: 10.1093/mnras/stz1439.
- Barnes, J. E. (1992). *The Astrophysical Journal* 393, pages 484–507. issn: 0004-637X. doi: 10.1086/171522.
- Barone, T. M. et al. (2018). *The Astrophysical Journal* 856(1), page 64. issn: 0004-637X. doi: 10.3847/1538-4357/aaaf6e.
- Barsanti, S. et al. (2018). *The Astrophysical Journal* 857(1), page 71. issn: 0004-637X. doi: 10.3847/1538-4357/aab61a.
- Barsanti, S. et al. (2021). *The Astrophysical Journal* 906(2), page 100. issn: 0004-637X. doi: 10.3847/1538-4357/abc956.
- Bartko, H. et al. (2009). *The Astrophysical Journal* 708(1), pages 834–840. issn: 0004-637X. doi: 10.1088/0004-637X/708/1/834.
- Barton, E. J., Geller, M. J., and Kenyon, S. J. (2000). *The Astrophysical Journal* 530(2), page 660. issn: 0004-637X. doi: 10.1086/308392.
- Bastian, N., Covey, K. R., and Meyer, M. R. (2010). *Annual Review of Astronomy and Astrophysics* 48(1), pages 339–389. doi: 10.1146/annurev-astro-082708-101642.
- Batsleer, P. and Dejonghe, H. (1993). *Astronomy and Astrophysics* 271, page 104. issn: 0004-6361. url: <http://adsabs.harvard.edu/abs/1993A%26A...271..104B>.
- Beasley, M. A. et al. (2015). *Monthly Notices of the Royal Astronomical Society* 451(4), pages 3400–3418. issn: 0035-8711. doi: 10.1093/mnras/stv943.
- Beckmann, R. S. et al. (2017). *Monthly Notices of the Royal Astronomical Society* 472(1), pages 949–965. issn: 0035-8711. doi: 10.1093/mnras/stx1831.
- Beckwith, S. V. W. et al. (2006). *The Astronomical Journal* 132(5), pages 1729–1755. issn: 0004-6256, 1538-3881. doi: 10.1086/507302.
- Begeman, K. G. (1989). *Astronomy and Astrophysics* 223, pages 47–60. issn: 0004-6361. url: <http://adsabs.harvard.edu/abs/1989A%26A...223..47B>.
- Bekki, K., Couch, W. J., and Shioya, Y. (2002). *The Astrophysical Journal* 577(2), page 651. issn: 0004-637X. doi: 10.1086/342221.
- Bender, R. (1988). *Astronomy and Astrophysics* 202, pages L5–L8. issn: 0004-6361. url: <http://adsabs.harvard.edu/abs/1988A%26A...202L...5B>.
- Bendo, G. J. and Barnes, J. E. (2000). *Monthly Notices of the Royal Astronomical Society* 316(2), pages 315–325. issn: 0035-8711. doi: 10.1046/j.1365-8711.2000.03475.x.
- Bennett, C. L. et al. (2003). *The Astrophysical Journal Supplement Series* 148(1), page 1. issn: 0067-0049. doi: 10.1086/377253.

- Bergemann, M. et al. (2014). *Astronomy & Astrophysics* 565, A89. issn: 0004-6361, 1432-0746. doi: 10.1051/0004-6361/201423456.
- Bertola, F. (1966). *Memorie della Societa Astronomica Italiana* 37, page 433. url: <http://adsabs.harvard.edu/abs/1966MmSAI..37..433B>.
- Bertola, F. and Bernacca, P. L. (1967). *Memorie della Societa Astronomica Italiana* 38, page 189. url: <http://adsabs.harvard.edu/abs/1967MmSAI..38..189B>.
- Bertola, F. and Capaccioli, M. (1975). *The Astrophysical Journal* 200, pages 439–445. doi: 10.1086/153808.
- Bertola, F. and Capaccioli, M. (1977). *The Astrophysical Journal* 211, pages 697–699. doi: 10.1086/154980.
- Bertola, F. and Capaccioli, M. (1978). *The Astrophysical Journal* 219, pages 404–407. doi: 10.1086/155792.
- Bertola, F. and Galletta, G. (1979). *Astronomy and Astrophysics* 77, pages 363–365. issn: 0004-6361. url: <http://adsabs.harvard.edu/abs/1979A%26A....77..363B>.
- Bertola, F., Vietri, M., and Zeilinger, W. W. (1991). *The Astrophysical Journal Letters* 374, pages L13–L16. doi: 10.1086/186060.
- Bhattacharya, S. et al. (2019). *Astronomy & Astrophysics* 631, A56.
- Bílek, M. et al. (2020). *Monthly Notices of the Royal Astronomical Society* 498(2), pages 2138–2166. issn: 0035-8711. doi: 10.1093/mnras/staa2248.
- Binétruy, P. (2013). *The Astronomy and Astrophysics Review* 21(1), page 67. issn: 1432-0754. doi: 10.1007/s00159-013-0067-2.
- Binney, J. J., Davies, R. L., and Illingworth, G. D. (1990). *The Astrophysical Journal* 361, pages 78–97. doi: 10.1086/169169.
- Binney, J. (1978). *Monthly Notices of the Royal Astronomical Society* 183(3), pages 501–514. issn: 0035-8711. doi: 10.1093/mnras/183.3.501.
- Binney, J. (1985). *Monthly Notices of the Royal Astronomical Society* 212(4), pages 767–781. issn: 0035-8711. doi: 10.1093/mnras/212.4.767.
- Binney, J. (2005). *Monthly Notices of the Royal Astronomical Society* 363(3), pages 937–942. issn: 0035-8711. doi: 10.1111/j.1365-2966.2005.09495.x.
- Binney, J. and Mamon, G. A. (1982). *Monthly Notices of the Royal Astronomical Society* 200(2), pages 361–375. issn: 0035-8711. doi: 10.1093/mnras/200.2.361.
- Binney, J. and Tremaine, S. (1987). Princeton University Press: Princeton, N.J. isbn: 978-0-691-08444-2 978-0-691-08445-9.
- Binney, J. et al. (1998). Princeton University Press. isbn: 978-0-691-02565-0.
- Blackman, C. P. (1980). *Monthly Notices of the Royal Astronomical Society* 191(1), pages 123–133. issn: 0035-8711. doi: 10.1093/mnras/191.1.123.
- Blackman, C. P. (1981). *Monthly Notices of the Royal Astronomical Society* 195(3), pages 451–466. issn: 0035-8711. doi: 10.1093/mnras/195.3.451.
- Blackman, C. P. (1982). *Monthly Notices of the Royal Astronomical Society* 200(2), pages 407–429. issn: 0035-8711. doi: 10.1093/mnras/200.2.407.
- Blackman, C. P. and Pence, W. D. (1982). *Monthly Notices of the Royal Astronomical Society* 198(2), pages 517–534. issn: 0035-8711. doi: 10.1093/mnras/198.2.517.
- Blumenthal, G. R. et al. (1984). *Nature* 311(5986), pages 517–525. issn: 1476-4687. doi: 10.1038/311517a0.
- Boecker, A. et al. (2020). *The Astrophysical Journal* 896(1), page 13. issn: 0004-637X. doi: 10.3847/1538-4357/ab919d.
- Boquien, M. et al. (2019). *Astronomy & Astrophysics* 622, A103. issn: 0004-6361, 1432-0746. doi: 10.1051/0004-6361/201834156.

- Borgne, J.-F. L. et al. (2003). *Astronomy & Astrophysics* 402(2), pages 433–442. issn: 0004-6361, 1432-0746. doi: 10.1051/0004-6361:20030243.
- Boroson, T. (1981). *The Astrophysical Journal Supplement Series* 46, pages 177–209. doi: 10.1086/190742.
- Bottrell, C. et al. (2019). *Monthly Notices of the Royal Astronomical Society* 486(1), pages 390–413. issn: 0035-8711, 1365-2966. doi: 10.1093/mnras/stz855.
- Bournaud, F., Combes, F., and Jog, C. J. (2004). *Astronomy & Astrophysics* 418(2), pages L27–L30. issn: 0004-6361, 1432-0746. doi: 10.1051/0004-6361:20040114.
- Bournaud, F., Duc, P.-A., and Emsellem, E. (2008). *Monthly Notices of the Royal Astronomical Society: Letters* 389(1), pages L8–L12. issn: 1745-3925. doi: 10.1111/j.1745-3933.2008.00511.x.
- Bouwens, R. J. et al. (2015). *The Astrophysical Journal* 803(1), page 34. issn: 0004-637X. doi: 10.1088/0004-637X/803/1/34.
- Breda, I. et al. (2020). *Astronomy & Astrophysics* 635, A177. issn: 0004-6361, 1432-0746. doi: 10.1051/0004-6361/201937193.
- Bremer, M. N. et al. (2018). *Monthly Notices of the Royal Astronomical Society* 476(1), pages 12–26. issn: 0035-8711. doi: 10.1093/mnras/sty124.
- Bressan, A., Chiosi, C., and Fagotto, F. (1994). *The Astrophysical Journal Supplement Series* 94, pages 63–115. doi: 10.1086/192073.
- Brinchmann, J. et al. (2004). *Monthly Notices of the Royal Astronomical Society* 351(4), pages 1151–1179. issn: 0035-8711. doi: 10.1111/j.1365-2966.2004.07881.x.
- Bruzual, G. and Charlot, S. (2003). *Monthly Notices of the Royal Astronomical Society* 344(4), pages 1000–1028. issn: 0035-8711. doi: 10.1046/j.1365-8711.2003.06897.x.
- Bruzual, G. A. (1983). *The Astrophysical Journal* 273, pages 105–127. doi: 10.1086/161352.
- Bruzual, G. A. and Charlot, S. (1993). *The Astrophysical Journal* 405, pages 538–553. doi: 10.1086/172385.
- Bruzzone, S. M. et al. (2020). *Monthly Notices of the Royal Astronomical Society* 491(2), pages 2366–2390. issn: 0035-8711. doi: 10.1093/mnras/stz3151.
- Bryant, J. J. et al. (2015). *Monthly Notices of the Royal Astronomical Society* 447(3), pages 2857–2879. issn: 0035-8711. doi: 10.1093/mnras/stu2635.
- Bryant, J. J. et al. (2016). *Ground-Based and Airborne Instrumentation for Astronomy VI*. Volume 9908. International Society for Optics and Photonics, 99081F. doi: 10.1117/12.2230740.
- Bryant, J. J. et al. (2018). *Ground-Based and Airborne Instrumentation for Astronomy VII*. Volume 10702. International Society for Optics and Photonics, 107021H. doi: 10.1117/12.2309893.
- Bundy, K. et al. (2015). *The Astrophysical Journal, Volume 798, Issue 1, article id. 7, 24 pp. (2015)*. 798, page 7. doi: 10.1088/0004-637X/798/1/7.
- Burbidge, E. M. and Burbidge, G. R. (1959). *The Astrophysical Journal* 129, page 271. doi: 10.1086/146617.
- Burgarella, D., Buat, V., and Iglesias-Páramo, J. (2005). *Monthly Notices of the Royal Astronomical Society* 360(4), pages 1413–1425. issn: 0035-8711. doi: 10.1111/j.1365-2966.2005.09131.x.
- Burstein, D. (1979). *The Astrophysical Journal* 234, pages 829–836. doi: 10.1086/157563.
- Byun, Y. I. and Freeman, K. C. (1995). *The Astrophysical Journal* 448, page 563. doi: 10.1086/175986.
- Cai, Z.-Y., Zotti, G. D., and Bonato, M. (2020). *The Astrophysical Journal* 891(1), page 74. issn: 0004-637X. doi: 10.3847/1538-4357/ab7231.

- Cañameras, R. et al. (2017). *Astronomy & Astrophysics* 600, page L3. issn: 0004-6361, 1432-0746. doi: 10.1051/0004-6361/201630359.
- Cappellari, M. (2008). *Monthly Notices of the Royal Astronomical Society* 390(1), pages 71–86. issn: 0035-8711. doi: 10.1111/j.1365-2966.2008.13754.x.
- Cappellari, M. (2017). *Monthly Notices of the Royal Astronomical Society, Volume 466, Issue 1, p.798-811* 466, pages 798–811. doi: 10.1093/mnras/stw3020.
- Cappellari, M. and Emsellem, E. (2004). *Publications of the Astronomical Society of the Pacific* 116(816), page 138. issn: 1538-3873. doi: 10.1086/381875.
- Cappellari, M. et al. (2007). *Monthly Notices of the Royal Astronomical Society* 379(2), pages 418–444. issn: 0035-8711. doi: 10.1111/j.1365-2966.2007.11963.x.
- Cappellari, M. et al. (2011a). *Monthly Notices of the Royal Astronomical Society, Volume 413, Issue 2, pp. 813-836* 413(2), pages 813–836. issn: 0035-8711. doi: 10.1111/j.1365-2966.2010.18174.x.
- Cappellari, M. et al. (2011b). *Monthly Notices of the Royal Astronomical Society* 416(3), pages 1680–1696. issn: 0035-8711. doi: 10.1111/j.1365-2966.2011.18600.x.
- Cappellari, M. et al. (2012). *Nature, Volume 484, Issue 7395, pp. 485-488* (2012). 484, pages 485–488. doi: 10.1038/nature10972.
- Carignan, C. and Freeman, K. C. (1985). *The Astrophysical Journal* 294, pages 494–501. issn: 0004-637X. doi: 10.1086/163316.
- Carnall, A. C. et al. (2018). *Monthly Notices of the Royal Astronomical Society* 480(4), pages 4379–4401. issn: 0035-8711. doi: 10.1093/mnras/sty2169.
- Casertano, S. (1983). *Monthly Notices of the Royal Astronomical Society* 203(3), pages 735–747. issn: 0035-8711. doi: 10.1093/mnras/203.3.735.
- Chabrier, G. (2003). *Publications of the Astronomical Society of the Pacific* 115(809), page 763. issn: 1538-3873. doi: 10.1086/376392.
- Chan, J. C. C. et al. (2018). *The Astrophysical Journal* 856(1), page 8. issn: 0004-637X. doi: 10.3847/1538-4357/aaadb4.
- Chanamé, J., Kleyna, J., and van der Marel, R. (2008). *The Astrophysical Journal* 682(2), pages 841–860. issn: 0004-637X, 1538-4357. doi: 10.1086/589429.
- Chen, Y.-P. et al. (2014). *Astronomy & Astrophysics* 565, A117. issn: 0004-6361, 1432-0746. doi: 10.1051/0004-6361/201322505.
- Chen, Y.-P. et al. (2020). *The Astrophysical Journal* 899(1), page 62. issn: 0004-637X. doi: 10.3847/1538-4357/ab9f35.
- Chevallard, J. and Charlot, S. (2016). *Monthly Notices of the Royal Astronomical Society* 462(2), pages 1415–1443. issn: 0035-8711. doi: 10.1093/mnras/stw1756.
- Chilingarian, I. V. et al. (2010). *Astronomy & Astrophysics* 518, A61. issn: 0004-6361, 1432-0746. doi: 10.1051/0004-6361/200912938.
- Choi, J. et al. (2016). *The Astrophysical Journal* 823(2), page 102. issn: 0004-637X. doi: 10.3847/0004-637X/823/2/102.
- Cibinel, A. et al. (2013). *The Astrophysical Journal* 777(2), page 116. issn: 0004-637X. doi: 10.1088/0004-637X/777/2/116.
- Ciotti, L., Lanzoni, B., and Volonteri, M. (2007). *The Astrophysical Journal* 658(1), pages 65–77. issn: 0004-637X. doi: 10.1086/510773.
- Ciotti, L., Zhao, H., and de Zeeuw, P. T. (2012). *Monthly Notices of the Royal Astronomical Society* 422, pages 2058–2071. doi: 10.1111/j.1365-2966.2012.20716.x.
- Coc, A. and Vangioni, E. (2017). *International Journal of Modern Physics E* 26(08), page 1741002. issn: 0218-3013. doi: 10.1142/S0218301317410026.

- Coelho, P. R. T. (2014). *Monthly Notices of the Royal Astronomical Society* 440(2), pages 1027–1043. ISSN: 0035-8711. doi: 10.1093/mnras/stu365.
- Coenda, V. et al. (2020). *Astronomy & Astrophysics* 642, A132. ISSN: 0004-6361, 1432-0746. doi: 10.1051/0004-6361/202038774.
- Colless, M. et al. (2001). *Monthly Notices of the Royal Astronomical Society* 328(4), pages 1039–1063. ISSN: 0035-8711. doi: 10.1046/j.1365-8711.2001.04902.x.
- Collier, W. P., Smith, R. J., and Lucey, J. R. (2020). *Monthly Notices of the Royal Astronomical Society* 494(1), pages 271–292. ISSN: 0035-8711. doi: 10.1093/mnras/staa602.
- Comte, G., Monnet, G., and Rosado, M. (1979). *Astronomy and Astrophysics* 72, pages 73–81. ISSN: 0004-6361. URL: <http://adsabs.harvard.edu/abs/1979A%26A....72...73C>.
- Conroy, C. and Dokkum, P. G. van (2012). *The Astrophysical Journal* 760(1), page 71. ISSN: 0004-637X. doi: 10.1088/0004-637X/760/1/71.
- Conroy, C., Dokkum, P. G. van, and Villaume, A. (2017). *The Astrophysical Journal* 837(2), page 166. ISSN: 0004-637X. doi: 10.3847/1538-4357/aa6190.
- Conroy, C. and Gunn, J. E. (2010). *The Astrophysical Journal* 712(2), pages 833–857. ISSN: 0004-637X. doi: 10.1088/0004-637X/712/2/833.
- Conroy, C., Gunn, J. E., and White, M. (2009). *The Astrophysical Journal* 699(1), pages 486–506. ISSN: 0004-637X. doi: 10.1088/0004-637X/699/1/486.
- Conroy, C. et al. (2013). *The Astrophysical Journal* 776(2), page L26. ISSN: 2041-8205. doi: 10.1088/2041-8205/776/2/L26.
- Conselice, C. J. et al. (2016). *The Astrophysical Journal* 830(2), page 83. ISSN: 1538-4357. doi: 10.3847/0004-637X/830/2/83.
- Contopoulos, G. (1960). *Zeitschrift fur Astrophysik* 49, page 273. ISSN: 0372-8331. URL: <http://adsabs.harvard.edu/abs/1960ZA.....49..273C>.
- Cook, R. H. W. et al. (2019). *Monthly Notices of the Royal Astronomical Society* 490(3), pages 4060–4079. ISSN: 0035-8711. doi: 10.1093/mnras/stz2789.
- Corsini, E. M. et al. (2018). *Astronomy & Astrophysics* 618, A172. ISSN: 0004-6361, 1432-0746. doi: 10.1051/0004-6361/201832625.
- Cortese, L. et al. (2014). *The Astrophysical Journal* 795(2), page L37. ISSN: 2041-8205. doi: 10.1088/2041-8205/795/2/L37.
- Cortijo-Ferrero, C. et al. (2017). *Astronomy & Astrophysics* 607, A70. ISSN: 0004-6361, 1432-0746. doi: 10.1051/0004-6361/201731217.
- Cretton, N. et al. (1999). *The Astrophysical Journal Supplement Series* 124(2), page 383. ISSN: 0067-0049. doi: 10.1086/313264.
- Cretton, N. et al. (2001). *The Astrophysical Journal* 554(1), page 291. ISSN: 0004-637X. doi: 10.1086/321362.
- Cretton, N. (1997). *The Nature of Elliptical Galaxies; 2nd Stromlo Symposium*. Edited by Arnaboldi, M., Da Costa, G. S., and Saha, P. Volume 116. Astronomical Society of the Pacific Conference Series, page 97.
- Cretton, N. and van den Bosch, F. C. (1999). *The Astrophysical Journal* 514, pages 704–724. ISSN: 0004-637X. doi: 10.1086/306971.
- Croom, S. M. et al. (2012). *Monthly Notices of the Royal Astronomical Society* 421(1), pages 872–893. ISSN: 0035-8711. doi: 10.1111/j.1365-2966.2011.20365.x.
- Croton, D. J. et al. (2006). *Monthly Notices of the Royal Astronomical Society* 365(1), pages 11–28. ISSN: 0035-8711. doi: 10.1111/j.1365-2966.2005.09675.x.
- Cuddeford, P. (1991). *Monthly Notices of the Royal Astronomical Society* 253(3), pages 414–426. ISSN: 0035-8711. doi: 10.1093/mnras/253.3.414.

- D'Eugenio, F. et al. (2013). *Monthly Notices of the Royal Astronomical Society* 429(2), pages 1258–1266. ISSN: 0035-8711. doi: 10.1093/mnras/sts406.
- D'Eugenio, F. et al. (2018). *Monthly Notices of the Royal Astronomical Society* 479(2), pages 1807–1821. ISSN: 0035-8711. doi: 10.1093/mnras/sty1424.
- D'Eugenio, F. et al. (2020). *Monthly Notices of the Royal Astronomical Society* 497(1), pages 389–404. ISSN: 0035-8711. doi: 10.1093/mnras/staa1937.
- D'Onghia, E. et al. (2006). *Monthly Notices of the Royal Astronomical Society* 372(4), pages 1525–1530. ISSN: 0035-8711. doi: 10.1111/j.1365-2966.2006.10996.x.
- da Cunha, E. et al. (2017/ed). *Publications of the Astronomical Society of Australia* 34. ISSN: 1323-3580, 1448-6083. doi: 10.1017/pasa.2017.41.
- Dabringhausen, J., Kroupa, P., and Baumgardt, H. (2009). *Monthly Notices of the Royal Astronomical Society* 394(3), pages 1529–1543. ISSN: 0035-8711. doi: 10.1111/j.1365-2966.2009.14425.x.
- Danziger, I. J., Goss, W. M., and Wellington, K. J. (1981). *Monthly Notices of the Royal Astronomical Society* 196(4), pages 845–856. ISSN: 0035-8711. doi: 10.1093/mnras/196.4.845.
- Davies, L. J. M. et al. (2019). *Monthly Notices of the Royal Astronomical Society* 483(4), pages 5444–5458. ISSN: 0035-8711. doi: 10.1093/mnras/sty3393.
- Davies, R. et al. (2018). *Ground-Based and Airborne Instrumentation for Astronomy VII*. Volume 10702. International Society for Optics and Photonics, page 1070209. doi: 10.1117/12.2311480.
- Davies, R. L. et al. (1983). *The Astrophysical Journal* 266, pages 41–57. ISSN: 0004-637X. doi: 10.1086/160757.
- Davies, R. L. (1981). *Monthly Notices of the Royal Astronomical Society* 194(4), pages 879–902. ISSN: 0035-8711. doi: 10.1093/mnras/194.4.879.
- Davies, R. L. et al. (2001). *The Astrophysical Journal* 548(1), page L33. ISSN: 0004-637X. doi: 10.1086/318930.
- Davis, M. et al. (1985). *The Astrophysical Journal* 292, pages 371–394. ISSN: 0004-637X. doi: 10.1086/163168.
- Davis, T. A. and McDermid, R. M. (2017). *Monthly Notices of the Royal Astronomical Society* 464(1), pages 453–468. ISSN: 0035-8711. doi: 10.1093/mnras/stw2366.
- de Lapparent, V., Geller, M. J., and Huchra, J. P. (1986). *The Astrophysical Journal Letters* 302, pages L1–L5. ISSN: 0004-637X. doi: 10.1086/184625.
- De Lorenzi, F. et al. (2007). *Monthly Notices of the Royal Astronomical Society* 376(1), pages 71–88. ISSN: 0035-8711. doi: 10.1111/j.1365-2966.2007.11434.x.
- de Martino, I. et al. (2020). *Universe* 6(8), page 107. doi: 10.3390/universe6080107.
- De Masi, C. et al. (2019). *Monthly Notices of the Royal Astronomical Society* 483(2), pages 2217–2235. ISSN: 0035-8711. doi: 10.1093/mnras/sty3127.
- de Vaucouleurs, G. (1948). *Annales d'Astrophysique* 11, page 247. URL: <http://adsabs.harvard.edu/abs/1948AnAp...11..247D>.
- de Vaucouleurs, G. (1959). *Astrophysik IV: Sternsysteme / Astrophysics IV: Stellar Systems*. Edited by Flügge, S. *Handbuch Der Physik / Encyclopedia of Physics*. Springer: Berlin, Heidelberg, pages 275–310. ISBN: 978-3-642-45932-0. doi: 10.1007/978-3-642-45932-0\_7.
- de Zeeuw, T. (1985). *Monthly Notices of the Royal Astronomical Society* 216(3), pages 599–612. ISSN: 0035-8711. doi: 10.1093/mnras/216.3.599.
- Dehnen, W. and Gerhard, O. E. (1993). *Monthly Notices of the Royal Astronomical Society* 261(2), pages 311–336. ISSN: 0035-8711. doi: 10.1093/mnras/261.2.311.

- Dehnen, W. and Gerhard, O. E. (1994). *Monthly Notices of the Royal Astronomical Society* 268(4), pages 1019–1032. issn: 0035-8711. doi: 10.1093/mnras/268.4.1019.
- Dejonghe, H. and de Zeeuw, T. (1988). *The Astrophysical Journal* 333, pages 90–129. doi: 10.1086/166727.
- Dejonghe, H. and Merritt, D. (1992). *The Astrophysical Journal* 391, pages 531–549. issn: 0004-637X. doi: 10.1086/171368.
- Delisle, S. and Hardy, E. (1992). *The Astronomical Journal* 103, pages 711–727. doi: 10.1086/116096.
- Demoulin, M.-H. (1970). *The Astrophysical Journal Letters* 160, page L79. doi: 10.1086/180532.
- Dicke, R. H. et al. (1965). *The Astrophysical Journal* 142, pages 414–419. issn: 0004-637X. doi: 10.1086/148306.
- Djorgovski, S. and Davis, M. (1987). *The Astrophysical Journal* 313, pages 59–68. doi: 10.1086/164948.
- Dobbie, P. D. et al. (2014). *Monthly Notices of the Royal Astronomical Society* 442(2), pages 1680–1692. issn: 0035-8711. doi: 10.1093/mnras/stu926.
- Dorman, C. E. et al. (2015). *The Astrophysical Journal* 803(1), page 24. issn: 0004-637X. doi: 10.1088/0004-637X/803/1/24.
- Dotter, A. (2016). *The Astrophysical Journal Supplement Series* 222(1), page 8. issn: 0067-0049. doi: 10.3847/0067-0049/222/1/8.
- Dotter, A. et al. (2007). *The Astronomical Journal* 134(1), page 376. issn: 1538-3881. doi: 10.1086/517915.
- Dressler, A. (1980). *The Astrophysical Journal* 236, page 351. issn: 0004-637X, 1538-4357. doi: 10.1086/157753.
- Dressler, A. et al. (1987). *The Astrophysical Journal* 313, pages 42–58. doi: 10.1086/164947.
- Driver, S. P. et al. (2013). *Monthly Notices of the Royal Astronomical Society* 430(4), pages 2622–2632. issn: 0035-8711. doi: 10.1093/mnras/sts717.
- Drory, N. et al. (2015). *The Astronomical Journal* 149(2), page 77. issn: 1538-3881. doi: 10.1088/0004-6256/149/2/77.
- Edvardsson, B. et al. (1993). *Astronomy and Astrophysics* 275, page 101. issn: 0004-6361. url: <http://adsabs.harvard.edu/abs/1993A%26A...275..101E>.
- Eftekhari, E. et al. (2019). *Monthly Notices of the Royal Astronomical Society* 486(3), pages 3788–3804. issn: 0035-8711. doi: 10.1093/mnras/stz1113.
- Einasto, J., Kaasik, A., and Saar, E. (1974). *Nature* 250(5464), pages 309–310. issn: 1476-4687. doi: 10.1038/250309a0.
- Einstein, A. (1905). *Annalen der Physik* vol. 4, t. 17. url: <http://sedici.unlp.edu.ar/handle/10915/2786>.
- Einstein, A. (1916). *Annalen der Physik* 354(7), pages 769–822. issn: 1521-3889. doi: 10.1002/andp.19163540702.
- Eisenhauer, F. et al. (2003). *Instrument Design and Performance for Optical/Infrared Ground-Based Telescopes*. Volume 4841. International Society for Optics and Photonics, pages 1548–1561. doi: 10.1117/12.459468.
- Ellis, S. C. et al. (2012). *Ground-Based and Airborne Instrumentation for Astronomy IV*. Volume 8446. International Society for Optics and Photonics, page 84460V. doi: 10.1117/12.925812.
- Ellis, S. C. et al. (2016). *Ground-Based and Airborne Instrumentation for Astronomy VI*. Volume 9908. International Society for Optics and Photonics, 99081Q. doi: 10.1117/12.2232107.

- Ellison, S. L. et al. (2018). *Monthly Notices of the Royal Astronomical Society* 474(2), pages 2039–2054. issn: 0035-8711, 1365-2966. doi: 10.1093/mnras/stx2882.
- Elmegreen, B. G. (2009). *The Evolving ISM in the Milky Way and Nearby Galaxies*. eprint: arXiv:0803.3154, page 14. url: <http://adsabs.harvard.edu/abs/2009eimw.confE..14E>.
- Emsellem, E., Dejonghe, H., and Bacon, R. (1999). *Monthly Notices of the Royal Astronomical Society* 303(3), pages 495–514. issn: 0035-8711. doi: 10.1046/j.1365-8711.1999.02210.x.
- Emsellem, E. et al. (2007). *Monthly Notices of the Royal Astronomical Society* 379(2), pages 401–417. issn: 0035-8711. doi: 10.1111/j.1365-2966.2007.11752.x.
- Ene, I. et al. (2018). *Monthly Notices of the Royal Astronomical Society* 479(2), pages 2810–2826. issn: 0035-8711. doi: 10.1093/mnras/sty1649.
- Ene, I. et al. (2020). *The Astrophysical Journal* 891(1), page 65. issn: 0004-637X. doi: 10.3847/1538-4357/ab7016.
- Espinoza, P., Selman, F. J., and Melnick, J. (2009). *Astronomy & Astrophysics* 501(2), pages 563–583. issn: 0004-6361, 1432-0746. doi: 10.1051/0004-6361/20078597.
- Faber, S. M. and Jackson, R. E. (1976). *The Astrophysical Journal* 204, pages 668–683. doi: 10.1086/154215.
- Faisst, A. L. et al. (2017). *The Astrophysical Journal* 839(2), page 71. issn: 0004-637X. doi: 10.3847/1538-4357/aa697a.
- Falcón-Barroso, J. et al. (2011). *Astronomy & Astrophysics* 532, A95. issn: 0004-6361, 1432-0746. doi: 10.1051/0004-6361/201116842.
- Falcón-Barroso, J. et al. (2006). *Monthly Notices of the Royal Astronomical Society* 369(2), pages 529–566. issn: 0035-8711. doi: 10.1111/j.1365-2966.2006.10261.x.
- Famaey, B., Van Caelenbergh, K., and Dejonghe, H. (2002). *Monthly Notices of the Royal Astronomical Society* 335(1), pages 201–215. issn: 0035-8711. doi: 10.1046/j.1365-8711.2002.05642.x.
- Fanelli, M. N. et al. (1992). *The Astrophysical Journal Supplement Series* 82, pages 197–245. doi: 10.1086/191714.
- Fardal, M. A. et al. (2007). *Monthly Notices of the Royal Astronomical Society* 379(3), pages 985–1002. issn: 0035-8711. doi: 10.1111/j.1365-2966.2007.11522.x.
- Fasano, G. et al. (2010). *Monthly Notices of the Royal Astronomical Society* 404(3), pages 1490–1504. issn: 0035-8711. doi: 10.1111/j.1365-2966.2010.16361.x.
- Fernandes, R. C. et al. (2005). *Monthly Notices of the Royal Astronomical Society* 358(2), pages 363–378. issn: 0035-8711. doi: 10.1111/j.1365-2966.2005.08752.x.
- Ferreras, I. et al. (2013). *Monthly Notices of the Royal Astronomical Society: Letters* 429(1), pages L15–L19. issn: 1745-3925. doi: 10.1093/mnrasl/sls014.
- Ferreras, I. et al. (2015). *Monthly Notices of the Royal Astronomical Society: Letters* 448(1), pages L82–L86. issn: 1745-3925. doi: 10.1093/mnrasl/slv003.
- Ferreras, I. et al. (2019). *Monthly Notices of the Royal Astronomical Society* 489(1), pages 608–622. issn: 0035-8711. doi: 10.1093/mnras/stz2095.
- Feuillet, D. K. et al. (2019). *Monthly Notices of the Royal Astronomical Society* 489(2), pages 1742–1752. issn: 0035-8711. doi: 10.1093/mnras/stz2221.
- Fioc, M. and Rocca-Volmerange, B. (1997). *Astronomy and Astrophysics* 326, pages 950–962. issn: 0004-6361. url: <http://adsabs.harvard.edu/abs/1997A%26A...326..950F>.
- Fogarty, L. M. R. et al. (2014). *Monthly Notices of the Royal Astronomical Society* 443(1), pages 485–503. issn: 0035-8711. doi: 10.1093/mnras/stu1165.
- Fontanot, F. et al. (2018). *Monthly Notices of the Royal Astronomical Society* 479(4), pages 5678–5685. issn: 0035-8711. doi: 10.1093/mnras/sty1768.

- Foster, C. et al. (2017). *Monthly Notices of the Royal Astronomical Society* 472(1), pages 966–978. issn: 0035-8711. doi: 10.1093/mnras/stx1869.
- Franx, M. and de Zeeuw, T. (1992). *The Astrophysical Journal Letters* 392, pages L47–L50. issn: 0004-637X. doi: 10.1086/186422.
- Franx, M., Illingworth, G., and de Zeeuw, T. (1991). *The Astrophysical Journal* 383, pages 112–134. doi: 10.1086/170769.
- Franx, M. and Illingworth, G. D. (1988). *The Astrophysical Journal Letters* 327, pages L55–L59. doi: 10.1086/185139.
- Fraser-McKelvie, A. et al. (2019). *Monthly Notices of the Royal Astronomical Society: Letters* 488(1), pages L6–L11. issn: 1745-3925. doi: 10.1093/mnrasl/slz085.
- Freeman, K. C. (2003). *Science* 302(5652), pages 1902–1903. issn: 0036-8075, 1095-9203. doi: 10.1126/science.1091466.
- Fritz, J. et al. (2007). *Astronomy & Astrophysics* 470(1), pages 137–152. issn: 0004-6361, 1432-0746. doi: 10.1051/0004-6361:20077097.
- Fumagalli, M., O'Meara, J. M., and Prochaska, J. X. (2011). *Science* 334(6060), pages 1245–1249. issn: 0036-8075, 1095-9203. doi: 10.1126/science.1213581.
- Gadotti, D. A. (2009). *Monthly Notices of the Royal Astronomical Society* 393(4), pages 1531–1552. issn: 0035-8711. doi: 10.1111/j.1365-2966.2008.14257.x.
- Gallazzi, A. et al. (2005). *Monthly Notices of the Royal Astronomical Society* 362(1), pages 41–58. issn: 0035-8711. doi: 10.1111/j.1365-2966.2005.09321.x.
- Gallazzi, A. et al. (2008). *Monthly Notices of the Royal Astronomical Society* 383(4), pages 1439–1458. issn: 0035-8711. doi: 10.1111/j.1365-2966.2007.12632.x.
- Gargiulo, A. et al. (2019). *Astronomy & Astrophysics* 631, A15. issn: 0004-6361, 1432-0746. doi: 10.1051/0004-6361/201833600.
- Ge, J. et al. (2019). *Monthly Notices of the Royal Astronomical Society* 485(2), pages 1675–1693. issn: 0035-8711. doi: 10.1093/mnras/stz418.
- Gebhardt, K. et al. (2000). *The Astronomical Journal* 119(3), pages 1157–1171. issn: 1538-3881. doi: 10.1086/301240.
- Geha, M. et al. (2013). *The Astrophysical Journal* 771(1), page 29. issn: 0004-637X. doi: 10.1088/0004-637X/771/1/29.
- Gennaro, M. et al. (2018). *The Astrophysical Journal* 855(1), page 20. issn: 0004-637X. doi: 10.3847/1538-4357/aaa973.
- Gentile, G. et al. (2007). *Monthly Notices of the Royal Astronomical Society* 375(1), pages 199–212. issn: 0035-8711. doi: 10.1111/j.1365-2966.2006.11283.x.
- Gerhard, O. and Binney, J. (1996). *Monthly Notices of the Royal Astronomical Society* 279(3), pages 993–1004. issn: 0035-8711. doi: 10.1093/mnras/279.3.993.
- Gerhard, O. E. (1993). *Monthly Notices of the Royal Astronomical Society* 265(1), pages 213–230. issn: 0035-8711. doi: 10.1093/mnras/265.1.213.
- Gerhard, O. E. and Michael Fall, S. (1983). *Monthly Notices of the Royal Astronomical Society* 203(4), pages 1253–1268. issn: 0035-8711. doi: 10.1093/mnras/203.4.1253.
- Gerhard, O. O. E. and Binney, J. (1985). *Monthly Notices of the Royal Astronomical Society* 216(2), pages 467–502. issn: 0035-8711. doi: 10.1093/mnras/216.2.467.
- Girardi, L. et al. (2000). *Astronomy and Astrophysics Supplement Series* 141(3), pages 371–383. issn: 0365-0138, 1286-4846. doi: 10.1051/aas:2000126.
- Girardi, L. et al. (2002). *Astronomy & Astrophysics* 391(1), pages 195–212. issn: 0004-6361, 1432-0746. doi: 10.1051/0004-6361:20020612.
- Goddard, D. et al. (2017). *Monthly Notices of the Royal Astronomical Society* 465(1), pages 688–700. issn: 0035-8711. doi: 10.1093/mnras/stw2719.

- Gomes, J. M. and Papaderos, P. (2017). *Astronomy & Astrophysics* 603, A63. issn: 0004-6361, 1432-0746. doi: 10.1051/0004-6361/201628986.
- Gonneau, A. et al. (2020). *Astronomy & Astrophysics* 634, A133. issn: 0004-6361, 1432-0746. doi: 10.1051/0004-6361/201936825.
- Goudfrooij, P. and Asa'd, R. (2020). *Monthly Notices of the Royal Astronomical Society* 501(1), pages 440–466. issn: 0035-8711, 1365-2966. doi: 10.1093/mnras/staa3617. arXiv: 2011.08244.
- Governato, F. et al. (2009). *Monthly Notices of the Royal Astronomical Society* 398(1), pages 312–320. issn: 0035-8711. doi: 10.1111/j.1365-2966.2009.15143.x.
- Gration, A. and Wilkinson, M. I. (2019). *Monthly Notices of the Royal Astronomical Society* 485(4), pages 4878–4892. issn: 0035-8711. doi: 10.1093/mnras/stz605.
- Greene, J. E. et al. (2018). *The Astrophysical Journal* 852(1), page 36. issn: 0004-637X. doi: 10.3847/1538-4357/aa9bde.
- Grieves, N. et al. (2018). *Monthly Notices of the Royal Astronomical Society* 481(3), pages 3244–3265. issn: 0035-8711. doi: 10.1093/mnras/sty2431.
- Grossi, M. et al. (2020). *Monthly Notices of the Royal Astronomical Society* 498(2), pages 1939–1950. issn: 0035-8711. doi: 10.1093/mnras/staa2382.
- Gunawardhana, M. L. P. et al. (2011). *Monthly Notices of the Royal Astronomical Society* 415(2), pages 1647–1662. issn: 0035-8711. doi: 10.1111/j.1365-2966.2011.18800.x.
- Gunn, J. E. and Gott III, J. R. (1972). *The Astrophysical Journal* 176, page 1. issn: 0004-637X. doi: 10.1086/151605.
- Gustafsson, B. et al. (2008). *Astronomy & Astrophysics* 486(3), pages 951–970. issn: 0004-6361, 1432-0746. doi: 10.1051/0004-6361:200809724.
- Hacar, A. et al. (2018). *Astronomy & Astrophysics* 610, A77. issn: 0004-6361, 1432-0746. doi: 10.1051/0004-6361/201731894.
- Haghi, H. et al. (2017). *The Astrophysical Journal* 839(1), page 60. issn: 0004-637X. doi: 10.3847/1538-4357/aa6719.
- Hamacher, D. W. (2012). PhD thesis. Australia : Macquarie University. url: <http://hdl.handle.net/1959.14/268547>.
- Han, Y. and Han, Z. (2012). *The Astrophysical Journal* 749(2), page 123. issn: 0004-637X. doi: 10.1088/0004-637X/749/2/123.
- Han, Y. and Han, Z. (2018). *The Astrophysical Journal Supplement Series* 240(1), page 3. issn: 0067-0049. doi: 10.3847/1538-4365/aaeffa.
- Hayden, M. R. et al. (2017). *Astronomy & Astrophysics* 608, page L1. issn: 0004-6361, 1432-0746. doi: 10.1051/0004-6361/201731494.
- Haynes, R. D. (1995). *Interdisciplinary Science Reviews* 20(3), pages 187–197. issn: 0308-0188. doi: 10.1179/ISR.1995.20.3.187.
- Haynes, R. D. (2000). *Astronomy Across Cultures: The History of Non-Western Astronomy*. Edited by Selin, H. and Xiaochun, S. Springer Netherlands: Dordrecht, pages 53–90. isbn: 978-94-011-4179-6. doi: 10.1007/978-94-011-4179-6\_3.
- Hertzsprung, E. (1911). *Publikationen des Astrophysikalischen Observatoriums zu Potsdam* 63. url: <http://adsabs.harvard.edu/abs/1911POPot..63.....H>.
- Hidalgo, S. L. et al. (2018). *The Astrophysical Journal* 856(2), page 125. issn: 0004-637X. doi: 10.3847/1538-4357/aab158.
- Hill, G. J. et al. (2014). *Ground-Based and Airborne Instrumentation for Astronomy V*. Volume 9147. International Society for Optics and Photonics, 91470Q. doi: 10.1117/12.2056911.

- Hirschmann, M. et al. (2015). *Monthly Notices of the Royal Astronomical Society* 449(1), pages 528–550. issn: 0035-8711. doi: 10.1093/mnras/stv274.
- Hoffmann, K. H. et al. (2018). *Monthly Notices of the Royal Astronomical Society* 478(2), pages 2113–2118. issn: 0035-8711. doi: 10.1093/mnras/sty1251.
- Hopkins, A. M. (2018). *Publications of the Astronomical Society of Australia* 35, e039. issn: 1323-3580, 1448-6083. doi: 10.1017/pasa.2018.29.
- Hopkins, A. M. and Beacom, J. F. (2006). *The Astrophysical Journal* 651(1), page 142. issn: 0004-637X. doi: 10.1086/506610.
- Hopkins, P. F., Quataert, E., and Murray, N. (2011). *Monthly Notices of the Royal Astronomical Society* 417(2), pages 950–973. issn: 0035-8711. doi: 10.1111/j.1365-2966.2011.19306.x.
- Hopkins, P. F. et al. (2006). *The Astrophysical Journal Supplement Series* 163(1), page 1. issn: 0067-0049. doi: 10.1086/499298.
- Hopkins, P. F. et al. (2014). *Monthly Notices of the Royal Astronomical Society* 445(1), pages 581–603. issn: 0035-8711. doi: 10.1093/mnras/stu1738.
- Hosek Jr, M. W. et al. (2019). *The Astrophysical Journal* 870(1), page 44. issn: 0004-637X. doi: 10.3847/1538-4357/aaef90.
- Houghton, R. C. W. et al. (2013). *Monthly Notices of the Royal Astronomical Society* 436(1), pages 19–33. issn: 0035-8711. doi: 10.1093/mnras/stt1399.
- Hoversten, E. A. and Glazebrook, K. (2008). *The Astrophysical Journal* 675(1), page 163. issn: 0004-637X. doi: 10.1086/524095.
- Huang, S. et al. (2013). *The Astrophysical Journal* 766(1), page 47. issn: 0004-637X. doi: 10.1088/0004-637X/766/1/47.
- Huang, S. et al. (2018). *Monthly Notices of the Royal Astronomical Society* 480(1), pages 521–537. issn: 0035-8711. doi: 10.1093/mnras/sty1136.
- Hubble, E. P. (1926). *The Astrophysical Journal* 64. issn: 0004-637X. doi: 10.1086/143018.
- Hubble, E. P. (1927). *The Observatory* 50, pages 276–281. issn: 0029-7704. url: <http://adsabs.harvard.edu/abs/1927Obs....50..276H>.
- Hubble, E. P. (1930). *The Astrophysical Journal* 71. doi: 10.1086/143250.
- Hubble, E. (1929). *Proceedings of the National Academy of Science* 15, pages 168–173. issn: 0027-8424. doi: 10.1073/pnas.15.3.168.
- Hunter, C. and Qian, E. (1993). *Monthly Notices of the Royal Astronomical Society* 262(2), pages 401–428. issn: 0035-8711. doi: 10.1093/mnras/262.2.401.
- Illingworth, G. (1977). *The Astrophysical Journal Letters* 218, pages L43–L47. doi: 10.1086/182572.
- Iodice, E. et al. (2016). *The Astrophysical Journal* 820(1), page 42. issn: 0004-637X. doi: 10.3847/0004-637X/820/1/42.
- Iodice, E. et al. (2017). *The Astrophysical Journal* 839(1), page 21. issn: 0004-637X. doi: 10.3847/1538-4357/aa6846.
- Iodice, E. et al. (2019). *Astronomy & Astrophysics* 623, A1. issn: 0004-6361, 1432-0746. doi: 10.1051/0004-6361/201833741.
- Ivanov, V. D. et al. (2019). *Astronomy & Astrophysics* 629, A100. issn: 0004-6361, 1432-0746. doi: 10.1051/0004-6361/201936178.
- Janz, J. et al. (2012). *The Astrophysical Journal* 745(2), page L24. issn: 2041-8205. doi: 10.1088/2041-8205/745/2/L24.
- Jarvis, B. J. and Peletier, R. F. (1991). *Astronomy and Astrophysics* 247, pages 315–319. issn: 0004-6361. url: <http://adsabs.harvard.edu/abs/1991A%26A...247..315J>.

- Jeans, J. H. (1915). *Monthly Notices of the Royal Astronomical Society* 76(2), pages 70–84. ISSN: 0035-8711. doi: 10.1093/mnras/76.2.70.
- Jedrzejewski, R. and Schechter, P. L. (1988). *The Astrophysical Journal Letters* 330, pages L87–L91. doi: 10.1086/185211.
- Jiang, Z. and Ossipkov, L. (2007). *Monthly Notices of the Royal Astronomical Society* 379(3), pages 1133–1142. ISSN: 0035-8711. doi: 10.1111/j.1365-2966.2007.11992.x.
- Jones, D. H. et al. (2009). *Monthly Notices of the Royal Astronomical Society* 399(2), pages 683–698. ISSN: 0035-8711. doi: 10.1111/j.1365-2966.2009.15338.x.
- Jong, R. S. de (1996). *Astronomy and Astrophysics Supplement Series* 118(3), pages 557–573. ISSN: 0365-0138, 1286-4846. doi: 10.1051/aas:1996220.
- Kannan, R. et al. (2015). *Monthly Notices of the Royal Astronomical Society* 452(4), pages 4347–4360. ISSN: 0035-8711, 1365-2966. doi: 10.1093/mnras/stv1633.
- Kauffmann, G. et al. (2003). *Monthly Notices of the Royal Astronomical Society* 341(1), pages 54–69. ISSN: 0035-8711. doi: 10.1046/j.1365-8711.2003.06292.x.
- Kelz, A. et al. (2006). *Publications of the Astronomical Society of the Pacific* 118(839), page 129. ISSN: 1538-3873. doi: 10.1086/497455.
- Kennicutt, R. C. and Evans, N. J. (2012). *Annual Review of Astronomy and Astrophysics* 50(1), pages 531–608. ISSN: 0066-4146. doi: 10.1146/annurev-astro-081811-125610.
- Kent, S. M. (1985). *The Astrophysical Journal Supplement Series* 59, pages 115–159. doi: 10.1086/191066.
- Kent, S. M. (1986). *The Astronomical Journal* 91, pages 1301–1327. ISSN: 0004-6256. doi: 10.1086/114106.
- Kewley, L. J. and Ellison, S. L. (2008). *The Astrophysical Journal* 681(2), page 1183. ISSN: 0004-637X. doi: 10.1086/587500.
- Khalatyan, A. et al. (2008). *Monthly Notices of the Royal Astronomical Society* 387(1), pages 13–30. ISSN: 0035-8711. doi: 10.1111/j.1365-2966.2008.13093.x.
- Khosroshahi, H. G., Wadadekar, Y., and Kembhavi, A. (2000). *The Astrophysical Journal* 533(1), page 162. ISSN: 0004-637X. doi: 10.1086/308654.
- Kimm, T. and Yi, S. K. (2007). *The Astrophysical Journal* 670(2), page 1048. ISSN: 0004-637X. doi: 10.1086/522573.
- King, I. R. and Minkowski, R. (1966). *The Astrophysical Journal* 143, page 1002. doi: 10.1086/148580.
- Kofman, L. A., Gnedin, N. Y., and Bahcall, N. A. (1993). *The Astrophysical Journal* 413, pages 1–9. ISSN: 0004-637X. doi: 10.1086/172970.
- Koleva, M. et al. (2009). *Astronomy & Astrophysics* 501(3), pages 1269–1279. ISSN: 0004-6361, 1432-0746. doi: 10.1051/0004-6361/200811467.
- Kormendy, J. (1977). *The Astrophysical Journal* 217, pages 406–419. doi: 10.1086/155589.
- Kormendy, J. and Bender, R. (1996). *The Astrophysical Journal* 464(2), pages L119–L122. ISSN: 0004637X. doi: 10.1086/310095.
- Kormendy, J. and Bender, R. (2011). *The Astrophysical Journal Supplement Series* 198(1), page 2. ISSN: 0067-0049. doi: 10.1088/0067-0049/198/1/2.
- Kovač, K. et al. (2010). *The Astrophysical Journal* 718(1), pages 86–104. ISSN: 0004-637X. doi: 10.1088/0004-637X/718/1/86.
- Kowalczyk, K. et al. (2019). *Monthly Notices of the Royal Astronomical Society* 482(4), pages 5241–5249. ISSN: 0035-8711. doi: 10.1093/mnras/sty3100.
- Krajnović, D. et al. (2005). *Monthly Notices of the Royal Astronomical Society* 357(4), pages 1113–1133. ISSN: 0035-8711. doi: 10.1111/j.1365-2966.2005.08715.x.

- Krajnović, D. et al. (2011). *Monthly Notices of the Royal Astronomical Society, Volume 414, Issue 4, pp. 2923–2949.* 414(4), pages 2923–2949. ISSN: 0035-8711. doi: 10.1111/j.1365-2966.2011.18560.x.
- Krajnović, D. et al. (2013). *Monthly Notices of the Royal Astronomical Society, Volume 432, Issue 3, p.1768-1795* 432(3), pages 1768–1795. ISSN: 0035-8711. doi: 10.1093/mnras/sts315.
- Kroupa, P. (2001). *Monthly Notices of the Royal Astronomical Society* 322(2), pages 231–246. ISSN: 0035-8711. doi: 10.1046/j.1365-8711.2001.04022.x.
- Kroupa, P. et al. (2013). *Planets, Stars and Stellar Systems: Volume 5: Galactic Structure and Stellar Populations.* Edited by Oswalt, T. D. and Gilmore, G. Springer Netherlands: Dordrecht, pages 115–242. ISBN: 978-94-007-5612-0. doi: 10.1007/978-94-007-5612-0\_4.
- Kuijken, K. and Merrifield, M. R. (1993). *Monthly Notices of the Royal Astronomical Society* 264(3), pages 712–720. ISSN: 0035-8711. doi: 10.1093/mnras/264.3.712.
- Kuzmin, G. (1956). *Astronomicheskii Zhurnal* 33, page 27.
- La Barbera, F. et al. (2019). *Monthly Notices of the Royal Astronomical Society* 489(3), pages 4090–4110. ISSN: 0035-8711, 1365-2966. doi: 10.1093/mnras/stz2192.
- La Barbera, F. et al. (2013). *Monthly Notices of the Royal Astronomical Society* 433(4), pages 3017–3047. ISSN: 0035-8711. doi: 10.1093/mnras/stt943.
- La Barbera, F., Ferreras, I., and Vazdekis, A. (2015). *Monthly Notices of the Royal Astronomical Society: Letters* 449(1), pages L137–L141. ISSN: 1745-3925. doi: 10.1093/mnrasl/slv029.
- La Barbera, F. et al. (2016). *Monthly Notices of the Royal Astronomical Society* 457(2), pages 1468–1489. ISSN: 0035-8711. doi: 10.1093/mnras/stv2996.
- Lacerna, I. et al. (2020). *Astronomy & Astrophysics* 644, A117. ISSN: 0004-6361, 1432-0746. doi: 10.1051/0004-6361/202037503.
- Lada, C. J. and Lada, E. A. (2003). *Annual Review of Astronomy and Astrophysics* 41(1), pages 57–115. doi: 10.1146/annurev.astro.41.011802.094844.
- Lagattuta, D. J. et al. (2017). *The Astrophysical Journal* 846(2), page 166. ISSN: 0004-637X. doi: 10.3847/1538-4357/aa8563.
- Lagos, C. d. P. et al. (2018). *Monthly Notices of the Royal Astronomical Society* 473(4), pages 4956–4974. ISSN: 0035-8711. doi: 10.1093/mnras/stx2667.
- Lambas, D. G., Maddox, S. J., and Loveday, J. (1992). *Monthly Notices of the Royal Astronomical Society* 258(2), pages 404–414. ISSN: 0035-8711. doi: 10.1093/mnras/258.2.404.
- Larkin, J. et al. (2006). *Ground-Based and Airborne Instrumentation for Astronomy.* Volume 6269. International Society for Optics and Photonics, 62691A. doi: 10.1117/12.672061.
- Larson, R. B. (1990). *Publications of the Astronomical Society of the Pacific* 102, pages 709–722. ISSN: 0004-6280. doi: 10.1086/132694.
- Lauer, T. R. et al. (1995). *The Astronomical Journal* 110, page 2622. ISSN: 0004-6256. doi: 10.1086/117719.
- Lauer, T. R. (1986). *The Astrophysical Journal* 311, pages 34–44. ISSN: 0004-637X. doi: 10.1086/164752.
- Lauer, T. R. et al. (2021). *The Astrophysical Journal* 906(2), page 77. ISSN: 0004-637X. doi: 10.3847/1538-4357/abc881.
- Leach, R. (1981). *The Astrophysical Journal* 248, pages 485–498. doi: 10.1086/159173.
- Leaman, R. et al. (2017). *Monthly Notices of the Royal Astronomical Society* 472(2), pages 1879–1896. ISSN: 0035-8711. doi: 10.1093/mnras/stx2014.

- Lee, H. et al. (2006). *The Astrophysical Journal* 647(2), page 970. issn: 0004-637X. doi: 10.1086/505573.
- Lee, J. C., Hwang, H. S., and Chung, H. (2018). *Monthly Notices of the Royal Astronomical Society* 477(2), pages 1567–1577. issn: 0035-8711. doi: 10.1093/mnras/sty729.
- LeFevre, O. et al. (2003). *Instrument Design and Performance for Optical/Infrared Ground-Based Telescopes*. Volume 4841. International Society for Optics and Photonics, pages 1670–1681. doi: 10.1117/12.460959.
- Leier, D. et al. (2016). *Monthly Notices of the Royal Astronomical Society* 459(4), pages 3677–3692. issn: 0035-8711. doi: 10.1093/mnras/stw885.
- Leja, J. et al. (2017). *The Astrophysical Journal* 837(2), page 170. issn: 0004-637X. doi: 10.3847/1538-4357/aa5ffe.
- Lejeune, T., Cuisinier, F., and Buser, R. (1998). *Astronomy and Astrophysics Supplement Series* 130(1), pages 65–75. issn: 0365-0138, 1286-4846. doi: 10.1051/aas:1998405.
- Lejeune, T., Cuisinier, F., and Buser, R. (1997). *Astronomy and Astrophysics Supplement Series* 125(2), pages 229–246. issn: 0365-0138, 1286-4846. doi: 10.1051/aas:1997373.
- Lelli, F., McGaugh, S. S., and Schombert, J. M. (2016). *The Astronomical Journal* 152(6), page 157. issn: 1538-3881. doi: 10.3847/0004-6256/152/6/157.
- Lequeux, J. et al. (1979). *Astronomy and Astrophysics* 80, pages 155–166. issn: 0004-6361. url: <http://adsabs.harvard.edu/abs/1979A%26A....80..155L>.
- Li, H. et al. (2017). *The Astrophysical Journal* 838(2), page 77. issn: 0004-637X. doi: 10.3847/1538-4357/aa662a.
- Li, H. et al. (2018a). *Monthly Notices of the Royal Astronomical Society* 476(2), pages 1765–1775. issn: 0035-8711. doi: 10.1093/mnras/sty334.
- Li, H. et al. (2018b). *The Astrophysical Journal* 863(2), page L19. issn: 2041-8205. doi: 10.3847/2041-8213/aad54b.
- Li, S. et al. (2020). *The Astrophysical Journal* 896(2), page 110. issn: 0004-637X. doi: 10.3847/1538-4357/ab84f1.
- Libeskind, N. I. et al. (2012). *Monthly Notices of the Royal Astronomical Society: Letters* 421(1), pages L137–L141. issn: 1745-3925. doi: 10.1111/j.1745-3933.2012.01222.x.
- Lyubenova, M. et al. (2016). *Monthly Notices of the Royal Astronomical Society* 463(3), pages 3220–3225. issn: 0035-8711. doi: 10.1093/mnras/stw2434.
- Mackereth, J. T. et al. (2019). *Monthly Notices of the Royal Astronomical Society* 482(3), pages 3426–3442. issn: 0035-8711. doi: 10.1093/mnras/sty2955.
- Madau, P. and Dickinson, M. (2014). *Annual Review of Astronomy and Astrophysics* 52(1), pages 415–486. doi: 10.1146/annurev-astro-081811-125615.
- Magorrian, J. (1995). *Monthly Notices of the Royal Astronomical Society* 277(4), pages 1185–1190. issn: 0035-8711. doi: 10.1093/mnras/277.4.1185.
- Magorrian, J. et al. (1998). *The Astronomical Journal* 115(6), page 2285. issn: 1538-3881. doi: 10.1086/300353.
- Mamon, G. A. et al. (2019). *Astronomy & Astrophysics* 631, A131. issn: 0004-6361, 1432-0746. doi: 10.1051/0004-6361/201935081.
- Mannucci, F. et al. (2010). *Monthly Notices of the Royal Astronomical Society* 408(4), pages 2115–2127. issn: 0035-8711. doi: 10.1111/j.1365-2966.2010.17291.x.
- Mapelli, M. (2015). *Galaxies* 3(4), pages 192–201. doi: 10.3390/galaxies3040192.
- Maraston, C. (2005). *Monthly Notices of the Royal Astronomical Society* 362(3), pages 799–825. issn: 0035-8711. doi: 10.1111/j.1365-2966.2005.09270.x.
- Maraston, C. and Strömbäck, G. (2011). *Monthly Notices of the Royal Astronomical Society* 418(4), pages 2785–2811. issn: 0035-8711. doi: 10.1111/j.1365-2966.2011.19738.x.

- Maraston, C. et al. (2020). *Monthly Notices of the Royal Astronomical Society*, staa1489. issn: 0035-8711, 1365-2966. doi: 10.1093/mnras/staa1489. arXiv: 1911.05748.
- Martig, M., Minchev, I., and Flynn, C. (2014). *Monthly Notices of the Royal Astronomical Society* 443(3), pages 2452–2462. issn: 0035-8711. doi: 10.1093/mnras/stu1322.
- Martín-Navarro, I. et al. (2019). *Astronomy & Astrophysics* 626, A124. issn: 0004-6361, 1432-0746. doi: 10.1051/0004-6361/201935360.
- Martín-Navarro, I. et al. (2015). *The Astrophysical Journal* 806(2), page L31. issn: 2041-8205. doi: 10.1088/2041-8205/806/2/L31.
- Martins, L. P. et al. (2005). *Monthly Notices of the Royal Astronomical Society* 358(1), pages 49–65. issn: 0035-8711. doi: 10.1111/j.1365-2966.2005.08703.x.
- Martinsson, T. P. K. et al. (2013). *Astronomy & Astrophysics* 557, A131. issn: 0004-6361, 1432-0746. doi: 10.1051/0004-6361/201321390.
- Massari, D. et al. (2020). *Astronomy & Astrophysics* 633, A36. issn: 0004-6361, 1432-0746. doi: 10.1051/0004-6361/201935613.
- Massey, P. (2002). *The Astrophysical Journal Supplement Series* 141, pages 81–122. issn: 0067-0049. doi: 10.1086/338286.
- Matteucci, F. (1994). *Astronomy and Astrophysics* 288, pages 57–64. issn: 0004-6361. url: <http://adsabs.harvard.edu/abs/1994A%26A...288...57M>.
- Mayer, L. et al. (2001). *Astrophysics and Space Science* 276(2), pages 375–382. issn: 1572-946X. doi: 10.1023/A:1017562225479.
- McClure, R. D. and van den Bergh, S. (1968). *The Astronomical Journal* 73, pages 313–337. doi: 10.1086/110634.
- McDermid, R. M. et al. (2006a). *New Astronomy Reviews*. Adaptive Optics-Assisted Integral-Field Spectroscopy 49(10), pages 521–535. issn: 1387-6473. doi: 10.1016/j.newar.2005.10.025.
- McDermid, R. M. et al. (2006b). *Monthly Notices of the Royal Astronomical Society* 373(3), pages 906–958. issn: 0035-8711. doi: 10.1111/j.1365-2966.2006.11065.x.
- McDermid, R. M. et al. (2014). *The Astrophysical Journal* 792(2), page L37. issn: 2041-8205. doi: 10.1088/2041-8205/792/2/L37.
- McDermid, R. M. et al. (2015). *Monthly Notices of the Royal Astronomical Society, Volume 448, Issue 4, p.3484-3513* 448(4), pages 3484–3513. issn: 0035-8711. doi: 10.1093/mnras/stv105.
- McDermid, R. M. et al. (2020). *arXiv e-prints* 2009, arXiv:2009.09242. url: <http://adsabs.harvard.edu/abs/2020arXiv200909242M>.
- McGregor, P. J. et al. (2003). *Instrument Design and Performance for Optical/Infrared Ground-Based Telescopes*. Volume 4841. International Society for Optics and Photonics, pages 1581–1591. doi: 10.1117/12.459448.
- McGregor, P. J. et al. (2012). *Ground-Based and Airborne Instrumentation for Astronomy IV*. Volume 8446. International Society for Optics and Photonics, page 84461I. doi: 10.1117/12.925259.
- McKee, C. F. and Ostriker, E. C. (2007). *Annual Review of Astronomy and Astrophysics* 45(1), pages 565–687. doi: 10.1146/annurev.astro.45.051806.110602.
- Mehlert, D. et al. (2003). *Astronomy & Astrophysics* 407(2), pages 423–435. issn: 0004-6361, 1432-0746. doi: 10.1051/0004-6361:20030886.
- Mendel, J. T. et al. (2020). *The Astrophysical Journal* 899(1), page 87. issn: 0004-637X. doi: 10.3847/1538-4357/ab9ffcc.
- Méndez-Abreu, J. et al. (2010). *Astronomy & Astrophysics* 521, A71. issn: 0004-6361, 1432-0746. doi: 10.1051/0004-6361/201014130.

- Méndez-Abreu, J. et al. (2017). *Astronomy & Astrophysics* 598, A32. issn: 0004-6361, 1432-0746. doi: 10.1051/0004-6361/201629525.
- Mentz, J. J. et al. (2016). *Monthly Notices of the Royal Astronomical Society* 463(3), pages 2819–2838. issn: 0035-8711. doi: 10.1093/mnras/stw2129.
- Meusinger, H., Reimann, H. G., and Stecklum, B. (1991). *Astronomy and Astrophysics* 245, pages 57–74. issn: 0004-6361. url: <http://adsabs.harvard.edu/abs/1991A%26A...245...57M>.
- Mihos, J. C. (1995). *The Astrophysical Journal Letters* 438, pages L75–L78. issn: 0004-637X. doi: 10.1086/187719.
- Mihos, J. C. and Hernquist, L. (1996). *The Astrophysical Journal* 464, page 641. issn: 0004-637X. doi: 10.1086/177353.
- Miller, G. E. and Scalo, J. M. (1979). *The Astrophysical Journal Supplement Series* 41, pages 513–547. doi: 10.1086/190629.
- Minchev, I. et al. (2014). *The Astrophysical Journal Letters* 781(1), page L20.
- Mizuno, T. and Hamajima, K. (1987). *Publications of the Astronomical Society of Japan* 39, pages 221–235. issn: 0004-6264. url: <http://adsabs.harvard.edu/abs/1987PASJ...39..221M>.
- Molaeinezhad, A. et al. (2017). *Monthly Notices of the Royal Astronomical Society* 467(1), pages 353–368. issn: 0035-8711. doi: 10.1093/mnras/stx051.
- Moore, B., Lake, G., and Katz, N. (1998). *The Astrophysical Journal* 495(1), page 139. issn: 0004-637X. doi: 10.1086/305264.
- Moriondo, G., Giovanardi, C., and Hunt, L. K. (1998). *Astronomy and Astrophysics Supplement Series* 130(1), pages 81–108. issn: 0365-0138, 1286-4846. doi: 10.1051/aas:1998408.
- Morrissey, P. et al. (2018). *The Astrophysical Journal* 864(1), page 93. issn: 0004-637X. doi: 10.3847/1538-4357/aad597.
- Morton, D. C. and Chevalier, R. A. (1973). *The Astrophysical Journal* 179, pages 55–68. doi: 10.1086/151846.
- Morton, D. C. and Chevalier, R. A. (1972). *The Astrophysical Journal* 174, page 489. doi: 10.1086/151511.
- Naab, T. and Burkert, A. (2003). *The Astrophysical Journal* 597(2), page 893. issn: 0004-637X. doi: 10.1086/378581.
- Naab, T., Burkert, A., and Hernquist, L. (1999). *The Astrophysical Journal* 523(2), pages L133–L136. issn: 1538-4357. doi: 10.1086/312275.
- Naab, T. and Ostriker, J. P. (2017). *Annual Review of Astronomy and Astrophysics* 55(1), pages 59–109. issn: 0066-4146. doi: 10.1146/annurev-astro-081913-040019.
- Naab, T. et al. (2007). *The Astrophysical Journal* 658(2), page 710. issn: 0004-637X. doi: 10.1086/510841.
- Nagai, R. and Miyamoto, M. (1976). *Publications of the Astronomical Society of Japan* 28, pages 1–17. issn: 0004-6264. url: <http://adsabs.harvard.edu/abs/1976PASJ...28....1N>.
- Nanayakkara, T. et al. (2017). *Monthly Notices of the Royal Astronomical Society* 468(3), pages 3071–3108. issn: 0035-8711, 1365-2966. doi: 10.1093/mnras/stx605.
- Narayanan, D. and Davé, R. (2013). *Monthly Notices of the Royal Astronomical Society* 436(4), pages 2892–2906. issn: 0035-8711. doi: 10.1093/mnras/stt1548.
- Ness, M. et al. (2013). *Monthly Notices of the Royal Astronomical Society* 432(3), pages 2092–2103. issn: 0035-8711. doi: 10.1093/mnras/stt533.
- Neureiter, B. et al. (2021). *Monthly Notices of the Royal Astronomical Society* 500(1), pages 1437–1465. issn: 0035-8711. doi: 10.1093/mnras/staa3014.

- Newman, A. B. et al. (2017). *The Astrophysical Journal* 845(2), page 157. issn: 1538-4357. doi: 10.3847/1538-4357/aa816d. arXiv: 1612.00065.
- Ng, Y. K. et al. (1997). *Astronomy and Astrophysics* 324, pages 65–79. issn: 0004-6361. url: <http://adsabs.harvard.edu/abs/1997A%26A...324...65N>.
- Noeske, K. G. et al. (2007). *The Astrophysical Journal Letters* 660(1), page L43. issn: 1538-4357. doi: 10.1086/517926.
- Noll, S. et al. (2009). *Astronomy & Astrophysics* 507(3), pages 1793–1813. issn: 0004-6361, 1432-0746. doi: 10.1051/0004-6361/200912497.
- Noordermeer, E. et al. (2007). *Monthly Notices of the Royal Astronomical Society* 376(4), pages 1513–1546. issn: 0035-8711. doi: 10.1111/j.1365-2966.2007.11533.x.
- Nordström, B. et al. (2004). *Astronomy & Astrophysics* 418(3), pages 989–1019. issn: 0004-6361, 1432-0746. doi: 10.1051/0004-6361:20035959.
- Norris, R. P. (2009). *Communicating Astronomy with the Public Journal* 9, page 5.
- Norris, R. P. (2016). *Publications of the Astronomical Society of Australia* 33. issn: 1323-3580, 1448-6083. doi: 10.1017/pasa.2016.25.
- Ocvirk, P. et al. (2006). *Monthly Notices of the Royal Astronomical Society* 365(1), pages 74–84. issn: 0035-8711. doi: 10.1111/j.1365-2966.2005.09323.x.
- Oh, S. et al. (2018). *The Astrophysical Journal Supplement Series* 237(1), page 14. issn: 0067-0049. doi: 10.3847/1538-4365/aacd47.
- Oh, S. et al. (2020). *Monthly Notices of the Royal Astronomical Society*, staa1330. issn: 0035-8711, 1365-2966. doi: 10.1093/mnras/staa1330.
- Oldham, L. J. and Auger, M. W. (2018a). *Monthly Notices of the Royal Astronomical Society* 476(1), pages 133–150. issn: 0035-8711. doi: 10.1093/mnras/sty065.
- Oldham, L. J. and Auger, M. W. (2018b). *Monthly Notices of the Royal Astronomical Society* 474, pages 4169–4185. doi: 10.1093/mnras/stx2969.
- Ollongren, A. (1962). *Bulletin of the Astronomical Institutes of the Netherlands* 16, page 241. issn: 0365-8910. url: <http://adsabs.harvard.edu/abs/1962BAN....16..241O>.
- Oort, J. H. (1983). *Annual Review of Astronomy and Astrophysics* 21, pages 373–428. issn: 0066-4146. doi: 10.1146/annurev.aa.21.090183.002105.
- Oser, L. et al. (2010). *The Astrophysical Journal* 725(2), pages 2312–2323. issn: 0004-637X. doi: 10.1088/0004-637X/725/2/2312.
- Ostriker, J. P., Peebles, P. J. E., and Yahil, A. (1974). *The Astrophysical Journal Letters* 193, pages L1–L4. issn: 0004-637X. doi: 10.1086/181617.
- Ota, K. et al. (2010). *The Astrophysical Journal* 722(1), pages 803–811. issn: 0004-637X. doi: 10.1088/0004-637X/722/1/803.
- Ouchi, M. et al. (2010). *The Astrophysical Journal* 723(1), pages 869–894. issn: 0004-637X. doi: 10.1088/0004-637X/723/1/869.
- Owers, M. S. et al. (2019). *The Astrophysical Journal* 873(1), page 52. issn: 0004-637X. doi: 10.3847/1538-4357/ab0201.
- Ozaki, S. et al. (2014). *Advances in Optical and Mechanical Technologies for Telescopes and Instrumentation*. Volume 9151. International Society for Optics and Photonics, page 915149. doi: 10.1117/12.2054838.
- Padilla, N. D. and Strauss, M. A. (2008). *Monthly Notices of the Royal Astronomical Society* 388(3), pages 1321–1334. issn: 0035-8711. doi: 10.1111/j.1365-2966.2008.13480.x.
- Padoan, P., Nordlund, Å., and Jones, B. J. T. (1997). *Monthly Notices of the Royal Astronomical Society* 288(1), pages 145–152. issn: 1365-2966. doi: 10.1093/mnras/288.1.145.
- Pak, M. et al. (2019). *The Astrophysical Journal* 880(2), page 149. issn: 0004-637X. doi: 10.3847/1538-4357/ab2ad6.

- Parikh, T. et al. (2018). *Monthly Notices of the Royal Astronomical Society* 477(3), pages 3954–3982. ISSN: 0035-8711. doi: 10.1093/mnras/sty785.
- Pasquini, L. et al. (2002). *The Messenger* 110, pages 1–9. URL: <http://adsabs.harvard.edu/abs/2002Msngr.110....1P>.
- Pastorello, N. et al. (2014). *Monthly Notices of the Royal Astronomical Society* 442(2), pages 1003–1039. ISSN: 0035-8711. doi: 10.1093/mnras/stu937.
- Paxton, B. et al. (2010). *The Astrophysical Journal Supplement Series* 192(1), page 3. ISSN: 0067-0049. doi: 10.1088/0067-0049/192/1/3.
- Paxton, B. et al. (2013). *The Astrophysical Journal Supplement Series* 208(1), page 4. ISSN: 0067-0049. doi: 10.1088/0067-0049/208/1/4.
- Paxton, B. et al. (2015). *The Astrophysical Journal Supplement Series* 220(1), page 15. ISSN: 0067-0049. doi: 10.1088/0067-0049/220/1/15.
- Peacock, J. A. et al. (2001). *Nature* 410(6825), pages 169–173. ISSN: 1476-4687. doi: 10.1038/35065528.
- Peng, C. Y. et al. (2002). *The Astronomical Journal* 124(1), pages 266–293. ISSN: 1538-3881. doi: 10.1086/340952.
- Peng, C. Y. et al. (2010a). *The Astronomical Journal* 139(6), pages 2097–2129. ISSN: 1538-3881. doi: 10.1088/0004-6256/139/6/2097.
- Peng, Y.-j. et al. (2010b). *The Astrophysical Journal* 721(1), page 193. ISSN: 0004-637X. doi: 10.1088/0004-637X/721/1/193.
- Penzias, A. A. and Wilson, R. W. (1965). *The Astrophysical Journal* 142, pages 419–421. ISSN: 0004-637X. doi: 10.1086/148307.
- Perlmutter, S. et al. (1999). *The Astrophysical Journal* 517(2), page 565. ISSN: 0004-637X. doi: 10.1086/307221.
- Persic, M. and Salucci, P. (1988). *Monthly Notices of the Royal Astronomical Society* 234(1), pages 131–154. ISSN: 0035-8711. doi: 10.1093/mnras/234.1.131.
- Persic, M. and Salucci, P. (1995). *The Astrophysical Journal Supplement Series* 99, page 501. doi: 10.1086/192195.
- Persic, M., Salucci, P., and Stel, F. (1996). *Monthly Notices of the Royal Astronomical Society* 281, pages 27–47. doi: 10.1093/mnras/278.1.27.
- Petrou, M. (1983a). *Monthly Notices of the Royal Astronomical Society* 202(4), pages 1195–1207. ISSN: 0035-8711. doi: 10.1093/mnras/202.4.1195.
- Petrou, M. (1983b). *Monthly Notices of the Royal Astronomical Society* 202(4), pages 1209–1219. ISSN: 0035-8711. doi: 10.1093/mnras/202.4.1209.
- Piatti, A. E. (2012). *Monthly Notices of the Royal Astronomical Society* 422(2), pages 1109–1121. ISSN: 0035-8711. doi: 10.1111/j.1365-2966.2012.20684.x.
- Pickles, A. J. (1998). *Publications of the Astronomical Society of the Pacific* 110(749), page 863. ISSN: 1538-3873. doi: 10.1086/316197.
- Pietrinferni, A. et al. (2004). *The Astrophysical Journal* 612(1), page 168. ISSN: 0004-637X. doi: 10.1086/422498.
- Pipino, A. et al. (2014). *The Astrophysical Journal* 797(2), page 127. ISSN: 0004-637X. doi: 10.1088/0004-637X/797/2/127.
- Poggianti, B. M. et al. (2006). *The Astrophysical Journal* 642(1), page 188. ISSN: 0004-637X. doi: 10.1086/500666.
- Porter, T. A., Johnson, R. P., and Graham, P. W. (2011). *Annual Review of Astronomy and Astrophysics* 49(1), pages 155–194. doi: 10.1146/annurev-astro-081710-102528.
- Portinari, L., Chiosi, C., and Bressan, A. (1998). *Astronomy and Astrophysics* 334, pages 505–539. ISSN: 0004-6361. URL: <http://adsabs.harvard.edu/abs/1998A%26A...334..505P>.

- Posacki, S. et al. (2015). *Monthly Notices of the Royal Astronomical Society* 446(1), pages 493–509. issn: 0035-8711. doi: 10.1093/mnras/stu2098.
- Postman, M. and Geller, M. J. (1984). *The Astrophysical Journal* 281, pages 95–99. issn: 0004-637X. doi: 10.1086/162078.
- Prugniel, P. and Soubiran, C. (2001). *Astronomy & Astrophysics* 369(3), pages 1048–1057. issn: 0004-6361, 1432-0746. doi: 10.1051/0004-6361:20010163.
- Rawle, T. D., Smith, R. J., and Lucey, J. R. (2010). *Monthly Notices of the Royal Astronomical Society* 401(2), pages 852–866. issn: 0035-8711. doi: 10.1111/j.1365-2966.2009.15722.x.
- Read, J. I. and Steger, P. (2017). *Monthly Notices of the Royal Astronomical Society* 471(4), pages 4541–4558. issn: 0035-8711. doi: 10.1093/mnras/stx1798.
- Reid, I. N., Gizis, J. E., and Hawley, S. L. (2002). *The Astronomical Journal* 124(5), page 2721. issn: 1538-3881. doi: 10.1086/343777.
- Reis, S. N. dos et al. (2020). *Astronomy & Astrophysics* 634, A11. issn: 0004-6361, 1432-0746. doi: 10.1051/0004-6361/201936276.
- Renzini, A. and Peng, Y.-j. (2015). *The Astrophysical Journal Letters* 801(2), page L29. issn: 2041-8205. doi: 10.1088/2041-8205/801/2/L29.
- Richstone, D. O. and Tremaine, S. (1984). *The Astrophysical Journal* 286, pages 27–37. issn: 0004-637X. doi: 10.1086/162572.
- Richstone, D. O. (1987/ed). *Symposium - International Astronomical Union* 127, pages 261–269. issn: 0074-1809. doi: 10.1017/S0074180900185237.
- Riess, A. G. et al. (1998). *The Astronomical Journal* 116(3), page 1009. issn: 1538-3881. doi: 10.1086/300499.
- Rix, H.-W. and Zaritsky, D. (1995). *The Astrophysical Journal* 447, page 82. doi: 10.1086/175858.
- Rix, H.-W. et al. (1997). *The Astrophysical Journal* 488(2), page 702. issn: 0004-637X. doi: 10.1086/304733.
- Robijn, F. H. A. and de Zeeuw, P. T. (1996). *Monthly Notices of the Royal Astronomical Society* 279(2), pages 673–692. issn: 0035-8711. doi: 10.1093/mnras/279.2.673.
- Robotham, A. S. G. et al. (2020). *Monthly Notices of the Royal Astronomical Society* 495(1), pages 905–931. issn: 0035-8711. doi: 10.1093/mnras/staa1116.
- Rocha-Pinto, H. J. et al. (2004). *Astronomy & Astrophysics* 423(2), pages 517–535.
- Rodríguez, S., Padilla, N. D., and García Lambas, D. (2016). *Monthly Notices of the Royal Astronomical Society* 456(1), pages 571–577. issn: 0035-8711. doi: 10.1093/mnras/stv2660.
- Rodríguez-Merino, L. H. et al. (2005). *The Astrophysical Journal* 626(1), page 411. issn: 0004-637X. doi: 10.1086/429858.
- Romanowsky, A. J. and Fall, S. M. (2012). *The Astrophysical Journal Supplement Series* 203(2), page 17. issn: 0067-0049. doi: 10.1088/0067-0049/203/2/17.
- Rosani, G. et al. (2018). *Monthly Notices of the Royal Astronomical Society* 476(4), pages 5233–5252. issn: 0035-8711. doi: 10.1093/mnras/sty528.
- Rubin, V. C. and Ford Jr., W. K. (1970). *Astrophysical Journal*, vol. 159, p.379 159, page 379. doi: 10.1086/150317.
- Russell, H. N. (1914). *Popular Astronomy* 22, pages 275–294. issn: 0197-7482. url: <http://adsabs.harvard.edu/abs/1914PA.....22..275R>.
- Rybicki, G. B. (1987). *Symposium - International Astronomical Union* 127, pages 397–398. issn: 0074-1809. doi: 10.1017/S0074180900185420.

- Ryden, B. S. (2004). *The Astrophysical Journal* 601(1), page 214. issn: 0004-637X. doi: 10.1086/380437.
- Ryden, B. S. (2006). *The Astrophysical Journal* 641(2), page 773. issn: 0004-637X. doi: 10.1086/500497.
- Ryden, B. S., Lauer, T. R., and Postman, M. (1993). *The Astrophysical Journal* 410, pages 515–519. doi: 10.1086/172769.
- Saaf, A. F. (1968). *The Astrophysical Journal* 154, page 483. issn: 0004-637X. doi: 10.1086/149776.
- Saha, P. (1992). *Monthly Notices of the Royal Astronomical Society* 254(1), pages 132–138. issn: 0035-8711. doi: 10.1093/mnras/254.1.132.
- Salo, H. et al. (2015). *The Astrophysical Journal Supplement Series* 219(1), page 4. issn: 0067-0049. doi: 10.1088/0067-0049/219/1/4.
- Salpeter, E. E. (1955). *Astrophysical Journal*, vol. 121, p.161 121, page 161. doi: 10.1086/145971.
- Salucci, P. (2019). *The Astronomy and Astrophysics Review* 27(1), page 2. issn: 1432-0754. doi: 10.1007/s00159-018-0113-1.
- Sanchez, S. F. et al. (2016). *Revista Mexicana de Astronomía y Astrofísica* 52, page 33. arXiv: 1509.08552 [astro-ph.IM].
- Sánchez-Blázquez, P. et al. (2006). *Monthly Notices of the Royal Astronomical Society* 371(2), pages 703–718. issn: 0035-8711. doi: 10.1111/j.1365-2966.2006.10699.x.
- Sandage, A., Freeman, K. C., and Stokes, N. R. (1970). *The Astrophysical Journal* 160, page 831. doi: 10.1086/150475.
- Santucci, G. et al. (2020). *The Astrophysical Journal* 896(1), page 75. issn: 0004-637X. doi: 10.3847/1538-4357/ab92a9.
- Sargent, W. L. W. et al. (1978). *The Astrophysical Journal* 221, pages 731–744. doi: 10.1086/156077.
- Sarzi, M. et al. (2000). *Astronomy and Astrophysics* 360, pages 439–446. issn: 0004-6361. url: <http://adsabs.harvard.edu/abs/2000A&lt;26A...360..439S>.
- Sarzi, M. et al. (2006). *Monthly Notices of the Royal Astronomical Society* 366(4), pages 1151–1200. issn: 0035-8711. doi: 10.1111/j.1365-2966.2005.09839.x.
- Sarzi, M. et al. (2018). *Monthly Notices of the Royal Astronomical Society* 478(3), pages 4084–4100. issn: 0035-8711. doi: 10.1093/mnras/sty1092.
- Satoh, C. (1980). *Publications of the Astronomical Society of Japan* 32, page 41. issn: 0004-6264. url: <http://adsabs.harvard.edu/abs/1980PASJ...32...41S>.
- Scalo, J. M. (1986). *Fundamentals of Cosmic Physics* 11, pages 1–278. url: <http://adsabs.harvard.edu/abs/1986FCPh...11....1S>.
- Scalo, J. (1998). *The Stellar Initial Mass Function (38th Herstmonceux Conference)*. Volume 142. eprint: arXiv:astro-ph/9712317, page 201. isbn: 1050-3390. url: <https://ui.adsabs.harvard.edu/abs/1998ASPC..142..201S>.
- Schaefer, A. L. et al. (2019). *The Astrophysical Journal* 884(2), page 156. issn: 0004-637X. doi: 10.3847/1538-4357/ab43ca.
- Schechter, P. L. and Gunn, J. E. (1979). *The Astrophysical Journal* 229, pages 472–484. doi: 10.1086/156978.
- Schlafly, E. F. and Finkbeiner, D. P. (2011). *The Astrophysical Journal* 737(2), page 103. issn: 0004-637X. doi: 10.1088/0004-637X/737/2/103.
- Schlegel, D. J., Finkbeiner, D. P., and Davis, M. (1998). *The Astrophysical Journal* 500(2), page 525. issn: 0004-637X. doi: 10.1086/305772.
- Schmidt, M. (1963). *The Astrophysical Journal* 137, page 758. doi: 10.1086/147553.

- Schoenmakers, R. H. M., Franx, M., and de Zeeuw, P. T. (1997). *Monthly Notices of the Royal Astronomical Society* 292(2), pages 349–364. ISSN: 0035-8711. doi: 10.1093/mnras/292.2.349.
- Schwarzschild, K. (1907). *Nachrichten von der Gesellschaft der Wissenschaften zu Goettingen, Mathematisch-Physikalische Klasse* 5, page 614. URL: <http://adsabs.harvard.edu/abs/1907NWGot...5..614S>.
- Schwarzschild, M. (1979). *Astrophysical Journal, Part 1*, vol. 232, Aug. 15, 1979, p. 236-247. 232, pages 236–247. doi: 10.1086/157282.
- Schweizer, F. (1980). *The Astrophysical Journal* 237, pages 303–318. doi: 10.1086/157870.
- Schweizer, F. (1996). *The Astronomical Journal* 111, page 109. ISSN: 0004-6256. doi: 10.1086/117765.
- Scorza, C. et al. (1998). *Astronomy and Astrophysics Supplement Series* 131(2), pages 265–286. ISSN: 0365-0138, 1286-4846. doi: 10.1051/aas:1998432.
- Scott, N. et al. (2017). *Monthly Notices of the Royal Astronomical Society* 472(3), pages 2833–2855. ISSN: 0035-8711. doi: 10.1093/mnras/stx2166.
- Seabroke, G. M. and Gilmore, G. (2007). *Monthly Notices of the Royal Astronomical Society* 380(4), pages 1348–1368. ISSN: 0035-8711. doi: 10.1111/j.1365-2966.2007.12210.x.
- Selman, F. et al. (1999). *Astronomy and Astrophysics* 347, pages 532–549. ISSN: 0004-6361. URL: <http://adsabs.harvard.edu/abs/1999A%26A...347..532S>.
- Sérsic, J. L. (1963). *Boletin de la Asociacion Argentina de Astronomia La Plata Argentina* 6, pages 41–43. ISSN: 0571-3285. URL: <http://adsabs.harvard.edu/abs/1963BAAA....6...41S>.
- Sharma, S. et al. (2014). *The Astrophysical Journal* 793(1), page 51. ISSN: 0004-637X. doi: 10.1088/0004-637X/793/1/51.
- Sharp, R. et al. (2016). *Ground-Based and Airborne Instrumentation for Astronomy VI*. Volume 9908. International Society for Optics and Photonics, 99081Y. doi: 10.1117/12.2231561.
- Sharples, R. et al. (2013). *The Messenger* 151, pages 21–23. URL: <http://adsabs.harvard.edu/abs/2013Msngr.151...21S>.
- Shaw, M. A. and Gilmore, G. (1989). *Monthly Notices of the Royal Astronomical Society* 237(4), pages 903–927. ISSN: 0035-8711. doi: 10.1093/mnras/237.4.903.
- Sheth, R. K. et al. (2003). *The Astrophysical Journal* 594(1), pages 225–231. ISSN: 0004-637X. doi: 10.1086/376794.
- Shetty, S. and Cappellari, M. (2014). *The Astrophysical Journal* 786(2), page L10. ISSN: 2041-8205. doi: 10.1088/2041-8205/786/2/L10.
- Sil'chenko, O. K. (2016). *Astronomy Letters* 42(3), pages 163–172. ISSN: 1562-6873. doi: 10.1134/S1063773716030051.
- Slipher, V. M. (1917). *Proceedings of the American Philosophical Society* 56, pages 403–409. URL: <http://adsabs.harvard.edu/abs/1917PAPhS..56..403S>.
- Smith, B. D. et al. (2009). *The Astrophysical Journal* 691(1), pages 441–451. ISSN: 0004-637X. doi: 10.1088/0004-637X/691/1/441.
- Smith, R. J. et al. (2020). *Monthly Notices of the Royal Astronomical Society: Letters* 493(1), pages L33–L38. ISSN: 1745-3925. doi: 10.1093/mnrasl/slaa003.
- Smith, R. J. (2014). *Monthly Notices of the Royal Astronomical Society: Letters* 443(1), pages L69–L73. ISSN: 1745-3925. doi: 10.1093/mnrasl/slu082.
- Smith, R. J. (2020). *Annual Review of Astronomy and Astrophysics* 58(1), pages 577–615. ISSN: 0066-4146. doi: 10.1146/annurev-astro-032620-020217.
- Smith, R. J. and Lucey, J. R. (2013). *Monthly Notices of the Royal Astronomical Society* 434(3), pages 1964–1977. ISSN: 0035-8711. doi: 10.1093/mnras/stt1141.

- Smith, R. J., Lucey, J. R., and Carter, D. (2012). *Monthly Notices of the Royal Astronomical Society, Volume 426, Issue 4, pp. 2994-3007.* 426, pages 2994–3007. doi: 10.1111/j.1365-2966.2012.21922.x.
- Smoot, G. F. et al. (1992). *The Astrophysical Journal Letters* 396, pages L1–L5. doi: 10.1086/186504.
- Sofue, Y. (2016). *Publications of the Astronomical Society of Japan* 68(1). issn: 0004-6264. doi: 10.1093/pasj/psv103.
- Sofue, Y. (2020). *Galaxies* 8(2), page 37. doi: 10.3390/galaxies8020037.
- Sofue, Y. and Rubin, V. (2001). *Annual Review of Astronomy and Astrophysics* 39(1), pages 137–174. doi: 10.1146/annurev.astro.39.1.137.
- Somerville, R. S. and Davé, R. (2015). *Annual Review of Astronomy and Astrophysics* 53(1), pages 51–113. doi: 10.1146/annurev-astro-082812-140951.
- Sonnenfeld, A. et al. (2018). *Monthly Notices of the Royal Astronomical Society* 481(1), pages 164–184. issn: 0035-8711, 1365-2966. doi: 10.1093/mnras/sty2262.
- Souza, R. E. de, Gadotti, D. A., and Anjos, S. dos (2004). *The Astrophysical Journal Supplement Series* 153(2), page 411. issn: 0067-0049. doi: 10.1086/421554.
- Sparre, M. and Springel, V. (2017). *Monthly Notices of the Royal Astronomical Society* 470(4), pages 3946–3958. issn: 0035-8711. doi: 10.1093/mnras/stx1516.
- Speagle, J. S. et al. (2014). *The Astrophysical Journal Supplement Series* 214(2), page 15. issn: 0067-0049. doi: 10.1088/0067-0049/214/2/15.
- Spindler, A. and Wake, D. (2017). *Monthly Notices of the Royal Astronomical Society* 468(1), pages 333–345. issn: 0035-8711, 1365-2966. doi: 10.1093/mnras/stx427.
- Spinello, C., Trager, S. C., and Koopmans, L. V. E. (2015). *The Astrophysical Journal* 803(2), page 87. issn: 0004-637X. doi: 10.1088/0004-637X/803/2/87.
- Spinello, C. et al. (2011). *Monthly Notices of the Royal Astronomical Society* 417(4), pages 3000–3009. issn: 0035-8711. doi: 10.1111/j.1365-2966.2011.19458.x.
- Spinello, C. et al. (2012). *The Astrophysical Journal* 753(2), page L32. issn: 2041-8205. doi: 10.1088/2041-8205/753/2/L32.
- Spinello, C. et al. (2014). *Monthly Notices of the Royal Astronomical Society* 438(2), pages 1483–1499. issn: 0035-8711. doi: 10.1093/mnras/stt2282.
- Spolaor, M. et al. (2009). *The Astrophysical Journal* 691(2), pages L138–L141. issn: 1538-4357. doi: 10.1088/0004-637X/691/2/L138.
- Springel, V. and Hernquist, L. (2005). *The Astrophysical Journal* 622(1), pages L9–L12. issn: 1538-4357. doi: 10.1086/429486.
- Stark, A. A. (1977). *The Astrophysical Journal* 213, pages 368–373. doi: 10.1086/155164.
- Stephens, I. W. et al. (2017). *The Astrophysical Journal* 834(1), page 94. issn: 0004-637X. doi: 10.3847/1538-4357/834/1/94.
- Stewart, K. R. et al. (2009). *The Astrophysical Journal* 702(2), pages 1005–1015. issn: 0004-637X, 1538-4357. doi: 10.1088/0004-637X/702/2/1005.
- Stewart, K. R. et al. (2013). *The Astrophysical Journal* 769(1), page 74. issn: 0004-637X. doi: 10.1088/0004-637X/769/1/74.
- Stiavelli, M. and Bertin, G. (1985). *Monthly Notices of the Royal Astronomical Society* 217(4), pages 735–752. issn: 0035-8711. doi: 10.1093/mnras/217.4.735.
- Stiavelli, M. and Bertin, G. (1987). *Monthly Notices of the Royal Astronomical Society* 229(1), pages 61–71. issn: 0035-8711. doi: 10.1093/mnras/229.1.61.
- Swaters, R. A., Madore, B. F., and Trewella, M. (2000). *The Astrophysical Journal* 531(2), pages L107–L110. issn: 1538-4357. doi: 10.1086/312540.

- Sweet, S. M. et al. (2020). *Monthly Notices of the Royal Astronomical Society* 494(4), pages 5421–5438. issn: 0035-8711. doi: 10.1093/mnras/staa1050.
- Syer, D. and Tremaine, S. (1996). *Monthly Notices of the Royal Astronomical Society* 282(1), pages 223–233. issn: 0035-8711. doi: 10.1093/mnras/282.1.223.
- Tanabashi, M. et al. (2018). *Physical Review D* 98(3), page 030001. doi: 10.1103/PhysRevD.98.030001.
- Taranu, D. S. et al. (2017). *The Astrophysical Journal* 850(1), page 70. issn: 0004-637X. doi: 10.3847/1538-4357/aa9221.
- Tecza, M. et al. (2006). *New Astronomy Reviews*. Adaptive Optics-Assisted Integral-Field Spectroscopy 49(10), pages 647–654. issn: 1387-6473. doi: 10.1016/j.newar.2005.10.019.
- Tempel, E. and Libeskind, N. I. (2013). *The Astrophysical Journal* 775(2), page L42. issn: 2041-8205. doi: 10.1088/2041-8205/775/2/L42.
- Thatte, N. A. et al. (2016). *Ground-Based and Airborne Instrumentation for Astronomy VI*. Volume 9908. International Society for Optics and Photonics, page 99081X. doi: 10.1117/12.2230629.
- Thomas, D. et al. (2005). *The Astrophysical Journal, Volume 621, Issue 2, pp. 673-694*. 621, pages 673–694. doi: 10.1086/426932.
- Thomas, J. et al. (2011). *Monthly Notices of the Royal Astronomical Society, Volume 415, Issue 1, pp. 545-562*. 415, pages 545–562. doi: 10.1111/j.1365-2966.2011.18725.x.
- Tinsley, B. M. (1978). *The Astrophysical Journal* 222, pages 14–22. doi: 10.1086/156116.
- Tojeiro, R. et al. (2007). *Monthly Notices of the Royal Astronomical Society* 381(3), pages 1252–1266. issn: 0035-8711. doi: 10.1111/j.1365-2966.2007.12323.x.
- Toomre, A. and Toomre, J. (1972). *The Astrophysical Journal* 178, pages 623–666. doi: 10.1086/151823.
- Tortora, C., Romanowsky, A. J., and Napolitano, N. R. (2013). *The Astrophysical Journal* 765(1), page 8. issn: 0004-637X. doi: 10.1088/0004-637X/765/1/8.
- Tortora, C. et al. (2014). *Monthly Notices of the Royal Astronomical Society, Volume 445, Issue 1, p.115-127* 445, pages 115–127. doi: 10.1093/mnras/stu1616.
- Trager, S. C. et al. (1998). *The Astrophysical Journal Supplement Series* 116(1), page 1. issn: 0067-0049. doi: 10.1086/313099.
- Tremblay, B. and Merritt, D. (1996). *The Astronomical Journal* 111, page 2243. issn: 0004-6256. doi: 10.1086/117959.
- Tremonti, C. A. et al. (2004). *The Astrophysical Journal* 613(2), page 898. issn: 0004-637X. doi: 10.1086/423264.
- Trenti, M. et al. (2010). *The Astrophysical Journal* 714(2), pages L202–L207. issn: 2041-8205. doi: 10.1088/2041-8205/714/2/L202.
- Trenti, M. and Shull, J. M. (2010). *The Astrophysical Journal* 712(1), pages 435–444. issn: 0004-637X. doi: 10.1088/0004-637X/712/1/435.
- Trenti, M. et al. (2012). *The Astrophysical Journal* 749(2), page L38. issn: 2041-8205. doi: 10.1088/2041-8205/749/2/L38.
- Treu, T. et al. (2010). *The Astrophysical Journal, Volume 709, Issue 2, pp. 1195-1202 (2010)*. 709, pages 1195–1202. doi: 10.1088/0004-637X/709/2/1195.
- Tsatsi, A. et al. (2017). *Astronomy & Astrophysics* 606, A62. issn: 0004-6361, 1432-0746. doi: 10.1051/0004-6361/201630218.
- Tully, R. B. and Fisher, J. R. (1977). *Astronomy and Astrophysics* 54, pages 661–673. issn: 0004-6361. url: <http://adsabs.harvard.edu/abs/1977A%26A....54..661T>.
- Twarog, B. A. (1980). *The Astrophysical Journal* 242, pages 242–259. doi: 10.1086/158460.

- Valluri, M. and Jog, C. J. (1990). *The Astrophysical Journal* 357, pages 367–372. issn: 0004-637X. doi: 10.1086/168927.
- Valluri, M., Merritt, D., and Emsellem, E. (2004). *The Astrophysical Journal* 602(1), page 66. issn: 0004-637X. doi: 10.1086/380896.
- Valluri, M. et al. (2007). *The Astrophysical Journal* 658(2), page 731. issn: 0004-637X. doi: 10.1086/511298.
- van Albada, T. S. and Sancisi, R. (1986). *Philosophical Transactions for the Royal Society of London. Series A, Mathematical and Physical Sciences, Volume 320, Issue 1556, pp. 447-464* 320, pages 447–464. issn: 0080-4614. doi: 10.1098/rsta.1986.0128.
- van Albada, T. S. et al. (1985). *The Astrophysical Journal* 295, pages 305–313. doi: 10.1086/163375.
- van de Sande, J. et al. (2018). *Nature Astronomy* 2(6), pages 483–488. issn: 2397-3366. doi: 10.1038/s41550-018-0436-x.
- van de Ven, G., De Zeeuw, P. T., and Van Den Bosch, R. C. E. (2008). *Monthly Notices of the Royal Astronomical Society* 385(2), pages 614–646. issn: 0035-8711. doi: 10.1111/j.1365-2966.2008.12873.x.
- van de Ven, G. et al. (2003). *Monthly Notices of the Royal Astronomical Society* 342(4), pages 1056–1082. issn: 0035-8711. doi: 10.1046/j.1365-8711.2003.06501.x.
- van den Bergh, S. (1976). *The Astrophysical Journal* 206, pages 883–887. doi: 10.1086/154452.
- van den Bosch, F. C. and de Zeeuw, P. T. (1996). *Monthly Notices of the Royal Astronomical Society* 283(2), pages 381–399. issn: 0035-8711. doi: 10.1093/mnras/283.2.381.
- van den Bosch, R. C. E. et al. (2008). *Monthly Notices of the Royal Astronomical Society* 385(2), pages 647–666. issn: 0035-8711. doi: 10.1111/j.1365-2966.2008.12874.x.
- van der Marel, R. P., Binney, J., and Davies, R. L. (1990). *Monthly Notices of the Royal Astronomical Society* 245, page 582. url: <http://adsabs.harvard.edu/abs/1990MNRAS.245..582V>.
- van der Marel, R. P. and Franx, M. (1993). *The Astrophysical Journal* 407, pages 525–539. doi: 10.1086/172534.
- van der Marel, R. P. et al. (1994). *Monthly Notices of the Royal Astronomical Society* 271(1), pages 99–117. issn: 0035-8711. doi: 10.1093/mnras/271.1.99.
- van der Marel, R. P. et al. (1998). *The Astrophysical Journal* 493(2), page 613. issn: 0004-637X. doi: 10.1086/305147.
- van Dokkum, P. et al. (2017). *The Astrophysical Journal* 841(2), page 68. issn: 1538-4357. doi: 10.3847/1538-4357/aa7135.
- van Dokkum, P. G. (2008). *The Astrophysical Journal* 674(1), page 29. issn: 0004-637X. doi: 10.1086/525014.
- van Dokkum, P. G. and Conroy, C. (2012). *The Astrophysical Journal* 760(1), page 70. issn: 0004-637X, 1538-4357. doi: 10.1088/0004-637X/760/1/70.
- Vasiliev, E. (2013). *Monthly Notices of the Royal Astronomical Society* 434(4), pages 3174–3195. issn: 0035-8711. doi: 10.1093/mnras/stt1235.
- Vasiliev, E. and Valluri, M. (2020). *The Astrophysical Journal* 889(1), page 39. issn: 1538-4357. doi: 10.3847/1538-4357/ab5fe0.
- Vaughan, S. P. et al. (2018a). *Monthly Notices of the Royal Astronomical Society* 475(1), pages 1073–1092. issn: 0035-8711, 1365-2966. doi: 10.1093/mnras/stx3199.
- Vaughan, S. P. et al. (2018b). *Monthly Notices of the Royal Astronomical Society* 479(2), pages 2443–2456. issn: 0035-8711. doi: 10.1093/mnras/sty1434.

- Vazdekis, A. et al. (1996). *The Astrophysical Journal Supplement Series* 106, page 307. issn: 0067-0049, 1538-4365. doi: 10.1086/192340.
- Vazdekis, A. et al. (2010). *Monthly Notices of the Royal Astronomical Society*. issn: 00358711, 13652966. doi: 10.1111/j.1365-2966.2010.16407.x.
- Vazdekis, A. et al. (2012). *Monthly Notices of the Royal Astronomical Society* 424(1), pages 157–171. issn: 00358711. doi: 10.1111/j.1365-2966.2012.21179.x.
- Vazdekis, A. et al. (2016). *Monthly Notices of the Royal Astronomical Society* 463(4), pages 3409–3436. issn: 0035-8711, 1365-2966. doi: 10.1093/mnras/stw2231.
- Veale, M. et al. (2017). *Monthly Notices of the Royal Astronomical Society* 471(2), pages 1428–1445. issn: 0035-8711. doi: 10.1093/mnras/stx1639.
- Ventou, E. et al. (2017). *Astronomy & Astrophysics* 608, A9. issn: 0004-6361, 1432-0746. doi: 10.1051/0004-6361/201731586.
- Verolme, E. K. and de Zeeuw, P. T. (2002). *Monthly Notices of the Royal Astronomical Society* 331(4), pages 959–968. issn: 0035-8711, 1365-2966. doi: 10.1046/j.1365-8711.2002.05244.x.
- Villanova, S. et al. (2014). *The Astrophysical Journal* 791(2), page 107. issn: 0004-637X. doi: 10.1088/0004-637X/791/2/107.
- Vincent, R. A. and Ryden, B. S. (2005). *The Astrophysical Journal* 623(1), page 137. issn: 0004-637X. doi: 10.1086/428765.
- Wadadekar, Y., Robbason, B., and Kembhavi, A. (1999). *The Astronomical Journal* 117(3), page 1219. issn: 1538-3881. doi: 10.1086/300754.
- Wagner, S. J., Bender, R., and Moellenhoff, C. (1988). *Astronomy and Astrophysics* 195, pages L5–L8. issn: 0004-6361. url: <http://adsabs.harvard.edu/abs/1988A%26A...195L..5W>.
- Walker, M. F. (1962). *The Astrophysical Journal* 136, page 695. doi: 10.1086/147429.
- Wang, H. et al. (2018). *The Astrophysical Journal* 852(1), page 31. issn: 0004-637X. doi: 10.3847/1538-4357/aa9e01.
- Wasserman, A. et al. (2018). *The Astrophysical Journal* 863(2), page L15. issn: 2041-8205. doi: 10.3847/2041-8213/aad779.
- Watkins, L. L. et al. (2013). *Monthly Notices of the Royal Astronomical Society* 436(3), pages 2598–2615. issn: 0035-8711. doi: 10.1093/mnras/stt1756.
- Weaver, J. et al. (2018). *Astronomy & Astrophysics* 614, A32. issn: 0004-6361, 1432-0746. doi: 10.1051/0004-6361/201732448.
- Wechsler, R. H. and Tinker, J. L. (2018). *Annual Review of Astronomy and Astrophysics* 56(1), pages 435–487. issn: 0066-4146. doi: 10.1146/annurev-astro-081817-051756.
- Wegner, G. A. et al. (2012). *The Astronomical Journal* 144(3), page 78. issn: 1538-3881. doi: 10.1088/0004-6256/144/3/78.
- Weidner, C. and Kroupa, P. (2005). *The Astrophysical Journal* 625(2), page 754. issn: 0004-637X. doi: 10.1086/429867.
- Weijmans, A.-M. et al. (2014). *Monthly Notices of the Royal Astronomical Society* 444(4), pages 3340–3356. issn: 0035-8711. doi: 10.1093/mnras/stu1603.
- Weiner, B. J. et al. (2006). *The Astrophysical Journal* 653(2), page 1027. issn: 0004-637X. doi: 10.1086/508921.
- Weinzirl, T. et al. (2009). *The Astrophysical Journal* 696(1), pages 411–447. issn: 0004-637X. doi: 10.1088/0004-637X/696/1/411.
- Welker, C. et al. (2020). *Monthly Notices of the Royal Astronomical Society* 491(2), pages 2864–2884. issn: 0035-8711. doi: 10.1093/mnras/stz2860. arXiv: 1909.12371.

- Westera, P. et al. (2002). *Astronomy & Astrophysics* 381(2), pages 524–538. issn: 0004-6361, 1432-0746. doi: 10.1051/0004-6361:20011493.
- White, S. D. M. and Rees, M. J. (1978). *Monthly Notices of the Royal Astronomical Society* 183(3), pages 341–358. issn: 0035-8711. doi: 10.1093/mnras/183.3.341.
- Whitford, A. E. (1977). *The Astrophysical Journal* 211, pages 527–538. doi: 10.1086/154959.
- Wielen, R. (1977). *Astronomy and Astrophysics* 60, pages 263–275. issn: 0004-6361. url: <http://adsabs.harvard.edu/abs/1977A%26A....60..263W>.
- Wilkins, S. M. et al. (2008). *Monthly Notices of the Royal Astronomical Society* 391(1), pages 363–368. issn: 0035-8711. doi: 10.1111/j.1365-2966.2008.13890.x.
- Wilkinson, D. M. et al. (2017). *Monthly Notices of the Royal Astronomical Society* 472(4), pages 4297–4326. issn: 0035-8711. doi: 10.1093/mnras/stx2215.
- Williams, R. E. et al. (1996). *The Astronomical Journal* 112, page 1335. issn: 0004-6256. doi: 10.1086/118105.
- Wing, R. F. and Ford Jr., W. K. (1969). *Publications of the Astronomical Society of the Pacific* 81, pages 527–529. issn: 0004-6280. doi: 10.1086/128814.
- Wu, X. and Tremaine, S. (2006). *The Astrophysical Journal* 643(1), pages 210–221. issn: 0004-637X, 1538-4357. doi: 10.1086/501515.
- Yan, Z., Jerabkova, T., and Kroupa, P. (2017). *Astronomy & Astrophysics* 607, A126. issn: 0004-6361, 1432-0746. doi: 10.1051/0004-6361/201730987.
- Yang, G. et al. (2019). *Monthly Notices of the Royal Astronomical Society*, stz3001. issn: 0035-8711, 1365-2966. doi: 10.1093/mnras/stz3001.
- Yi, S. et al. (2001). *The Astrophysical Journal Supplement Series* 136(2), page 417. issn: 0067-0049. doi: 10.1086/321795.
- York, D. G. et al. (2000). *The Astronomical Journal* 120, pages 1579–1587. doi: 10.1086/301513.
- Yoshino, A. and Ichikawa, T. (2008). *Publications of the Astronomical Society of Japan* 60(3), pages 493–520. issn: 0004-6264. doi: 10.1093/pasj/60.3.493.
- Yu, J. and Liu, C. (2018). *Monthly Notices of the Royal Astronomical Society* 475(1), pages 1093–1103. issn: 0035-8711. doi: 10.1093/mnras/stx3204.
- Yuma, S., Ohta, K., and Yabe, K. (2012). *The Astrophysical Journal* 761(1), page 19. issn: 0004-637X. doi: 10.1088/0004-637X/761/1/19.
- Zabel, N. et al. (2019). *Monthly Notices of the Royal Astronomical Society* 483(2), pages 2251–2268. issn: 0035-8711. doi: 10.1093/mnras/sty3234.
- Zahid, H. J. et al. (2012). *The Astrophysical Journal* 750(2), page 120. issn: 0004-637X. doi: 10.1088/0004-637X/750/2/120.
- Zavala, J. et al. (2016). *Monthly Notices of the Royal Astronomical Society* 460(4), pages 4466–4482. issn: 0035-8711. doi: 10.1093/mnras/stw1286.
- Zhang, Z.-Y. et al. (2018). *Nature* 558(7709), pages 260–263. issn: 1476-4687. doi: 10.1038/s41586-018-0196-x.
- Zhao, D. H. et al. (2003). *Monthly Notices of the Royal Astronomical Society* 339, pages 12–24. issn: 0035-8711. doi: 10.1046/j.1365-8711.2003.06135.x.
- Zhao, H. (1996). *Monthly Notices of the Royal Astronomical Society* 278(2), pages 488–496. issn: 0035-8711. doi: 10.1093/mnras/278.2.488.
- Zhao, H. (1997). *Monthly Notices of the Royal Astronomical Society* 287(3), pages 525–537. issn: 0035-8711. doi: 10.1093/mnras/287.3.525.
- Zhou, S. et al. (2019). *Monthly Notices of the Royal Astronomical Society* 485(4), pages 5256–5275. issn: 0035-8711. doi: 10.1093/mnras/stz764.

- Zieleniewski, S. et al. (2017). *Monthly Notices of the Royal Astronomical Society* 465(1), pages 192–212. ISSN: 0035-8711. doi: 10.1093/mnras/stw2712.
- Zinnecker, H. and Yorke, H. W. (2007). *Annual Review of Astronomy and Astrophysics* 45(1), pages 481–563. doi: 10.1146/annurev.astro.44.051905.092549.
- Zwicky, F. (1933). *Helvetica Physica Acta* 6, pages 110–127. ISSN: 0018-0238. URL: <http://adsabs.harvard.edu/abs/1933AcHPh...6..110Z>.
- Zyla, P. et al. (2020). *PTEP* 2020(8), page 083C01. doi: 10.1093/ptep/ptaa104.

---

## CHAPTER 2

---

# COMBINING STELLAR POPULATIONS WITH ORBIT-SUPERPOSITION DYNAMICAL MODELLING – THE FORMATION HISTORY OF THE LENTICULAR GALAXY NGC 3115

This chapter is a verbatim reproduction of the work published in

Poci, A. et al. (2019). “Combining Stellar Populations with Orbit-Superposition Dynamical Modelling: The Formation History of the Lenticular Galaxy NGC 3115”. *Monthly Notices of the Royal Astronomical Society* 487(3), pages 3776–3796. ISSN: 0035-8711. doi: 10.1093/mnras/stz1154

## Abstract

We present a combination of the Schwarzschild orbit-superposition dynamical modelling technique with the spatially-resolved mean stellar age and metallicity maps to uncover the formation history of galaxies. We apply this new approach to a remarkable 5-pointing mosaic of VLT/MUSE observations obtained by Guérou et al. (2016) extending to a maximum galactocentric distance of  $\sim 120''$  (5.6 kpc) along the major axis, corresponding to  $\sim 2.5 R_e$ . Our method first identifies ‘families’ of orbits from the dynamical model that represent dynamically-distinct structures of the galaxy. Individual ages and metallicities of these components are then fit for using the stellar-population information. Our results highlight components of the galaxy that are distinct in the combined stellar dynamics/populations space, which implies distinct formation paths. We find evidence for a dynamically-cold, metal-rich disk, consistent with a gradual in-situ formation. This disk is embedded in a generally-old population of stars, with kinematics ranging from dispersion-dominated in the centre to an old, diffuse, metal-poor stellar halo at the extremities. We find also a direct correlation between the dominant dynamical support of these components, and their associated age, akin to the relation observed in the Milky Way. This approach not only provides a powerful model for inferring the formation history of external galaxies, but also paves the way to a complete population-dynamical model.

## 2.1 Introduction

The present-day observed state of a galaxy is the result of the integration over its entire formation history, including external accretion/mergers, in-situ star-formation, and passive stellar evolution. To determine how and when a galaxy has built up its mass, it is necessary to disentangle its present-day state into spatially- and chemically-distinct events. Typically, the studies of stellar populations and dynamical properties have remained independent, however it is the union of these two aspects that is necessary to be able to investigate the origin of a galaxy’s mass over its formation history. These ideas have been investigated for some time for the Milky Way, where a wealth of chemical and dynamical information can be directly obtained for individual stars. We endeavour here to extend these analyses to external, unresolved galaxies.

Historically, dynamical models of galaxies have been utilised for a wide range of applications, from individual galaxy analyses to large statistical samples of the galaxy population. These efforts have attempted to place constraints on, among other properties, the mass of the super-massive black holes (SMBH) at the centres of external galaxies (see Kormendy and Ho, 2013 and references in Table 1 therein, and more recently Seth et al., 2014; Krajnović et al., 2018); the IMF mass normalisation (for instance, see Thomas et al., 2011; Cappellari et al., 2012; Lyubenova et al., 2016; Davis and McDermid, 2017; Li et al., 2017; Oldham and Auger, 2018); the dark-matter content/distribution in galaxies using stellar kinematics (for example, see Cappellari et al., 2013; Tortora et al., 2019) all the way down in mass to dwarf spheroidals (Jardel and Gebhardt, 2012), and using gas kinematics (for example, see Corbelli and Salucci, 2000; Gentile et al., 2004; Di Teodoro et al., 2019). Dynamical models have also been used to uncover new relationships between galaxy structural parameters, including the widely-used stellar spin-ellipticity ( $\lambda_r - \epsilon$ ) correlation (introduced in Emsellem et al., 2007), as well as other observed correlations with dynamical properties (Cappellari, 2016). Finally, dynamical models of individual galaxies have been used to probe internal dynamical structures in great detail (for instance, see Krajnović et al., 2005; van den Bosch et al., 2008; Krajnović et al., 2015; Zhu et al., 2016b), placing strong constraints on the formation mechanisms of those specific galaxies.

Independently, stellar-population models of galaxies have been utilised for their own range of applications, covering similar scales in sample size. These models have been applied to constrain the IMF shape, normalisation, and low-mass cut-off (for instance, see Conroy and Dokkum, 2012; Smith et al., 2012; Martín-Navarro et al., 2015; Alton et al., 2017; Rosani et al., 2018; Dries et al., 2018; Vaughan et al., 2018); the measurement and interpretation of  $\alpha$ -enhancement (as in Thomas et al., 2005; Conroy et al., 2013; Greene et al., 2015; McDermid et al., 2015); the measurement of spatial gradients in stellar properties (for instance, see Mehlert et al., 2003; Sánchez-Blázquez et al., 2007; Kuntschner et al., 2010; Li et al., 2018); assembly timescales for galaxy formation (Martín-Navarro et al., 2018). Similarly to dynamical models, stellar population models have been used to uncover new relationships between galaxy structural parameters through a variety of scaling relations (see Gallazzi et al., 2008; Graves et al., 2009a,b; McDermid et al., 2015; Walcher et al., 2015, for some such relations). Again, stellar population models of individual (or handfuls of) galaxies in great detail offer insight into the specific formation path of these galaxies, as well as the presence of sub-structures with distinct stellar populations (for instance, see Barbosa et al., 2016; Mentz et al., 2016; Streich et al., 2016).

Driven by the influx of spatially-resolved observations coming from integral-field units (IFU), more recent investigations have focused on attempting to infer structural, dynamical

and/or chemical properties for localised regions of galaxies, by decomposing them into physically-motivated components. In fact, this concept pre-dates the large-scale use of IFU with works dealing with, for instance, photometric disk/bulge decompositions of surface brightness profiles (for example, see Boroson, 1981; Kent, 1985; Cinzano and van der Marel, 1993; Scorza and Bender, 1995; Moriondo et al., 1998; Krajnović et al., 2013), including using multiple filters (Dimauro et al., 2018). Aside from surface brightness, radial profiles of other parameters have also been subject to analogous decompositions. For instance, the decomposition of gas (usually H<sub>I</sub>) circular velocity profiles into contributions from different galaxy sub-components is a well-established practise (as in van Albada et al., 1985; Carignan et al., 1988; Battaglia et al., 2006; Noordermeer et al., 2007; Swaters et al., 2012; Sofue, 2017; Aniyan et al., 2016, 2018), while decompositions of mass profiles have attempted to infer the contributions from dark matter and baryons (stars and globular clusters, gas, et cetera; Poci et al., 2017; Annunziatella et al., 2017; Bellstedt et al., 2018). These concepts have been extended to two dimensions, including multi-band photometric disk/bulge decompositions of images, rather than profiles (for instance, see Scorza et al., 1998; Souza et al., 2004; Norris et al., 2006; Simard et al., 2011; Méndez-Abreu et al., 2017; Dalla Bontà et al., 2018). Moreover, there have been recent efforts to conduct the decomposition directly on an observed spectrum (Johnston et al., 2012; Coccato et al., 2015; Tabor et al., 2017; Coccato et al., 2018), to similarly determine the contributions to various spectral features coming from ‘distinct’ galaxy subcomponents. This type of component-based approach attempts to isolate the distinct contributions to observed galaxies from regions which may or may not have had different origins and/or formation paths, however they have thus far dealt with the problem from only one perspective - dynamics *or* stellar populations.

These works, and others, have motivated a need for combining the aforementioned dynamical and chemical models in order to investigate the full formation history of a galaxy. This combination is in fact necessary to be able to determine the origin of the different components of a galaxy. There have been only a small number of works in which different chemical and dynamical populations are simultaneously treated, such as the models of Zhu et al. (2016b,a), which use globular clusters (GC) as discrete tracers of the kinematics, while simultaneously fitting for two (chemical) populations of GC (based on the discrete modelling prescription of Watkins et al., 2013). This showed that there are observable distinctions to be made in the combined populations/dynamics space (and indeed physical space) between different components of galaxies.

In this paper, we describe a new approach which aims to decompose a galaxy into dynamical and chemical components in order to infer its formation history. We present also an application of this method to a real galaxy; the nearby lenticular galaxy NGC 3115. § 2.2 describes the observational data used in this work. §§ 2.3 and 2.4 describe in detail the multiple aspects of our chemical and dynamical analyses, respectively. The results of our show case are presented in § 2.5. § 2.6 presents the formation history of NGC 3115 as determined from our method, and the connections between dynamical and chemical properties.

## 2.2 Observational Data and Kinematic Extraction

The observations used in this work were obtained and reduced by Guérou et al. (2016). NGC 3115 is the nearest lenticular (S0) galaxy to the Milky Way, with an orientation very close to edge-on. Tonry et al. (2001) used surface brightness fluctuations to measure a distance modulus for NGC 3115 of  $(m - M) = 29.93 \pm 0.09$ , placing it at a physical distance of

9.7 Mpc. It has an effective (half-light) radius of  $R_e = 47.32''/2.23$  kpc (Emsellem et al., 1999). Our data extends to a galactocentric radius of  $\sim 120''$  (5.6 kpc) along the major axis, and so we have coverage out to  $\sim 2.5R_e$ .

The data set has a pixel-scale of  $0.2'' \text{ pixel}^{-1}$  ( $9.4 \text{ pc pixel}^{-1}$ ), and consists of over 360,000 individual spectra. We refer the interested reader to Guérou et al. (2016) for further details regarding the observational procedure and data-reduction techniques.

For all subsequent analysis, we consider only the spectral range  $\lambda \in [4760, 6400] \text{ \AA}$ . This is to reduce the impact of residual sky emission lines on the extracted stellar kinematic and population properties. We spatially bin the reduced datacube using a Python implementation\* of the Voronoi tessellation algorithm (Cappellari and Copin, 2003) to a target signal-to-noise ratio ( $S/N$ ) of 90 per bin. This relatively high threshold is set to ensure an accurate recovery of (the moments of) the line-of-sight velocity distribution (LOSVD), as well as the subsequent stellar population analyses.

Although kinematics were extracted by Guérou et al. (2016), we re-derive the kinematics† here with the new  $S/N$  threshold for the spatial binning. This allows us to extract the first six Gauss-Hermite coefficients of the parametrised LOSVD, which provide important additional constraints on the dynamical model.

For the kinematic extraction, we use a Python implementation\* of the parametric Penalised PiXel-Fitting code **PPXF** (Cappellari and Emsellem, 2004; Cappellari, 2017), with 985 stellar templates from the empirical MILES library (Sánchez-Blázquez et al., 2006; Falcón-Barroso et al., 2011). **PPXF** finds the linear combination of the provided templates that, when convolved with an LOSVD parametrised by the 6 Gauss-Hermite coefficients, best matches the observed spectrum. Computing such a fit for every (Voronoi-binned) spectrum in the cube provides the best-fitting LOSVD (or parametrisation thereof) at every spatial location. Since the spectral resolutions of the MILES models and MUSE data are comparable, both sets of spectra are kept at their native resolution. Every bin is fit with the freedom of the full template library, and with an additive polynomial of order 16. This combination of additive polynomial and stellar templates is used to achieve the best possible fit to the spectrum, in order to most accurately recover the LOSVD, without being tied to any particular stellar population model. During the fitting, spurious spectral pixels/artefacts in the data are iteratively clipped. Errors for all 6 Gauss-Hermite moments are computed by Monte Carlo simulations on every spectrum individually for which kinematics are extracted. We derive a mean uncertainty (and apply a floor on these uncertainties during the dynamical model described in § 2.4), for  $V$  and  $\sigma$  of 10.30 (7.00) and 3.17 (2.00)  $\text{km s}^{-1}$ , respectively, and for moments 3 through 6 of 0.0016 (0.0016), 0.0020 (0.0019), 0.0016 (0.0016), 0.0021 (0.0020). The floor on the uncertainties prevents the dynamical model from preferentially fitting the central pixels (which have the smallest errors).

## 2.3 Spatially-Resolved Star-Formation History

Our analysis of NGC 3115 requires the computation of a spatially-resolved star-formation history (SFH). To do this, we employ full-spectral-fitting techniques, with the aim of investigating chemically-distinct components in our dataset. To fit the spectra, we again utilise **PPXF**, but use the MILES-IndoUS-CaT (MIUSCAT) Single Stellar Population (SSP) model library (Vazdekis et al., 2010) as templates. While we aim to compare our results with those from

---

\*Available at <http://www-astro.physics.ox.ac.uk/~mxc/software/>

†These data products are also available at <https://datacentral.org.au/teamdata/NGC3115/public/>

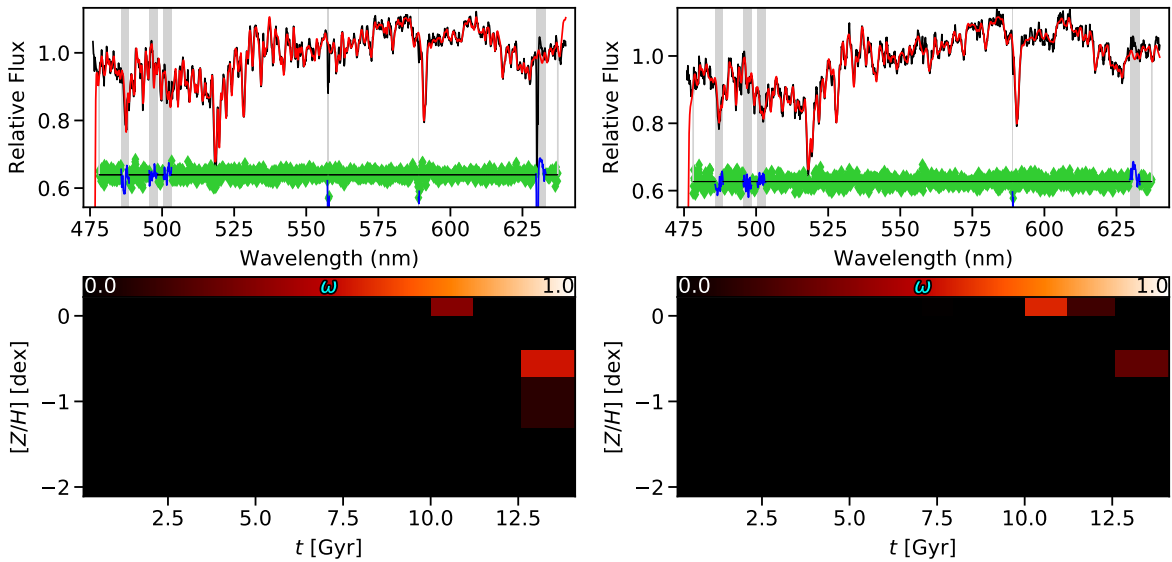


FIGURE 2.1: The fit in PPXF to the highest (left) and lowest (right)  $S/N$  spectra in the dataset, with  $S/N = 119$  and  $67$ , respectively. In each panel, the top row shows the data and model in black and red, respectively. The residuals are shown as green diamonds, and have been arbitrarily offset for presentation. The grey bands are masked during the fit. The outer-most pixels on either extremity have also been excluded to avoid edge effects. The bottom panels show the associated luminosity-weighted SFH, which illustrates the contributions from each age/metallicity bin to the corresponding spectrum.

Guérou et al. (2016), we adopt different SSP templates for our SFH. From an initial run of the dynamical model, we inferred a dynamical (enclosed) mass that was lower than the stellar mass derived assuming a Salpeter (1955) IMF (which was the assumption in Guérou et al., 2016). Such seemingly non-physical discrepancies have been found previously (Lyubenova et al., 2016), and is interpreted as evidence to exclude single-power-law IMF shapes. We therefore assume a Kroupa (2002) IMF for all stellar-population models in this work. The SSP library used here is based on the Padova isochrones (Girardi et al., 2000), with ages  $0.1 \leq t \leq 14.1$  Gyr and metallicities  $-1.71 \leq Z \leq 0.22$  dex<sup>‡</sup>. These models do not consider any  $\alpha$  abundances explicitly, and since they are based on empirical stars, therefore share the same  $\alpha$ -enhancement characteristics as the solar neighbourhood. During the PPXF fit, we employ a small fractional regularisation to reduce the intrinsic degeneracy of the fit. This regularisation prefers a smooth solution that would otherwise be degenerate with a ‘spiky’ SFH. We do not use any additive polynomial, as this would change the relative strengths of the spectral features, which would in turn impact the derived stellar population properties. We do, however, employ a multiplicative polynomial of order 16 in order to account for the continuum. The LOSVD are left free during the stellar-population fits. This is done to minimise any possible systematics and template mismatch, while maintaining good fits across the FOV. We confirmed that the resulting SFH<sup>†</sup> is consistent within the errors when the kinematics were fixed to those extracted in § 2.2.

Fig. 2.1 illustrates this fitting concept on the highest and lowest  $S/N$  spectra in the dataset, as well as the associated SSP weights for the ages,  $t$ , and metallicities,  $Z$ . We compute similar fits for every binned spectrum in the datacube to investigate the spatial behaviour of the stellar populations. For reasons discussed in § 2.4.2, we compute *luminosity*-weighted SSP properties by removing the relative normalisation of all the template spectra prior to

<sup>‡</sup>Determined from the “safe ranges” taken from the MILES website over the MUSE wavelength range

fitting.

## 2.4 Dynamical Model

In order to identify intrinsically-distinct components, we employ the Schwarzschild orbit-superposition technique (Schwarzschild, 1979). In this work we use a triaxial extension of the axisymmetric method originally presented in van der Marel et al. (1998) and Cretton et al. (1999), and developed further by Cappellari et al. (2006). This triaxial implementation is detailed extensively in van de Ven et al. (2008) and van den Bosch et al. (2008) and developed further by Zhu et al. (2018b,a). We present here a brief summary of the relevant aspects of this implementation, and refer the reader to the above references for further details.

### 2.4.1 Mass Model

The Schwarzschild orbit-superposition method generates galaxy models within a given stationary gravitational potential. Fitting Schwarzschild models to observations therefore requires finding the best input gravitational potential that reproduces the observable constraints. Since the gravitational potential can not be measured directly, we construct each input mass model as the combined contributions from a stellar mass model, a dark matter parametrisation, and a point-source central super-massive black-hole (SMBH) component.

#### Stellar-Mass Model

The stellar mass is a derived quantity, dependent on a number of assumptions relating the directly-observed stellar light to an implied stellar mass. This in turn requires a model of the observed surface brightness from which a mass can be derived. In this work, we use the surface-brightness model of NGC 3115 presented in Emsellem et al. (1999), which used the multi-Gaussian Expansion (MGE) technique (Monnet et al., 1992; Emsellem et al., 1994). MGE models fit a series of 2D Gaussians to the observed photometric isophotes. One advantage of using the MGE approach is that for any inclination that is trialled by the dynamical model, the Gaussians have an analytic deprojection into an intrinsic 3D model. This results in a fast (though not necessarily unique) description of the mass for that inclination, forming the framework within which the dynamical model is computed. Emsellem et al. (1999) used a combination of high-resolution HST and ground-based photometry to compute a photometric fit out to  $\sim 300''$ , which is necessary in order to ensure that the stellar mass model comfortably encloses the extent of such a nearby galaxy. The collapsed data cube and MGE surface brightness model are shown in Fig. 2.2.

Typical Schwarzschild model implementations, and many dynamical models in general, assume that the conversion from light to mass can be done with a single global scale for a given galaxy; that is, a spatially-constant stellar mass-to-light ratio ( $M_\star/L$ ). This implies that the observed light originates from only a single population of stars. In our work, however, we consider the interplay between dynamical and stellar-population structures, and so the spatial variations in the  $M_\star/L$  are of particular importance. Since we have already characterised the presence of multiple stellar populations within this galaxy in § 2.3, it is therefore possible to incorporate the spatial structures in the stellar populations to obtain a more accurate conversion from light to mass. It is imperative that we attempt to construct an accurate *input* mass model that takes into account this information in order to maintain self-consistency when we analyse the outputs. There have already been recent implementations of this for

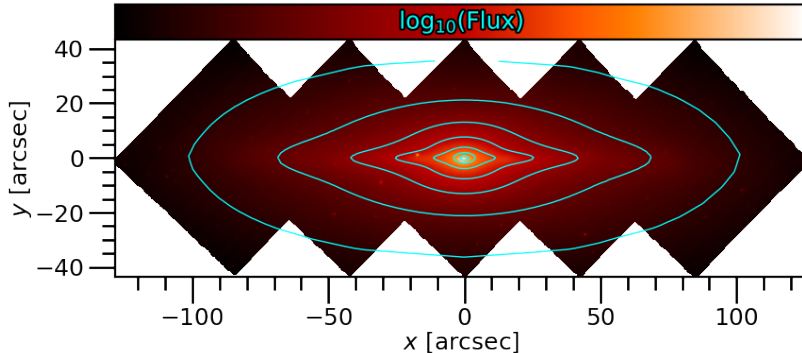


FIGURE 2.2: The reconstructed image from the 3D data cube in arbitrary flux units, and the surface-brightness MGE contours overplotted in 1 mag intervals.

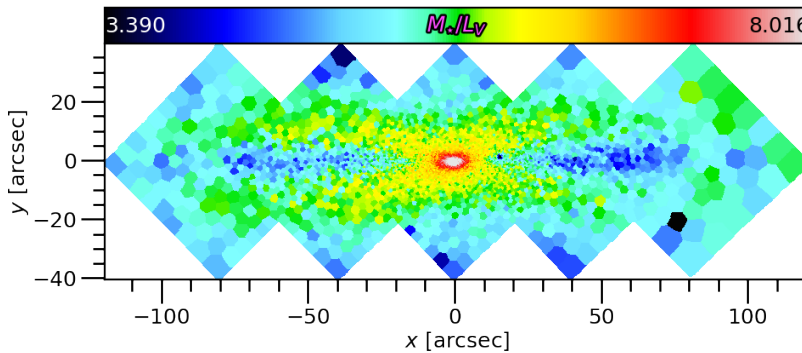


FIGURE 2.3: A map of  $M_\star/L$  in  $V$ -band inferred from full spectral fitting with variable age and metallicity, and assuming a Kroupa IMF.

other purely-dynamical modelling techniques by parametrising the derived  $M_\star/L$  map into a 1D radial profile, which is then used to scale the surface-brightness model accordingly (Poci et al., 2017; Mitzkus et al., 2017). We compute a  $V$ -band  $M_\star/L_V$  map for NGC 3115 based on the ppxf fits from § 2.3, shown in Fig. 2.3.  $V$ -band is consistent with both the spectral range used in the MUSE observations and the original photometry used by Emsellem et al. (1999). It is immediately clear, however, that the  $M_\star/L_V$  map of NGC 3115 can not be well-approximated by a radial profile due to the ‘lobe’ features along the major axis created by a relatively young stellar disk. In order to derive an accurate stellar-mass model, we take a different approach here in order to maintain the 2D information from the SFH. We scale the surface-brightness MGE ( $MGE_\mu$ ) by the MUSE  $M_\star/L_V$  map directly in order to obtain a mass ‘image’, to which we fit a new *mass density* MGE ( $MGE_\Sigma$ ).

One issue when comparing photometric and IFU observations is the difference in the size of the FOV. To overcome this, we first evaluate  $MGE_\mu$  on an image grid that is sufficiently large (comparable to the FOV used in Emsellem et al., 1999). We then cast the  $M_\star/L_V$  map onto the same image scale. To populate the pixels that lie outside of the MUSE FOV, we assume that the  $M_\star/L_V$  is constant at large radius. This already appears to be the case in the MUSE observations for  $R \gtrsim 80''$ , and so the exterior pixels are fixed to the average value of the outermost bins of Fig. 2.3. Fig. 2.4 presents  $MGE_\mu$  and  $MGE_\Sigma$  on the approximate scale of the stellar disk, which clearly highlights the impact of considering the 2D  $M_\star/L_V$  map. The  $MGE_\Sigma$  has rounder iso-mass contours (compared to  $MGE_\mu$ ) in the region where relatively young stars contribute a lot of luminosity but not much mass. Assuming a constant  $M_\star/L$  would have attributed too much mass to the disk region (along the major axis), which

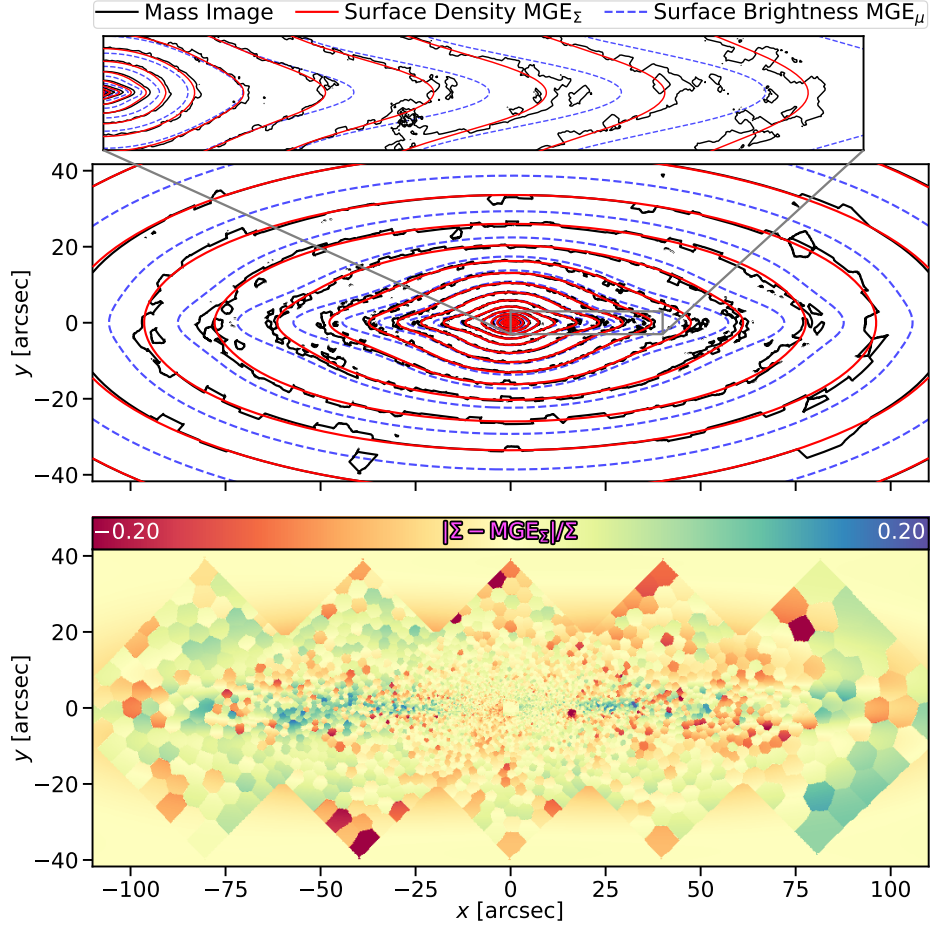


FIGURE 2.4: The fit in red to the iso-mass contours of the scaled mass image in black (top). The surface-brightness MGE is shown for reference in dashed blue. The panel shows the FOV of the IFU, while the zoom-in shows only the disk region between 0 and 40''. The fractional residuals between the mass ‘image’ and MGE $_{\Sigma}$  are shown in the bottom panel.

in turn would have biased the dynamical model and the inferred stellar populations. MGE $_{\Sigma}$  is tabulated in § 2.A<sup>†</sup>.

### Dark-Mass Model

To include contributions from non-luminous mass, we include a parametrisation of the dark matter (DM) halo by assuming it has the form of a generalised spherical Navarro, Frenk, and White (NFW; Navarro et al., 1996) halo, as described in Eq. (3) of Zhu et al. (2018a), but included here for completeness in Eq. (2.1).

$$M_{\text{DM}}(r) = M_{200} \cdot g(C_{\text{DM}}) \left[ \ln \left( 1 + \frac{rC_{\text{DM}}}{r_{200}} \right) - \frac{\frac{rC_{\text{DM}}}{r_{200}}}{1 + \frac{rC_{\text{DM}}}{r_{200}}} \right] \quad (2.1)$$

where  $g(C_{\text{DM}}) = \left[ \ln(1 + C_{\text{DM}}) - \frac{C_{\text{DM}}}{1+C_{\text{DM}}} \right]^{-1}$ , and  $M_{200} = 200 \times \frac{4}{3}\pi\rho_c r_{200}^3$ . Here,  $\rho_c = \frac{3H^2}{8\pi G}$  is the critical density of the Universe with Hubble constant  $H$  and gravitational constant  $G$ . While we do not test different dark matter prescriptions in this work, we note that the broader method described in this work is not tied to the specific parametrisation of the dark matter halo.

The central SMBH similarly contributes non-luminous mass to the mass model, and therefore affects which orbits exist within the gravitational potential. Our models include a spatially-localised non-luminous Plummer potential (Dejonghe, 1987) to represent the mass of the SMBH,  $M_\bullet$ , defined as

$$\Phi(r) = -\frac{GM_\bullet}{\sqrt{r^2 + a^2}} \quad (2.2)$$

where  $a$  is the Plummer core radius (effectively the SMBH softening length). In the region  $r \leq a$ , the gravitational potential of the model is dominated by the Plummer potential. We fix  $a = 0.008''$ , which is below the MUSE resolution, in order to avoid numerical issues when integrating orbits close to the SMBH.

### 2.4.2 Orbit Solution

The Schwarzschild code generates a library of orbits that are physically permitted for the given mass model. In our model, we sample the orbits over 42 logarithmically-spaced radial starting locations, which conserve the first integral of motion; the energy. There are also 15 linearly-spaced locations in  $I_2$ , the second conserved integral of motion. Finally, we sample the third (non-classical) conserved integral of motion,  $I_3$ , from 12 linearly-spaced starting locations. We may cheaply (without re-integrating) increase the size of the orbit library, by simply mirroring orbits about their integrals of motion to allow for counter-rotation. In the general triaxial code, this occurs only for those orbits which are sampled on the  $(x, z)$  meridional plane, doubling the number of those orbits. Moreover, to boost the number of box orbits accessible to the model, we launch a new set of box-only orbits, adding another factor to the orbit library (van den Bosch et al., 2008). Therefore, the full number of orbits in the model is  $N_{\text{orb.}} = 3 \times N_E \times N_{I_2} \times N_{I_3} = 3 \times 42 \times 15 \times 12 = 22680$ . In order to minimise the discreteness of the orbits, each starting position is ‘dithered’ (see Cappellari et al., 2006) in the three-dimensional integral space by a factor of 5, thereby sub-sampling each  $(E, I_2, I_3)$  location into a grid of  $5^3$  adjacent starting positions. This high sampling ensures that the small physical scale of the observation is probed sufficiently, while also covering a large enough volume to describe the full extent of the galaxy. Compared to the extensive work done on CALIFA data (Zhu et al., 2018a), our data has 5 times higher spatial resolution, and our orbit library is slightly over 5 times larger. Specifically, we can estimate the approximate density of orbits across our FOV. By taking the conservative approach of considering the orbital starting locations, we find an average of  $\sim 102$  orbits/arcsec $^2$ . From this density of orbits, we conclude the orbit library contains sufficient resolution to accommodate our data. Each of these orbits is integrated for 200 complete periods.

With a complete orbit library, the Schwarzschild code then solves for the weighted linear combination of these orbits that best reproduces the (projected) observations. The orbital weights are computed by a Non-Negative Least-Squares (NNLS) fit to all observed constraints simultaneously, producing a weight per orbit, per spatial bin. For a given combination of orbits, the combined model is projected and convolved with the PSF to mimic the observations, binned onto the same Voronoi bins, and finally, the intrinsic LOSVD of the model are compared to the measured kinematic moments in each spatial bin. It is clear here that each kinematic moment extracted from the observed spectra therefore provides additional constraining power, in order to discriminate between models with similar lower-order kinematic moments.

While the orbit *integration* is carried out in the gravitational potential (mass model), the orbit *solution* is fit to the observed luminosity-weighted properties – namely, the surface

brightness MGE, and all 6 kinematic moments. The linear combination of orbits is therefore luminosity-weighted also, consistent with the observations and the SFH described in § 2.3.

### 2.4.3 Model Free Parameters

The process described in § 2.4.2 is for the single fixed gravitational potential within which the orbits were integrated. While the *projected* mass model is fixed by  $MGE_{\Sigma}$ , the intrinsic galaxy shape that gives rise to this projection remains unknown. It is therefore necessary to optimise the free parameters of the intrinsic gravitational potential in order to obtain not only a best-fitting set of orbits for a given potential, but also the best-fitting potential itself. The parameters of the gravitational potential are described here.

For a triaxial system, the baryonic component can be described by three intrinsic shape parameters,  $(q, p, u)$ . These intrinsic shapes are translated into projected viewing angles according to Eqs. (7)–(9) of van den Bosch et al. (2008). While we fit for  $q$  and  $p$ , we fix the third intrinsic shape parameter to  $u = 0.99999$ . This imposes the assumption that the shape of the baryonic component of the galaxy does not depend on the azimuthal angle at which we are observing it (that is, invariant under rotations about the rotation axis). This is a reasonable assumption in our case, where we are modelling a nearly-edge-on, approximately axisymmetric galaxy.

There are also free parameters of the dark mass contributions to the gravitational potential. From Eq. (2.1), our model gains two free parameters; the concentration of dark matter  $C_{\text{DM}}$ , and the fraction of dark-to-stellar mass within  $r_{200}$ ,  $f_{\text{DM}}(r_{200}) = M_{200}/M_{\star}$ . We also vary  $M_{\bullet}$  in order to accurately probe the orbits in the central region of the galaxy.

The final free parameter of the Schwarzschild model is the  $M_{\text{dyn}}/L$  scaling, which we refer to as  $\Upsilon$  to avoid confusion with the SFH-derived  $M_{\star}/L_V$ . Although we have incorporated the shape of the stellar component into the gravitational potential using the MUSE  $M_{\star}/L_V$  map, this final free parameter is a global (spatially-constant) scale of the total mass. It allows the model to produce a deeper or more shallow potential, as required by the dynamics, due to possible systematics in the derived  $M_{\star}/L_V$  including the assumption about the IMF, as well as the accuracy of the dark matter parametrisation. Since  $\Upsilon$  is a global scaling, the shape of the gravitational potential does not change. Therefore, this parameter can be efficiently optimised by scaling all of the orbital velocities by  $\sqrt{\Upsilon}$ , and refitting the model. A value of  $\Upsilon = 1$  implies that the input gravitational potential, in terms of the absolute stellar  $M_{\star}/L$ , assumed  $M_{\bullet}$ , and assumed DM parametrisation, contains the correct enclosed mass to reproduce the observed kinematics.

We are thus left with 6 free parameters for the Schwarzschild model, described in Tab. 2.1. To find the global best-fitting model, we employ the following  $\chi^2$  grid search. From a starting guess for each parameter, we consider those locations which are  $\pm 5\Delta$  (the step size defined in Tab. 2.1) away. This is to ensure that a sufficient volume of the parameter-space is probed to avoid local minima. Including the central position, there are then 3 initial trials for each free parameter. In total, for  $N$  gravitational free parameters (excluding  $\Upsilon$ ), the model begins with  $3^N$  trials. Each of these  $3^5 = 243$  initial gravitational-potential models is evaluated for 3 values of  $\Upsilon$ . Once these have completed, the best-fitting location becomes the new ‘centre’, and each free parameter is explored in increments of  $\pm\Delta$  in a similar manner. This is repeated until a location is found such that all surrounding models in the  $ND$  space produce worse fits to the data, which is followed by one final run with  $\pm 0.5\Delta$  in order to accurately characterise the best-fitting region.

The metric for model comparison used in this work follows the formalism of Zhu et al.

Parameter	Description	$\Delta$	Start	Best
$m_{\text{BH}}$	Black-Hole Mass	0.75*	$1.000 \times 10^9$	$1.185 \times 10^9 M_{\odot}$
$q$	Intrinsic Shape	0.005	0.001	$3.500 \times 10^{-3}$
$p$	Intrinsic Shape	0.005	0.999	0.979
$u$	Intrinsic Shape	–	–	0.999
$\theta$	Viewing Angle	–	–	$85.200^\circ$
$\phi$	Viewing Angle	–	–	$88.743^\circ$
$\psi$	Viewing Angle	–	–	$90.004^\circ$
$C_{\text{DM}}$	DM Concentration	0.250	15.500	15.250
$\log_{10} [f_{\text{DM}}(r_{200})]$	DM Fraction at $r_{200}$	0.050	2.000	1.950
$\Upsilon$	Global $M/L$	0.005	1.000	$0.980 M_{\odot}/L_{\odot}$

TABLE 2.1: The free parameters of the Schwarzschild model, their corresponding step sizes,  $\Delta$ , and the final best-fitting values.  $u$  is fixed in our model, while  $\theta, \phi, \psi$  are derived from  $q, p, u$ . These parameters therefore have no  $\Delta$ . \* Note that the black-hole mass is sampled logarithmically, and so its  $\Delta$  is multiplicative rather than additive.

(2018a). That work introduced a normalised  $\chi^2$  metric in order to account for spatial pixels which are not truly independent. It is defined as

$$\chi_r^2 = \chi_{\text{kin}}^2 \cdot N_{\text{kin}} / \min(\chi_{\text{kin}}^2) \quad (2.3)$$

with

$$\chi_{\text{kin}}^2 = \sum_{g=1}^{N_{\text{GH}}} \sum_{a=1}^{N_{\text{aper}}} \left( \frac{d_{a,g} - m_{a,g}}{e_{a,g}} \right)^2$$

for the data, model, and error of the  $a$ -th aperture of the  $g$ -th Gauss-Hermite kinematic coefficient,  $d_{a,g}$ ,  $m_{a,g}$ , and  $e_{a,g}$ , respectively, and

$$\begin{aligned} N_{\text{kin}} &= N_{\text{GH}} \times N_{\text{aper}} \\ &= 6 \times 4881 \\ &= 29286 \end{aligned}$$

for the number of Gauss-Hermite coefficients fit in the Schwarzschild model,  $N_{\text{GH}}$ , and the number of spatial Voronoi apertures,  $N_{\text{aper}}$ . In this way, a standard deviation of this  $\chi_r^2$  distribution is given by  $\sqrt{2N_{\text{kin}}}$ , and the grid search for NGC 3115 is illustrated in Fig. 2.5. The corresponding best-fitting Schwarzschild model is shown in Fig. 2.6 for all seven projected constraints.

#### 2.4.4 Intrinsic Angular Momentum

Following the optimisation of the gravitational potential parameters, the best-fitting Schwarzschild model provides intrinsic information about the galaxy, instead of being typically limited to projected quantities. The orbits of the model have intrinsic 3D angular momentum and orbital anisotropy, and the model has true LOSVD rather than parametrisations of these distributions. These intrinsic properties are a key requirement for the application of our methodology.

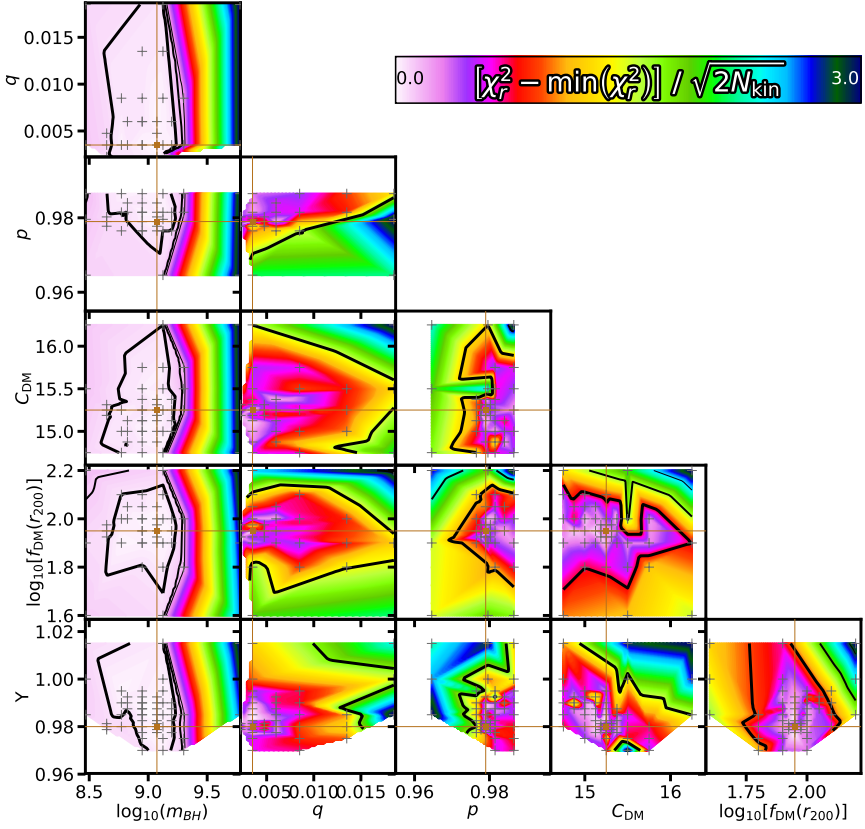


FIGURE 2.5: The grid search over the free parameters of the Schwarzschild model. Each panel shows the marginalised  $\Delta\chi^2$  contour surface in colour. The black solid lines show, from bold to thin, the  $1-$ ,  $2-$ , and  $3-\sigma$  ranges, respectively. The grey ‘+’ symbols show the underlying grid of models that were generated, and the magenta lines indicate the final best-fitting values.

One such property that we utilise directly here is the intrinsic angular momentum. Each orbit has a corresponding angular momentum vector  $\vec{L} = (L_x, L_y, L_z)$ . We consider a scaled version of this intrinsic angular momentum, the ‘circularity’, which was introduced by Zhu et al. (2018a) and is defined as

$$\lambda_z = \overline{L_z} / \left( \overline{r} \cdot \overline{V_2} \right) \quad (2.4)$$

with

$$\begin{aligned} \overline{L_z} &= \overline{xV_y - yV_x} \\ \overline{r} &= \sqrt{\overline{x^2 + y^2 + z^2}} \\ \overline{V_2}^2 &= \overline{V_x^2 + V_y^2 + V_z^2 + 2V_xV_y + 2V_xV_z + 2V_yV_z} \end{aligned}$$

We use the bar notation to denote that these values are averaged over all of the  $(x, y, z, V_x, V_y, V_z)$  points along a given orbit’s integrated path. The probability distribution of the  $\lambda_z - r$  plane for the best-fitting Schwarzschild model is shown in Fig. 2.7 (see § 2.4.5). It shows only the region constrained by the kinematics, even though the model orbits can extend beyond this in order to fit the full stellar MGE at large radius.

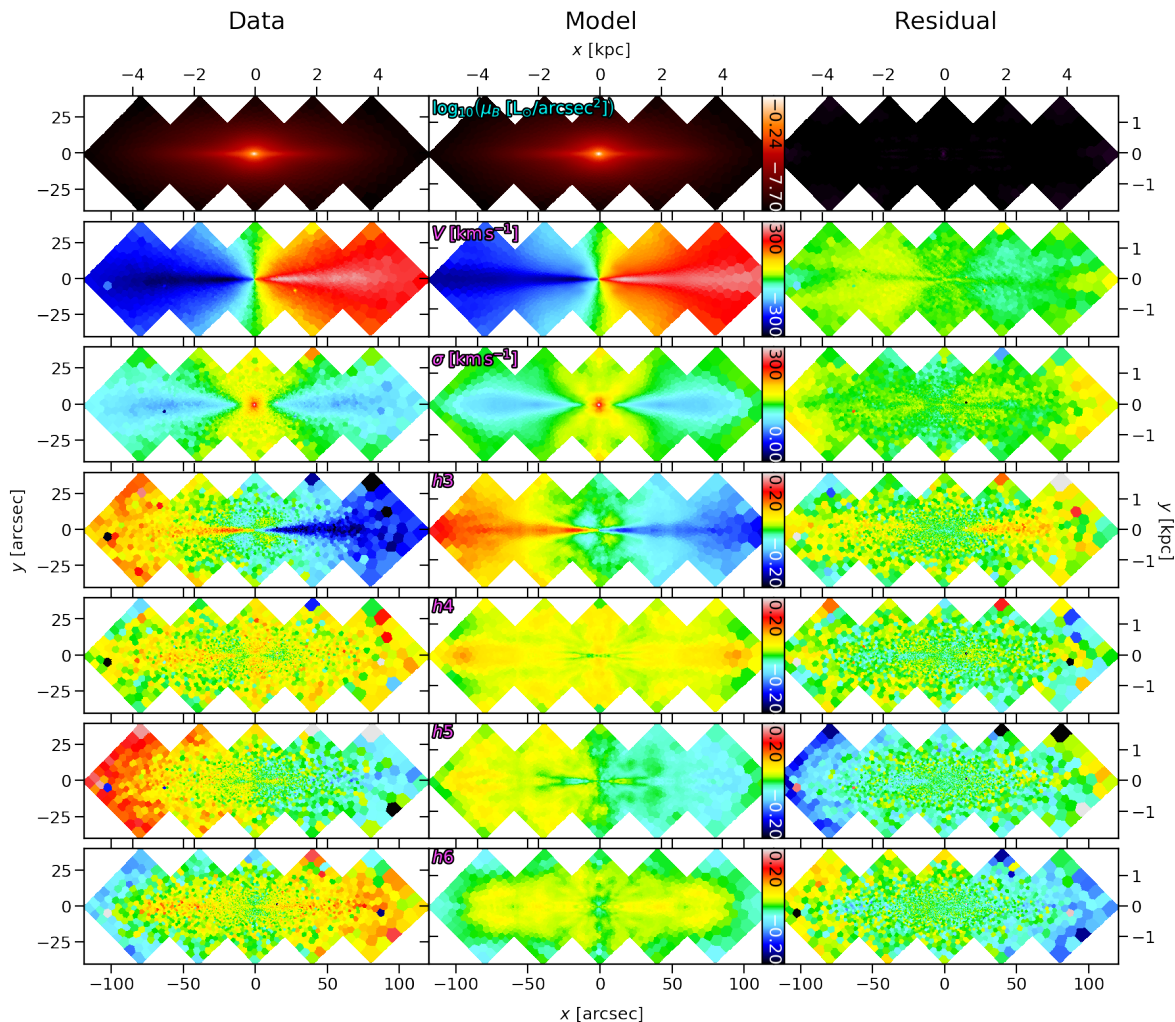


FIGURE 2.6: The data (left), model (center), and residuals (right) for the best-fitting Schwarzschild model of NGC 3115. From top to bottom (labelled in the top-left corner of each model panel) is the surface brightness, followed by all kinematic moments. The model is fit to the surface brightness MGE, rather than the surface brightness directly. The residuals for the surface brightness have been offset such that 0 is the black end of its corresponding colourbar. All other residual panels have been offset such that 0 corresponds to the green (centre) of their corresponding colourbars.

Circularity is a projection of the full 3D orbital distribution, and ‘clumps’ in this projection identify families of orbits with similar orbital characteristics in the meridional plane. This definition separates circular and box/radial orbits, having circularity values of  $|\lambda_z| = 1$  and  $\lambda_z = 0$ , respectively. It is analogous to the ‘stellar-spin’ parameter (defined in Emsellem et al., 2007) in that it is a metric to discriminate between rotation- and dispersion-supported systems (or orbits).

#### 2.4.5 Applying Stellar Populations to the Orbital Structures

At this point, we have a dynamical model, fitted to the observed kinematics, that provides information on the orbital distribution function by way of orbital luminosity weights. We now wish to couple this information to the observed stellar population properties, in terms of the (luminosity-weighted) mean age and metallicity maps. We do this by assigning individual ages and metallicities to the fitted orbital components, noting that a ‘component’ can be

composed of a collection of orbits from our dynamical model. We first consider how such components may be defined from the model, and then describe how we associate them with stellar population information to fit the observations.

## Dynamical Selection

The Schwarzschild model provides a full description of the orbital structure of our galaxy, being a combination of many hundreds of distinct orbital families. However, in terms of coherent galaxy sub-structures, we may expect far fewer components. In our own Milky Way, for instance, we broadly recognise a ‘thin disk’, ‘thick disk’, ‘bulge’, and ‘halo’. Indeed, as described in the introduction, such broad component definitions are often applied when considering the decomposition of external galaxies. By combining both stellar kinematics and populations, we here seek to test such ‘component’ concepts.

As described above, circularity phase-space gives a simple projection of the full orbital phase-space, from which broadly-distinct orbits can be tracked as a function of radius in the galaxy. We take advantage of this as a way of potentially reducing the number of distinct orbital families by instead grouping them to form ‘components’. This brings computational advantages by reducing the dimensionality of the problem, as well as giving a clear definition of what the (dynamically, chemically, and chronologically) distinct components are. We trial a number of conceptually-different approaches here, and compare their results.

**Sample I:** *Conventional Decomposition* We refer to Sample I as a ‘conventional’ decomposition because we define bins in circularity that closely approximate classic galactic components; namely, a thin disk, thick disk, and bulge. We use the ranges defined by Zhu et al. (2018a);  $\lambda_z > 0.8$ ,  $0.25 < \lambda_z \leq 0.8$ , and  $\lambda_z \leq 0.25$ , representing the thin disk, thick disk, and bulge, respectively.

**Sample II:** *Small Sampling in Circularit*y In this instance, we group the orbits into small bins of  $\lambda_z$ . We do not assign physical meaning to the resulting ‘components’, but merely investigate how the extra freedom affects the stellar-population fitting.

**Sample III:** *Small Sampling in Circularit*y and Radius This approach samples the 2D circularity space in small bins of circularity and radius. Once again, we avoid attributing physical meaning to these components, but investigate specifically if radial changes (compared to  $\lambda_z$  sampling only) can improve the fit significantly. For consistency, the  $\lambda_z$  bins are the same as Sample II. Also, to align with the sampling of the underlying orbits from the Schwarzschild model, the sampling of the circularity phase-space in radius is logarithmic in the inner region (but linear outside the FOV to avoid overly-large bins).

**Sample IV:** *Orbit-Based Decomposition* Finally, in the limit of increasingly smaller bins in circularity, each individual orbit may be considered as a separate component. Dealing directly with orbits is conceptually a more robust implementation, as it avoids issues with the ‘projection’ of the intrinsic 3D orbital phase-space into the circularity domain. It is, however, computationally expensive, and can result in an ill-conditioned problem for large numbers of orbits.

For each criterion, we consider only those components/orbits that are given non-zero weight in the best-fitting Schwarzschild model, as all others do not contribute any mass to the model.

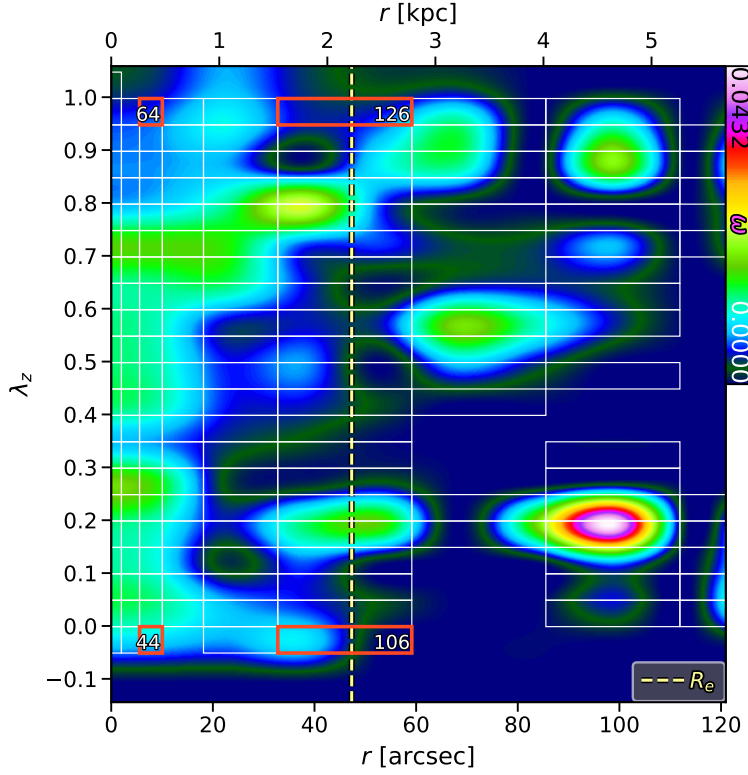


FIGURE 2.7: The  $\lambda_z - r$  phase-space of the best-fitting Schwarzschild model of NGC 3115. The density map is the orbital probability distribution (circularity; § 2.4.4), with the dynamical component selections of Sample III shown in white boxes. The vertical dashed line marks  $R_e$ . Highlighted and numbered are components representative of different regions of the circularity phase-space; see Fig. 2.8.

We refer to Sample III as the illustrative case for the remainder of this work (see § 2.5.1), and Fig. 2.7 shows the corresponding components in circularity phase-space. The gaps in the grid correspond to ‘components’ that have zero weight. By the nature of the Schwarzschild model, we can investigate these dynamical components in greater detail, in order to gauge their spatial extent and physical properties. Fig. 2.8 shows the surface brightness and kinematics of a subset of characteristic dynamical components, selected to contrast the different regions in the circularity phase-space. These properties are derived as statistical moments of the intrinsic LOSVD of each component – the integral, mean, and dispersion for the surface brightness, mean velocity and velocity dispersion, respectively. The dynamical decomposition effectively divides the LOSVD in each aperture amongst the resulting components. Each component’s LOSVD, therefore, need not be Gaussian. This is illustrated in Fig. 2.9, using the Sample I decomposition for clarity, and is why we restrict our visualisation of the components to the low-order kinematics. Nevertheless, it is clear from Fig. 2.8 that the lowest  $\lambda_z$  components are truly pressure-supported, while the highest  $\lambda_z$  components are rotation-supported.

## Dynamics/Stellar Populations Associations

The Schwarzschild model provides the luminosity-weights per aperture (Voronoi bin), *for each component*. The SFH provides the mean luminosity-weighted stellar-population properties per aperture. We can therefore assign such properties to the dynamical components, by equating their luminosity-weighted average with the SFH values. For a single aperture, this can be expressed as

$$\Phi^{\text{SFH}} = \frac{\sum_{j=1}^{N_{\text{comp.}}} \omega^j \phi^j}{\sum_{j=1}^{N_{\text{comp.}}} \omega^j} \quad (2.5)$$

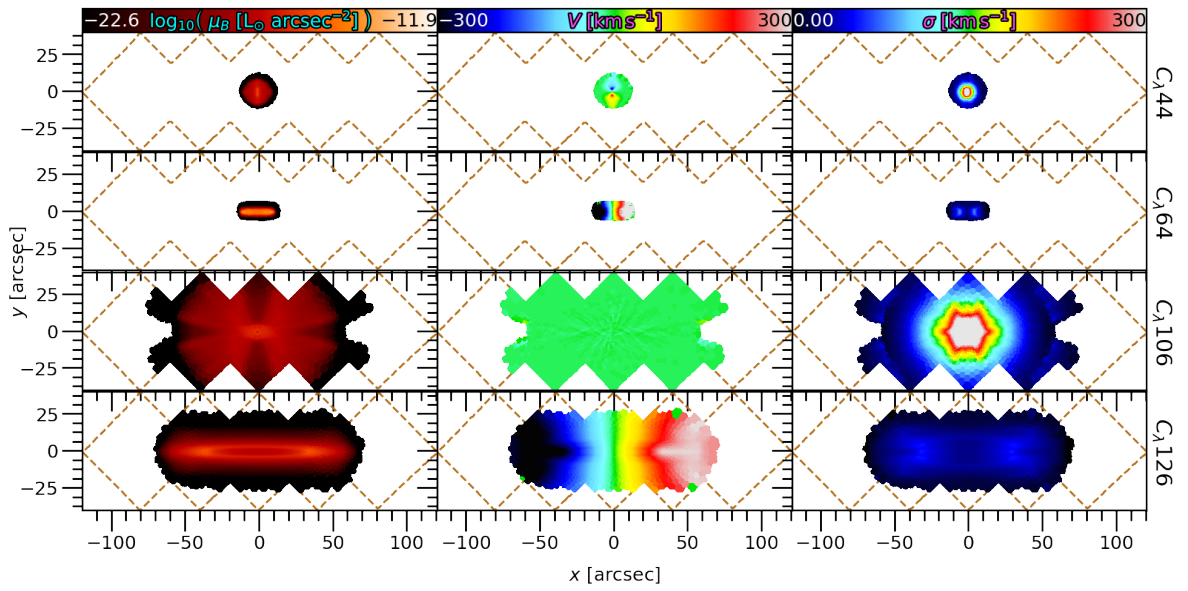


FIGURE 2.8: The surface brightness (left), mean velocity (middle), and velocity dispersion (right) of four characteristic dynamical components. Each component is presented on the same binning and FOV as the data for consistency. The FOV is outlined by the brown dashed line, and the component labels are on the far right of each row (refer to Fig. 2.7). Note that each of these components does *not* contribute equal mass to the dynamical model, but were selected to illustrate different regions in circularity phase-space.

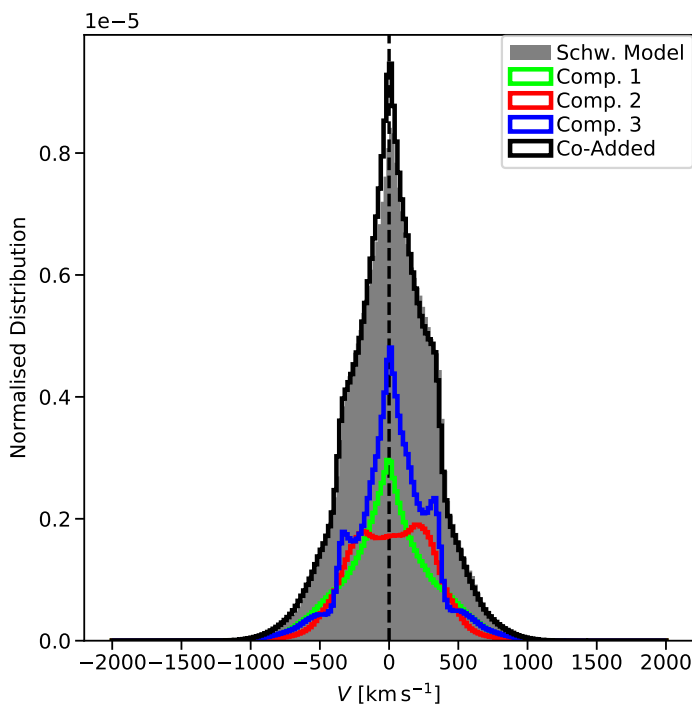


FIGURE 2.9: The LOSVD in a single aperture, for the dynamical components of Sample I (coloured histograms), their sum (black), and from the original Schwarzschild model (grey filled).

where  $\Phi^{\text{SFH}}$  is the luminosity-weighted stellar-population value ( $t$  or  $Z$ ) from the SFH,  $\omega^j$  is the orbital weight of the  $j$ -th dynamical component, and  $\phi^j$  is the unknown stellar-population value ( $t$  or  $Z$ ) of the  $j$ -th dynamical component. If we normalise the orbital weights beforehand, such that

$$\tilde{\omega}^j = \frac{\omega^j}{\sum_{j=1}^{N_{\text{comp}}} \omega^j}, \quad (2.6)$$

we can then express the entire problem, over all apertures, as a matrix equation

$$\begin{pmatrix} \tilde{\omega}_1^1 & \tilde{\omega}_1^2 & \cdots & \tilde{\omega}_1^{N_{\text{comp}}} \\ \tilde{\omega}_2^1 & \tilde{\omega}_2^2 & \cdots & \tilde{\omega}_2^{N_{\text{comp}}} \\ \vdots & \vdots & \ddots & \vdots \\ \tilde{\omega}_{N_{\text{aper}}}^1 & \tilde{\omega}_{N_{\text{aper}}}^2 & \cdots & \tilde{\omega}_{N_{\text{aper}}}^{N_{\text{comp}}} \end{pmatrix} \cdot \begin{pmatrix} \phi^1 \\ \phi^2 \\ \vdots \\ \phi^{N_{\text{comp}}} \end{pmatrix} = \begin{pmatrix} \Phi_1^{\text{SFH}} \\ \Phi_2^{\text{SFH}} \\ \vdots \\ \Phi_{N_{\text{aper}}}^{\text{SFH}} \end{pmatrix} \quad (2.7)$$

where one row in the matrix (superscripts) denotes the weights for all dynamical components in a single aperture – equivalent to Eq. (2.5) – and one column (subscripts) corresponds to the weights of a single dynamical component in all apertures. We now simply require a linear (computationally-efficient) matrix inversion in order to find the  $\vec{\phi}$ , which thereby associates the dynamically-identified components with individual stellar populations. For  $\phi$  and  $\Phi$  in this work, we investigate both age and metallicity. Through the use of luminosity-weighted summations of age and metallicity, our method rigorously and directly captures the equivalent properties measured from the spectral fitting of the data. This avoids the complications of linearly combining line index measurements, for instance as proposed in Long and Mao (2018). Such indices must be weighted by the flux in the pseudo-continuum band of the given index, and additional non-linear processes normally employed in such measurements (such as resolution matching, Lick-offset calibrations, velocity broadening, and emission subtraction) must be ignored or somehow accounted for. The matrix inversion in this work is done in the framework of a Bounded-Value Least-Squares (BVLS) fit, which is akin to NNLS problems, but rather than a positivity constraint, the solution bounds are specified explicitly. Here we impose the boundary values of the SSP library in order to maintain consistency with our SFH. This is not necessary in general – for instance, if  $\vec{\Phi}$  is generated without the use of an SSP library – and we emphasise that the best-fitting  $\vec{\phi}$  is continuous within the bounds and not tied to the specific sampling of any SSP library. While there exists mild covariances between the stellar age and metallicity, our spectral fits from § 2.3 employ a small linear regularisation. This regularisation assumes a smooth SFH in both age and metallicity in order to break the degeneracy. Moreover, in the subsequent fitting described in this section, our model needs to reproduce the spatial structure in the SFH maps, not just the age and metallicity values of an individual bin. This combination of spatial and temporal coherence allows our model to mitigate effects due to covariances. We therefore treat age and metallicity as orthogonal parameters, and simply fit them independently.

Note that the different decomposition criteria described in § 2.4.5 are merely re-distributions of the weights  $\tilde{\omega}^j$  into different numbers of  $N_{\text{comp}}$ , while Eq. (2.7) and the method itself remain unchanged.

## 2.5 Results

Here we present the main results of this work. We first present the various combinations of dynamical components and stellar population properties, and then how these combinations

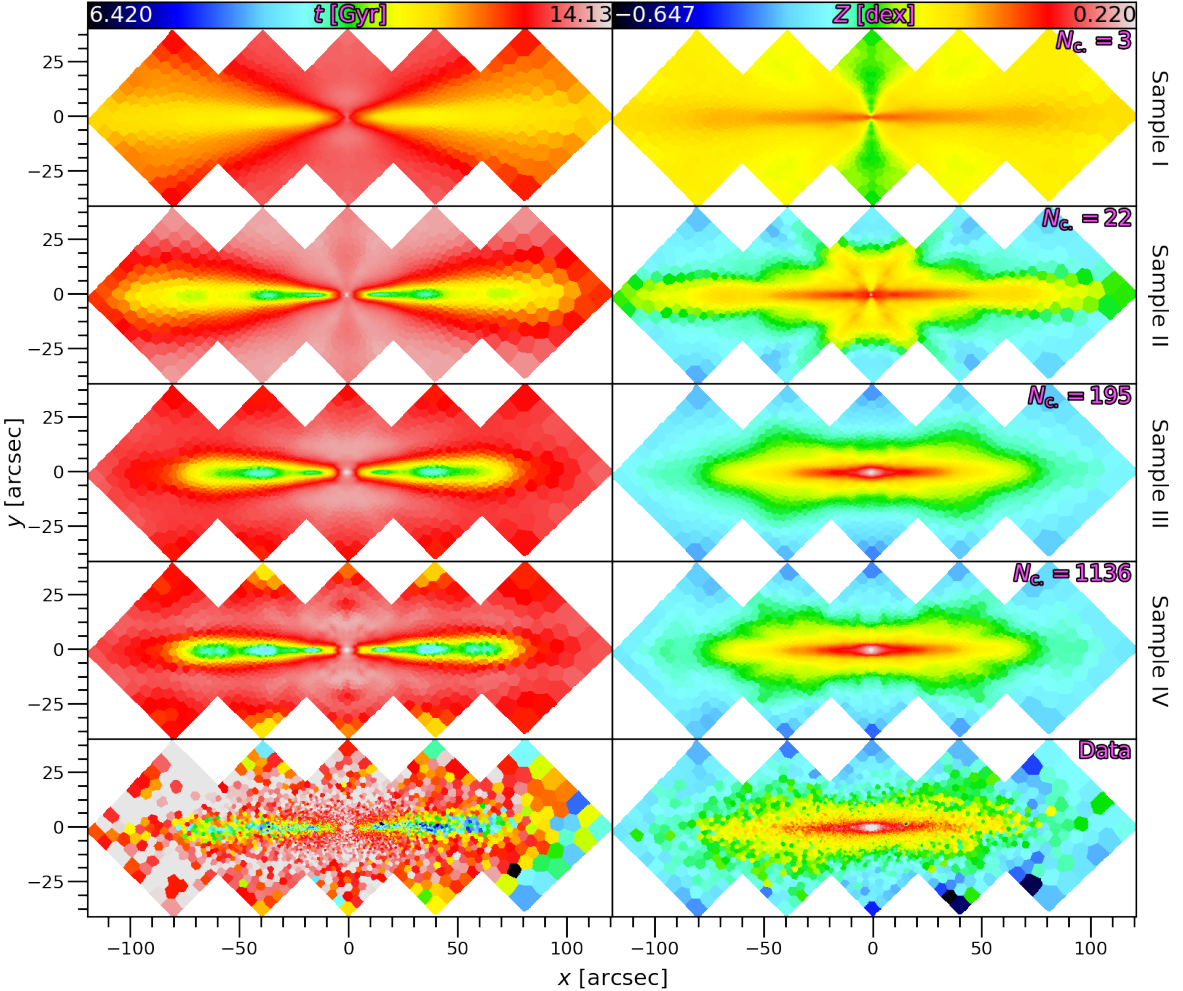


FIGURE 2.10: The luminosity-weighted age (left) and metallicity (right) maps. The first four rows are for the different dynamical selection criteria (§ 2.4.5), labelled on the far right. The number of dynamical components resulting from each sample is inset in the top right of each metallicity panel. The bottom row shows the maps derived from the SFH (§ 2.3).

lead to inferences of the formation history of this galaxy.

### 2.5.1 Constraining the Required Number of Dynamical Components

Fig. 2.10 shows the fits to the measured luminosity-weighted mean stellar age and metallicity for all of the sample criteria tested in this work (see § 2.4.5). It is immediately clear that the conventional few-component decompositions are completely unable to reproduce the structure in the stellar populations. This implies a rather dramatic disconnect between the photometric, kinematic, and chemical structures seen in the galaxy, at least from the point of view of a handful of components. However, we note that while the surface brightness of the components from Sample I follow typical Sérsic-law expectations, the assumption that they have a single monolithic formation is strongly inconsistent with the data. This suggests that studies assuming the conventional Sérsic approach and fitting a few components should include stellar population *gradients*, rather than a single population per component as done here, even for evolved objects like NGC 3115.

Similarly, it appears that regardless of the degree of freedom in  $\lambda_z$  as in Sample II, the fits are unable to reproduce the SFH, in particular the metallicity. This reaffirms the existence of

radial gradients in stellar populations, with these gradients being stronger in metallicity, as has been seen by many studies previously both in general (for example, see Sarzi et al., 2018; Parikh et al., 2018; Poetrodjojo et al., 2018) and specifically for NGC 3115 (for example, see Strom et al., 1976; Pastorello et al., 2014). However, we can additionally conclude here that these gradients must exist within each component *even at fixed  $\lambda_z$* .

Unsurprisingly, as the number of degrees of freedom (dynamical components) increases, so too does the quality of fit. Surprisingly, though, once the circularity phase-space is well-sampled in both dimensions as in Sample III, there already appears to be sufficient freedom in the model to reproduce the stellar-population maps, without having to consider every individual orbit. This is not necessarily expected *a priori*, but allows us to dramatically reduce the size of the parameter-space for subsequent analyses by using Sample III as the default dynamical decomposition moving forward. This is because, while there is a factor of 10 increase in  $N_{\text{comp.}}$  between Sample III and IV, their fits to the stellar-population maps are almost indistinguishable.

The fit described in § 2.4.5 is done on each bin of the observations. However, due to the fact that orbits from the Schwarzschild model overlap in projection, multiple orbits will contribute to the mean age and metallicity of a single bin. There are necessarily different weighted mixtures of ages and metallicities that give the same average values, producing a degeneracy when associating stellar-population properties to dynamical components. One option would be to reduce the number of components until the fit is adversely affected, however this requires arbitrary choices of which components to remove. A more natural approach is to apply linear regularisation. The regularisation scheme used here prefers solutions where adjacent dynamical components/orbits have similar stellar population properties given an otherwise degenerate alternative. It is described in detail in § 2.B.

### 2.5.2 Recovering the Dynamical SFH

Following these fits and adopting the results from Sample III, we now have a set of components for NGC 3115 with both fitted kinematics and stellar populations. We have already been able to investigate the structures in components of the galaxy based on a dynamical selection criterion (see Fig. 2.8). Now, however, we can investigate NGC 3115 from an orthogonal perspective: the nature of spatial structures in components selected on their stellar populations. This produces spatially-resolved maps for components of the galaxy in bins of age and metallicity, which is effectively a conventional SFH, except that it originates from the spatial distribution of *dynamical* components. A conventional full-spectral-fitting SFH was computed in Guérou et al. (2016). For comparison, we construct the same bins in age and metallicity as that work, which are shown in Figures 2.11 and 2.12, respectively. By considering for now just the left columns of Figures 2.11 and 2.12, it is clear that the bulk of the stellar mass is old, and in a spheroidal structure concentrated at the centre but extending across the FOV. We see a small portion of relatively young stars, that exist in a much more flattened structure along the plane of the galaxy. There is remarkable agreement between the purely spectral analysis in Guérou et al. (2016) and our combined approach, despite the fundamental differences between the two methodologies. Moreover, from the metallicity panels, we find a central elongated metal-rich component. This is surrounded by a near-solar diffuse component, which is slightly overdense in the centre. We find a portion of the mass in an even more diffuse metal-poor halo-like component. The absolute masses presented in each panel of Figures 2.11 and 2.12 are computed as the fractional mass (determined by the Schwarzschild model) of  $MGE_\Sigma$ , integrated within the MUSE FOV. This ensures that these

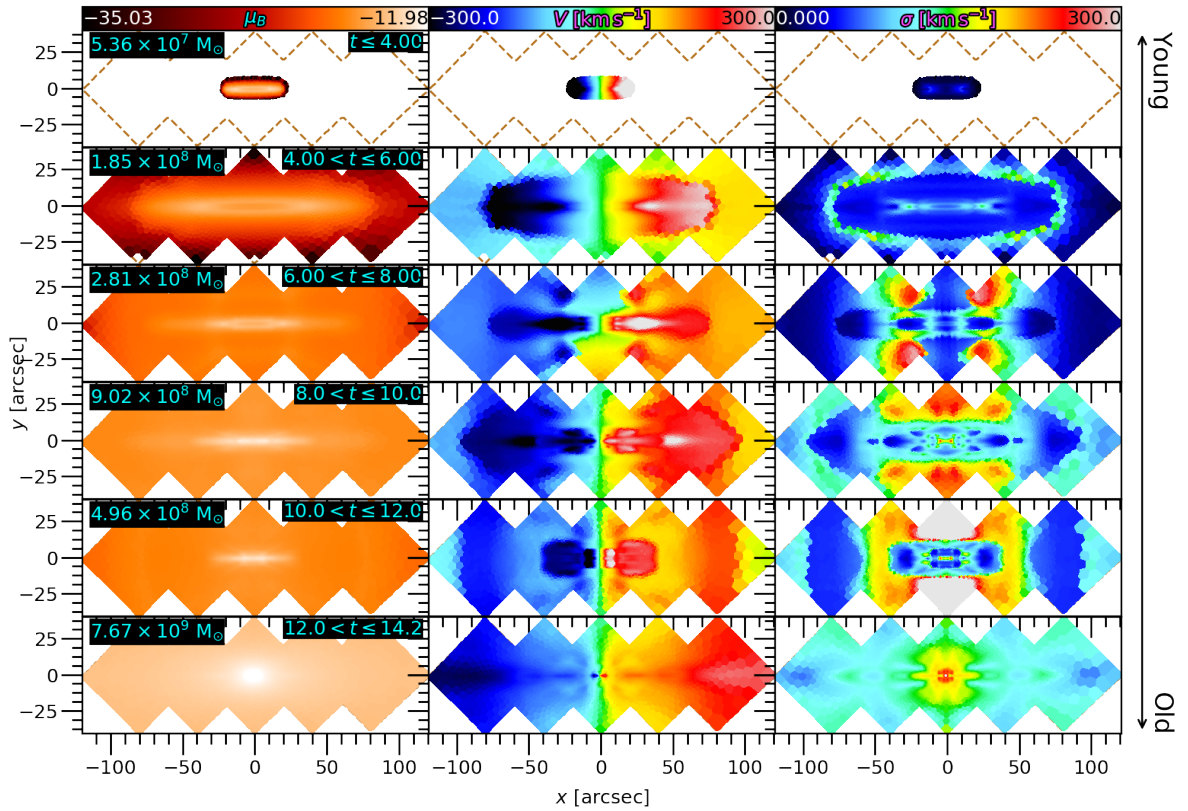


FIGURE 2.11: The surface brightness (left), mean velocity (middle) and velocity dispersion (right) of the dynamically-selected components, binned into their corresponding mean stellar age from young (top) to old (bottom). The bin ranges and corresponding stellar masses of each bin are inset in the upper right and left of each surface brightness panel, respectively.

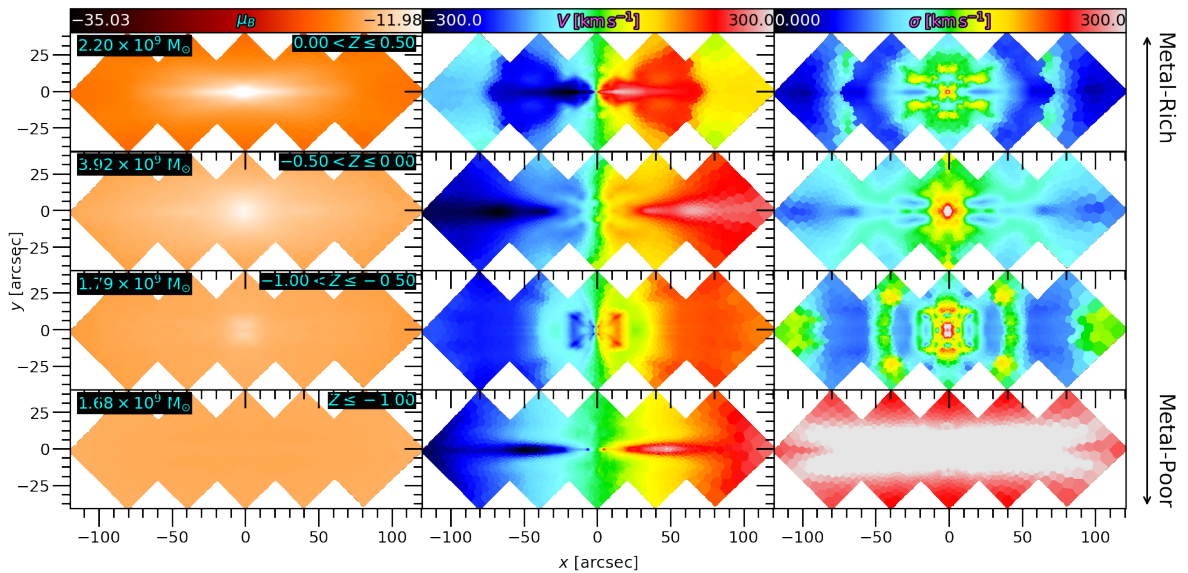


FIGURE 2.12: As Fig. 2.11, but for the stellar metallicity.

stellar mass measurements include the information from the stellar  $M_\star/L_V$  map, and are consistent with the dynamical model and the spectral SFH.

In addition to the conventional SFH analysis possible with this method, we can extract *intrinsic* kinematics for each of these age and metallicity bins. This is possible at present uniquely from our combined methodology. It allows us to investigate the chemistry and kinematics simultaneously and self-consistently, in a spatially-resolved manner. These kinematics are shown in the middle and right columns of Figures 2.11 and 2.12. As mentioned in § 2.4.5, the decomposition of the full Schwarzschild model by either dynamical (that section) or population (this section) properties necessarily divides up the LOSVD in each aperture. This is why the kinematics in Figures 2.11 and 2.12 may appear non-physical and discontinuous. These components do not exist in isolation, and the kinematics of each component are physically meaningful only in the context of the full dynamical model. Moreover, the bins in age and metallicity are discrete, further contributing to the discontinuities in the kinematic maps. However, visualising the results in this way is useful because it allows us to investigate the *relative* dynamical properties of the different stellar populations in a completely spatially-resolved manner. It is in fact quite clear from these figures that, for instance, the youngest ages are heavily rotationally-supported, and that the most metal-poor components are highly pressure-supported – findings that we expand on in the following sections.

### 2.5.3 Intrinsic Stellar Velocity Dispersion and Stellar Populations

We may delve further into the model by investigating its intrinsic properties, and any direct correlations between the dynamical and stellar-population properties. To this end, we study how the properties of the intrinsic velocity ellipsoid and the assigned stellar populations are related, focusing on the vertical velocity dispersion in order to isolate features in the disk plane. We present in this section the results of this investigation, based on the intrinsic properties derived from the Schwarzschild model and the subsequent population fits.

We consider the  $z$ -component of the velocity dispersion,  $\sigma_z$ , in order to probe the structure and properties of the disk region of NGC 3115. As we have the complete phase space information for every orbit in our model, we can compute the intrinsic moments of the orbital motions. This includes the first ‘true’ moment of the velocity distribution along the three principle axes ( $V_x, V_y, V_z$ ), the second moments, and all the cross-terms. The second moment of the velocity distribution can be approximated as

$$\langle V_k^2 \rangle = \sigma_k^2 + \langle V_k \rangle^2 \quad (2.8)$$

for first and second moments  $\langle V_k \rangle$  and  $\langle V_k^2 \rangle$ , respectively, and velocity dispersion  $\sigma_k$ , where  $k \in [x, y, z]$  is the Cartesian axis. Therefore, to compute the velocity dispersion, it follows trivially that

$$\sigma_k = \sqrt{\langle V_k^2 \rangle - \langle V_k \rangle^2} \quad (2.9)$$

The outputs of the Schwarzschild model are first transformed from Cartesian to cylindrical coordinates. To construct radial profiles, we transform the logarithmic energy sampling from the original Schwarzschild model from spherical coordinates to cylindrical coordinates. This produces a cylindrical radius equivalent to the original sampling in  $E$ . For clarity, we combine all the orbits within one PSF of the galaxy centre and treat this as a single position, as we cannot directly resolve this region. Radial profiles of the first and second moments –  $\langle V_z \rangle(R)$  and  $\langle V_z^2 \rangle(R)$ , respectively – are constructed by computing the luminosity-weighted

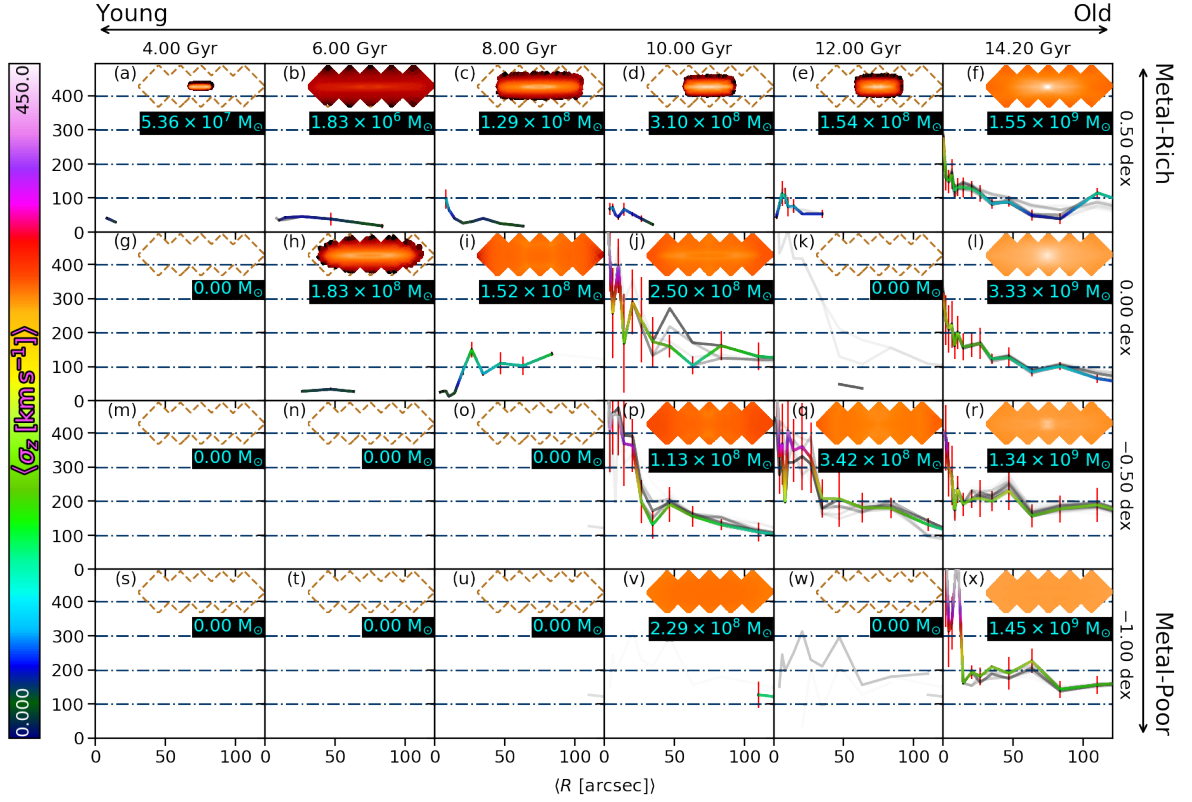


**FIGURE 2.13:** *Main:* The radial profiles of the  $z$ -component of the *intrinsic* velocity dispersion for the dynamical components grouped by their mean stellar-population properties. Each curve is coloured by its  $\sigma_z$  values to allow an easier quantitative comparison between panels. The variance within the annuli (see text) are shown as errorbars. The grey curves are Monte Carlo simulations of the stellar-population fits. They are computed by randomly perturbing the stellar-population maps from the spectral SFH (§ 2.3) within their measurement uncertainties, and re-fitting to the dynamical components. Each trial is plotted with high transparency, such that only the regions with high density of curves are visible. We note that, in a few instances, the Monte Carlo simulation has populated distinct panels from the best-fit model. *Inset:* The surface-brightness of each age/metallicity bin, observed at the best-fitting projection of the Schwarzschild model ( $\sim 85^\circ$ ) on the same FOV as the MUSE observations. All surface-brightness panels are on the same colour-scale. The absolute stellar masses are inset in cyan.

sum of the orbits' moments that lie within radial annuli. These are then converted into  $\sigma_z(R)$  with Eq. (2.9). Finally, all components belonging to a particular age and metallicity bin are averaged to produce stellar-population-selected velocity-dispersion profiles. These are shown in Fig. 2.13. The radial extent of each profile is determined by two factors; whether there is mass at a given radius from a given age/metallicity bin (that is, the spatial extent of the corresponding surface-brightness distribution), and whether Eq. (2.9) is numerically defined at a given location in a given bin, which depends on its particular combined kinematics from the dynamical model. We present the marginalised plots (over age and metallicity) in § 2.C

### 2.5.4 Modelling Systematics

Before interpreting the wealth of information in Fig. 2.13, we briefly discuss here the possible sources of systematic uncertainties arising from this method, and how reliable the subsequent formation history is.

In all of the dynamical samples presented in § 2.4.5, the components are defined by hard rectangular grids in the orbital probability distribution. It is possible that this is responsible for some of the substructure that can be seen in some panels of Fig. 2.8. Some components appear to be a superposition of underlying dynamical structures, indicating that those components could somehow be further divided until unique dynamical features are isolated. It may be possible to mitigate these effects to some extent by introducing a more complex method for grouping dynamically-similar orbits to define the components, but such a method would have to remain contiguous in the circularity phase-space in order to conserve the mass of the dynamical model. Testing and implementing a diverse range of methods for the dynamical selection is beyond the scope of this work.

By construction, each row of the matrix in Eq. (2.7) – each spatial bin of the observations – is assigned the same set of  $\vec{\phi}$ . The consequence of this is that each component is mono-age and mono-metallicity. For the triaxial Schwarzschild model, each component is also at least point-symmetric. Therefore, the resulting fit in Fig. 2.10 can not reproduce any asymmetry in the SFH maps, whether that asymmetry is physical or otherwise. There is mild (non-physical) asymmetry in the SFH maps for this particular data-set. The effect of this would be a slightly larger discrepancy between the data and model maps in Fig. 2.10 due to the implicit averaging between the  $\pm x$  sides. While we mitigate the most significant deviations by masking the right-most bins during the fit, there is still a gradual sky residual gradient across the FOV. This can be further seen in the youngest ages of the disk on the left and right sides, which would contribute to the uncertainties from that fit. However, such an issue is specific to the data-set in use here, and general applications of our method would not be subject to these uncertainties.

In § 2.5.1 and § 2.B, we address the possibility that the solutions to Eq. (2.7) may be unstable/degenerate. To estimate what impact this degeneracy may have specifically on our interpretation of Fig. 2.13, we run 100 Monte Carlo simulations by perturbing the measured SFH maps within their uncertainties, and re-fitting the dynamical components as described in § 2.4.5. Running through the entire analysis, we generate a new set of  $\sigma_z(R)$  curves for each trial, and these are plotted within each panel of Fig. 2.13. It is clear from the dense clustering of curves that the solutions are reasonably stable. It is possible for some components to traverse the bins in stellar populations, but this is only because their best-fit age and metallicity are close to the boundaries of the bins, while the absolute change in the individual ages and metallicities remains small.

More broadly, in order to accurately estimate the possible systematic uncertainties associated with a method of this nature, it is necessary to run our analysis on mock data derived from high-resolution hydrodynamical galaxy simulations. This effort is considerable in and of itself, and has been in preparation in parallel with our application here to real data (Zhu et al., in prep.). That work will test the accuracy and reliability of the recovery of stellar population properties for dynamically-selected components. However, in this work specifically, there is such clear structure in the stellar populations and kinematics due to the proximity of the galaxy and the quality of the data, that this method can be applied with confidence in its ability to recover the underlying properties of the galaxy.

## 2.6 Discussion

### 2.6.1 Galactic Components of NGC 3115

The many facets of our comprehensive model can be seen concisely in Fig. 2.13, in which we study the galaxy across stellar age and metallicity, and simultaneously with a metric for the spatially-resolved, intrinsic dynamical properties. We characterise these galactic features here.

*Old, Metal-Rich, Compact, Hot Spheroidal Bulge* Firstly, we find a bulge-like component at the oldest age, with a mild spread in metallicity. This is clear from the central, compact spheroidal peak in surface brightness in the three most metal-rich panels at 14.2 Gyr; panels (*f*), (*l*), and (*r*). This is accompanied by a corresponding central ( $R \lesssim 15''$ ) peak in  $\sigma_z$  in these bins ( $\sigma_z \gtrsim 100 \text{ km s}^{-1}$ ), indicating that this region is pressure-supported. This component has only undergone mild chemical enrichment, likely due to secular stellar-evolution processes, with no other significant evolution – neither in its kinematics nor populations. By making the appropriate cuts in age, metallicity, circularity, and radius in order to isolate only the bulge contributions to the relevant panels, we estimate that this component contains  $\sim 3.9 \times 10^9 M_\odot$ .

*Metal-Rich, Extended, Cold Disk* We also find evidence for a disk-like structure that is enriched, and present at *all* ages. This is clear from the surface brightness in panels (*a*) – (*f*), and also panel (*h*), which all show elongated structures in the plane of the galaxy. Again, this is corroborated by the dynamics, which show that this component has  $\sigma_z \lesssim 50 \text{ km s}^{-1}$  at intermediate radii where the disk dominates, implying that it is supported primarily by coherent rotation (cold orbits). In particular, even panel (*f*) has a signature of the disk in both the surface brightness and the velocity dispersion. This is an interesting finding, as a galactic component that is simultaneously cold, old, and enriched would be sensitive to any dynamical perturbations over the galaxy’s history. Therefore, the mere existence of such an old population in a disk configuration immediately implies a fairly quiescent history for NGC 3115. We see that star formation in the disk continued smoothly from the earliest times, gradually declining until it ceased  $\sim 4$  Gyr ago. The resulting stars are naturally enriched, and are progressively more dynamically cold – a progression that we quantify further in § 2.6.4. In our model, the disk component is  $\sim 1.6 \times 10^{10} M_\odot$ .

*Old, Metal-Poor, Diffuse, Hot Stellar Halo/Thick Disk* Finally, we find a diffuse halo/thick-disk-like component that is dynamically hot ( $\sigma_z \gtrsim 100 \text{ km s}^{-1}$ , including at large radius), metal-poor ( $[\text{Z}/\text{H}] \lesssim -0.50 \text{ dex}$ ), and mostly old ( $t \gtrsim 10 \text{ Gyr}$ ). This can be seen in panels (*p*) – (*x*), which all have a similar featureless spatial distribution, and relatively high  $\sigma_z$ . Panels (*j*) and (*l*) appear to have contributions from this component as well, but superimposed with contributions from the disk and bulge, respectively. This stellar halo/thick-disk component contains  $\sim 4.2 \times 10^{10} M_\odot$ .

### 2.6.2 Implications for the Formation History of NGC 3115

The current paradigm for galaxy formation, in particular of ETG, details the hierarchical assembly of massive galaxies via the merging of smaller systems, which result in expectedly

pressure-supported systems due to the nature of the merging process (for instance, see Somerville and Davé, 2015, and references therein for a general review). Merging during the lifetime of a galaxy is a key aspect, and often the focus, of many cosmological and/or hydrodynamical simulations (for example, see Bird et al., 2013; Athanassoula et al., 2016; Eliche-Moral et al., 2018). Moreover, merging is often invoked to explain many phenomena seen in observational studies (for example, see Arnold et al., 2011; Lidman et al., 2013; Guérout et al., 2016). However, these mergers are typically assumed to have been of two (or more) fully-formed progenitor galaxies, implying that sufficient cosmological time had passed for such galaxies to first form, then merge. As discussed above, we find a very old and dynamically cold population in the disk of NGC 3115, implying that any destructive major merger had to have occurred prior to the formation of this disk. Laurikainen et al. (2013) arrived at the same conclusion when they detected cold ‘lenses’ (an elliptical structure with a sharp inner edge in surface brightness; Kormendy, 1979) within S0 galaxies that were very old – also  $\sim 14$  Gyr. The Universe had, at such early times, considerably different physical conditions to the environments in which the simulated progenitor galaxies were formed. For instance, the progenitor galaxies in Athanassoula et al. (2016) were explicitly modelled after “nearby galaxies”. As a result, such scenarios may not appropriate for our inferences here, and we therefore look for a possible alternate formation mechanism to explain the results we see in Fig. 2.13.

One such mechanism is ‘compaction’ (Dekel et al., 2009; Zolotov et al., 2015) at early times. Compaction involves the rapid dissipative contraction of highly-perturbed gas into the central regions of galaxies in the form of cold streams. These streams can trigger star-formation in this region, which is reportedly quenched rapidly for massive galaxies (Zolotov et al., 2015). Therefore, compaction could also explain the enrichment gradient in the central bulge component, which is all at early times. Moreover, since the gas cooling is dissipative, and the cold streams are not as disruptive as major mergers, this method of formation could also explain the persistence of the old cold disk structure (Dekel et al., 2009), even if the streams entered after the old disk formed. The remaining gas which had been accreted via the cold streams would go on to form the main stellar disk at progressively younger ages until the gas reservoir is exhausted.

Irrespective of the formation mechanism for the central bulge and main disk, the outer stellar halo/thick-disk component is strongly consistent with an accreted origin, mainly from dry minor mergers. This is due to the combination of old ages, low metallicities, pressure-supported kinematics, and featureless yet extended surface brightness. This component forms a significant portion ( $\sim 0.68M_\star$ ) of the stellar mass of NGC 3115. Interestingly, the cosmological simulations of Oser et al. (2010) predict that for ‘intermediate mass’ galaxies such as NGC 3115, the accreted material constitutes  $\sim 65\%$  of the stellar mass at  $z = 0$ , which is remarkably consistent with our model. Given such a significant contribution to the stellar mass budget, persistent minor mergers could also explain how NGC 3115 transformed into an S0 galaxy, by building up the ‘thick’ disk and diluting any spiral arms that may have been present in the progenitor object. While previous works have claimed that either environmental perturbations (Bekki and Couch, 2011), internal disk instabilities (Saha and Cortesi, 2018), or major mergers (Querejeta et al., 2015; Tapia et al., 2017; Diaz et al., 2018; Fraser-McKelvie et al., 2018) are the likely formation paths for S0 morphologies, our model is inconsistent with these mechanisms. NGC 3115 is a field S0, making environmental perturbations unlikely, and both internal disk instabilities and major mergers would likely destroy the old disk structure that we find in our model.

### 2.6.3 Comparison to Previous Inferences

Due to its proximity, NGC 3115 has been studied widely in the literature, using many techniques that produce orthogonal constraints on the inferred formation history. We investigate here how our results compare with these works.

Arnold et al. (2011) use Supreme-Cam imaging and long-slit GC observations to study the kinematic and metallicity properties of NGC 3115. They found that an early violent major merger would explain the relatively high rotation and flattening of the central bulge component. Guérou et al. (2016) proposed that a small number of progenitors with  $\log_{10}(M_*/M_\odot) \sim 10$  is consistent with both the surviving angular momentum of this central component, as well as its enrichment at such early times.

Guérou et al. (2016) suggested that some portion of the gas reservoir that was present during the major merger survived the interaction, went on to cool and eventually form the dynamically cold, younger disk stars. Our results indicate that the cooling of the gas and the formation of new stars happens ‘immediately’ (within the oldest age bin), and stars continued to form on progressively colder orbits through to the 4 Gyr bin, until this gas was consumed. Their interpretation of the excess gas does indeed agree with our results, however our model does not need to invoke a major merger as the source, and an alternate origin for the gas could be the cold streams associated with an early compaction phase.

Arnold et al. (2011) claim that steeper metallicity gradients can also be the result of passive accretion of low-mass, low-metallicity satellites which lower the average metallicity in the outskirts, thereby steepening the gradient. This accretion is also consistent with the observed metallicity map for NGC 3115. Brodie et al. (2012) and Cantiello et al. (2014) find strong evidence that the observed colour bimodality in the GC population in NGC 3115 is driven by an underlying metallicity bimodality. This supports not just an accreted origin for the blue population of GC, but specifically accretion from dry minor-mergers, locking in the low metallicity of the in-falling objects. Our metal-poor, dynamically-hot, diffuse components also strongly favour passive accretion. This is because low-mass objects would be relatively metal-poor, and many such in-falling objects would impact at arbitrary angles imparting no net angular momentum, while increasing the  $\sigma_z$ .

### 2.6.4 Resolved Studies and Galaxy Formation Simulations

By exploiting the intrinsic, spatially-resolved properties of our model, we can begin to compare directly to results from resolved studies of the Milky-Way and Local Group, as well as cosmological hydrodynamical galaxy formation simulations. This allows us to leverage the look-back capabilities of the simulations as well as the resolving power of the local observations in order to strengthen the interpretation of our results. Moreover, by extending the intrinsic correlations seen in the Milky Way to external galaxies, we begin to gauge how unique the Milky Way is.

Age-velocity dispersion relations have been found in many resolved (Nordström et al., 2004; Grieves et al., 2018) and simulated (Martig et al., 2014) studies. They primarily conclude that stars born earlier have a higher velocity dispersion compared to those formed later. The underlying physical cause of this relation, however, has evaded a general consensus in the literature. Some scenarios broadly claim that the increase in velocity dispersion is a dynamical effect of internal interactions that build up over time, with a number of different specific mechanisms being proposed as the culprit. Since the older stars have been experiencing these interactions for a longer period of time, they should therefore show the

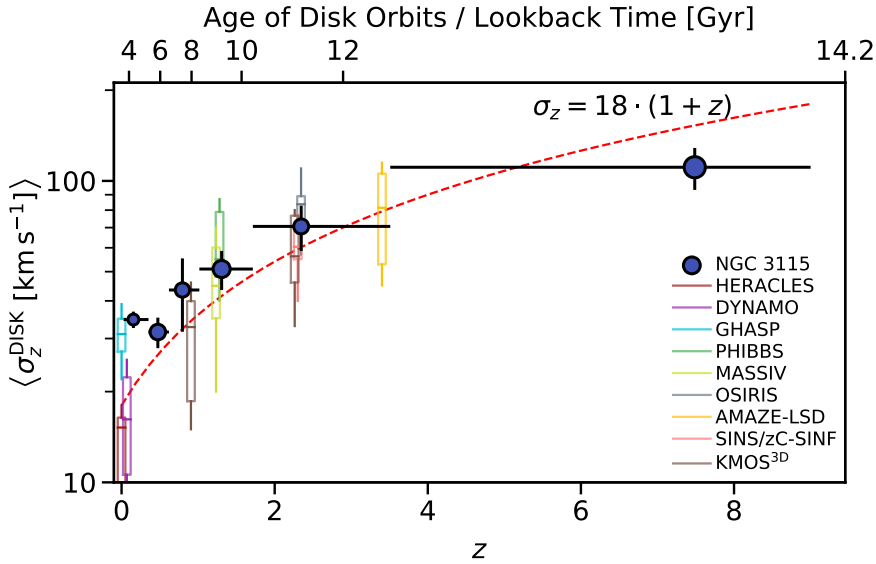


FIGURE 2.14: The vertical component of the intrinsic velocity dispersion of the orbits associated with the disk region (see text) of NGC 3115 (data points) as a function of redshift. These data are computed as the average of the radial profiles for the components with  $\lambda_z > 0.5$  and high metallicity. The data points are the centres of the age bins, vertical errorbars show the magnitude of the variation of each profile with radius, while horizontal errorbars show the widths of the age bins. The formation redshifts are approximated from the stellar ages assuming standard  $\Lambda$ CDM cosmology. The size of each point is proportional to the mass contained in that bin. Literature measurements are shown as box and whiskers according to the legend, and the red dashed line shows the  $18 \cdot (1 + z)$  evolution from Wisnioski et al. (2015) – though we note that these measurements are of *star-forming, gaseous* disks.

largest increase in velocity dispersion. Evidence in favour of such internal mechanisms has come from both observations (Yu and Liu, 2018) and simulations (Saha et al., 2010; Grand et al., 2016; Aumer et al., 2016). An alternative explanation is that in the early Universe, conditions were generally more chaotic (Wisnioski et al., 2015), so that any stars born at that time were more likely to have higher velocity dispersion. As conditions gradually settled over cosmic time, stars were being born in progressively lower-dispersion conditions. A number of studies have identified the conditions at birth as the dominant effect in determining a population’s present-day velocity dispersion, again both from resolved observations (Leaman et al., 2017) and simulations (Bird et al., 2013; Ma et al., 2017). Finally, the comparison between observations and simulations in Pinna et al. (2018) has identified the underlying complexity and inherent degeneracy in discriminating between these scenarios. They claim that many of the effects described above likely play a role to a varying degree, and that the imprint of some mechanisms fade over time, further complicating any attempt to constrain the physical cause of disk heating.

Our model allows us to estimate the intrinsic age-velocity dispersion relation, even though NGC 3115 is unresolved. It can be seen from Fig. 2.13 that, at fixed metallicity (the enriched components in particular), there is a mild increase in velocity dispersion with age, notably at all radii. This is quantified in Fig. 2.14, for the disk region of our model. To isolate this region, we make a conservative cut in circularity of  $\lambda_z > 0.5$  in order to exclude the most pressure-supported orbits, as well as select the highest metallicity bins. Owing to how distinct our methodology is for the derivation of these data, comparison to other works is complicated. Specifically, observations of the stellar velocity dispersion across redshift are difficult to obtain. We therefore look for qualitative comparisons to other works. For instance,

Wisnioski et al. (2015) measured, and compiled literature observations of, the *gas* velocity dispersion as a function of redshift. These data are taken from a range of surveys containing galaxies with  $\log_{10}(M_*/M_\odot) \in [10.1, 11.0]$ . We include these data in Fig. 2.14, which are specifically from HERACLES (Leroy et al., 2009), DYNAMO (Green et al., 2014), GHASP (Epinat et al., 2010), PHIBBS (Tacconi et al., 2013), MASSIV (Epinat et al., 2012), OSIRIS (Law et al., 2009), AMAZE-LSD (Gnerucci et al., 2011), SINS (Schreiber et al., 2009) and zC-SINF (Schreiber et al., 2014), and KMOS<sup>3D</sup> (Wisnioski et al., 2015). Pillepich et al. (2019) investigate both the gaseous and stellar velocity dispersion as a function of redshift in the IllustrisTNG cosmological simulations for *star-forming* galaxies. They find the same general redshift evolution as we see here for both gas and stars in their simulations. We emphasise here, however, that the data types, galaxy types, and techniques for measuring the velocity dispersion are not directly comparable between these three works. Both Wisnioski et al. (2015) and Pillepich et al. (2019) study ensemble population properties of gas and/or stellar kinematics in star-forming galaxies, while we consider only the stellar kinematics of a single, relatively-quiescent galaxy. Nevertheless, that the shape of this redshift evolution is so consistent between these works suggests that it is robust.

Interestingly, we also see in Fig. 2.13 an increase in velocity dispersion towards more metal-poor components, even at fixed age and again at all radii. This implies that metallicity has a significant contribution to the increase in  $\sigma_z$ , which is obscured when considering age at fixed metallicity as in Fig. 2.14, or when marginalising over all metallicities as in Fig. 2.C.1.

We can thus further constrain the physical mechanism driving the age-velocity dispersion relation by leveraging the formation scenario we've established in the previous sections. Following the reasoning in § 2.6.2, the presence of a relatively cold, yet very old disk implies an upper limit on how much internal ‘heating’ could have occurred in this galaxy, since such heating would gradually inflate the scale height of the disk’s old stellar population over the galaxy’s lifetime. Furthermore, any internal dynamical interactions that drive an increase in  $\sigma_z$  over time should be completely impartial to the metallicity of those stars. This is inconsistent with the rather significant change in  $\sigma_z$  with metallicity at fixed age in our model. Finally, if we interpret at face value the absolute agreement between our stellar velocity dispersion evolution and that of gas measurements in Fig. 2.14, this suggests that the stars inherited their dynamical properties from the gas and there was little-to-no subsequent evolution. Once again, this is suggestive of minimal, if any, amounts of disk heating throughout the entire evolutionary history of NGC 3115. Therefore, while we can not make strong conclusions about the true physical interpretation of the age-velocity dispersion relation, nor definitively exclude *any* disk heating over the lifetime of the galaxy, our model indicates that the conditions at birth have the most dominant impact on a population of star’s present day velocity dispersion.

## 2.6.5 Non-Axisymmetric Structures

The possibility of a bar-like structure and associated resonances within NGC 3115 has been discussed in the literature (Kormendy and Richstone, 1992, 1995; Guérou et al., 2016). These works all conclude that there is tentative evidence for such structures, but they can neither confirm nor refute their definitive existence. Guérou et al. (2016) finds many coincident kinematic features that would indicate the presence of a bar. They show, however, that a simple *N*-body model without a bar is able to reproduce these features. We can investigate our dynamical model for evidence of kinematic signatures indicative of a bar. We find no such evidence in the orbital composition, which is dominated by short-axis tube orbits everywhere,

with only a small gradual increase in the contribution from box orbits towards the centre. Our model reproduces the positive correlation between  $V$  and  $h3$  in the central off-axis region that is usually associated with a bar, despite being built in a static gravitational potential. We conclude therefore, as Guérout et al. (2016), that a bar is not strictly necessary to form this feature, but whose existence can not be conclusively ruled out by our model.

In general, the box/long-axis-tube orbits are a unique feature of a triaxial model, and the presence of a small fraction of these orbits towards the centre of our best-fit model implies a degree of triaxiality – and may also imply a bar. We measure a very small constant oblate-triaxiality over the full model of  $T = (1-p^2)/(1-q^2) = 0.042$ , with  $p = b/a$  and  $q = c/a$ , for the major, intermediate, and minor axis lengths,  $a$ ,  $b$ , and  $c$ , respectively. Despite the slight increase in non-axisymmetric orbits towards the centre, there is no corresponding increase in triaxiality. However, we note here that the potential for strong triaxiality is limited in our model, since we have fixed the intrinsic shape  $u = 0.999$ , and are using a projected mass model which has only a single position angle. More accurate constraints on the triaxiality would thus require relaxing both of these assumptions.

We therefore find that while our static triaxial model is able to fully reproduce the kinematics, conclusive evidence of a bar (or otherwise) would require a more direct modelling approach including a tumbling time-variable gravitational potential, such as the NMAGIC made-to-measure models (De Lorenzi et al., 2007; Morganti and Gerhard, 2012). More importantly for the general method presented here, Zhu et al. (2018b) showed that even for an intrinsically barred galaxy, this triaxial Schwarzschild code is able to accurately recover the underlying orbital distribution for the non-bar/resonance regions.

## 2.7 Conclusions

In this work, we have presented the application of a conceptually-new approach for the deduction of formation histories from IFU observations of external unresolved galaxies. We extracted and presented stellar kinematics and stellar-population properties across a  $\sim 240''$  FOV of a nearby S0 galaxy, NGC 3115. By fitting detailed Schwarzschild orbit-superposition dynamical models to the kinematics, we defined components within the galaxy that are dynamically distinct. These components were then assigned a mean stellar age and metallicity in order to reproduce the observed stellar population properties. This combination of spatial resolution, kinematics, and stellar populations allows us establish a complete history of the formation of NGC 3115:

- We find that in the early gas-rich Universe, cold streams funnelled into the core of the progenitor of NGC 3115 early in its formation. These streams caused the compaction of the bulge and its mild metallicity gradient
- The remaining gas from this event cooled and formed stars, which began shortly after the compaction phase. Star formation continued (though declining) through to the youngest stars on the coldest orbits and with the highest metallicity
- Meanwhile, many low-mass satellites were being accreted, fleshing out the halo/thick-disk with low-metallicity material, gradually converting NGC 3115 into its present-day early-type lenticular morphology

More generally, we have combined the stellar dynamics and populations in a comprehensive and self-consistent manner. This has allowed us to empirically conclude that conventional

galactic decomposition techniques – with few components – are unable to simultaneously fit a galaxy’s shape, kinematics, and stellar populations, unless gradients are considered. We have also determined that in the case of NGC 3115, the conditions in which a population of stars forms has the dominant effect on their observed present-day kinematics. This approach amounts to a significant step towards a completely simultaneous population-dynamical model, that will drive progress in the field of galaxy formation with remarkable detail and accuracy. In future work, we will incorporate other stellar-population parameters (namely, spatially-resolved measurements of the IMF and abundances) to further improve the accuracy of the combined model presented here.

This method is currently being tested on mock data in order to estimate the reliability of such an approach. Leveraging the simulations will also inform this methodology on which physical properties are the most important for discriminating between the different formation paths that built up the galaxy. Finally, the successful application of this methodology to a sample of galaxies in different environments will be able to uncover the dominating mechanism(s) of formation during these galaxies’ histories.

## Acknowledgements

We thank Adrien Guerou and Eric Emsellem for providing the reduced and calibrated MUSE data cube and the photometric MGE model, as well as for the stimulating discussion. We thank Emily Wisnioski for providing the literature measurements for Fig. 2.14. RMcD is the recipient of an Australian Research Council Future Fellowship (project number FT150100333). LZ acknowledges support from Shanghai Astronomical Observatory, Chinese Academy of Sciences under grant NO.Y895201009. GvdV acknowledges funding from the European Research Council (ERC) under the European Union’s Horizon 2020 research and innovation programme under grant agreement No 724857 (Consolidator Grant ArcheoDyn). We acknowledge support from the Australia-Germany Joint Research Cooperation Scheme funded by Universities Australia and the German Academic Exchange Service (DAAD). This work makes use of the `queenebee` compute cluster at Max-Planck-Institut für Astronomie, and the `OzStar` supercomputer at Swinburne University. The software used for data analysis include `MATPLOTLIB` (Hunter, 2007), `ASTROPY` (Astropy Collaboration et al., 2013), and the `SciPY` collection (Virtanen et al., 2020). We finally thank the anonymous referee, whose feedback greatly improved the clarity of this work.



# Bibliography

- Alton, P. D., Smith, R. J., and Lucey, J. R. (2017). *Monthly Notices of the Royal Astronomical Society*, Volume 468, Issue 2, p.1594-1615 468, pages 1594–1615. doi: 10.1093/mnras/stx464.
- Aniyan, S. et al. (2016). *Monthly Notices of the Royal Astronomical Society*, Volume 456, Issue 2, p.1484-1494 456, pages 1484–1494. doi: 10.1093/mnras/stv2730.
- Aniyan, S. et al. (2018). *Monthly Notices of the Royal Astronomical Society* 476(2), pages 1909–1930. issn: 0035-8711. doi: 10.1093/mnras/sty310.
- Annunziatella, M. et al. (2017). *The Astrophysical Journal* 851(2), page 81. issn: 0004-637X. doi: 10.3847/1538-4357/aa9845.
- Arnold, J. A. et al. (2011). *The Astrophysical Journal Letters*, Volume 736, Issue 2, article id. L26, 5 pp. (2011). 736, page L26. doi: 10.1088/2041-8205/736/2/L26.
- Astropy Collaboration et al. (2013). *Astronomy and Astrophysics* 558, A33. issn: 0004-6361. doi: 10.1051/0004-6361/201322068.
- Athanassoula, E. et al. (2016). *The Astrophysical Journal*, Volume 821, Issue 2, article id. 90, 17 pp. (2016). 821, page 90. doi: 10.3847/0004-637X/821/2/90.
- Aumer, M., Binney, J., and Schönrich, R. (2016). *Monthly Notices of the Royal Astronomical Society* 462, pages 1697–1713. doi: 10.1093/mnras/stw1639.
- Barbosa, C. E. et al. (2016). *Astronomy & Astrophysics*, Volume 589, id.A139, 16 pp. 589, A139. doi: 10.1051/0004-6361/201628137.
- Battaglia, G. et al. (2006). *Astronomy and Astrophysics*, Volume 447, Issue 1, February III 2006, pp.49-62 447, pages 49–62. doi: 10.1051/0004-6361:20053210.
- Bekki, K. and Couch, W. J. (2011). *Monthly Notices of the Royal Astronomical Society*, Volume 415, Issue 2, pp. 1783-1796. 415, pages 1783–1796. doi: 10.1111/j.1365-2966.2011.18821.x.
- Bellstedt, S. et al. (2018). *Monthly Notices of the Royal Astronomical Society* 476(4), pages 4543–4564. issn: 0035-8711. doi: 10.1093/mnras/sty456.
- Bird, J. C. et al. (2013). *The Astrophysical Journal* 773(1), page 43. issn: 0004-637X. doi: 10.1088/0004-637X/773/1/43.
- Boroson, T. (1981). *The Astrophysical Journal Supplement Series* 46, pages 177–209. doi: 10.1086/190742.
- Brodie, J. P. et al. (2012). *The Astrophysical Journal* 759(2), page L33. issn: 2041-8205. doi: 10.1088/2041-8205/759/2/L33.
- Cantiello, M. et al. (2014). *Astronomy & Astrophysics*, Volume 564, id.L3, 8 pp. 564, page L3. doi: 10.1051/0004-6361/201323272.
- Cappellari, M. (2016). *Annual Review of Astronomy and Astrophysics* 54(1), pages 597–665. issn: 0066-4146. doi: 10.1146/annurev-astro-082214-122432.
- Cappellari, M. (2017). *Monthly Notices of the Royal Astronomical Society*, Volume 466, Issue 1, p.798-811 466, pages 798–811. doi: 10.1093/mnras/stw3020.

- Cappellari, M. and Copin, Y. (2003). *Monthly Notice of the Royal Astronomical Society, Volume 342, Issue 2, pp. 345-354.* 342, pages 345–354. doi: 10.1046/j.1365-8711.2003.06541.x.
- Cappellari, M. and Emsellem, E. (2004). *Publications of the Astronomical Society of the Pacific* 116(816), page 138. issn: 1538-3873. doi: 10.1086/381875.
- Cappellari, M. et al. (2006). *Monthly Notices of the Royal Astronomical Society, Volume 366, Issue 4, pp. 1126-1150.* 366, pages 1126–1150. doi: 10.1111/j.1365-2966.2005.09981.x.
- Cappellari, M. et al. (2012). *Nature, Volume 484, Issue 7395, pp. 485-488 (2012).* 484, pages 485–488. doi: 10.1038/nature10972.
- Cappellari, M. et al. (2013). *Monthly Notices of the Royal Astronomical Society, Volume 432, Issue 3, p.1709-1741* 432(3), pages 1709–1741. issn: 0035-8711. doi: 10.1093/mnras/stt562.
- Carignan, C., Sancisi, R., and van Albada, T. S. (1988). *The Astronomical Journal* 95, pages 37–44. issn: 0004-6256. doi: 10.1086/114610.
- Cinzano, P. and van der Marel, R. P. (1993). *Structure, Dynamics and Chemical Evolution of Elliptical Galaxies. ESO Conference and Workshop Proceedings, Proceedings of an ESO/EIPC Workshop, Marciana Marina, Isola d'Elba, 25-30 May, 1992, Garching: European Southern Observatory (ESO), 1993, edited by I. John Danziger, W. W. Zeilinger, and Kurt Kjaer, p.105 45*, page 105. url: <http://adsabs.harvard.edu/abs/1993ESOC...45..105C>.
- Coccato, L. et al. (2015). *Astronomy & Astrophysics, Volume 581, id.A65, 10 pp.* 581, A65. doi: 10.1051/0004-6361/201526560.
- Coccato, L. et al. (2018). *Monthly Notices of the Royal Astronomical Society* 477(2), pages 1958–1969. issn: 0035-8711. doi: 10.1093/mnras/sty705.
- Conroy, C. and Dokkum, P. G. van (2012). *The Astrophysical Journal* 760(1), page 71. issn: 0004-637X. doi: 10.1088/0004-637X/760/1/71.
- Conroy, C., Graves, G. J., and Dokkum, P. G. van (2013). *The Astrophysical Journal* 780(1), page 33. issn: 0004-637X. doi: 10.1088/0004-637X/780/1/33.
- Corbelli, E. and Salucci, P. (2000). *Monthly Notices of the Royal Astronomical Society, Volume 311, Issue 2, pp. 441-447.* 311, pages 441–447. doi: 10.1046/j.1365-8711.2000.03075.x.
- Cretton, N. et al. (1999). *The Astrophysical Journal Supplement Series* 124(2), page 383. issn: 0067-0049. doi: 10.1086/313264.
- Dalla Bontà, E. et al. (2018). *Monthly Notices of the Royal Astronomical Society* 474(1), pages 339–387. issn: 0035-8711. doi: 10.1093/mnras/stx2477.
- Davis, T. A. and McDermid, R. M. (2017). *Monthly Notices of the Royal Astronomical Society* 464(1), pages 453–468. issn: 0035-8711. doi: 10.1093/mnras/stw2366.
- De Lorenzi, F. et al. (2007). *Monthly Notices of the Royal Astronomical Society* 376(1), pages 71–88. issn: 0035-8711. doi: 10.1111/j.1365-2966.2007.11434.x.
- Dejonghe, H. (1987). *Monthly Notices of the Royal Astronomical Society* 224(1), pages 13–39. issn: 0035-8711. doi: 10.1093/mnras/224.1.13.
- Dekel, A. et al. (2009). *Nature* 457(7228), pages 451–454. issn: 1476-4687. doi: 10.1038/nature07648.
- Di Teodoro, E. M. et al. (2019). *Monthly Notices of the Royal Astronomical Society* 483(1), pages 392–406. issn: 0035-8711. doi: 10.1093/mnras/sty3095.
- Diaz, J. et al. (2018). *Monthly Notices of the Royal Astronomical Society* 477(2), pages 2030–2041. issn: 0035-8711. doi: 10.1093/mnras/sty743.
- Dimauro, P. et al. (2018). *Monthly Notices of the Royal Astronomical Society* 478(4), pages 5410–5426. issn: 0035-8711. doi: 10.1093/mnras/sty1379.

- Dries, M. et al. (2018). *Monthly Notices of the Royal Astronomical Society* 474(3), pages 3500–3515. ISSN: 0035-8711. doi: 10.1093/mnras/stx2979.
- Eliche-Moral, M. C. et al. (2018). *Astronomy & Astrophysics* 617, A113. ISSN: 0004-6361, 1432-0746. doi: 10.1051/0004-6361/201832911.
- Emsellem, E., Monnet, G., and Bacon, R. (1994). *Astronomy and Astrophysics, Vol. 285, p.723-738 (1994)* 285, pages 723–738. URL: <https://ui.adsabs.harvard.edu/abs/1994A&A...285..723E>.
- Emsellem, E., Dejonghe, H., and Bacon, R. (1999). *Monthly Notices of the Royal Astronomical Society* 303(3), pages 495–514. ISSN: 0035-8711. doi: 10.1046/j.1365-8711.1999.02210.x.
- Emsellem, E. et al. (2007). *Monthly Notices of the Royal Astronomical Society* 379(2), pages 401–417. ISSN: 0035-8711. doi: 10.1111/j.1365-2966.2007.11752.x.
- Epinat, B. et al. (2010). *Monthly Notices of the Royal Astronomical Society* 401(4), pages 2113–2147. ISSN: 0035-8711. doi: 10.1111/j.1365-2966.2009.15688.x.
- Epinat, B. et al. (2012). *Astronomy & Astrophysics* 539, A92. ISSN: 0004-6361, 1432-0746. doi: 10.1051/0004-6361/201117711.
- Falcón-Barroso, J. et al. (2011). *Astronomy & Astrophysics* 532, A95. ISSN: 0004-6361, 1432-0746. doi: 10.1051/0004-6361/201116842.
- Fraser-Mckelvie, A. et al. (2018). *Monthly Notices of the Royal Astronomical Society* 481(4), pages 5580–5591. ISSN: 0035-8711. doi: 10.1093/mnras/sty2563.
- Gallazzi, A. et al. (2008). *Monthly Notices of the Royal Astronomical Society* 383(4), pages 1439–1458. ISSN: 0035-8711. doi: 10.1111/j.1365-2966.2007.12632.x.
- Gentile, G. et al. (2004). *Monthly Notices of the Royal Astronomical Society* 351(3), pages 903–922. ISSN: 0035-8711. doi: 10.1111/j.1365-2966.2004.07836.x.
- Girardi, L. et al. (2000). *Astronomy and Astrophysics Supplement Series* 141(3), pages 371–383. ISSN: 0365-0138, 1286-4846. doi: 10.1051/aas:2000126.
- Gnerucci, A. et al. (2011). *Astronomy & Astrophysics* 528, A88. ISSN: 0004-6361, 1432-0746. doi: 10.1051/0004-6361/201015465.
- Grand, R. J. J. et al. (2016). *Monthly Notices of the Royal Astronomical Society* 459(1), pages 199–219. ISSN: 0035-8711. doi: 10.1093/mnras/stw601.
- Graves, G. J., Faber, S. M., and Schiavon, R. P. (2009a). *The Astrophysical Journal* 693(1), pages 486–506. ISSN: 0004-637X. doi: 10.1088/0004-637X/693/1/486.
- Graves, G. J., Faber, S. M., and Schiavon, R. P. (2009b). *The Astrophysical Journal* 698(2), pages 1590–1608. ISSN: 0004-637X. doi: 10.1088/0004-637X/698/2/1590.
- Green, A. W. et al. (2014). *Monthly Notices of the Royal Astronomical Society* 437(2), pages 1070–1095. ISSN: 0035-8711. doi: 10.1093/mnras/stt1882.
- Greene, J. E. et al. (2015). *The Astrophysical Journal* 807(1), page 11. ISSN: 0004-637X. doi: 10.1088/0004-637X/807/1/11.
- Grieves, N. et al. (2018). *Monthly Notices of the Royal Astronomical Society* 481(3), pages 3244–3265. ISSN: 0035-8711. doi: 10.1093/mnras/sty2431.
- Guérou, A. et al. (2016). *Astronomy & Astrophysics* 591, A143. ISSN: 0004-6361, 1432-0746. doi: 10.1051/0004-6361/201628743.
- Hunter, J. D. (2007). *Computing in Science and Engineering, vol. 9, no. 3, pp. 90-95* 9(3), pages 90–95. doi: 10.1109/MCSE.2007.55.
- Jardel, J. R. and Gebhardt, K. (2012). *The Astrophysical Journal* 746(1), page 89. ISSN: 0004-637X. doi: 10.1088/0004-637X/746/1/89.
- Johnston, E. J. et al. (2012). *Monthly Notices of the Royal Astronomical Society, Volume 422, Issue 3, pp. 2590-2599*. 422, pages 2590–2599. doi: 10.1111/j.1365-2966.2012.20813.x.

- Kent, S. M. (1985). *The Astrophysical Journal Supplement Series* 59, pages 115–159. doi: 10.1086/191066.
- Kormendy, J. (1979). *The Astrophysical Journal* 227, pages 714–728. issn: 0004-637X, 1538-4357. doi: 10.1086/156782.
- Kormendy, J. and Ho, L. C. (2013). *Annual Review of Astronomy and Astrophysics* 51(1), pages 511–653. issn: 0066-4146. doi: 10.1146/annurev-astro-082708-101811.
- Kormendy, J. and Richstone, D. (1992). *The Astrophysical Journal* 393, page 559. issn: 0004-637X, 1538-4357. doi: 10.1086/171528.
- Kormendy, J. and Richstone, D. (1995). *Annual Review of Astronomy and Astrophysics* 33, page 581. issn: 0066-4146. doi: 10.1146/annurev.aa.33.090195.003053.
- Krajnović, D. et al. (2005). *Monthly Notices of the Royal Astronomical Society* 357(4), pages 1113–1133. issn: 0035-8711. doi: 10.1111/j.1365-2966.2005.08715.x.
- Krajnović, D. et al. (2013). *Monthly Notices of the Royal Astronomical Society, Volume 432, Issue 3, p.1768-1795* 432(3), pages 1768–1795. issn: 0035-8711. doi: 10.1093/mnras/sts315.
- Krajnović, D. et al. (2015). *Monthly Notices of the Royal Astronomical Society* 452(1), pages 2–18. issn: 0035-8711. doi: 10.1093/mnras/stv958.
- Krajnović, D. et al. (2018). *Monthly Notices of the Royal Astronomical Society* 477(3), pages 3030–3064. issn: 0035-8711. doi: 10.1093/mnras/sty778.
- Kroupa, P. (2002). *Science* 295(5552), pages 82–91. issn: 0036-8075, 1095-9203. doi: 10.1126/science.1067524.
- Kuntschner, H. et al. (2010). *Monthly Notices of the Royal Astronomical Society* 408(1), pages 97–132. issn: 0035-8711. doi: 10.1111/j.1365-2966.2010.17161.x.
- Laurikainen, E. et al. (2013). *Monthly Notices of the Royal Astronomical Society* 430(4), pages 3489–3509. issn: 0035-8711. doi: 10.1093/mnras/stt150.
- Law, D. R. et al. (2009). *The Astrophysical Journal* 697(2), pages 2057–2082. issn: 0004-637X. doi: 10.1088/0004-637X/697/2/2057.
- Leaman, R. et al. (2017). *Monthly Notices of the Royal Astronomical Society* 472(2), pages 1879–1896. issn: 0035-8711. doi: 10.1093/mnras/stx2014.
- Leroy, A. K. et al. (2009). *The Astronomical Journal* 137(6), pages 4670–4696. issn: 1538-3881. doi: 10.1088/0004-6256/137/6/4670.
- Li, H. et al. (2017). *The Astrophysical Journal* 838(2), page 77. issn: 0004-637X. doi: 10.3847/1538-4357/aa662a.
- Li, H. et al. (2018). *Monthly Notices of the Royal Astronomical Society* 476(2), pages 1765–1775. issn: 0035-8711. doi: 10.1093/mnras/sty334.
- Lidman, C. et al. (2013). *Monthly Notices of the Royal Astronomical Society* 433(1), pages 825–837. issn: 0035-8711. doi: 10.1093/mnras/stt777.
- Long, R. J. and Mao, S. (2018). *Research in Astronomy and Astrophysics* 18(12), page 145. issn: 1674-4527. doi: 10.1088/1674-4527/18/12/145.
- Lyubenova, M. et al. (2016). *Monthly Notices of the Royal Astronomical Society* 463(3), pages 3220–3225. issn: 0035-8711. doi: 10.1093/mnras/stw2434.
- Ma, X. et al. (2017). *Monthly Notices of the Royal Astronomical Society* 467(2), pages 2430–2444. issn: 0035-8711. doi: 10.1093/mnras/stx273.
- Martig, M., Minchev, I., and Flynn, C. (2014). *Monthly Notices of the Royal Astronomical Society* 443(3), pages 2452–2462. issn: 0035-8711. doi: 10.1093/mnras/stu1322.
- Martín-Navarro, I. et al. (2015). *The Astrophysical Journal* 806(2), page L31. issn: 2041-8205. doi: 10.1088/2041-8205/806/2/L31.

- Martín-Navarro, I. et al. (2018). *Monthly Notices of the Royal Astronomical Society* 475(3), pages 3700–3729. ISSN: 0035-8711. doi: 10.1093/mnras/stx3346.
- McDermid, R. M. et al. (2015). *Monthly Notices of the Royal Astronomical Society, Volume 448, Issue 4, p.3484-3513* 448(4), pages 3484–3513. ISSN: 0035-8711. doi: 10.1093/mnras/stv105.
- Mehlert, D. et al. (2003). *Astronomy & Astrophysics* 407(2), pages 423–435. ISSN: 0004-6361, 1432-0746. doi: 10.1051/0004-6361:20030886.
- Méndez-Abreu, J. et al. (2017). *Astronomy & Astrophysics* 598, A32. ISSN: 0004-6361, 1432-0746. doi: 10.1051/0004-6361/201629525.
- Mentz, J. J. et al. (2016). *Monthly Notices of the Royal Astronomical Society* 463(3), pages 2819–2838. ISSN: 0035-8711. doi: 10.1093/mnras/stw2129.
- Mitzkus, M., Cappellari, M., and Walcher, C. J. (2017). *Monthly Notices of the Royal Astronomical Society* 464(4), pages 4789–4806. ISSN: 0035-8711. doi: 10.1093/mnras/stw2677.
- Monnet, G., Bacon, R., and Emsellem, E. (1992). *Astronomy and Astrophysics* 253, pages 366–373. ISSN: 0004-6361. URL: <http://adsabs.harvard.edu/abs/1992A%26A...253..366M>.
- Morganti, L. and Gerhard, O. (2012). *Monthly Notices of the Royal Astronomical Society* 422(2), pages 1571–1585. ISSN: 0035-8711. doi: 10.1111/j.1365-2966.2012.20733.x.
- Moriondo, G., Giovanardi, C., and Hunt, L. K. (1998). *Astronomy and Astrophysics Supplement Series* 130(1), pages 81–108. ISSN: 0365-0138, 1286-4846. doi: 10.1051/aas:1998408.
- Navarro, J. F., Frenk, C. S., and White, S. D. M. (1996). *The Astrophysical Journal* 462, page 563. ISSN: 0004-637X. doi: 10.1086/177173.
- Noordermeer, E. et al. (2007). *Monthly Notices of the Royal Astronomical Society* 376(4), pages 1513–1546. ISSN: 0035-8711. doi: 10.1111/j.1365-2966.2007.11533.x.
- Nordström, B. et al. (2004). *Astronomy & Astrophysics* 418(3), pages 989–1019. ISSN: 0004-6361, 1432-0746. doi: 10.1051/0004-6361:20035959.
- Norris, M. A., Sharples, R. M., and Kuntschner, H. (2006). *Monthly Notices of the Royal Astronomical Society* 367(2), pages 815–824. ISSN: 0035-8711. doi: 10.1111/j.1365-2966.2005.09992.x.
- Oldham, L. J. and Auger, M. W. (2018). *Monthly Notices of the Royal Astronomical Society* 474, pages 4169–4185. doi: 10.1093/mnras/stx2969.
- Oser, L. et al. (2010). *The Astrophysical Journal* 725(2), pages 2312–2323. ISSN: 0004-637X. doi: 10.1088/0004-637X/725/2/2312.
- Parikh, T. et al. (2018). *Monthly Notices of the Royal Astronomical Society* 477(3), pages 3954–3982. ISSN: 0035-8711. doi: 10.1093/mnras/sty785.
- Pastorello, N. et al. (2014). *Monthly Notices of the Royal Astronomical Society* 442(2), pages 1003–1039. ISSN: 0035-8711. doi: 10.1093/mnras/stu937.
- Pillepich, A. et al. (2019). *Monthly Notices of the Royal Astronomical Society* 490(3), pages 3196–3233. ISSN: 0035-8711. doi: 10.1093/mnras/stz2338.
- Pinna, F. et al. (2018). *Monthly Notices of the Royal Astronomical Society* 475(2), pages 2697–2712. ISSN: 0035-8711. doi: 10.1093/mnras/stx3331.
- Poci, A., Cappellari, M., and McDermid, R. M. (2017). *Monthly Notices of the Royal Astronomical Society* 467(2), pages 1397–1413. ISSN: 0035-8711. doi: 10.1093/mnras/stx101.
- Poetrodjojo, H. et al. (2018). *Monthly Notices of the Royal Astronomical Society* 479(4), pages 5235–5265. ISSN: 0035-8711. doi: 10.1093/mnras/sty1782.
- Press, W. et al. (2007). Cambridge University Press. ISBN: 978-0-521-88068-8. URL: <https://books.google.com.au/books?id=1aAOdzK3FegC>.

- Querejeta, M. et al. (2015). *Astronomy & Astrophysics* 579, page L2. issn: 0004-6361, 1432-0746. doi: 10.1051/0004-6361/201526354.
- Rosani, G. et al. (2018). *Monthly Notices of the Royal Astronomical Society* 476(4), pages 5233–5252. issn: 0035-8711. doi: 10.1093/mnras/sty528.
- Saha, K. and Cortesi, A. (2018). *The Astrophysical Journal* 862(1), page L12. issn: 2041-8205. doi: 10.3847/2041-8213/aad23a.
- Saha, K., Tseng, Y.-H., and Taam, R. E. (2010). *The Astrophysical Journal* 721(2), pages 1878–1890. issn: 0004-637X. doi: 10.1088/0004-637X/721/2/1878.
- Salpeter, E. E. (1955). *Astrophysical Journal*, vol. 121, p.161 121, page 161. doi: 10.1086/145971.
- Sánchez-Blázquez, P. et al. (2006). *Monthly Notices of the Royal Astronomical Society* 371(2), pages 703–718. issn: 0035-8711. doi: 10.1111/j.1365-2966.2006.10699.x.
- Sánchez-Blázquez, P. et al. (2007). *Monthly Notices of the Royal Astronomical Society* 377(2), pages 759–786. issn: 0035-8711. doi: 10.1111/j.1365-2966.2007.11647.x.
- Sarzi, M. et al. (2018). *Monthly Notices of the Royal Astronomical Society* 478(3), pages 4084–4100. issn: 0035-8711. doi: 10.1093/mnras/sty1092.
- Schreiber, N. M. F. et al. (2009). *The Astrophysical Journal* 706(2), pages 1364–1428. issn: 0004-637X. doi: 10.1088/0004-637X/706/2/1364.
- Schreiber, N. M. F. et al. (2014). *The Astrophysical Journal* 787(1), page 38. issn: 0004-637X. doi: 10.1088/0004-637X/787/1/38.
- Schwarzchild, M. (1979). *Astrophysical Journal, Part 1*, vol. 232, Aug. 15, 1979, p. 236-247. 232, pages 236–247. doi: 10.1086/157282.
- Scorza, C. and Bender, R. (1995). *Astronomy and Astrophysics*, Vol. 293, p.20-43 (1995) 293, pages 20–43. url: <https://ui.adsabs.harvard.edu/abs/1995A&A...293...20S>.
- Scorza, C. et al. (1998). *Astronomy and Astrophysics Supplement Series* 131(2), pages 265–286. issn: 0365-0138, 1286-4846. doi: 10.1051/aas:1998432.
- Seth, A. C. et al. (2014). *Nature* 513(7518), pages 398–400. issn: 1476-4687. doi: 10.1038/nature13762.
- Simard, L. et al. (2011). *The Astrophysical Journal Supplement Series* 196(1), page 11. issn: 0067-0049. doi: 10.1088/0067-0049/196/1/11.
- Smith, R. J., Lucey, J. R., and Carter, D. (2012). *Monthly Notices of the Royal Astronomical Society, Volume 426, Issue 4*, pp. 2994-3007. 426, pages 2994–3007. doi: 10.1111/j.1365-2966.2012.21922.x.
- Sofue, Y. (2017). *Publications of the Astronomical Society of Japan* 69, R1. doi: 10.1093/pasj/psw103.
- Somerville, R. S. and Davé, R. (2015). *Annual Review of Astronomy and Astrophysics* 53(1), pages 51–113. doi: 10.1146/annurev-astro-082812-140951.
- Souza, R. E. de, Gadotti, D. A., and Anjos, S. dos (2004). *The Astrophysical Journal Supplement Series* 153(2), page 411. issn: 0067-0049. doi: 10.1086/421554.
- Streich, D. et al. (2016). *Astronomy & Astrophysics* 585, A97. issn: 0004-6361, 1432-0746. doi: 10.1051/0004-6361/201526013.
- Strom, S. E. et al. (1976). *Astrophysical Journal* 204, pages 684–693. url: <https://ui.adsabs.harvard.edu/abs/1976ApJ...204..684S/abstract>.
- Swaters, R. A. et al. (2012). *Monthly Notices of the Royal Astronomical Society* 425(3), pages 2299–2308. issn: 0035-8711. doi: 10.1111/j.1365-2966.2012.21599.x.
- Tabor, M. et al. (2017). *Monthly Notices of the Royal Astronomical Society, Volume 466, Issue 2*, p.2024-2033 466, pages 2024–2033. doi: 10.1093/mnras/stw3183.

- Tacconi, L. J. et al. (2013). *The Astrophysical Journal* 768(1), page 74. issn: 0004-637X. doi: 10.1088/0004-637X/768/1/74.
- Tapia, T. et al. (2017). *Astronomy & Astrophysics* 604, A105. issn: 0004-6361, 1432-0746. doi: 10.1051/0004-6361/201628821.
- Thomas, D. et al. (2005). *The Astrophysical Journal, Volume 621, Issue 2, pp. 673-694.* 621, pages 673–694. doi: 10.1086/426932.
- Thomas, J. et al. (2011). *Monthly Notices of the Royal Astronomical Society, Volume 415, Issue 1, pp. 545-562.* 415, pages 545–562. doi: 10.1111/j.1365-2966.2011.18725.x.
- Tonry, J. L. et al. (2001). *The Astrophysical Journal* 546(2), page 681. issn: 0004-637X. doi: 10.1086/318301.
- Tortora, C. et al. (2019). *Monthly Notices of the Royal Astronomical Society*, stz2320. issn: 0035-8711, 1365-2966. doi: 10.1093/mnras/stz2320.
- van Albada, T. S. et al. (1985). *The Astrophysical Journal* 295, pages 305–313. doi: 10.1086/163375.
- van de Ven, G., De Zeeuw, P. T., and Van Den Bosch, R. C. E. (2008). *Monthly Notices of the Royal Astronomical Society* 385(2), pages 614–646. issn: 0035-8711. doi: 10.1111/j.1365-2966.2008.12873.x.
- van den Bosch, R. C. E. et al. (2008). *Monthly Notices of the Royal Astronomical Society* 385(2), pages 647–666. issn: 0035-8711. doi: 10.1111/j.1365-2966.2008.12874.x.
- van der Marel, R. P. et al. (1998). *The Astrophysical Journal* 493(2), page 613. issn: 0004-637X. doi: 10.1086/305147.
- Vaughan, S. P. et al. (2018). *Monthly Notices of the Royal Astronomical Society* 475(1), pages 1073–1092. issn: 0035-8711, 1365-2966. doi: 10.1093/mnras/stx3199.
- Vazdekis, A. et al. (2010). *Monthly Notices of the Royal Astronomical Society*. issn: 00358711, 13652966. doi: 10.1111/j.1365-2966.2010.16407.x.
- Virtanen, P. et al. (2020). *Nature Methods* 17(3), pages 261–272. issn: 1548-7105. doi: 10.1038/s41592-019-0686-2.
- Walcher, C. J. et al. (2015). *Astronomy & Astrophysics* 582, A46. issn: 0004-6361, 1432-0746. doi: 10.1051/0004-6361/201525924.
- Watkins, L. L. et al. (2013). *Monthly Notices of the Royal Astronomical Society* 436(3), pages 2598–2615. issn: 0035-8711. doi: 10.1093/mnras/stt1756.
- Wisnioski, E. et al. (2015). *The Astrophysical Journal* 799(2), page 209. issn: 0004-637X. doi: 10.1088/0004-637X/799/2/209.
- Yu, J. and Liu, C. (2018). *Monthly Notices of the Royal Astronomical Society* 475(1), pages 1093–1103. issn: 0035-8711. doi: 10.1093/mnras/stx3204.
- Zhu, L. et al. (2016a). *Monthly Notices of the Royal Astronomical Society* 463(1), pages 1117–1135. issn: 0035-8711. doi: 10.1093/mnras/stw2081.
- Zhu, L. et al. (2016b). *Monthly Notices of the Royal Astronomical Society* 462(4), pages 4001–4017. issn: 0035-8711. doi: 10.1093/mnras/stw1931.
- Zhu, L. et al. (2018a). *Monthly Notices of the Royal Astronomical Society* 473(3), pages 3000–3018. issn: 0035-8711. doi: 10.1093/mnras/stx2409.
- Zhu, L. et al. (2018b). *Nature Astronomy* 2(3), pages 233–238. issn: 2397-3366. doi: 10.1038/s41550-017-0348-1.
- Zolotov, A. et al. (2015). *Monthly Notices of the Royal Astronomical Society, Volume 450, Issue 3, p.2327-2353* 450, pages 2327–2353. doi: 10.1093/mnras/stv740.



# Appendices

Surface Density [ $M_\odot \text{ pc}^{-2}$ ]	Dispersion [arcsec]	Axis Ratio
5623394.70903	0.03032	0.77577
357987.40788	0.11242	0.91562
172654.34365	0.23796	0.85209
234126.41656	0.48308	0.13169
111845.72296	0.74309	0.68875
140311.08130	1.19400	0.16491
100124.68062	2.01498	0.51298
38315.21897	3.84575	0.56651
10990.86889	8.73513	0.59807
12437.27038	14.37909	0.08915
4097.35539	16.31765	0.48822
2438.79282	26.88008	0.12718
1679.17630	44.55499	0.31224
465.76916	77.95736	0.38720
175.55995	120.52598	0.55757
21.59472	249.74553	0.71771

TABLE 2.A.1: The counts, widths, and axis ratios of the Gaussians in our  $\text{MGE}_\Sigma$  model.

## Appendix 2.A Mass Surface Density MGE

We present in Tab. 2.A.1 the MGE fit to the mass surface-density ‘image’ described in § 2.4.1, which requires 16 Gaussians in order to accurately describe the mass distribution.

## Appendix 2.B Regularisation in the Dynamical Star-Formation History

By fitting the spatially-resolved luminosity-weighted maps of stellar-population properties (described in § 2.4.5) with a given number of dynamical components, there is inevitably some level of degeneracy between solutions to Eq. (2.7), which increases with increasing  $N_{\text{comp.}}$ . In order to reduce the impact of this degeneracy on the analyses that followed, we implemented a linear regularisation into the BVLS fit. This regularisation, as is widely used in astrophysical problems, penalises solutions which vary sharply in the parameter-space under consideration. For instance, regularisation in the context of Schwarzschild dynamical models would penalise solutions which have significantly different contributions from neighbouring orbits that have similar physical properties. The motivation for this is that most physical systems should undergo changes in their properties smoothly across physical parameters, rather than discretely.

In our application of regularisation to Eq. (2.7), we wish to impose a smoothness in the distribution of ages and metallicities that are assigned to the dynamically-selected components. In this way, we prefer solutions (which would otherwise be degenerate) that assign similar stellar-population properties to dynamical components that have similar physical properties.

For the regularisation, we minimise a linear approximation (as it is a linear problem) to the integral of the second-order Laplacian. Given in §19.5 of Press et al. (2007), this can be

expressed as the following:

$$\int \left[ \vec{\phi}''(x) \right]^2 dx \propto \sum_{\mu=0}^{N_{\text{comp}}-3} \left[ -\phi_\mu + 2\phi_{\mu+1} - \phi_{\mu+2} \right]^2 \quad (2.10)$$

for the solution vector of unknowns,  $\vec{\phi}$ , of length  $N_{\text{comp}}$ .

(2.11)

This formalism assumes that sequential  $\mu$  are adjacent in the physical parameters of interest – in the case of our dynamically-selected components, this means neighbouring in  $\lambda_z$  and  $R$ . However, as seen in Fig. 2.7, this is not the case for some components; where sequential labels wrap around to the next column, they have significantly different physical properties. In order to retain the information about which components are truly adjacent in physical properties, and avoid regularising over non-neighbouring components, we instead construct a 2D and 3D regularisation matrix for the dynamical components and orbits, respectively (which are defined by 2 and 3 parameters, respectively). This matrix preserves the second-order Laplacian given in Eq. (2.10) for each dimension, and is unique for every set of  $[\mu, \mu+2]$ . In order to apply the matrix to the BVLS fit, it is flattened into a single row in the same way in which the components and orbits are reduced to a single dimension along the  $N_{\text{comp}}$  axis of Eq. (2.7). In this way, the location of the regularisation constraints preserves the memory of which components are neighbouring in physical parameters. Since Eq. (2.10) affects only 3 components, this operation is repeated for each set of  $[\mu, \mu+2]$ , adding a row to Eq. (2.7) each time. In practise it is implemented in an analogous fashion to what is described in Cappellari (2016). The effect of this is illustrated in Fig. 2.B.1, which compares a completely free, unregularised fit with a regularised fit which was used for the results presented in this work. This figure illustrates that the regularisation does indeed act in the desired way, by producing ‘smoother’ variations between the grid cells, compared to the unregularised fit. Importantly, there is a statistically-insignificant difference between the  $\chi^2$  values of the two fits, implying the regularisation is indeed acting only to break the degeneracy.

## Appendix 2.C Marginalised Intrinsic Velocity Dispersion Profiles

In Figures 2.C.1 and 2.C.2, we present the radial profiles of the intrinsic vertical velocity dispersion for the dynamically-selected components of our model, binned only in age, and only in metallicity, respectively.

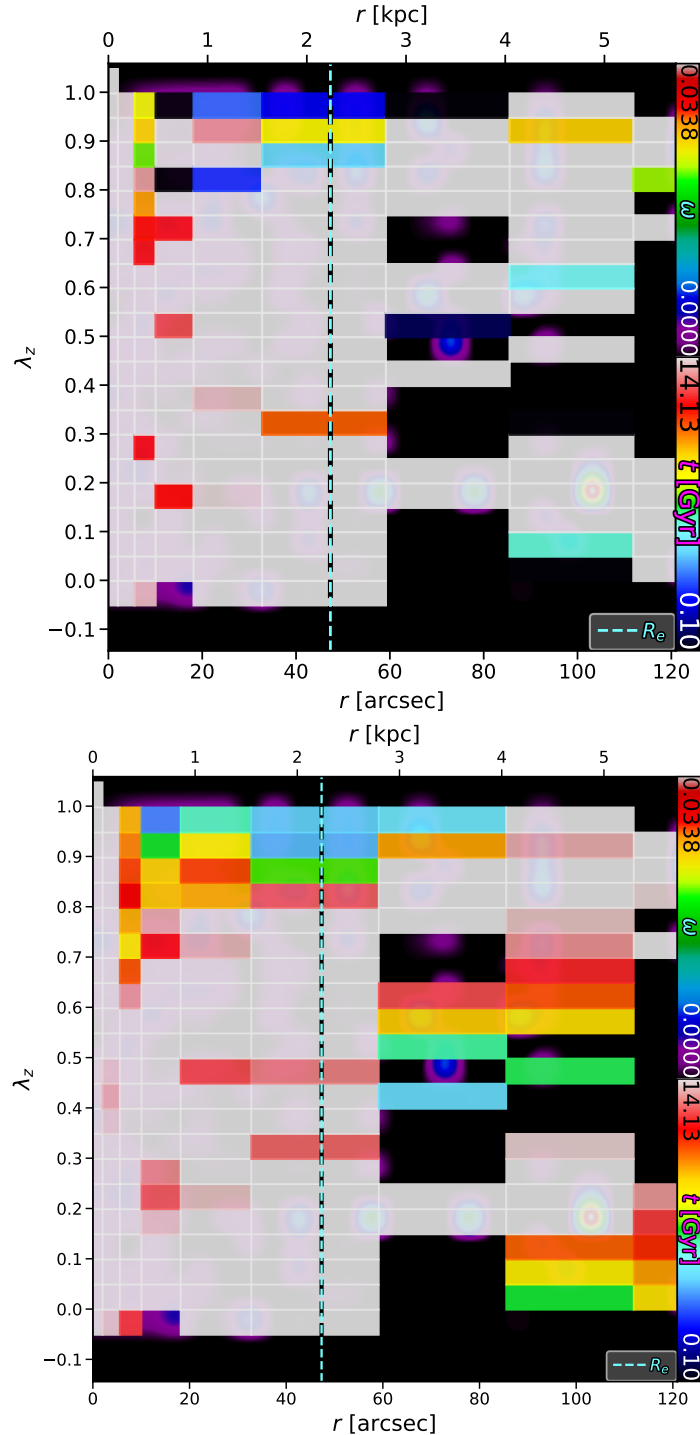


FIGURE 2.B.1: The circularity phase-space, as shown in Fig. 2.7, but where the components are additionally coloured by their assigned mean stellar age. The top panel shows an unregularised fit, while the bottom panel shows the regularisation that was used throughout this work.

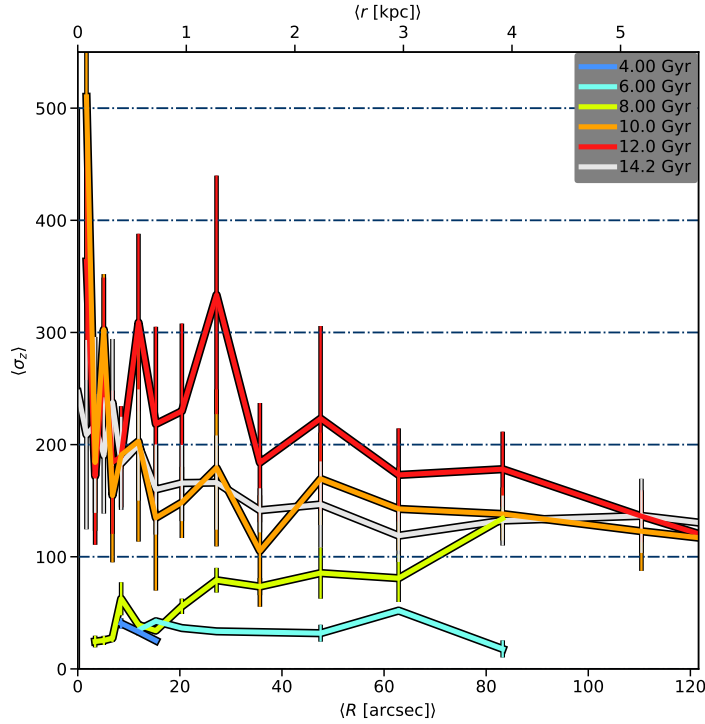


FIGURE 2.C.1: Radial profiles of the intrinsic vertical velocity dispersion for dynamical components binned by their mean stellar age (averaged over metallicities). The absolute stellar mass of each bin is given in Fig. 2.11. As with Fig. 2.13, the variance within the annuli are shown as errorbars.

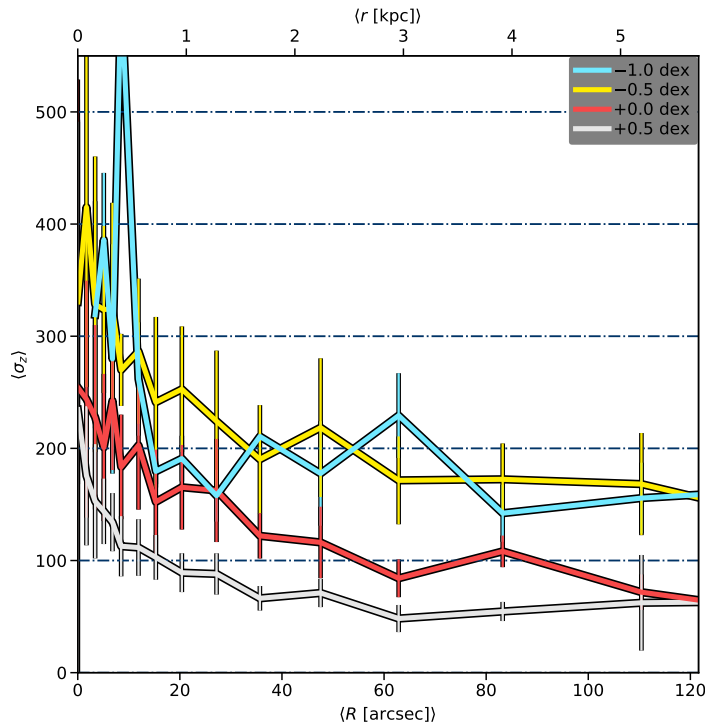


FIGURE 2.C.2: As Fig. 2.C.1, but binned by mean stellar metallicity (averaged over ages).The absolute stellar mass of each bin is given in Fig. 2.12.



---

## CHAPTER 3

---

# **THE FORNAX3D PROJECT: ASSEMBLY HISTORIES OF LENTICULAR GALAXIES FROM A COMBINED DYNAMICAL AND POPULATION ORBITAL ANALYSIS**

This chapter is a verbatim reproduction of the work published in

Poci, A. et al. (2021). “The Fornax3D Project: Assembly Histories of Lenticular Galaxies from a Combined Dynamical and Population Orbital Analysis”. *Astronomy & Astrophysics*. ISSN: 0004-6361, 1432-0746. doi: 10.1051/0004-6361/202039644

## Abstract

In order to assess the impact of the environment on the formation and evolution of galaxies, accurate assembly histories of such galaxies are needed. However, these measurements are observationally difficult owing to the diversity of formation paths that lead to the same present-day state of a galaxy. In this work, we apply a powerful new technique in order to observationally derive accurate assembly histories through a self-consistent combined stellar dynamical and population galaxy model. We present this approach for three edge-on lenticular galaxies from the Fornax3D project — FCC 153, FCC 170, and FCC 177 — in order to infer their mass assembly histories individually and in the context of the Fornax cluster. The method was tested on mock data from simulations to quantify its reliability. We find that the galaxies studied here have all been able to form dynamically-cold (intrinsic vertical velocity dispersion  $\sigma_z \lesssim 50 \text{ km s}^{-1}$ ) stellar disks after cluster infall. Moreover, the pre-existing (old) high angular momentum components have retained their angular momentum (orbital circularity  $\lambda_z > 0.8$ ) through to the present day. Comparing the derived assembly histories with a comparable galaxy in a low-density environment — NGC 3115 — we find evidence for cluster-driven suppression of stellar accretion and merging. We measured the intrinsic stellar age–velocity-dispersion relation and find that the shape of the relation is consistent with galaxies in the literature across redshift. There is tentative evidence for enhancement in the luminosity-weighted intrinsic vertical velocity dispersion due to the cluster environment. But importantly, there is an indication that metallicity may be a key driver of this relation. We finally speculate that the cluster environment is responsible for the S0 morphology of these galaxies via the gradual external perturbations, or ‘harassment’, generated within the cluster.

### 3.1 Introduction

Galaxy formation and evolution is the culmination of competing forces and processes over each galaxy’s lifetime. These processes can be internal to the galaxy, such as the energy generated by the central super-massive black hole (SMBH) or the winds generated by star formation. They can also have external origins, such as the gravitational potential of other galaxies (Toomre and Toomre, 1972) or cosmic gas filaments. Due to this ‘superposition’ of evolutionary processes, it is difficult to isolate the impact on the galaxy from only one of them, especially when many are still occurring. The environment which a galaxy inhabits has long been suspected of altering its evolutionary path (Gunn and Gott, 1972; Dressler, 1980; Postman and Geller, 1984; Ryden et al., 1993), but with conflicting results on the exact impact. Field environments are relatively simple and provide a control sample for comparison with higher-density environments such as groups and clusters. This comparison is not straight forward, however, since cluster environments are a complex mixture of many, often dramatic, physical processes such as gravitational disruption (owing to the significantly deeper gravitational potential), hydrodynamic effects due to the hot intra-cluster medium (ICM), and thermodynamic effects such as shocks due to the high relative velocities that a galaxy can experience when it first encounters the ICM during in-fall.

A number of correlations have been observed between galactic observables and some metric for the local environment. Historically, the projected density of galaxies or  $N$ -th nearest neighbour measurements of the local density have been found to correlate with visual morphology (e.g. Dressler, 1980; Cappellari et al., 2011b; Oh et al., 2018; Gargiulo et al., 2019) and invoked to explain morphological transformations (e.g. Bekki et al., 2002; Kauffmann et al., 2004; Blanton et al., 2005; D’Onofrio et al., 2015; Coccato et al., 2020). Yet morphology has also been observed to correlate with stellar mass at fixed local density (van der Wel, 2008), and so the underlying cause is difficult to discern. This problem permeates through most observed correlations. Some works have shown that galaxies exhibit a lower net angular momentum for a higher local density (e.g. Cappellari et al., 2011a; Cortese et al., 2019; Graham et al., 2019; Cole et al., 2020), while others find that there is no additional dependence on the environment once the correlation between the angular momentum and stellar mass is accounted for (Brough et al., 2017). Finally, the stellar population parameters also suffer from conflicting correlations. Some observations indicate reduced star-formation activity (e.g. Balogh et al., 2004; Poggianti et al., 2006; Allen et al., 2016; Owers et al., 2019), a higher stellar metallicity (e.g. Schaefer et al., 2019), older stellar ages (e.g. Thomas et al., 2005; McDermid et al., 2015), and a lower gas content (e.g. Zabel et al., 2019) for higher local density, while others indicate that stellar mass is the driver instead of environment (Alpaslan et al., 2015; Goddard et al., 2017). Many of these correlations have also been found in recent cosmological hydrodynamical simulations (e.g. Choi et al., 2018; Wang et al., 2018a; Wang et al., 2018b). More broadly, it is not straight forward to disentangle the effects of mass and environment, and it is likely that both play a role (Peng et al., 2010; Smith et al., 2012; McDermid et al., 2015; Wang et al., 2020), and joint analyses over all available parameters are needed such as those applied by Christlein and Zabludoff (2005) to global galaxy properties. The morphology, mass, and other galactic properties are intricately connected through each galaxy’s unique assembly history. It is therefore clear that to uncover what impact the environment has, if any, the complete assembly history must be investigated directly as a function of the environment.

The dynamical memory of galaxies plays an important role in attempting to disentangle such assembly histories, assisted by the (often long) dynamical times of galactic systems. As

such, the stellar kinematics can provide insight into this history. Dynamical models of stellar kinematics have been employed to measure constraints on galaxy formation for a variety of morphological types and environments, based on a number of different principles. The Jeans equations have been readily applied owing to their relative simplicity and computational efficiency (e.g. Cappellari et al., 2013; Watkins et al., 2013; Zhu et al., 2016b,a; Poci et al., 2017; Bellstedt et al., 2018; Nguyen et al., 2019; Nitschai et al., 2020; Li et al., 2020 and Cappellari, 2016 for a review), though with specific assumptions about the intrinsic velocity distributions of galaxies. Distribution-function models (e.g. Cole and Binney, 2017; Taranu et al., 2017; Pascale et al., 2018) can be quite general and computationally-efficient, but usually use parametric expressions which may not provide enough freedom. Finally, the Schwarzschild (1979) orbit-superposition method provides a general approach without the assumption of specific distribution functions or density distributions, while also providing a wealth of information on the intrinsic properties of the model. Though it is far more computationally-expensive, it has seen a growing diversity of applications (e.g. van der Marel et al., 1998; Cretton et al., 1999; Verolme and de Zeeuw, 2002; Gebhardt et al., 2003; Valluri et al., 2004; Cappellari et al., 2006; Krajnović et al., 2009, 2015; Vasiliev, 2013, 2019; Leung et al., 2018; Zhu et al., 2018b,a; Vasiliev and Valluri, 2020). Through these models, a galaxy’s merger history can be traced through the potentially-complex observed kinematics, but only when confronted with a sufficiently-sophisticated dynamical model which can access the underlying intrinsic properties (e.g. van den Bosch et al., 2008; Lyubenova et al., 2013; Krajnović et al., 2015). However, purely-dynamical models can not produce a chronological assembly history, since they lack information about the ages of the stars and where they might have originated.

This work is part of the Fornax3D survey; an observational programme to study the Fornax galaxy cluster with the Multi-Unit Spectroscopic Explorer (MUSE) at VLT. In total, the survey observed 31 members of the Fornax cluster with  $m_B < 15$  mag, at or interior to the Virial radius ( $R_{\text{vir}} \sim 0.7$  Mpc; Drinkwater et al., 2001). Fornax is a well-surveyed (Drinkwater et al., 2001; Jordán et al., 2007; Davies et al., 2013; Muñoz et al., 2015; Iodice et al., 2016; Pota et al., 2018; Sarzi et al., 2018; Zabel et al., 2019; Scott et al., 2020) galaxy cluster at a distance  $D \sim 20$  Mpc, and with a total halo mass of  $\log_{10}(M_{\text{halo}}/\text{M}_\odot) \sim 13.85$  (Jordán et al., 2007). The application of the Schwarzschild models to Fornax3D data was showcased in Sarzi et al. (2018), and a qualitative comparison to the stellar populations was made in Martín-Navarro et al. (2019). In this work, we aim to measure complete chronological histories of three edge-on S0 galaxies – FCC 153, FCC 170, and FCC 177 – by quantitatively combining these sophisticated dynamical modelling techniques with the measured stellar populations. They are discussed in conjunction with a previous application of this method (Poci et al., 2019) to a massive [ $\log_{10}(M_\star/\text{M}_\odot) \sim 11$ ] field S0, NGC 3115, to probe any potential impact of the cluster environment.

This work is organised as follows: the data and target selection are briefly outlined in § 3.2, and the combined dynamical and population modelling is detailed in § 3.3. Results for each galaxy are presented in § 3.4. The implications of these results in the context of the Fornax cluster and specific quantitative correlations are investigated in § 3.5.

## 3.2 Data and Targets

### 3.2.1 Photometry

The photometric data for this work is taken from the Fornax Deep Survey (FDS; Iodice et al., 2016; Venhola et al., 2018), which acquired deep photometry of the Fornax cluster out to  $R_{\text{vir}}$  in the  $u$ ,  $g$ ,  $r$ , and  $i$  bands using the Very Large Telescope (VLT) Survey Telescope (VST). We utilise the  $r$ -band photometry to model the surface brightness distribution of these galaxies. We also make use of the  $g - i$  colour to characterise the mass distribution beyond the field-of-view (FOV) of the spectroscopy (see § 3.3.1). FDS data extend down to a surface brightness of  $\mu_r \sim 28$  mag arcsec $^{-2}$  in the  $r$  band. Distances to these galaxies were measured in Blakeslee et al. (2009) via surface-brightness fluctuations. We adopt those measurements here, given in Tab. 3.1.

### 3.2.2 Spectroscopy

The spectral data are taken from the Fornax3D project (Sarzi et al., 2018). In this work, all data products are computed on the spectral range  $\lambda \in [4600, 6700]$  Å. This range avoids the problematic sky emission lines and telluric effects. It is wide enough, however, to include many of the important absorption features for the stellar population analyses. Moreover it encapsulates the bandwidth of the  $r$  filter of VST which is utilised in conjunction with the spectroscopy to describe the luminosity density of the stellar kinematic tracer. To prepare the data products, the data-cubes are spatially binned to a target signal-to-noise ratio ( $S/N$ ) of 100 using the Python implementation\* of the Voronoi binning technique (Cappellari and Copin, 2003). This ensures that the kinematic and stellar-population measurements can achieve measurement errors  $\lesssim 5\%$  (shown in § 3.B).

Kinematics are extracted for each binned spectrum using the pPXF (Cappellari and Emsellem, 2004; Cappellari, 2017) Python package†, which determines the line-of-sight velocity distribution (LOSVD) through moments of the Gauss-Hermite series. We extract the first six moments of the LOSVD in each bin; mean velocity  $V$ , velocity dispersion  $\sigma$ , skewness  $h_3$ , kurtosis  $h_4$ , and higher-order deviations  $h_5$  and  $h_6$ . pPXF is run with the MILES empirical stellar library (Falcón-Barroso et al., 2011), and with an additive polynomial of degree 10 in order to accurately reproduce the line shapes. Naturally, spectra are dominated by the brightest components of the observed galaxies through the LOS, and so the extracted kinematics are effectively luminosity-weighted.

Star formation histories (SFH) and their mean stellar population properties are extracted by running pPXF with the E-MILES single stellar population (SSP) templates (Vazdekis et al., 2016) using the ‘BaSTI’ isochrone models (Pietrinferni et al., 2004). A multiplicative polynomial of degree 10 is included in order to account for the continuum without affecting the relative line shapes. The SSP models are normalised such that we measure luminosity-weighted stellar populations, in order to maintain consistency with the stellar kinematics and subsequent dynamical model (described in § 3.3.2). The stellar-population fits use a first-derivative linear regularisation with  $\Delta = 1.0$ , which prefers a smoother solution in the case of degeneracy between the SSP models. We assume a fixed Kroupa (2002) galaxy initial mass function (IMF). The canonical Salpeter (1955) IMF has been shown to disagree with the mass-to-light ratios from stellar dynamics (Lyubenova et al., 2016), while the low central

\*Available at <https://pypi.org/project/vorbin/>

†Available at <https://pypi.org/project/ppxf/>

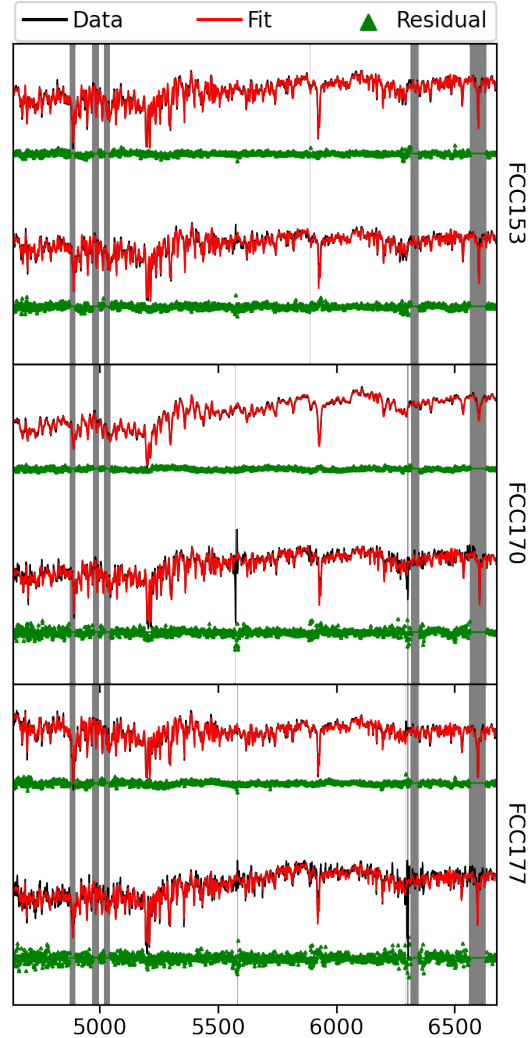


FIGURE 3.1: Fits (red) to spectra (black) from the centre and outer regions (top and bottom of each pair of spectra, respectively) for our galaxy sample, as labelled on the right. Residuals are shown in green, offset for presentation. The grey bands show regions which are masked during the fit. All spectra are normalised, but vertically offset for presentation. It can be seen that the outer spectra are more noisy, as expected, but that in all cases the data are reproduced well by the fit.

velocity dispersion of these galaxies (Iodice et al., 2019b) is consistent with an IMF which is relatively deficient of dwarf stars (e.g. Thomas et al., 2011; Cappellari et al., 2012; Wegner et al., 2012). In this work, we explore the projected distribution of mean stellar age ( $t$ ) and metallicity (total metal abundance,  $[Z/H]$ ). Representative spectral fits are presented in Fig. 3.1.

The solutions from the stellar-population run of pPXF and the predictions from E-MILES (Vazdekis et al., 2010) then enable the derivation of the  $R$ -band stellar mass-to-light ratio ( $M_\star/L_R$ ) for each spectrum, using the mass in stars and stellar remnants for the assumed IMF. This is utilised for the dynamical modelling (§ 3.3.1). We generate Monte Carlo fits to the spectra by adding random noise within the variance spectra in the data-cubes. Each spectrum is re-fit 100 times to generate a new distribution of SSP weights. Luminosity-weighted properties are re-derived for each weight distribution. The ‘uncertainty’ in a given aperture is then estimated from the variance of luminosity-weighted properties across all Monte Carlo simulations in that aperture. These uncertainty maps (shown in § 3.B) are utilised to gauge the stability of our final results.

Similar data products have already been measured for these galaxies as part of Fornax3D (Pinna et al., 2019a,b; Iodice et al., 2019b). The motivation for re-extracting them in this work is to achieve higher  $S/N$  for higher-precision stellar population parameters (see, for instance, Asa'd and Goudfrooij, 2020) and to minimise the impact of measuring  $\sigma_{\text{los}} \lesssim \sigma_{\text{inst}}$

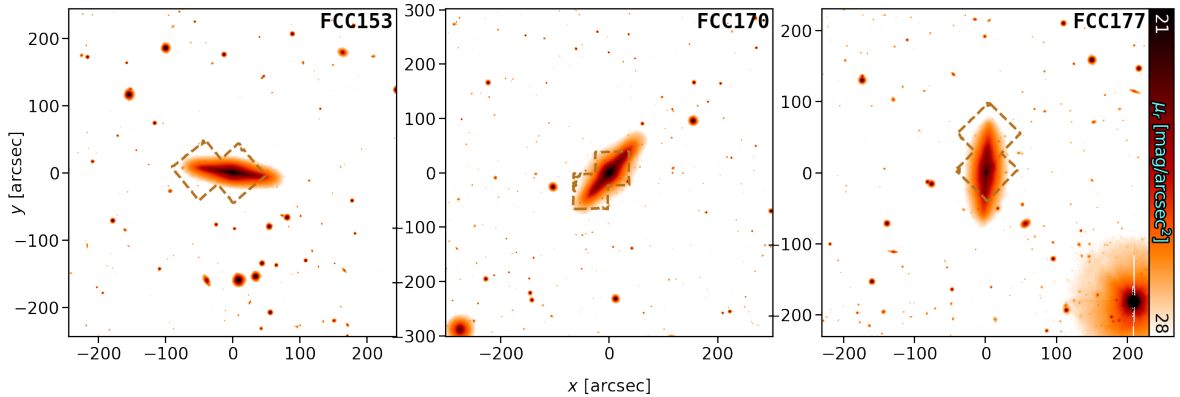


FIGURE 3.2: Full  $r$ -band images from FDS, overlaid with the MUSE FOV in dashed brown for FCC 153 (*left*), FCC 170 (*middle*), and FCC 177 (*right*).

(for the line-of-sight velocity dispersion and instrumental velocity resolution  $\sigma_{\text{los}}$  and  $\sigma_{\text{inst}}$ , respectively; Cappellari, 2017), albeit on larger spatial bins. Moreover, we fit the specific wavelength range, as discussed above. Finally, luminosity-weighted stellar populations are required for the analyses in this work as described above, while previous measurements are mass-weighted (Pinna et al., 2019a,b). The new kinematics from this work are consistent with previous measurements. The luminosity-weighted ages are systematically younger than the mass-weighted determinations while the metallicities are consistent, as expected (Serra and Trager, 2007; McDermid et al., 2015).

### 3.2.3 Targets

For this work, due to the nature of our dynamical and population orbital analysis (§ 3.3), we selected a sub-sample of three galaxies: FCC 153, FCC 170, and FCC 177. These galaxies are all approximately edge-on, and have S0 morphology. They are suitable targets for our analysis because they show no signs of dust or spiral arms. This is important because the dynamical model assumes a steady-state gravitational potential while spiral arms are transient, and dust would impact the inferences of the stellar populations. Additionally, our methodology (§ 3.3) is most robust for edge-on systems. Each galaxy has a central and outer pointing from the Fornax3D survey, ensuring that the vast majority of the stellar body is covered while retaining the high spatial resolution of MUSE. The FDS  $r$ -band images of the three galaxies are shown in Fig. 3.2, with the MUSE outline shown in dashed brown. As measured from the FDS data, FCC 153, FCC 170, and FCC 177 are at a projected distance of  $1.17^\circ$ ,  $0.42^\circ$ , and  $0.79^\circ$  from the cluster core, respectively (Iodice et al., 2019a). These galaxies have integrated  $g - i$  colours of  $0.77 \pm 0.07$ ,  $1.07 \pm 0.02$ , and  $1.80 \pm 0.03$ , and  $r$ -band surface-brightness radial profiles which extend down to  $28.9$ ,  $29.2$ , and  $29.5$  mag  $\text{arcsec}^{-2}$ , respectively, as derived from the FDS photometry (Iodice et al., 2019a).

These galaxies are the focus of the spectral analyses presented in Pinna et al. (2019a,b), where their SFH are discussed in the context of the Fornax cluster. Those works conclude that FCC 170 matured more rapidly, having plausibly evolved in an earlier group environment in the initial stages of the Fornax cluster assembly. Conversely, FCC 153 and FCC 177 are seen to exhibit relatively smooth SFH in their thin disk regions. In the study on stellar accretion fractions in members of the Fornax cluster, Spavone et al. (2020) find that it is difficult to photometrically disentangle the various components of these three galaxies, since they have indistinguishable surface brightness profiles. They find that low accretion fractions

( $\lesssim 50\%$ ) are typical for other galaxies at cluster-centric radii similar to FCC 153 and FCC 177. Conversely, for galaxies in the region close to FCC 170, higher accretion fractions ( $\gtrsim 50\%$ ) are derived. We aim, as part of this work, to place constraints on this fraction even for the galaxies which are photometrically degenerate.

### 3.3 Stellar Content of Galaxies

We endeavour to consider the complete stellar information content available through observations. The model we fit to these data was the self-consistent combination of Schwarzschild orbit-superposition dynamical models, using a triaxial implementation (van de Ven et al., 2008; van den Bosch et al., 2008), and stellar-population measurements derived from full spectral fitting. We employed the method described in Poci et al. (2019) for this combination. We therefore refer to that work and references therein for details, but lay out the basic structure of the method and the differences with that work in this section.

We also ensured that our data are tracing the galaxies themselves, and not components of the cluster environment. The FDS data show that FCC 170 is within the large-scale intra-cluster light (ICL) detected towards the cluster centre (Iodice et al., 2019b). This ICL component was measured to have total integrated magnitudes of  $12.1 \pm 0.3$  and  $11.4 \pm 0.3$  in  $g$ - and  $r$ -band, respectively, over an area of  $\sim 432$  arcmin $^2$  (assuming a uniform surface brightness distribution; Iodice et al., 2017). At the distance and direction from the cluster centre to FCC 170, the ICL has a  $r$ -band surface brightness of  $\sim 27.5$  mag arcsec $^{-2}$  (Iodice et al., 2017). In contrast, the spectroscopic data from the Fornax3D survey have a  $r$ -band target depth of 25 mag arcsec $^{-2}$  in the faintest regions covered by the FOV. For our sample, the FOV extend to 4.90, 5.63, and 9.61 kpc along the major axis for FCC 153, FCC 170, and FCC 177, respectively, at our adopted distances (see Tab. 3.1). In all three cases, therefore, we expect the impact of the ICL on the measured properties to be negligible, being at least  $\sim 100$  times fainter than the faintest regions of the galaxies within our spectroscopic FOV.

#### 3.3.1 Stellar Mass Model

One of the most crucial aspects of a dynamical model of stellar kinematics is the input mass model in which the observed tracer population resides. This is often derived from the observed photometry. We begin by fitting a multi-Gaussian Expansion (MGE; Monnet et al., 1992; Emsellem et al., 1994) to the  $r$ -band photometry from FDS using a Python implementation<sup>‡</sup> (Cappellari, 2002). This produces a projected surface-brightness model ( $MGE_\mu$ ), which serves as the luminous tracer of the gravitational potential of the galaxy. These models are shown in § 3.A.

To reconstruct the mass, the surface brightness must be converted into surface mass density. While standard implementations of Schwarzschild (and indeed dynamical) models assume a spatially-constant conversion from luminosity to mass, we exploit the spatially-resolved map of stellar  $M_\star/L_R$  in order to account for the prominent structures and variations in the stellar populations that are resolved by the high-quality spectroscopy. We make additional use of the deep FDS photometry to constrain the stellar populations outside of the spectroscopic FOV to constrain the dynamical model well beyond the measured kinematics. We use the predictions from the E-MILES SSP models to derive a relation between  $g - i$  colours and  $M_\star/L_R$ , which we assume to be of the form  $\log_{10}(M_\star/L_R) \propto (g - i)$  as found

---

<sup>‡</sup>Available at <https://pypi.org/project/mgefit/>

empirically (Tortora et al., 2011; Wilkins et al., 2013; McGaugh and Schombert, 2014; Du and McGaugh, 2020). The smaller spectroscopic FOV, which is used where available, is thus augmented by the larger photometric FOV to generate  $M_\star/L_R$  on the same extent as the photometry. While the spectroscopic measurements of  $M_\star/L_R$  reach  $\lesssim 60''$  for the three galaxies, the depth of the FDS survey allows this coverage to be extended to  $\sim 150''$  providing a dramatic improvement to the constraints of the mass model. Using this large-scale combined (spectroscopic and photometric)  $M_\star/L_R$  map,  $MGE_\mu$  is then converted to a map of surface mass density, to which a mass density MGE ( $MGE_\Sigma$ ) is fit. The fits and results for all  $MGE_\Sigma$  are given in § 3.A. Figures 3.A.1 to 3.A.3 show deviations of up to  $\pm 30\%$  compared to a spatially-constant  $M_\star/L_R$  (in projection). This approach takes into account not just these deviations in the absolute scale, but also the structures of the stellar populations, producing a more accurate mass model and subsequent dynamical model.

The photometric measurements of  $M_\star/L_R$  are effectively ‘SSP-equivalent’, while the spectroscopic values are derived from the full SFH. To mitigate any systematic offsets this may cause, the photometrically-derived values are re-scaled to match the spectroscopic values in the overlapping regions. We emphasise that the rapidly-varying spatial structures in the stellar populations — caused primarily by the thin edge-on disks — are captured by the spectroscopy, while the photometry is utilised only in the region where variations are mild. Coupled with the intrinsic symmetry of the MGE fitting, the photometric  $M_\star/L_R$  serves to extend the range of the MGE model and stabilise the shape of the gravitational potential in that region. It can be seen in Figures 3.A.1 to 3.A.3 that there are no systematic offsets at the transition from spectroscopically- to photometrically-derived  $M_\star/L_R$ , and the level of noise in the colour region is no greater than the pixel-to-pixel scatter in images to which MGE is typically applied. Overall, this procedure allows for the stellar populations to be more robustly accounted for.

### 3.3.2 Schwarzschild Dynamical Models

The basic premise of the Schwarzschild method is to numerically integrate a large number of permitted orbits within a model for the gravitational potential, then measure their kinematics and compare to observations. For real observations, the gravitational potential is of course unknown and must be iteratively fit for. To achieve this, we used a triaxial implementation of the Schwarzschild method that has been robustly developed and validated (van den Bosch et al., 2008; van de Ven et al., 2008; Zhu et al., 2018b,a, 2020; Jin et al., 2019). In this implementation, a single model is described by seven parameters: (a) the three parameters describing the intrinsic shape and viewing direction of the stellar mass distribution,  $q = C/A$ ,  $p = B/A$ , and  $u = A'/A$ , where  $A$ ,  $B$ , and  $C$  are the intrinsic major, intermediate, and minor axes, respectively, and  $A'$  is the projected major axis (b) the mass of the central SMBH,  $M_\bullet$  (c) the parameters of the dark matter (DM) profile, which is implemented as a spherical Navarro-Frenk-White (NFW) model (Navarro et al., 1996). These are the concentration  $C_{\text{DM}}$  and dark mass fraction at  $r_{200}$ ,  $f_{\text{DM}}$  (d) a global dynamical mass-to-light ratio, which we denote  $\Upsilon$ . This parameter can shift the global depth of the potential in order to better match the observed kinematics, but does not change its shape nor therefore which orbital families can reside within it.  $\Upsilon$  is included to account for any deviations in the absolute depth of the gravitational potential due to the assumption of the IMF when computing the  $M_\star/L$  and/or systematics in the assumed DM halo model.

We streamlined the search through this large parameter-space by making reasonable assumptions about some of these parameters. The masses of the SMBH were fixed according

to the empirical  $M_\bullet - \sigma_e$  relation of Kormendy and Ho (2013), using the  $\sigma_e$  measurements for these galaxies reported in Iodice et al. (2019b). In addition, we estimated the sphere of influence  $r_i$  of each SMBH, which is utilised by the model but is not a free parameter, using the relation of van den Bosch et al. (2015). This is expected to have little impact on the model however — for the galaxy with the largest central velocity dispersion, FCC 170,  $r_i \approx 0.08''$ , which is below the pixel scale of MUSE. In addition, the stellar shape parameter  $u$  was fixed to  $u = (1.0 - \epsilon)$  for some small number  $\epsilon$  to avoid numerical issues. This assumption is reasonable since regular fast-rotator galaxies are found to be consistent with oblate intrinsic shapes (Weijmans et al., 2014). We note that mild triaxiality is still permitted in these models, with the condition that the potential must be axisymmetric in projection. The parameter-space is thus reduced to five dimensions;  $q, p, C_{\text{DM}}, f_{\text{DM}}, \Upsilon$ .

Each Schwarzschild model corresponds to a unique intrinsic gravitational potential. The orbital families which can reside within each gravitational potential are therefore also unique. Thus, each location in the hyper-parameter-space is accompanied by its own library of numerically-integrated orbits. These orbits are characterised by the integrals of motion which they conserve, namely the binding energy  $E$ , angular momentum  $I_2$ , and the third non-classical conserved integral  $I_3$ . Each library of orbits was generated by sampling these integrals in  $(E, I_2, I_3) = (30, 20, 10)$  steps (logarithmically for  $E$  and linearly for  $I_2$  and  $I_3$ ; see Cretton et al., 2000, for details of the integral sampling). The region around the best-fit model was re-computed with a higher orbit sampling of  $(E, I_2, I_3) = (60, 30, 15)$  to increase the resolution of the resulting intrinsic properties. To avoid discreteness in these libraries, each orbit was dithered by a factor of 5, creating a cloud of orbits around each  $(E, I_2, I_3)$ . Using a Non-Negative Least-Squares (NNLS; Lawson and Hanson, 1995) fit, the model selects the best sub-set of orbits from each library which reproduces the observed kinematics in projection. It simultaneously fits a boundary constraint, which in this work is the projected luminosity distribution, such that the weights assigned to the orbits during NNLS are luminosity weights. Thus, each unique gravitational potential has a corresponding unique set of best-fit orbits.

By construction,  $\Upsilon$  does not change the shape of the gravitational potential. In a gravitational potential with a fixed shape but varying  $\Upsilon$ , the families of orbits do not change. Rather, the velocities of these orbits are simply scaled up or down to reflect a deeper or more shallow potential, respectively, and the NNLS fit is repeated for the scaled orbits. Therefore only four parameters require the computationally-expensive numerical integration of an orbit library. The five free parameters were optimised using an adaptive grid search, whose direction and step-size depend on the existing set of evaluated models, with a large initial spread to avoid local minima. The search terminated once all surrounding models were worse fits to the data. The kinematic fits are shown in the top seven rows of Figures 3.7 to 3.9. The parameter-space searches and best-fit parameters are presented in § 3.B.

To avoid artificial bias in the model due to systematic asymmetries in the data, the even (odd) kinematic moments were point-(anti)symmetrised to be consistent with the intrinsic model symmetry<sup>§</sup>. These asymmetries present deviations of up to  $\sim 6 \text{ km s}^{-1}$  in velocity and velocity dispersion with respect to the symmetrised kinematics, which is of order the measurement uncertainties on the kinematics. The ‘raw’ un-symmetrised kinematics and their Monte Carlo-derived errors are shown in § 3.B.

The Schwarzschild models allow us to investigate the distribution of mass within these galaxies. Enclosed mass profiles are presented in Fig. 3.3, where the maximum extent of the

---

<sup>§</sup>using the `plotbin` package, available at <https://pypi.org/project/plotbin/>

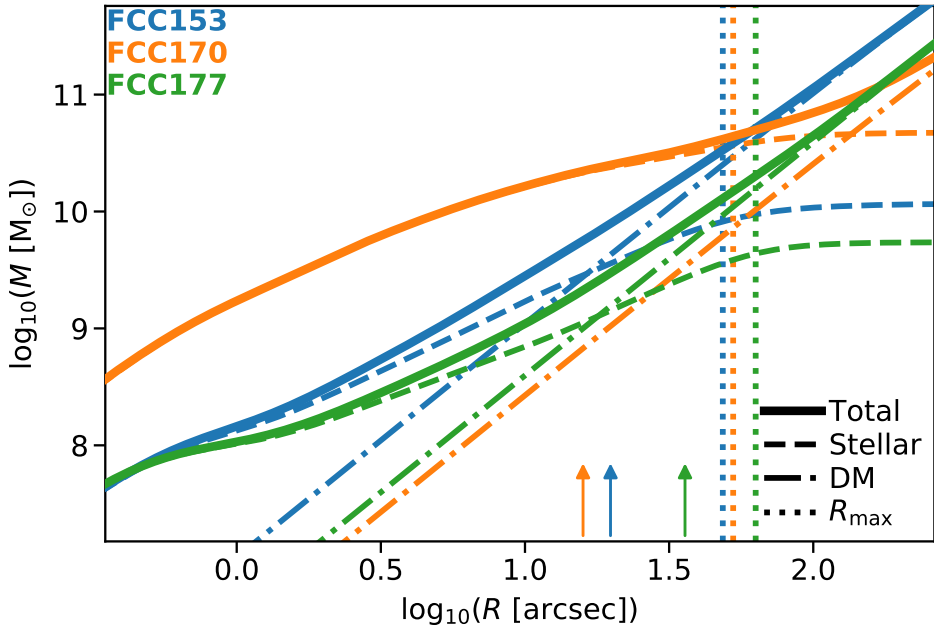


FIGURE 3.3: Enclosed-mass profiles of the total (dynamical) mass (solid line), stellar mass (dashed line), and DM (dot-dashed line) for the three galaxies. The effective radii are denoted by the small arrows, and the radial extent of each spectroscopic FOV is shown by the vertical dotted line. The lower radial bound of the figure is set to half the width of the point-spread function from the spectroscopic observations.

spectroscopy is marked by  $R_{\mathrm{max}}$ , while useful quantities are provided in Tab. 3.1. It can be seen that FCC 170 is baryon-dominated within the spectroscopic FOV, while FCC 153 and FCC 177 transition to DM-dominated at or below their effective radii (given in Tab. 3.1). We also define  $R_{\mathrm{enc}}$ , the spherical radius which encloses 98% of the stellar mass (derived by integrating the stellar mass profile). This reduces the dependence of the mass profile on the lowest surface-brightness (most uncertain) regions. These radii are in good quantitative agreement with the maximum extent of the surface brightness profiles of Spavone et al. (2020). The corresponding stellar and DM masses within  $R_{\mathrm{enc}}$  are denoted by  $M_{\mathrm{enc}}^*$  and  $M_{\mathrm{enc}}^{\mathrm{DM}}$ , respectively. These are given in Tab. 3.1. The amount of stellar mass outside of the spectroscopic FOV can be estimated as  $\log_{10} [M_*(R = R_{\mathrm{max}})/M_*(R = R_{\mathrm{enc}})]$ . This gives 0.12, 0.09, and 0.07 dex, for FCC 153, FCC 170, and FCC 177, respectively. While the mass in this region ( $R_{\mathrm{max}} < R < R_{\mathrm{enc}}$ ) is not directly constrained by the kinematics, it is still constrained by the mass model described in § 3.3.1. We explore these mass distributions further in the sections below.

### 3.3.3 Dynamical Decomposition

From the best-fit dynamical model, we used the phase-space of circularity (Zhu et al., 2018a),  $\lambda_z$ , and cylindrical radius,  $R$ , in order to conduct a dynamical decomposition. This radius represents the time-averaged cylindrical radius of each orbit over its orbital period. The circularity is a normalised measure of the intrinsic orbital angular momentum, and we used it here to divide the Schwarzschild model into orbits with varying degree of rotation ( $|\lambda_z| \sim 1$ ) or pressure ( $\lambda_z \sim 0$ ) support. In order to account for the structure in the kinematics and stellar-population maps simultaneously, and motivated by tests conducted in Poci et al. (2019), we divided the phase-space into many ( $\sim 10^2$ ) ‘components’. This was achieved by imposing

Galaxy	$D$ [Mpc]	$R_e$	$M_e^*$ [log <sub>10</sub> M <sub>⊙</sub> ]	$M_e^{\text{DM}}$ [log <sub>10</sub> M <sub>⊙</sub> ]	$R_{\text{enc}}$	$M_{\text{enc}}^*$ [log <sub>10</sub> M <sub>⊙</sub> ]	$M_{\text{enc}}^{\text{DM}}$ [log <sub>10</sub> M <sub>⊙</sub> ]
(1)	(2)	(3)	(4)	(5)	(6)	(7)	(8)
FCC 153	20.8	19.80'' 2.00 kpc	9.55	9.63	165.78'' 16.72 kpc	10.06	11.43
FCC 170	21.9	15.90'' 1.69 kpc	10.33	8.83	148.39'' 15.76 kpc	10.67	10.74
FCC 177	20.0	35.90'' 3.48 kpc	9.43	9.71	133.347'' 12.93 kpc	9.73	10.84

TABLE 3.1: Physical properties of the galaxy sample. (1) galaxy name (2) distance to the galaxy measured by Blakeslee et al. (2009) using surface-brightness fluctuations (3)  $r$ -band effective radius taken from Iodice et al. (2019a) and converted into physical units at our adopted distances (3) – (4) stellar and DM masses enclosed within  $R_e$ , respectively (5) radius which encloses 98% of the stellar mass (6) – (7) stellar and DM masses enclosed within  $R_{\text{enc}}$ , respectively.

a log-linear grid on the circularity phase-space. The radial axis was sampled logarithmically, but with a floor on the grid size. This preserves the orbital sampling from the Schwarzschild model<sup>¶</sup> but avoids generating cells in the circularity phase-space which are below the spatial resolution of the data. The circularity axis was sampled linearly. This phase-space and corresponding dynamical decompositions are presented in Figures 3.4 to 3.6 for FCC 153, FCC 170, and FCC 177, respectively. This sampling in  $\lambda_z - R$  was used for all three galaxies, however the final distribution of ‘components’ depends on the circularity distribution of each galaxy’s best-fitting Schwarzschild model.

A single component is composed of a unique subset of the orbit library of its parent Schwarzschild model. The decomposition is an effective way of simply bundling orbits of similar properties — in this case, angular momentum and radius. Kinematics, masses, and mass densities are computed for each component individually, based on its specific subset of orbits and those orbits’ relative contribution to the original dynamical model. Thus, each component has fixed projected kinematics and spatial distributions.

### 3.3.4 Adding Stellar Populations

We now describe the extension beyond the standard Schwarzschild approach for the inclusion of the stellar population measurements. In order to self-consistently combine the kinematics and stellar populations, we exploited the fact that both the derivation of the SFH from full spectral fitting and the construction of the Schwarzschild model are based on the same principle; they are weighted integrations over many distinct populations, integrated through the line-of-sight (LOS). Specifically, the measured stellar populations are luminosity-weighted by construction as described in § 3.2.2, and the orbital weights are constrained by the surface brightness even though their dynamical properties are computed in the total gravitational potential. Therefore, we assume that the distributions of stellar and dynamical populations are the same. The weight distributions from the dynamical models were then used to derive the distributions of stellar populations that reproduce their observed maps. The result is that

<sup>¶</sup>The binding energy  $E$ , which is sampled logarithmically in the Schwarzschild models, is equivalent to the radius for a circular orbit

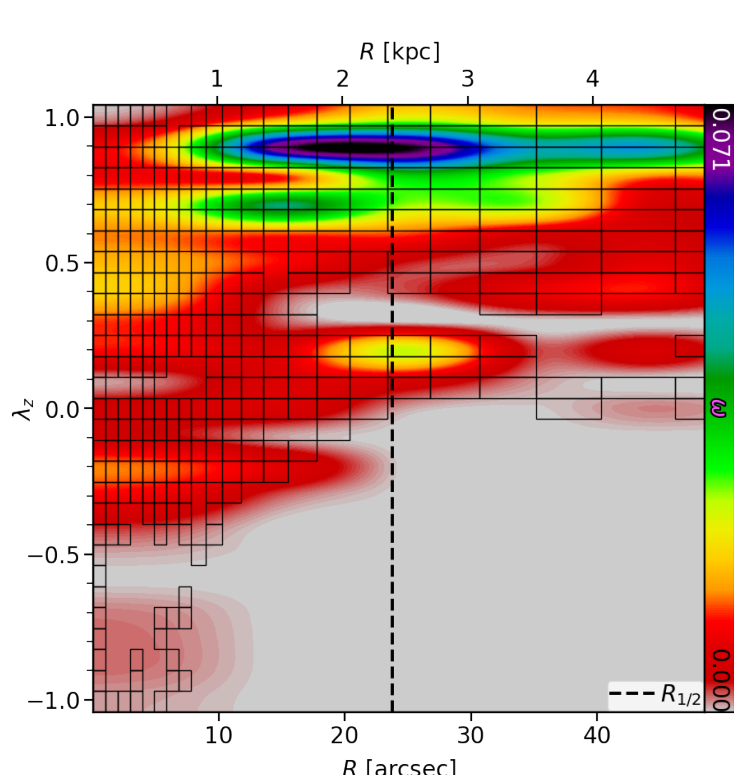


FIGURE 3.4: Phase-space of circularity  $\lambda_z$  as a function of cylindrical radius  $R$  for the best-fit model of FCC 153. The colour represents the orbital weight from the Schwarzschild model, which has been normalised to an integral of unity. The dynamical decomposition is overlaid in black, where only those components which have non-zero contribution to the original model are defined. The figure is shown on the radial extent of the spectroscopy for clarity, but the decomposition is conducted over the full Schwarzschild model. The black dashed line is the half-mass radius, derived from  $MGE_\Sigma$ , shown for scale. The distribution indicates the prevalence of high-angular-momentum (cold disk-like) co-rotating orbits in this galaxy, with very little contribution from hot ( $\lambda_z \sim 0$ ) or counter-rotating ( $\lambda_z < 0$ ) orbits.

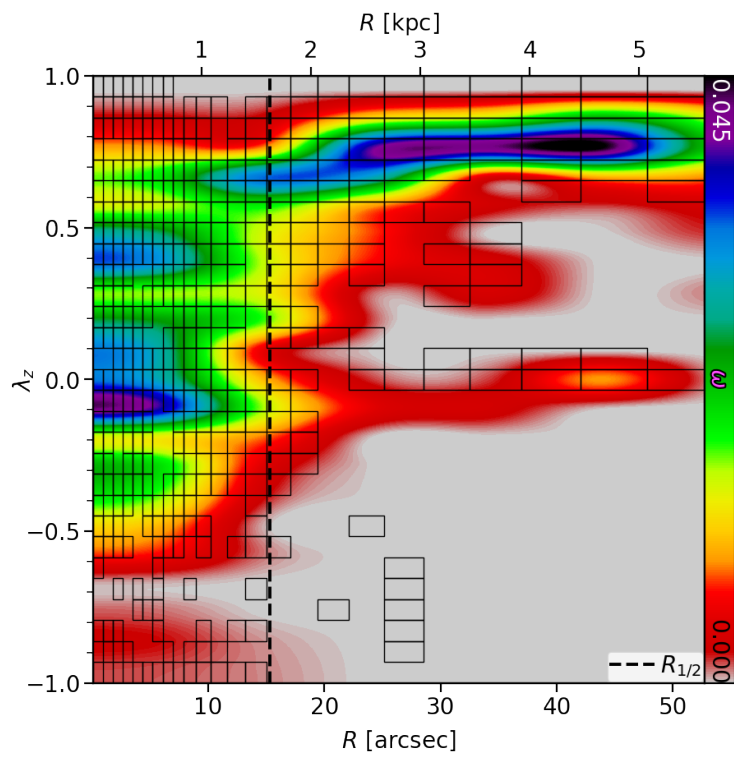


FIGURE 3.5: Same as Fig. 3.4, but for FCC 170. This galaxy has a large contribution from hot central orbits, with most of the cold orbits appearing at larger radius.

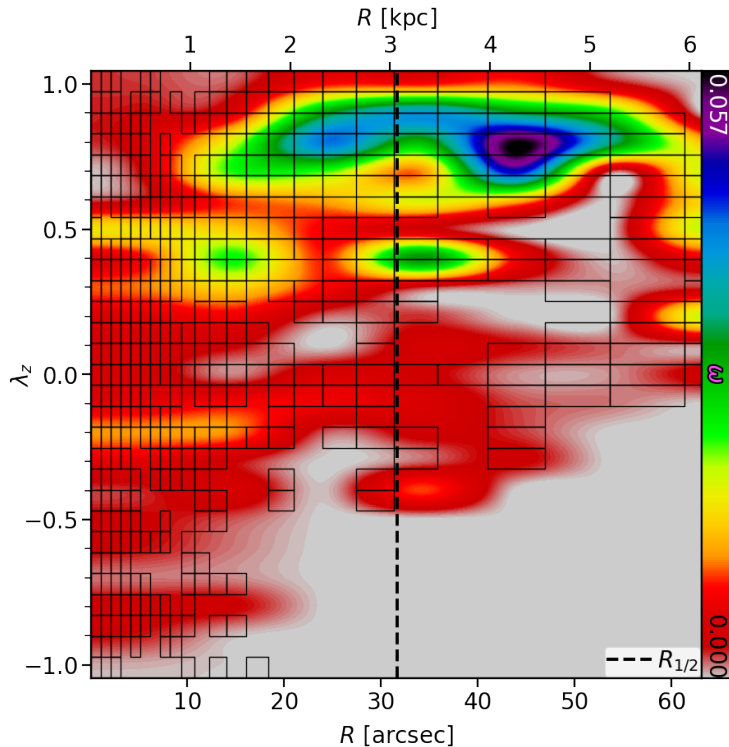


FIGURE 3.6: Same as Fig. 3.4, but for FCC 177. Similarly to FCC 153, this galaxy is dominated by co-rotating cold orbits.

each orbit which contributes to the dynamical model now has an associated age and metallicity. Each dynamical component can thus be considered a mono-abundance population. By fitting age and metallicity independently, we avoided the possibility of degeneracies between them, as well as having to assume a specific age-metallicity relation. Instead, regularisation was utilised for each stellar-population fit, and is analogous to what is routinely used for spectral-fitting analyses such as in § 3.2.2. The specific implementation is detailed in Poci et al. (2019). We tested this approach using mock data from the Auriga simulations (Grand et al., 2016), presented in § 3.C, and find that the main results of this work are accurate to  $\lesssim 10\%$  (Fig. 3.C.4). An alternative approach which uses a chemical-evolution model to derive the age-metallicity relation is presented in Zhu et al. (2020).

The subsequent integration through the LOS of the stellar orbits reproduces all measured kinematic and stellar-population maps. Fits to all maps are shown in Figures 3.7 to 3.9. We also conducted Monte Carlo simulations by re-fitting the stellar-population maps 100 times after randomly perturbing them within their measurement errors. These fits re-distribute the dynamical components in the  $t - [\text{Z}/\text{H}]$  plane (without changing their kinematics), and so were used to estimate the uncertainties of our results. Using all available information – kinematics, ages, metallicities, and density distributions – we can now investigate the formation events that built up each galaxy.

### 3.4 Combined Dynamical and Stellar Populations

The combination of dynamical and stellar populations is imperative to be able to decode the integrated assembly history into its constituent events. We do this using the diagnostic power of Figures 3.10 to 3.12 for FCC 153, FCC 170, and FCC 177, respectively. These figures show radial profiles of the intrinsic vertical stellar velocity dispersion  $\sigma_z(R)$  and the projected surface brightness distributions for each galaxy as a function of both age and metallicity. This

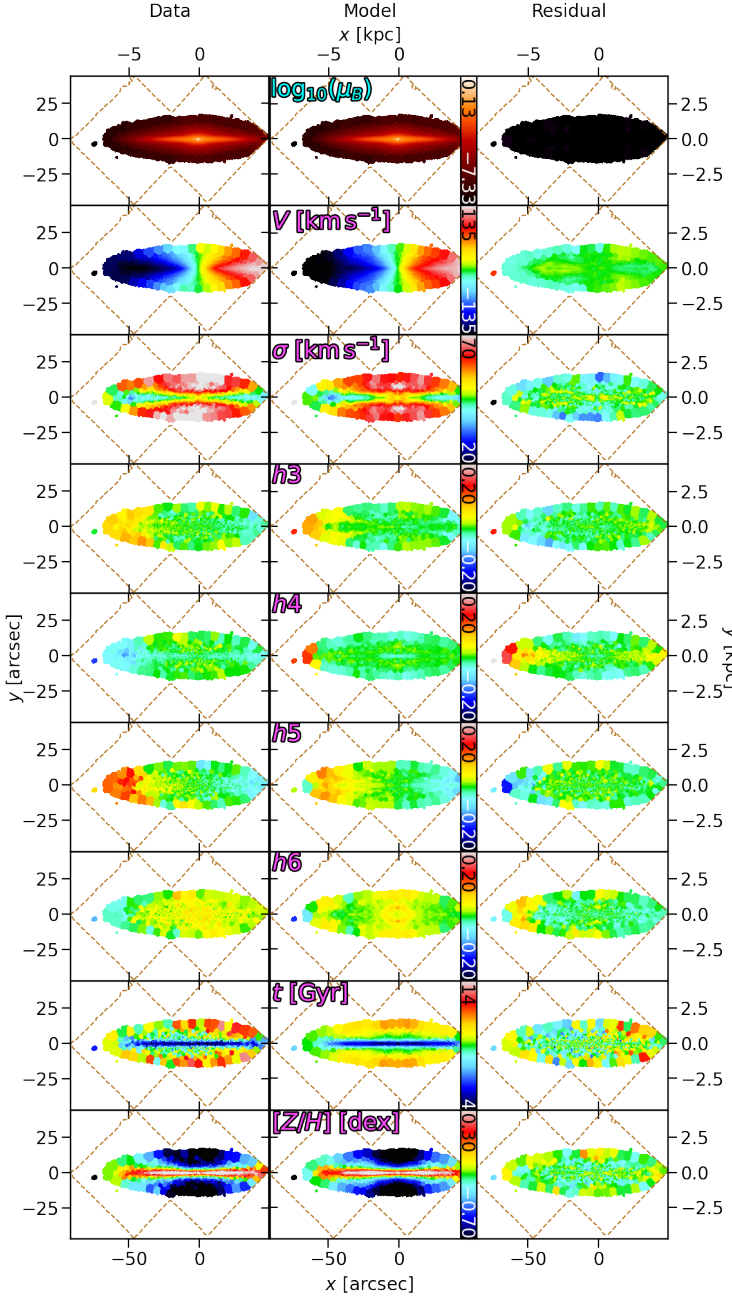


**FIGURE 3.7:** Best-fitting Schwarzschild model for FCC 153. The data (*left*), fits (*middle*), and residuals (*right*) of, from top to bottom, the dynamical model (surface brightness, velocity, velocity dispersion, and  $h_3 - h_6$ ), and the subsequent stellar-population fitting (age and metallicity). The outline of the MUSE mosaic is shown in dashed brown. All residual panels show the absolute differences (data - model), but are offset such that green is zero. The stellar-population maps share a common colour-bar between galaxies for comparison. We note that for FCC 153, since the observed metallicity map reaches 0.4 dex along the major axis, and is itself an average through the LOS, we extend the upper bound for the individual components during the stellar-population fitting to 1.0 dex.

combination of kinematic and population constraints effectively produces star-formation and accretion histories simultaneously, resulting in genuine mass assembly histories. The vertical velocity dispersion is a useful metric for discriminating between different dynamical structures, as well as being comparable to a variety of different observations (explored below). However, for dissecting the model into different dynamical regimes, we used the intrinsic orbital circularity to determine dynamical temperature as this property is inherently connected to the intrinsic orbital phase-space. Before exploring each galaxy individually, we first qualitatively discuss how various features of these figures are interpreted.

The presence of cold kinematics and flattened ('disk'-like) mass distributions are interpreted as *in situ* star formation, especially (though not necessarily) at high metallicity. Metal-rich and metal-poor stars in this regime would indicate that the gas likely originated from internal (recycling) and external (accretion) sources, respectively. This selection is in principle independent of age.

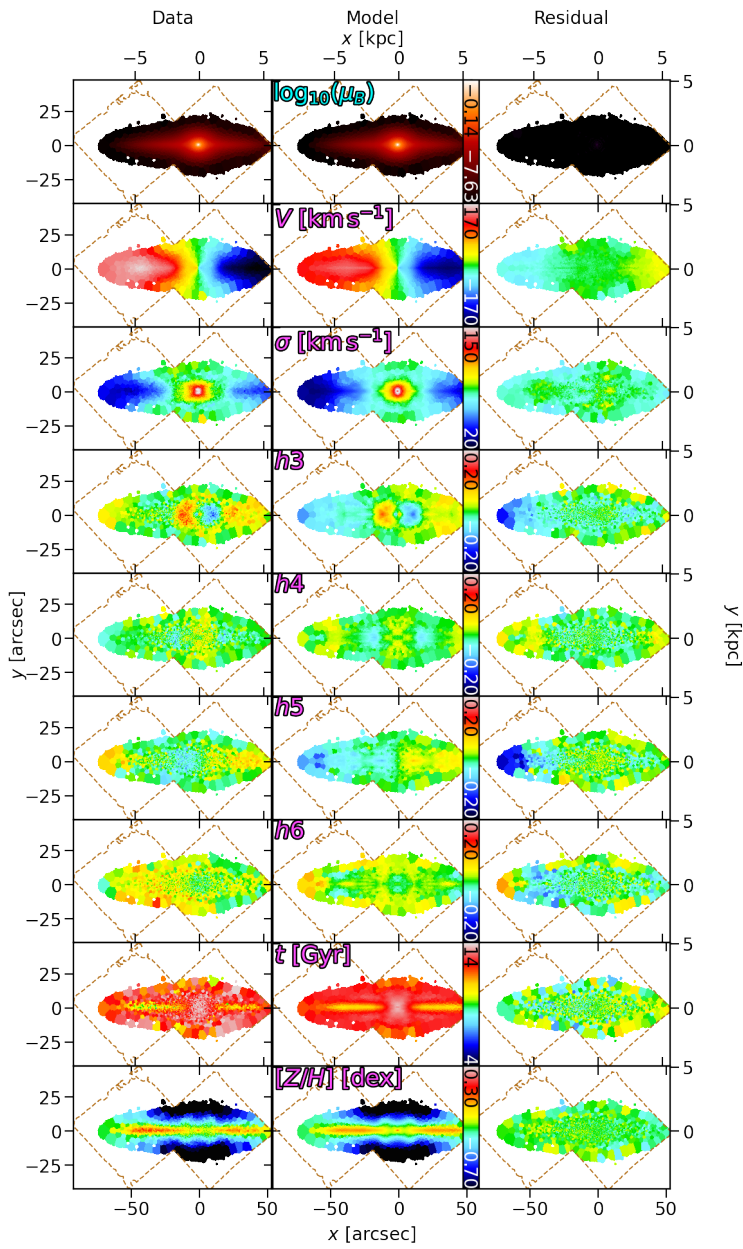


FIGURE 3.8: Same as Fig. 3.7, but for FCC 170.

Centralised spheroidal distributions which are dynamically hot are interpreted as the in situ core or ‘bulge’. There is no strict selection on the stellar populations, since a large diversity has been observed in this region, especially if a stellar bar is or was present in the galaxy (Morelli et al., 2008, 2016; Coelho and Gadotti, 2011; Zhao, 2012; Florido et al., 2015; Seidel et al., 2015; Corsini et al., 2018; Barsanti et al., 2021). Orbits at large radius with hot kinematics and with metallicities towards the metal-poor tail of the host galaxy’s distribution are interpreted as the result of stellar accretion from many lower-mass systems. Such accretion is expected to be at least dynamically ‘warm’. This is because, although the impact of satellites may be preferentially along a particular axis (Shao et al., 2019), accreted stars would nevertheless be on dynamically hotter orbits compared to the in situ cold disk. In the event of minor merging, the accreted systems will, by definition, be lower mass than the host, and via the mass-metallicity relation will thus have lower metallicities on average. Since the age of the accreted stars depends critically on the SFH of the satellites, we make no selection on age for the ‘accreted’ stars. It is possible that some orbits in this regime

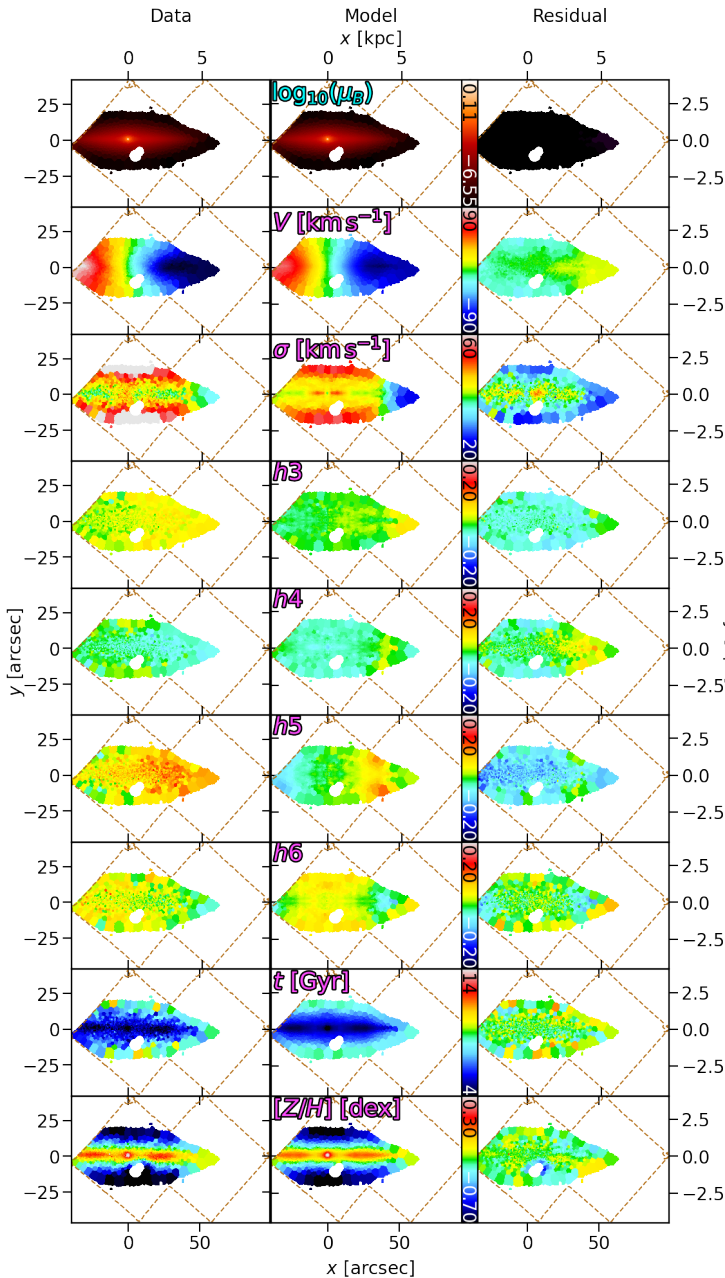


FIGURE 3.9: Same as Fig. 3.7, but for FCC 177.

have an *in situ* origin, from either past major mergers or significant external perturbations (since low-mass accretion events themselves are not expected to perturb the existing disk significantly; Hopkins et al., 2008). We nevertheless interpret this region as accretion under the assumption that it is dominated by *ex situ* material, subject to possible contamination by *in situ* material.

In the remainder of this section, the results are discussed briefly for each galaxy in the context of their individual assembly histories. We constrain the origin of dominant structures in each galaxy, which includes identifying the fraction of likely accreted material. Since the condition described above for the selection of accreted material favours orbits at larger radii, the limited spectroscopic FOV can bias these estimates. We instead estimate the accretion fraction as  $f_{\text{acc}} = M_{\text{acc}}^* / M_{\text{enc}}^*$ , where the accreted stellar mass  $M_{\text{acc}}^*$  is approximated for each galaxy below, and the total enclosed stellar mass  $M_{\text{enc}}^*$  is given in Tab. 3.1. This proposed accreted fraction is discussed further in § 3.5.

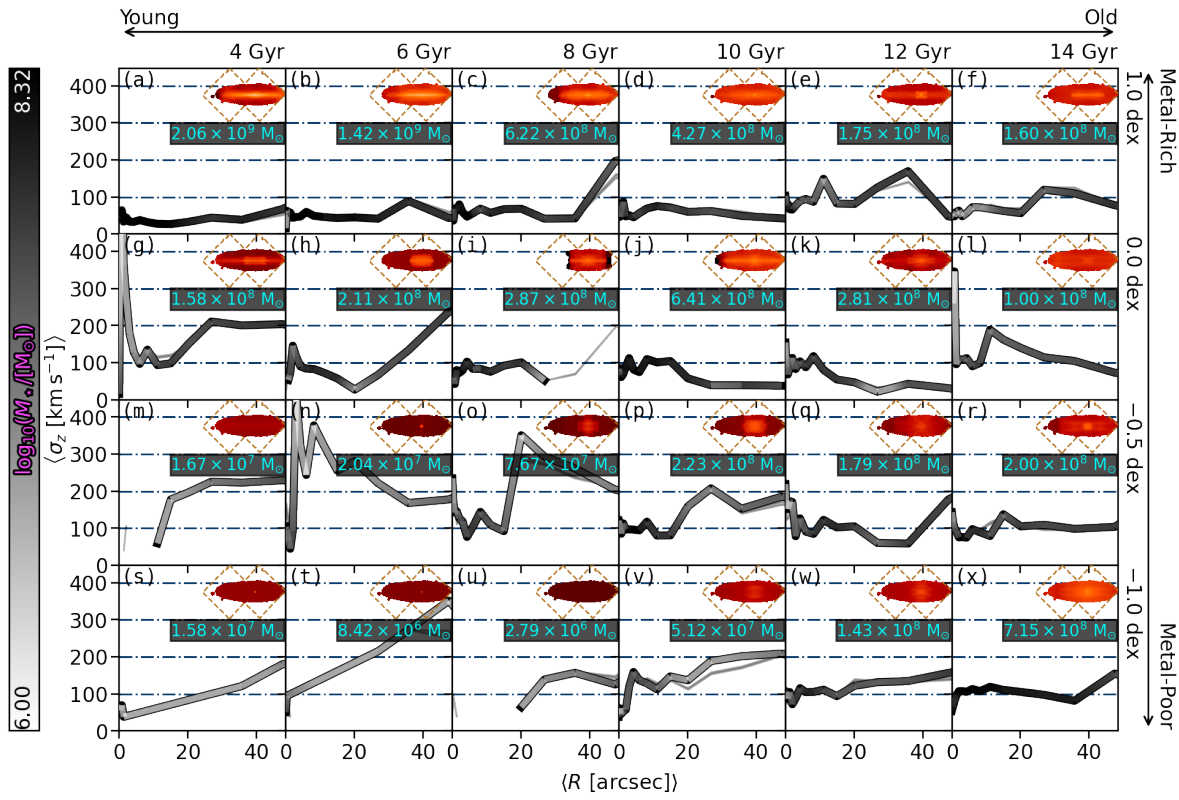


FIGURE 3.10: Mass assembly history for FCC 153. The panels are ordered by increasing mean stellar age (*left to right*) and decreasing mean stellar metallicity (*top to bottom*). The value given at the top and right of each column and row, respectively, denotes its upper bound (inclusive). Each panel is composed of a radial profile of the vertical stellar velocity dispersion  $\sigma_z$  (black/white curve), the surface brightness distribution at the best-fitting projection (*top-right*) with the outline of the MUSE mosaic shown in dashed brown, and the total stellar mass within the FOV for that panel. The  $\sigma_z(R)$  profiles are coloured according to the stellar mass in that panel at that radius (sampled within the logarithmic radial bins). This indicates the spatial region in which each curve contributes most (white regions), and which regions may be impacted by numerical noise (black regions). The grey shaded regions show the spread of velocity dispersion profiles for 100 Monte Carlo fits to the stellar-population maps. This galaxy exhibits a dominant disk-like, metal-rich component that has steadily formed over the last  $\sim 10$  Gyr.

### 3.4.1 FCC 153

FCC 153 is suspected of being an ‘intermediate in-faller’ to the Fornax cluster ( $4 < t_{\text{in-fall}} < 8$  Gyr; as estimated from the cluster projected phase-space diagram in Iodice et al., 2019b). Fig. 3.10 exhibits the largest spread of metallicity of the three galaxies studied here. FCC 153 also shows the strongest recent star-formation activity, having formed the most stellar mass ( $\sim 3 \times 10^9 M_\odot$ ) in recent times ( $< 6$  Gyr), and in a kinematically-cold configuration. In fact, our model reveals that it has retained cold kinematics over all redshifts with even the oldest bins containing stars with  $\sigma_z \sim 50$  km s $^{-1}$ . The combination of late-time star-formation and persistent cold kinematics implies that the integrated assembly history of this galaxy (all mergers and interactions combined) has had a minimal impact, at least in the region covered by the spectroscopy. There is a suggestion of stellar accretion through the old, kinematically-warm, metal-poor population forming part of the stellar ‘halo’. We can use the model to estimate the mass in accreted stars by quantitatively isolating the orbits which meet the qualitative criteria discussed above. Specifically, orbits are selected with  $[Z/H] \leq -0.5$  dex

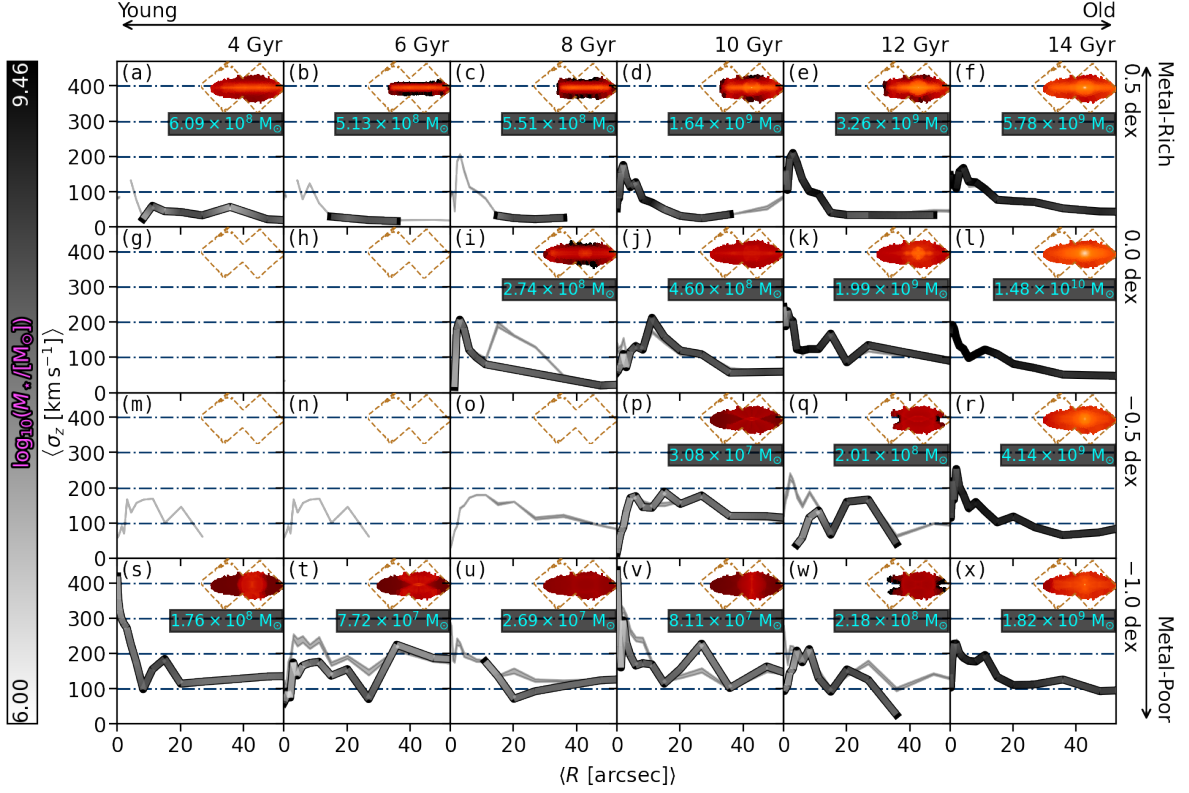


FIGURE 3.11: Same as Fig. 3.10, but for FCC 170. This galaxy is dominated by an old central pressure-supported spheroidal component spanning  $\sim 1$  dex in metallicity. It has a secondary contribution from a progressively thinner and younger disk-like component, and a potential minor contribution from a warm metal-poor halo-like component.

(lower half of Fig. 3.10),  $|\lambda_z| \leq 0.5$ , and mean guiding radius  $\bar{r} \geq 2$  kpc ( $\sim 20''$ ) to exclude any potential in situ ‘bulge’-like orbits (see Fig. 3.4). This selection results in  $f_{\text{acc}} \sim 10\%$ . Under the assumption that these criteria isolate the accreted stars, we estimate an accreted mass of  $M_{\text{acc}}^* \sim 1 \times 10^9 M_\odot$ . This selection has a luminosity-weighted average age and metallicity of  $t = 11.8$  Gyr and  $[Z/H] = -1.3$  dex, respectively. Compared to the other two galaxies in this work, FCC 153 has the highest  $f_{\text{acc}}$ , and its relatively late in-fall may explain that. This is supported by the average age of the tentative accreted material, which implies that the main accretion events (those which dominate the luminosity-weighted average) occurred  $\lesssim 11.8$  Gyr ago.

### 3.4.2 FCC 170

FCC 170 is believed to be an ancient in-faller to the Fornax cluster ( $t_{\text{in-fall}} > 8$  Gyr; as estimated from the cluster projected phase-space diagram in Iodice et al., 2019b). It is the most distinct galaxy of those modelled in this work, being the most massive (Tab. 3.1). It is also believed to be situated closest to the cluster core. FCC 170 appears to have ceased the majority of its star formation the earliest, and its early in-fall and current position in the cluster likely played a role. The galaxy is very old, but we see evidence of recent star-formation, again in a cold configuration seemingly in spite of its environment (Fig. 3.11). Overall, FCC 170 has relatively-high velocity dispersion everywhere with respect to the other two galaxies. Yet the central regions (where we probe with the spectroscopy) have remained heavily rotationally-supported over its history, with  $\sigma_z \lesssim 100$  km s $^{-1}$ . Applying the same

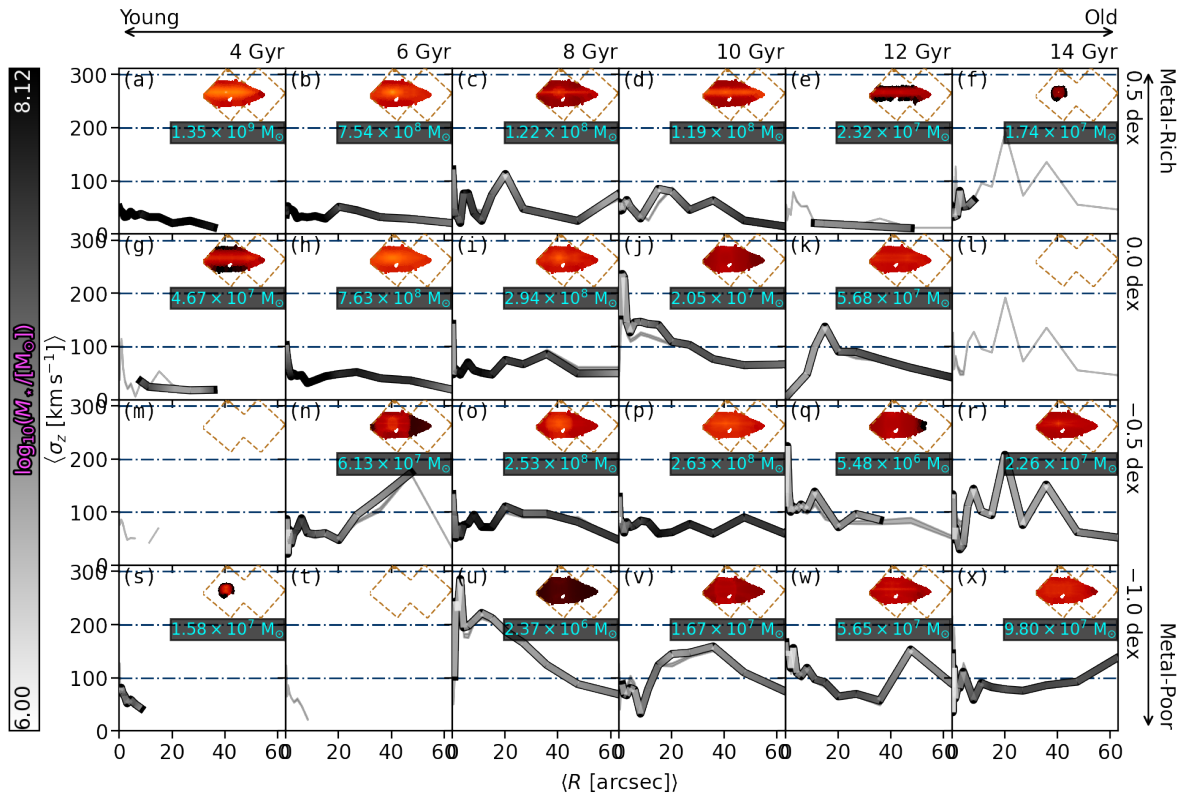


FIGURE 3.12: Same as Fig. 3.10, but for FCC 177. This galaxy appears to have begun forming late. It is dominated by a young, thin disk, with contributions from dynamically-warmer and slightly older stars.

accretion criteria as for FCC 153, we estimate an accretion fraction of  $f_{\text{acc}} \sim 7\%$ , implying  $M_{\text{acc}} \sim 3 \times 10^9 M_{\odot}$  with a luminosity-weighted average age and metallicity of  $t = 13.3$  Gyr and  $[\text{Z}/\text{H}] = -1.3$  dex, respectively. With respect to FCC 153, this implies that FCC 170 experienced more accretion events of lower mass (lower metallicity).

### 3.4.3 FCC 177

FCC 177 is also believed to be an ancient in-faller (Iodice et al., 2019b), as for FCC 170. It has the lowest stellar mass and highest DM fraction of the three galaxies studied here (Tab. 3.1). It exhibits low velocity dispersion ( $\sigma_z < 100 \text{ km s}^{-1}$ ) everywhere and at all times, with the younger, metal-rich populations reaching  $\sigma_z \lesssim 20 \text{ km s}^{-1}$  (Fig. 3.12). We find evidence for a delayed formation, with only a small fraction of old populations ( $t \gtrsim 12$  Gyr) and without any clear spatial structures. At later times, FCC 177 appears to have sustained modest and roughly-constant star-formation for  $t \lesssim 10$  Gyr. This combination of prolonged star-formation and cold kinematics is especially surprising given its early in-fall, and poses problems for the expectation of group pre-processing and cluster quenching processes. The mass budget of FCC 177 is more complicated to disentangle, especially due to the relatively diffuse mass at old ages. In fact, FCC 177 has formed the largest percentage of its stellar mass in recent times, compared to the other two galaxies. Moreover, our assembly history indicates that for lookback times greater than 10 Gyr ago, FCC 177 had just  $\log_{10}(M_{\star}/M_{\odot}) \sim 8$ , implying that the in situ component formed during that time would be lower metallicity with respect to the other two galaxies during the same period. This caveat notwithstanding, applying the same criteria as for the other galaxies, we estimate  $f_{\text{acc}} \sim 6\%$ . This results in

$M_{\text{acc}}^{\star} \sim 3 \times 10^8 M_{\odot}$ , with luminosity-weighted average age and metallicity of  $t = 12.8$  Gyr and  $[\text{Z}/\text{H}] = -1.5$  dex, respectively.

## 3.5 Mass Assembly Histories in Context

In this section we review all the evidence afforded by this technique in the context of the Fornax cluster in order to investigate the dominant processes that built up the stellar mass in these galaxies. By analysing the trends in Figures 3.10 to 3.12, and exploring them more quantitatively throughout this section, we can constrain certain formation mechanisms.

Interestingly, we see a diversity in the assembly histories of the three galaxies studied here via the different distributions of mass between Figures 3.10 to 3.12. Yet the persistence of kinematically-cold orbits is common throughout all of the galaxies for all stellar ages. The observation of such kinematics for old populations places constraints on both internal and external disruption processes. Owing to the archaeological nature of the methodology employed here, all stars are observed in their present-day, not formation, configurations. It is clear, therefore, that in order for these orbits to remain kinematically-cold, those stars need to not only form as such, but also experience little-to-no subsequent disruption until the epoch of observation. This implies that neither internal instabilities nor the cluster potential (or other members) can cause significant perturbations to the kinematics of the central regions of these galaxies (though this is discussed further in §§ 3.5.1 and 3.5.2). For the same reason, we argue that these galaxies have likely not experienced any high-mass-ratio mergers, as they would have similarly disrupted these old cold orbits (Hopkins et al., 2008).

There seems to be no lack of historic star-formation activity in these galaxies. This is perhaps most surprising for FCC 170 which exhibits by far the oldest mean stellar age, and is purported to reside in the central region of the cluster. We find evidence for the continued formation of stars in all three galaxies down to relatively young ages, and at super-solar metallicity. These episodes occurred comfortably after each galaxy is suspected to have entered the cluster. Their metallicity is consistent with self-enrichment, and thus in conjunction with their kinematics, these stars very likely formed in-situ from recycled gas.

The accretion of low-mass stellar systems is expected to deposit material into the outer stellar ‘halo’ regions of galaxies. It is also expected to contribute significantly to the present-day stellar mass of galaxies (Oser et al., 2010). We have estimated, however, low accretion fractions ( $< 10\%$ ) for the galaxies studied here. There are two sources of uncertainty in the  $f_{\text{acc}}$  estimates in this work; contamination by in situ stars in the region we consider ‘accreted’, and excluding some accreted material which resides at lower radius. We can not strictly exclude an in situ contribution to these accretion fractions, but such contamination would imply an intrinsic accreted fraction even lower than estimated here. Without major mergers, any in situ stars that satisfy the proposed criteria for accretion are difficult to explain, unless external perturbations from the cluster have caused dramatic transformations. Moreover, Karademir et al. (2019) find that mergers with smaller mass ratios deposit stars at larger radii. Once again, since we have argued against major (or even a significant amount of minor) mergers, it is plausible that at least the majority of accretion for these galaxies resides at large radius. Davison et al. (2020) similarly find that for galaxies in the EAGLE simulation, most of the accreted mass is deposited beyond the half-mass radius  $r_{1/2}$  for host stellar masses within the range of our Fornax galaxies. We nevertheless caution that  $f_{\text{acc}}$  is subject to these uncertainties, and highlight that the other main conclusions of this work do not depend on the measurements of accretion. While the mass models are constrained over the full extent of the

galaxies using the FDS photometry (§ 3.3.1), we can not exclude higher accretion fractions being found at larger radii as inferred by, for instance, Pulsoni et al. (2018) for the stellar mass range probed by our sample.

A lack of accretion can be explained by the high relative motions of member galaxies within a cluster, and reduced merging has been seen previously for cluster members with respect to the field (Berrier et al., 2008; Pipino et al., 2014). Specifically for the Fornax cluster, its members and their globular cluster (GC) populations have been analysed previously (Jordán et al., 2015; Fahrion et al., 2020). Fahrion et al. (2020) finds that FCC 170 has a significantly reduced number of GC for its stellar mass, and those that it has are notably metal-poor. While the numbers of GC for FCC 153 and FCC 177 are less unusual, since the hosts are themselves lower stellar mass, their GC are also more metal-poor compared to the stellar body by  $\sim 1$  dex. This implies that the GC originated in lower-mass systems. Once again, this suggests a lack of major mergers, and low incidence of minor merging for the three galaxies studied here. Low accretion fractions for these three galaxies were also inferred from the analysis of Pinna et al. (2019a). These galaxies appear to have been shut off from sources of external material by the cluster environment, which has likely stifled their growth. Their stellar mass assembly was able to continue through *in situ* star formation, but has ceased in the present day likely due to the exhaustion of internal gas in conjunction with the lack of replenishment.

### 3.5.1 The Stellar Age–Velocity-Dispersion Relation

Here we quantitatively explore some of the correlations alluded to in the assembly histories. To this end, we investigate the vertical component of the intrinsic stellar velocity dispersion,  $\sigma_z$ , as a function of formation time of the stars (converted to redshift assuming the cosmology of Ade et al., 2016, as implemented in `astropy`). This stellar age–velocity-dispersion relation (AVR) has been studied previously in the Local Group (Wielen, 1977; Nordström et al., 2004; Rocha-Pinto et al., 2004; Seabroke and Gilmore, 2007; Martig et al., 2014; Sharma et al., 2014; Beasley et al., 2015; Hayden et al., 2017; Grieves et al., 2018; Bhattacharya et al., 2019; Mackereth et al., 2019) and a number of cosmological and idealised simulations (Bird et al., 2013; Aumer et al., 2016; Grand et al., 2016; Kumamoto et al., 2017). The gas-phase AVR is also well-studied e.g. Wisnioski et al., 2015. While the stellar AVR is derived through the properties of stars of different ages within individual galaxies, in contrast, the gas-phase AVR is measured via the global properties of different galaxies observed directly at different redshifts. In all cases,  $\sigma_z$  is seen to decrease towards the present day, but with competing explanations as to the physical driver of this relation. It is often thought to be the result of either internal instabilities whose cumulative effects have disturbed older stars more (Saha et al., 2010; Aumer et al., 2016; Grand et al., 2016; Yu and Liu, 2018) or that populations of stars which formed at high redshift inherited higher random motion from their surroundings, which has been decreasing towards the present day as conditions stabilise (Noguchi, 1998; Bournaud et al., 2009; Bird et al., 2013; Leaman et al., 2017; Ma et al., 2017). Since the AVR pertains to the conditions which lead to star-formation, the measurements of these properties are restricted to the disk plane, as this is where *in situ* star-formation is expected to occur.

The stellar AVR measured in this work for the three Fornax galaxies are presented in Fig. 3.13, with comparisons to literature measurements. We track the velocity dispersion as a function of formation redshift, marginalised over metallicity and radius. That is, at fixed age, the metallicities are averaged according to their luminosity-weighted contribution to the model, then similarly for radius. This maintains the appropriate weighting such that

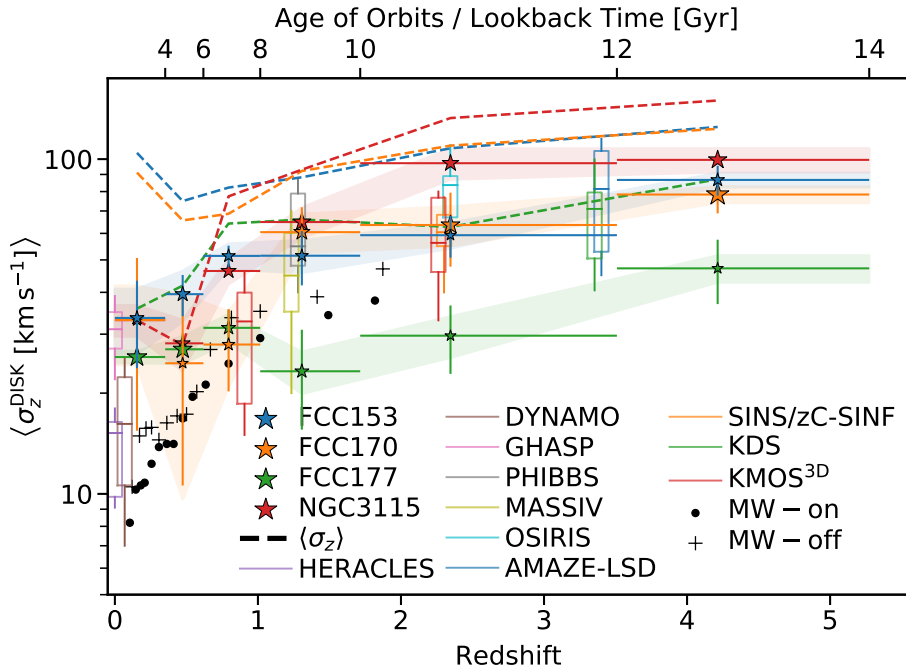


FIGURE 3.13: Stellar disk AVR as derived from our models. The coloured stars are the galaxies modelled in this work (and Poci et al., 2019, for NGC 3115). The symbol size is proportional to the fractional stellar mass in each age bin, for each galaxy independently. The horizontal error-bars denote the width of the age bin. The vertical error bars are computed as the weighted standard deviation within each age bin, for the best-fit model. The shaded regions show the spread in  $\sigma_z$  for 100 Monte Carlo fits to the stellar-population maps. The dashed curves show the stellar AVR of the four S0 galaxies when all orbits are included (no selection on orbital circularity). The box-whisker plots are literature measurements of cold gas disks, from HERACLES (Leroy et al., 2009), DYNAMO (Green et al., 2014), GHASP (Epinat et al., 2010), PHIBBS (Tacconi et al., 2013), MASSIV (Epinat et al., 2012), OSIRIS (Law et al., 2009), AMAZE-LSD (Gnerucci et al., 2011), SINS (Schreiber et al., 2009) and zC-SINF (Schreiber et al., 2014), KMOS<sup>3D</sup> (Wisnioski et al., 2015), and KDS (Turner et al., 2017). The black dots and crosses are Milky-Way stellar measurements (Yu and Liu, 2018) for stars on ( $|z| < 270$  pc) and off ( $|z| > 270$  pc) the plane, respectively. Galaxy disks become dynamically colder towards the present day. The cluster S0 galaxies have a higher contribution from warmer orbits at more recent times compared to the field galaxy (comparing the full and disk-only  $\sigma_z$ ). The Milky-Way, despite its higher stellar mass, is dynamically colder than the S0 galaxies studied here.

the final  $\sigma_z$  measurements are also luminosity-weighted. For consistency with literature measurements, we measure these properties for the ‘disk’-like orbits of the models; that is, we consider only those orbits with  $|\lambda_z| \geq 0.8$ . The resulting relations are shown by the large stars in Fig. 3.13. Additionally, the relations for all orbits (with no selection on circularity) are given by the dashed curves.

All of these galaxies show the same general trend of decreasing  $\sigma_z$  with decreasing stellar age. The trends we measure for the stellar  $\sigma_z$  are flatter than those for direct gas measurements, as the stars do not reach the coldest dynamical temperatures observed in gas in the present day. This is in agreement with predictions from simulations (Pillepich et al., 2019). We also see that the field galaxy NGC 3115, despite being two times more massive than our most massive Fornax object, exhibits comparable vertical velocity dispersion. By comparing the disk AVR to the full-orbit AVR, it can be seen that all three Fornax galaxies show a measurable contribution from non-disk-like orbits at all ages. Together, these observations imply that we

are likely measuring the impact of the cluster on the dynamics of its galaxies due to so-called ‘harassment’ (Moore et al., 1996); frequent though minor gravitational interactions between galaxies in close proximity. External perturbations have also been seen to cause heating coincident with the time of the interaction (Grand et al., 2016).

Our results are also compared in Fig. 3.13 to data from the Milky-Way, both on ( $|z| < 270$  pc) and off ( $|z| > 270$  pc) the disk plane (Yu and Liu, 2018). For comparison, the physical pixel scale of the data used in this work is  $\sim 20$  pc/pixel, but with a real physical resolution of  $\sim 70$  pc due to the point-spread function of the observations. So while our models are not separated based on height above the plane, they still probe the most dynamically-cold physical scales, meaning that any differences between these results are not due to spatial resolution effects. All four S0 galaxies exhibit a systematic increase of  $\sigma_z$  with respect to the Milky-Way, which is expected since galaxies that can support spiral arms should be dynamically colder. In this case, the offset is likely a combination of the different morphology and environment, yet the general shape of the relation is preserved despite these differences.

As discussed above, each galaxy retains a significant portion of mass with cold kinematics and disk-like morphology at the oldest age. Specifically, these oldest age bins (as seen in the present day) exhibit  $\sigma_z \sim 50$  km s $^{-1}$  on the disk plane at intermediate radii and high metallicity. This is inconsistent with internal heating whose effect should be maximal for the oldest stars. For instance, the simulations of Aumer et al. (2016) show that for the oldest stars, internal heating will increase  $\sigma_z$  by  $\sim 15 - 20$  km s $^{-1}$  above the value at birth. For the old stars we measure in the present day which have  $\sigma_z \sim 50$  km s $^{-1}$ , this would imply that they were born with  $\sigma_z \sim 30 - 35$  km s $^{-1}$  at  $z = 4 - 5$ , which is significantly lower than the gas measurements at that epoch. Therefore, we conclude that the AVR for these galaxies is the result of hotter dynamical temperatures at early times, while further minor heating is contributed by the cluster interactions.

Closer inspection of Figures 3.10 to 3.12 indicates a 3D correlation between mean  $\sigma_z$ , stellar age, and stellar metallicity, yet the results of Fig. 3.13 marginalise over metallicity. We therefore compute these relations without such marginalisation, to investigate the impact of age and metallicity independently. These are presented in Fig. 3.14. In order to avoid numerical noise which could be introduced through the increasingly-complex selection criteria, we conduct this analysis on the full diversity of orbits (without selecting on circularity). The curves in Fig. 3.14 are constructed by collecting individual rows and columns of Figures 3.10 to 3.12. Each panel of those figures is integrated along the radial profile, preserving the luminosity weighting at each point, to produce a single  $\sigma_z$  measurement for that panel. Each row in the assembly histories corresponds to a single curve of the AVR at fixed metallicity (left column of Fig. 3.14), while each column in the assembly histories corresponds to a single curve of the  $[Z/H] - \sigma_z$  relation at fixed age (right column of Fig. 3.14). The Spearman rank correlation coefficient  $r$ , which indicates the strength and direction of a trend, is computed using the `scipy` implementation for all curves in a given panel. The corresponding  $p$ -value is also shown for each panel, which indicates the probability that the two axes are uncorrelated.

We observe a significant  $[Z/H] - \sigma_z$  correlation at fixed age, such that the more metal-poor stars are dynamically hotter. Similar correlations between the metallicity and vertical velocity dispersion have been seen previously for the Milky-Way (for the iron abundance  $[Fe/H]$ , and typically with non-trivial selection functions; Meusinger et al., 1991; Ness et al., 2013; Minchev et al., 2014; Grieves et al., 2018; Arentsen et al., 2020) and for M 31 (Dorman et al., 2015) but those results are marginalised over age. Similarly, all previous studies of the stellar AVR have been marginalised over metallicity — with the exception of **sharma2020**, discussed below. Interestingly, Guiglion et al. (2015) see the inverse trend

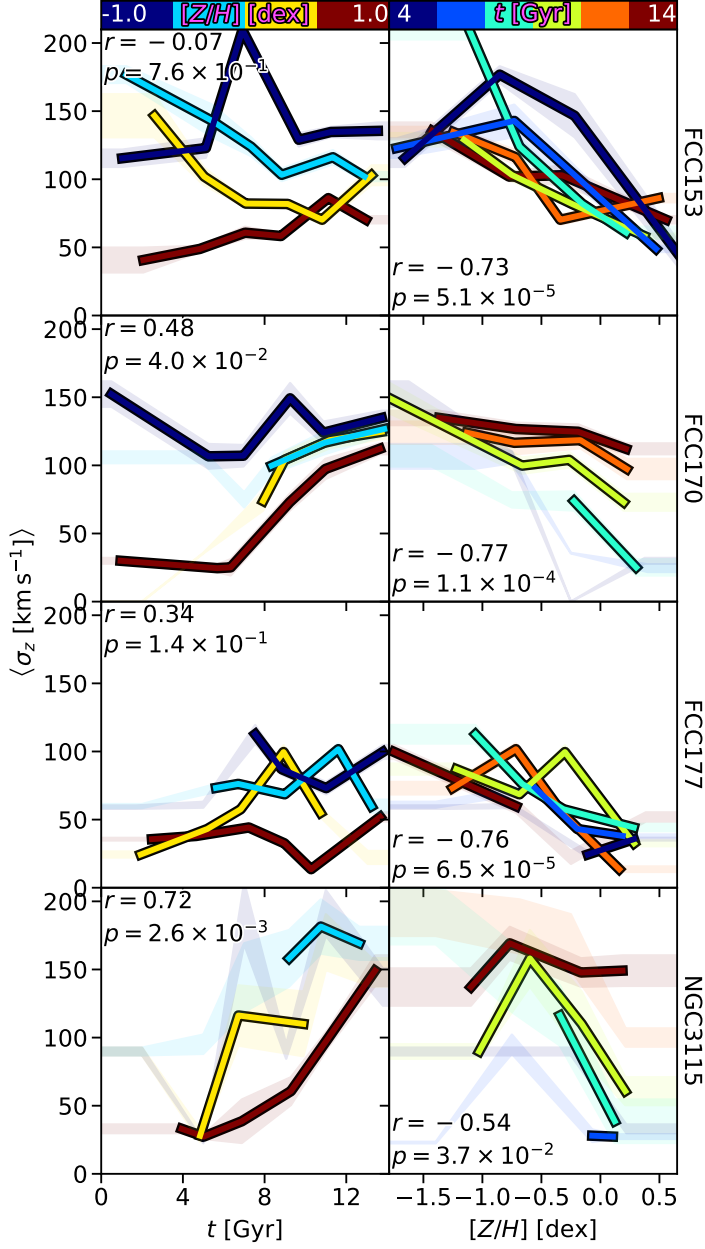


FIGURE 3.14: Correlations of  $\sigma_z$  with stellar age at fixed metallicity (left), and stellar metallicity at fixed age (right) for, from top to bottom, the three galaxies studied in this work, and the field S0 NGC 3115 (Poci et al., 2019). The curves are coloured by their age/metallicity bin corresponding to those of Figures 3.10 to 3.12. The Spearman rank coefficient  $r$  and the associated  $p$ -value, computed for all curves collectively in a given panel, are inset. The shaded regions correspond to the variations derived from 100 Monte Carlo fits to the stellar population maps. The stellar AVR at fixed metallicity exhibits lower significance than the  $[Z/H] - \sigma_z$  at fixed age.

of  $\sigma_z$  with  $[\text{Mg}/\text{Fe}]$  at fixed  $[\text{Fe}/\text{H}]$  for the Milky-Way. Fig. 3.14 shows that the AVR is a weak correlation once metallicity is accounted for, quantified by the correlation coefficients in each case. At fixed age, the  $[\text{Z}/\text{H}] - \sigma_z$  relation is significantly more correlated than the AVR at fixed metallicity. We emphasise that the stellar AVR in Fig. 3.13 (even the dashed full-orbit curves) exhibits a correlation which is consistent with previous measurements when metallicity is not taken into account. This means that the result in Fig. 3.14 can not be due to any degeneracy between age and metallicity in our models. Furthermore, age and metallicity are fit independently in § 3.3.4, and the spatial coherence of the dynamical components (each spatial bin is not independent) is exploited to reduce possible degeneracies within each fit. At face value, this result implies that  $[\text{Z}/\text{H}] - \sigma_z$  is the underlying physical correlation, while the impact of age (or formation redshift) is of secondary importance. In this scenario, the stellar AVR would manifest through the age-metallicity relation and its scatter. Finally, while the results in Fig. 3.14 include the full diversity of orbits from our models, we confirmed, by removing the suspected accretion components (via the same selection identified in § 3.4) that

neither the direction nor the relative significance of these correlations change. This implies that the results of Fig. 3.14 are not merely driven by the fact that accreted material is often dynamically hotter and relatively metal-poor, but rather that it is inherent to what we identify as the *in situ* component.

We posit that the  $[Z/H] - \sigma_z$  relation is driven by the successive ‘generations’ of star formation, each becoming more enriched and more dynamically-cold than those before (in the absence of accretion which would result in the chemical and dynamical mixing of the populations). This could be the case if, for instance, mass segregation of metals occurs vertically as well as radially. Alternatively, this would be the result if higher-metallicity gas requires colder kinematics before star formation is possible, or if the cooling effects of metals naturally produces more dynamically-cold disks if the gas is more metal-rich. Choi and Nagamine (2009) show that metal cooling can significantly increase the star-formation efficiency of the inter-stellar medium, though there is no direct link in that work to dynamics.

Yet measurements of the gas-phase AVR show clear trends with redshift, and the physical interpretation in that case explicitly includes a redshift dependence. However this redshift dependence is via gas depletion through the cosmic specific SFR (such as in Whitaker et al., 2014); in that scenario, galaxies with larger gas fractions experience larger inter-stellar medium turbulence, and higher  $\sigma_z$  is imparted to the stars upon star formation (Leaman et al., 2017). So in much the same way as the scenario proposed here for the stellar AVR, the gas-phase AVR is tied to episodes of star formation, which happen to decline on average with redshift. This subtle difference is especially important when analysing individual galaxies with individual assembly histories. There also remains significant scatter at fixed redshift within the gas-phase AVR that needs to be accounted for, which indicates a potential additional dimension to this issue. Naturally, these star-formation episodes lead to enrichment of the gas over cosmic time (Daigne et al., 2006; Kobayashi et al., 2007). Therefore, if metallicity is the underlying physical driver of the gas-phase AVR, it would still manifest as an observed redshift dependence without intrinsically depending on redshift directly. But this is only, at present, a circumstantial argument in lieu of an explicit experiment for gas disks.

In any case, a testable prediction of this hypothesis is that at fixed present-day stellar mass (and without significant *ex situ* contributions or perturbations), galaxies with higher SFR (that is, faster chemical enrichment) should achieve dynamically-colder orbits at fixed age — or alternatively, the stellar AVR should have a steeper slope. This is because in such a scenario, the absolute cosmic time is not the driver of the AVR, but rather the time it takes for a particular galaxy to achieve a particular degree of enrichment. Since the stellar metallicity and  $\sigma_z$  will depend on both stellar mass and accretion history, it is imperative to control for those parameters to test this prediction. This is at present not possible for the sample of galaxies for which our analysis has been performed, but should be accessible to theoretical models and simulations. In fact, Just and Jahreiß (2010) explicitly investigate the effect of SFR on the stellar AVR, tailored to fit the Milky-Way, through a series of models. That work finds that for similar forms of the SFH, the model with a higher SFR has lower vertical velocity dispersion, despite peaking at earlier epochs.

The outlier in this respect from Fig. 3.14 is NGC 3115. We have already established that accretion has played a minor role in the stellar mass assembly of the three Fornax galaxies. Conversely, Poci et al. (2019) conclude that NGC 3115 assembled  $\sim 68\%$  of its present-day stellar mass from external sources. Moreover, given the higher stellar mass of NGC 3115, these accreted systems could be higher mass, and therefore more enriched on average, compared to lower-mass satellites accreted onto lower-mass hosts. Thus the age and metallicity trends would be significantly phase-mixed, as is seen by the reduced correlation

coefficients. The persistence of an AVR, only at high metallicity, may be indicative of secular evolution following the last accretion event.

A similar analysis has been performed for the Milky-Way using a combination of many of the recent photometric and spectroscopic surveys (**sharma2020**). That work finds a strong  $[Z/H] - \sigma_z$  relation at fixed age. Yet they also find a persistent stellar AVR at fixed metallicity, but only at young ages. The AVR then flattens and correlates solely with metallicity at old ages. Yu and Liu (2018) see similar trends with two bins of metallicity. **sharma2020** interpret the  $[Z/H] - \sigma_z$  correlation as a connection between  $\sigma_z$  and the stellar birth radius. However, in the case of the Fornax galaxies, we see no clear (monotonic) radial gradients of metallicity in Figures 3.7 to 3.9. Comparisons to that work are complicated, however, by the selection functions of the Milky-Way data sets, and so these results may be tracing different physical regimes.

### 3.5.2 S0 Formation

All of our results indicate that the Fornax galaxies have undergone mild transformations due to the cluster potential, primarily in their outer regions. They have been able to retain their cold central kinematics, yet in a thicker configuration compared to the field. We posit, thus, that their S0 morphology is a result of these interactions. This is neither of the explanations typically invoked to explain the transformations of galaxies into S0; mergers (Chilingarian et al., 2009; Querejeta et al., 2015; Tapia et al., 2017; Poci et al., 2019) or the ‘fading’ of spiral galaxies (Larson et al., 1980; Bekki et al., 2002; D’Onofrio et al., 2015; Mishra et al., 2018; Rizzo et al., 2018). While cluster environments are common in the faded-spiral scenario, it is predicated on the supposed spiral progenitor first ceasing star-formation due to the environment (for instance, Boselli and Gavazzi, 2006; Book and Benson, 2010; Peng et al., 2012; Mendel et al., 2013; Bekki, 2014), allowing it to subsequently transform into an S0 galaxy. Yet we see evidence for significant star formation activity well beyond the suspected time of in-fall to the cluster for all three galaxies. Gas was therefore readily available until relatively recently. The evidence for a lack of stellar accretion has been discussed, in agreement with other cluster studies, rendering this formation path unlikely as well. This is also consistent with the deductions of Comerón et al. (2019) and Pinna et al. (2019a) who find that accretion does not play a major role in the formation of ‘thick’ disks in local galaxies.

An alternative scenario proposed by Diaz et al. (2018) states that at high redshift, gas-rich satellite accretion onto compact elliptical galaxies leads to the formation of the disk component of the resulting S0. Our models impose the constraint that if this scenario occurred for the three Fornax galaxies, such accretion would have had to occur  $\gtrsim 12$  Gyr ago for FCC 153 and FCC 170, and  $\gtrsim 10$  Gyr ago for FCC 177, since it must precede the formation of the dynamically-cold disk. However, this scenario supposes that the compact elliptical, which goes on to form the ‘bulge’ of the subsequent S0, is responsible for the suppression of spiral arms in the disk. Conversely, our data suggest that only FCC 170 has a significant contribution from a central pressure-supported structure. More broadly, a diversity of S0 properties is emerging (Fraser-McKelvie et al., 2018; Coccato et al., 2020; Deeley et al., 2020; Tous et al., 2020), and it is unlikely that a single formation path is responsible for this diversity.

### 3.5.3 The Fornax Galaxy Cluster Population

The photometric catalogue of Ferguson (1989), covering 40 sq. degrees, contains 35 S0-like galaxies (some of which have uncertain classification), with 20 being brighter than the magnitude limit of the Fornax3D survey ( $m_B \leq 15$ ). Of these, 12 were observed by Fornax3D, accounting for 60% (34%) of bright (all) lenticular galaxies in the Fornax cluster. Our analysis on the sub-sample of three galaxies, chosen for the reasons discussed above, can not therefore account for the expected diversity of evolutionary pathways within the cluster's galaxy population. So while we infer no major mergers for these galaxies, for instance, we can not exclude this formation path for some of the other cluster S0 galaxies. We have, however, probed the relative extremes in terms of assembly histories, with FCC 170 and FCC 177 forming the majority of their stellar content at early and late times, respectively. This analysis has simultaneously uncovered properties which appear to be approximately independent of assembly history - namely the stellar AVR - which we thus expect to hold for all but the most violent histories. To confidently infer the histories of the remaining galaxies from Fornax3D, this analysis must be applied to each of them individually. This is the goal of future work.

## 3.6 Conclusions

In this work we modelled three edge-on S0 galaxies in the Fornax cluster as part of the Fornax3D project. We applied sophisticated dynamical and stellar-population techniques to self-consistently model the entire stellar information content. These models were used to infer how each galaxy formed, and allowed us to place strong constraints on some of the hypothesised processes that affect galaxy formation and evolution, in particular in the cluster environment. These findings are summarised here:

- All three galaxies retain a strongly-rotating component that has persisted for many dynamical times. These structures can be composed of both young and old stars, implying that they have survived the galaxy's entry into the cluster and subsequent evolution therein (Figures 3.10 to 3.12).
- There is evidence of continued star-formation in all three galaxies, to varying degrees. Owing to the metallicity and kinematics, we suggest this star formation is almost exclusively in-situ through recycled gas, as there is no evidence of gas accretion (Figures 3.10 to 3.12).
- Our results are suggestive of a suppression of stellar accretion. We postulate that this is driven by the relative motions of galaxies within the cluster (Figures 3.10 to 3.12), as proposed in previous works.
- There is evidence against internal heating as the cause of the stellar age–velocity-dispersion relation, suggesting that older stars were created with inherently-higher  $\sigma_z$ , in agreement with the results of Poci et al. (2019). There is tentative evidence that the relations for the cluster galaxies are elevated with respect to the field (Fig. 3.13), implying that harassment may be responsible for mild dynamical heating.
- We find tentative observational evidence of a potential fundamental stellar  $[Z/H] - \sigma_z$  relation which we argue may contribute significantly to the observed age–velocity-dispersion relation (Fig. 3.14).

We endeavour in future work to incorporate more detailed stellar-population analyses, including variable IMF, while continuing to apply this methodology to a variety of galaxies. Deriving these histories for other galaxies will enable a more thorough understanding of how galaxies piece together their mass, and which processes have dominant effects in various regimes.

## Acknowledgements

We thank Lorenzo Morelli, Thomas Spriggs, and Adrian Bittner for discussions on this work. AP acknowledges financial support from Macquarie University and the ESO Studentship Programme. RMM is the recipient of an Australian Research Council Future Fellowship (project number FT150100333). LZ acknowledges the support from National Natural Science Foundation of China under grant No. Y945271001, and the National Key R&D Program of China under grant No. 2018YFA0404501. GvdV acknowledges funding from the European Research Council (ERC) under the European Union’s Horizon 2020 research and innovation programme under grant agreement no. 724857 (Consolidator Grant ArcheoDyn). EMC is supported by MIUR grant PRIN 2017 20173ML3WW\_001 and by Padua University grants DOR1715817/17, DOR1885254/18, and DOR1935272/19. JF-B, IMN, and FP acknowledge support through the RAVET project by the grant PID2019-107427GB-C32 from The Spanish Ministry of Science and Innovation.

Based on observations collected at the European Southern Observatory under ESO programme 296.B-5054(A). This work makes use of the SciGar compute cluster at ESO, and the OzStar supercomputer at Swinburne University. The work also makes use of existing software packages for data analysis and presentation, including ASTROPY (Astropy Collaboration et al., 2013), CYTHON (Behnel et al., 2011), IPYTHON (Perez and Granger, 2007), MATPLOTLIB (Hunter, 2007), NUMPY (Harris et al., 2020), the SciPY ecosystem (Virtanen et al., 2020), and STATSMODELS (Seabold and Perktold, 2010). We finally thank the anonymous referee, whose feedback greatly improved the depth and clarity of this work.



# Bibliography

- Ade, P. a. R. et al. (2016). *Astronomy & Astrophysics* 594, A13. issn: 0004-6361, 1432-0746. doi: 10.1051/0004-6361/201525830.
- Allen, R. J. et al. (2016). *The Astrophysical Journal* 826(1), page 60. issn: 0004-637X. doi: 10.3847/0004-637X/826/1/60.
- Alpaslan, M. et al. (2015). *Monthly Notices of the Royal Astronomical Society* 451(3), pages 3249–3268. issn: 0035-8711. doi: 10.1093/mnras/stv1176.
- Arentsen, A. et al. (2020). *Monthly Notices of the Royal Astronomical Society: Letters* 491(1), pages L11–L16. issn: 1745-3925. doi: 10.1093/mnrasl/slz156.
- Asa'd, R. and Goudfrooij, P. (2020). *Monthly Notices of the Royal Astronomical Society* 498(2), pages 2814–2832. issn: 0035-8711. doi: 10.1093/mnras/staa2515.
- Astropy Collaboration et al. (2013). *Astronomy and Astrophysics* 558, A33. issn: 0004-6361. doi: 10.1051/0004-6361/201322068.
- Aumer, M., Binney, J., and Schönrich, R. (2016). *Monthly Notices of the Royal Astronomical Society* 462, pages 1697–1713. doi: 10.1093/mnras/stw1639.
- Balogh, M. et al. (2004). *Monthly Notices of the Royal Astronomical Society* 348(4), pages 1355–1372. issn: 0035-8711. doi: 10.1111/j.1365-2966.2004.07453.x.
- Barsanti, S. et al. (2021). *The Astrophysical Journal* 906(2), page 100. issn: 0004-637X. doi: 10.3847/1538-4357/abc956.
- Beasley, M. A. et al. (2015). *Monthly Notices of the Royal Astronomical Society* 451(4), pages 3400–3418. issn: 0035-8711. doi: 10.1093/mnras/stv943.
- Behnel, S. et al. (2011). *Computing in Science Engineering* 13(2), pages 31–39. issn: 1558-366X. doi: 10.1109/MCSE.2010.118.
- Bekki, K. (2014). *Monthly Notices of the Royal Astronomical Society* 438(1), pages 444–462. issn: 0035-8711. doi: 10.1093/mnras/stt2216.
- Bekki, K., Couch, W. J., and Shioya, Y. (2002). *The Astrophysical Journal* 577(2), page 651. issn: 0004-637X. doi: 10.1086/342221.
- Bellstedt, S. et al. (2018). *Monthly Notices of the Royal Astronomical Society* 476(4), pages 4543–4564. issn: 0035-8711. doi: 10.1093/mnras/sty456.
- Berrier, J. C. et al. (2008). *The Astrophysical Journal* 690(2), pages 1292–1302. issn: 0004-637X. doi: 10.1088/0004-637X/690/2/1292.
- Bhattacharya, S. et al. (2019). *Astronomy & Astrophysics* 631, A56.
- Bird, J. C. et al. (2013). *The Astrophysical Journal* 773(1), page 43. issn: 0004-637X. doi: 10.1088/0004-637X/773/1/43.
- Blakeslee, J. P. et al. (2009). *The Astrophysical Journal* 694(1), pages 556–572. issn: 0004-637X. doi: 10.1088/0004-637X/694/1/556.
- Blanton, M. R. et al. (2005). *The Astrophysical Journal* 629(1), page 143. issn: 0004-637X. doi: 10.1086/422897.
- Book, L. G. and Benson, A. J. (2010). *The Astrophysical Journal* 716(1), pages 810–818. issn: 0004-637X. doi: 10.1088/0004-637X/716/1/810.

- Boselli, A. and Gavazzi, G. (2006). *Publications of the Astronomical Society of the Pacific* 118(842), page 517. issn: 1538-3873. doi: 10.1086/500691.
- Bournaud, F., Elmegreen, B. G., and Martig, M. (2009). *The Astrophysical Journal* 707(1), pages L1–L5. issn: 1538-4357. doi: 10.1088/0004-637X/707/1/L1.
- Brough, S. et al. (2017). *The Astrophysical Journal* 844(1), page 59. issn: 0004-637X. doi: 10.3847/1538-4357/aa7a11.
- Cappellari, M. (2002). *Monthly Notices of the Royal Astronomical Society, Volume 333, Issue 2, pp. 400-410.* 333, pages 400–410. doi: 10.1046/j.1365-8711.2002.05412.x.
- Cappellari, M. (2016). *Annual Review of Astronomy and Astrophysics* 54(1), pages 597–665. issn: 0066-4146. doi: 10.1146/annurev-astro-082214-122432.
- Cappellari, M. (2017). *Monthly Notices of the Royal Astronomical Society, Volume 466, Issue 1, p.798-811* 466, pages 798–811. doi: 10.1093/mnras/stw3020.
- Cappellari, M. and Copin, Y. (2003). *Monthly Notice of the Royal Astronomical Society, Volume 342, Issue 2, pp. 345-354.* 342, pages 345–354. doi: 10.1046/j.1365-8711.2003.06541.x.
- Cappellari, M. and Emsellem, E. (2004). *Publications of the Astronomical Society of the Pacific* 116(816), page 138. issn: 1538-3873. doi: 10.1086/381875.
- Cappellari, M. et al. (2006). *Monthly Notices of the Royal Astronomical Society, Volume 366, Issue 4, pp. 1126-1150.* 366, pages 1126–1150. doi: 10.1111/j.1365-2966.2005.09981.x.
- Cappellari, M. et al. (2011a). *Monthly Notices of the Royal Astronomical Society, Volume 413, Issue 2, pp. 813-836.* 413(2), pages 813–836. issn: 0035-8711. doi: 10.1111/j.1365-2966.2010.18174.x.
- Cappellari, M. et al. (2011b). *Monthly Notices of the Royal Astronomical Society* 416(3), pages 1680–1696. issn: 0035-8711. doi: 10.1111/j.1365-2966.2011.18600.x.
- Cappellari, M. et al. (2012). *Nature, Volume 484, Issue 7395, pp. 485-488 (2012).* 484, pages 485–488. doi: 10.1038/nature10972.
- Cappellari, M. et al. (2013). *Monthly Notices of the Royal Astronomical Society, Volume 432, Issue 3, p.1862-1893* 432(3), pages 1862–1893. issn: 0035-8711. doi: 10.1093/mnras/stt644.
- Chilingarian, I. V. et al. (2009). *Astronomy & Astrophysics* 504(2), pages 389–400. issn: 0004-6361, 1432-0746. doi: 10.1051/0004-6361/200911684.
- Choi, H. et al. (2018). *The Astrophysical Journal* 856(2), page 114. issn: 0004-637X. doi: 10.3847/1538-4357/aab08f.
- Choi, J.-H. and Nagamine, K. (2009). *Monthly Notices of the Royal Astronomical Society* 393(4), pages 1595–1607. issn: 0035-8711. doi: 10.1111/j.1365-2966.2008.14297.x.
- Christlein, D. and Zabludoff, A. I. (2005). *The Astrophysical Journal* 621(1), page 201. issn: 0004-637X. doi: 10.1086/427427.
- Coccato, L. et al. (2020). *Monthly Notices of the Royal Astronomical Society* 492(2), pages 2955–2972. issn: 0035-8711. doi: 10.1093/mnras/stz3592.
- Coelho, P. and Gadotti, D. A. (2011). *The Astrophysical Journal* 743(1), page L13. issn: 2041-8205. doi: 10.1088/2041-8205/743/1/L13.
- Cole, D. R. and Binney, J. (2017). *Monthly Notices of the Royal Astronomical Society* 465(1), pages 798–810. issn: 0035-8711. doi: 10.1093/mnras/stw2775.
- Cole, J. et al. (2020). *The Astrophysical Journal* 890(2), page L25. issn: 2041-8205. doi: 10.3847/2041-8213/ab7241.
- Comerón, S. et al. (2019). *Astronomy & Astrophysics* 623, A89. issn: 0004-6361, 1432-0746. doi: 10.1051/0004-6361/201833653.

- Corsini, E. M. et al. (2018). *Astronomy & Astrophysics* 618, A172. issn: 0004-6361, 1432-0746. doi: 10.1051/0004-6361/201832625.
- Cortese, L. et al. (2019). *Monthly Notices of the Royal Astronomical Society* 485(2), pages 2656–2665. issn: 0035-8711. doi: 10.1093/mnras/stz485.
- Cretton, N. et al. (1999). *The Astrophysical Journal Supplement Series* 124(2), page 383. issn: 0067-0049. doi: 10.1086/313264.
- Cretton, N., Rix, H.-W., and Zeeuw, P. T. de (2000). *The Astrophysical Journal* 536(1), page 319. issn: 0004-637X. doi: 10.1086/308921.
- D’Onofrio, M., Marziani, P., and Buson, L. (2015). *Frontiers in Astronomy and Space Sciences* 2. issn: 2296-987X. doi: 10.3389/fspas.2015.00004.
- Daigne, F. et al. (2006). *The Astrophysical Journal* 647(2), pages 773–786. issn: 0004-637X. doi: 10.1086/503092.
- Davies, J. I. et al. (2013). *Monthly Notices of the Royal Astronomical Society* 428(1), pages 834–844. issn: 0035-8711. doi: 10.1093/mnras/sts082.
- Davison, T. A. et al. (2020). *Monthly Notices of the Royal Astronomical Society* 497(1), pages 81–93. issn: 0035-8711. doi: 10.1093/mnras/staa1816.
- Deeley, S. et al. (2020). *Monthly Notices of the Royal Astronomical Society* 498(2), pages 2372–2383. issn: 0035-8711. doi: 10.1093/mnras/staa2417.
- Diaz, J. et al. (2018). *Monthly Notices of the Royal Astronomical Society* 477(2), pages 2030–2041. issn: 0035-8711. doi: 10.1093/mnras/sty743.
- Dorman, C. E. et al. (2015). *The Astrophysical Journal* 803(1), page 24. issn: 0004-637X. doi: 10.1088/0004-637X/803/1/24.
- Dressler, A. (1980). *The Astrophysical Journal* 236, page 351. issn: 0004-637X, 1538-4357. doi: 10.1086/157753.
- Drinkwater, M. J., Gregg, M. D., and Colless, M. (2001). *The Astrophysical Journal Letters* 548(2), page L139. issn: 1538-4357. doi: 10.1086/319113.
- Du, W. and McGaugh, S. S. (2020). *The Astronomical Journal* 160(3), page 122. issn: 1538-3881. doi: 10.3847/1538-3881/aba754.
- Emsellem, E., Monnet, G., and Bacon, R. (1994). *Astronomy and Astrophysics*, Vol. 285, p.723-738 (1994) 285, pages 723–738. url: <https://ui.adsabs.harvard.edu/abs/1994A&A...285..723E>.
- Epinat, B. et al. (2010). *Monthly Notices of the Royal Astronomical Society* 401(4), pages 2113–2147. issn: 0035-8711. doi: 10.1111/j.1365-2966.2009.15688.x.
- Epinat, B. et al. (2012). *Astronomy & Astrophysics* 539, A92. issn: 0004-6361, 1432-0746. doi: 10.1051/0004-6361/201117711.
- Fahrion, K. et al. (2020). *Astronomy & Astrophysics* 634, A53. issn: 0004-6361, 1432-0746. doi: 10.1051/0004-6361/201937120.
- Falcón-Barroso, J. et al. (2011). *Astronomy & Astrophysics* 532, A95. issn: 0004-6361, 1432-0746. doi: 10.1051/0004-6361/201116842.
- Ferguson, H. C. (1989). *The Astronomical Journal* 98, pages 367–418. issn: 0004-6256. doi: 10.1086/115152.
- Florido, E. et al. (2015). *Astronomy & Astrophysics* 584, A88. issn: 0004-6361, 1432-0746. doi: 10.1051/0004-6361/201526191.
- Fraser-McKelvie, A. et al. (2018). *Monthly Notices of the Royal Astronomical Society* 481(4), pages 5580–5591. issn: 0035-8711. doi: 10.1093/mnras/sty2563.
- Gargiulo, A. et al. (2019). *Astronomy & Astrophysics* 631, A15. issn: 0004-6361, 1432-0746. doi: 10.1051/0004-6361/201833600.

- Gebhardt, K. et al. (2003). *The Astrophysical Journal* 583(1), page 92. issn: 0004-637X. doi: 10.1086/345081.
- Gnerucci, A. et al. (2011). *Astronomy & Astrophysics* 528, A88. issn: 0004-6361, 1432-0746. doi: 10.1051/0004-6361/201015465.
- Goddard, D. et al. (2017). *Monthly Notices of the Royal Astronomical Society* 465(1), pages 688–700. issn: 0035-8711. doi: 10.1093/mnras/stw2719.
- Graham, M. T. et al. (2019). *arXiv:1910.05139 [astro-ph]*. arXiv: 1910.05139 [astro-ph]. URL: <http://arxiv.org/abs/1910.05139>.
- Grand, R. J. J. et al. (2016). *Monthly Notices of the Royal Astronomical Society* 459(1), pages 199–219. issn: 0035-8711. doi: 10.1093/mnras/stw601.
- Grand, R. J. J. et al. (2017). *Monthly Notices of the Royal Astronomical Society*, stx071. issn: 0035-8711, 1365-2966. doi: 10.1093/mnras/stx071.
- Green, A. W. et al. (2014). *Monthly Notices of the Royal Astronomical Society* 437(2), pages 1070–1095. issn: 0035-8711. doi: 10.1093/mnras/stt1882.
- Grieves, N. et al. (2018). *Monthly Notices of the Royal Astronomical Society* 481(3), pages 3244–3265. issn: 0035-8711. doi: 10.1093/mnras/sty2431.
- Guiglion, G. et al. (2015). *Astronomy & Astrophysics* 583, A91. issn: 0004-6361, 1432-0746. doi: 10.1051/0004-6361/201525883.
- Gunn, J. E. and Gott III, J. R. (1972). *The Astrophysical Journal* 176, page 1. issn: 0004-637X. doi: 10.1086/151605.
- Harris, C. R. et al. (2020). *Nature* 585(7825), pages 357–362. issn: 1476-4687. doi: 10.1038/s41586-020-2649-2.
- Hayden, M. R. et al. (2017). *Astronomy & Astrophysics* 608, page L1. issn: 0004-6361, 1432-0746. doi: 10.1051/0004-6361/201731494.
- Hopkins, P. F. et al. (2008). *The Astrophysical Journal* 688(2), pages 757–769. issn: 0004-637X. doi: 10.1086/592087.
- Hunter, J. D. (2007). *Computing in Science and Engineering*, vol. 9, no. 3, pp. 90-95 9(3), pages 90–95. doi: 10.1109/MCSE.2007.55.
- Iodice, E. et al. (2016). *The Astrophysical Journal* 820(1), page 42. issn: 0004-637X. doi: 10.3847/0004-637X/820/1/42.
- Iodice, E. et al. (2017). *The Astrophysical Journal* 851(2), page 75. issn: 0004-637X. doi: 10.3847/1538-4357/aa9b30.
- Iodice, E. et al. (2019a). *Astronomy & Astrophysics* 623, A1. issn: 0004-6361, 1432-0746. doi: 10.1051/0004-6361/201833741.
- Iodice, E. et al. (2019b). *Astronomy & Astrophysics* 627, A136. issn: 0004-6361, 1432-0746. doi: 10.1051/0004-6361/201935721.
- Jin, Y. et al. (2019). *Monthly Notices of the Royal Astronomical Society* 486(4), pages 4753–4772. issn: 0035-8711. doi: 10.1093/mnras/stz1170.
- Jordán, A. et al. (2007). *The Astrophysical Journal Supplement Series* 169(2), page 213. issn: 0067-0049. doi: 10.1086/512778.
- Jordán, A. et al. (2015). *The Astrophysical Journal Supplement Series* 221, page 13. doi: 10.1088/0067-0049/221/1/13.
- Just, A. and Jahreiß, H. (2010). *Monthly Notices of the Royal Astronomical Society* 402(1), pages 461–478. issn: 0035-8711. doi: 10.1111/j.1365-2966.2009.15893.x.
- Karademir, G. S. et al. (2019). *Monthly Notices of the Royal Astronomical Society* 487(1), pages 318–332. issn: 0035-8711. doi: 10.1093/mnras/stz1251.
- Kauffmann, G. et al. (2004). *Monthly Notices of the Royal Astronomical Society* 353(3), pages 713–731. issn: 0035-8711. doi: 10.1111/j.1365-2966.2004.08117.x.

- Kobayashi, C., Springel, V., and White, S. D. M. (2007). *Monthly Notices of the Royal Astronomical Society* 376(4), pages 1465–1479. ISSN: 0035-8711. doi: 10.1111/j.1365-2966.2007.11555.x.
- Kormendy, J. and Ho, L. C. (2013). *Annual Review of Astronomy and Astrophysics* 51(1), pages 511–653. ISSN: 0066-4146. doi: 10.1146/annurev-astro-082708-101811.
- Krajnović, D. et al. (2009). *Monthly Notices of the Royal Astronomical Society* 399(4), pages 1839–1857. ISSN: 0035-8711. doi: 10.1111/j.1365-2966.2009.15415.x.
- Krajnović, D. et al. (2015). *Monthly Notices of the Royal Astronomical Society* 452(1), pages 2–18. ISSN: 0035-8711. doi: 10.1093/mnras/stv958.
- Kroupa, P. (2002). *Science* 295(5552), pages 82–91. ISSN: 0036-8075, 1095-9203. doi: 10.1126/science.1067524.
- Kumamoto, J., Baba, J., and Saitoh, T. R. (2017). *Publications of the Astronomical Society of Japan* 69(2). ISSN: 0004-6264. doi: 10.1093/pasj/psx005.
- Larson, R. B., Tinsley, B. M., and Caldwell, C. N. (1980). *The Astrophysical Journal* 237, pages 692–707. ISSN: 0004-637X. doi: 10.1086/157917.
- Law, D. R. et al. (2009). *The Astrophysical Journal* 697(2), pages 2057–2082. ISSN: 0004-637X. doi: 10.1088/0004-637X/697/2/2057.
- Lawson, C. L. and Hanson, R. J. (1995). Classics in Applied Mathematics. Society for Industrial and Applied Mathematics. ISBN: 978-0-89871-356-5. doi: 10.1137/1.9781611971217.
- Leaman, R. et al. (2017). *Monthly Notices of the Royal Astronomical Society* 472(2), pages 1879–1896. ISSN: 0035-8711. doi: 10.1093/mnras/stx2014.
- Leroy, A. K. et al. (2009). *The Astronomical Journal* 137(6), pages 4670–4696. ISSN: 1538-3881. doi: 10.1088/0004-6256/137/6/4670.
- Leung, G. Y. C. et al. (2018). *Monthly Notices of the Royal Astronomical Society* 477(1), pages 254–292. ISSN: 0035-8711. doi: 10.1093/mnras/sty288.
- Li, C. et al. (2020). *Monthly Notices of the Royal Astronomical Society* 492(2), pages 2775–2795. ISSN: 0035-8711, 1365-2966. doi: 10.1093/mnras/staa027.
- Lyubenova, M. et al. (2016). *Monthly Notices of the Royal Astronomical Society* 463(3), pages 3220–3225. ISSN: 0035-8711. doi: 10.1093/mnras/stw2434.
- Lyubenova, M. et al. (2013). *Monthly Notices of the Royal Astronomical Society* 431(4), pages 3364–3372. ISSN: 0035-8711. doi: 10.1093/mnras/stt414.
- Ma, X. et al. (2017). *Monthly Notices of the Royal Astronomical Society* 467(2), pages 2430–2444. ISSN: 0035-8711. doi: 10.1093/mnras/stx273.
- Mackereth, J. T. et al. (2019). *Monthly Notices of the Royal Astronomical Society* 482(3), pages 3426–3442. ISSN: 0035-8711. doi: 10.1093/mnras/sty2955.
- Martig, M., Minchev, I., and Flynn, C. (2014). *Monthly Notices of the Royal Astronomical Society* 443(3), pages 2452–2462. ISSN: 0035-8711. doi: 10.1093/mnras/stu1322.
- Martín-Navarro, I. et al. (2019). *Astronomy & Astrophysics* 626, A124. ISSN: 0004-6361, 1432-0746. doi: 10.1051/0004-6361/201935360.
- McDermid, R. M. et al. (2015). *Monthly Notices of the Royal Astronomical Society, Volume 448, Issue 4, p.3484-3513* 448(4), pages 3484–3513. ISSN: 0035-8711. doi: 10.1093/mnras/stv105.
- McGaugh, S. S. and Schombert, J. M. (2014). *The Astronomical Journal* 148(5), page 77. ISSN: 1538-3881. doi: 10.1088/0004-6256/148/5/77.
- Mendel, J. T. et al. (2013). *Monthly Notices of the Royal Astronomical Society* 429(3), pages 2212–2227. ISSN: 0035-8711. doi: 10.1093/mnras/sts489.

- Meusinger, H., Reimann, H. G., and Stecklum, B. (1991). *Astronomy and Astrophysics* 245, pages 57–74. ISSN: 0004-6361. URL: <http://adsabs.harvard.edu/abs/1991A%26A...245...57M>.
- Minchev, I. et al. (2014). *The Astrophysical Journal Letters* 781(1), page L20.
- Mishra, P. K., Wadadekar, Y., and Barway, S. (2018). *Monthly Notices of the Royal Astronomical Society* 478(1), pages 351–358. ISSN: 0035-8711. doi: 10.1093/mnras/sty1107.
- Monnet, G., Bacon, R., and Emsellem, E. (1992). *Astronomy and Astrophysics* 253, pages 366–373. ISSN: 0004-6361. URL: <http://adsabs.harvard.edu/abs/1992A%26A...253..366M>.
- Moore, B. et al. (1996). *Nature* 379(6566), pages 613–616. ISSN: 1476-4687. doi: 10.1038/379613a0.
- Morelli, L. et al. (2008). *Monthly Notices of the Royal Astronomical Society* 389(1), pages 341–363. ISSN: 0035-8711. doi: 10.1111/j.1365-2966.2008.13566.x.
- Morelli, L. et al. (2016). *Monthly Notices of the Royal Astronomical Society* 463(4), pages 4396–4421. ISSN: 0035-8711. doi: 10.1093/mnras/stw2285.
- Muñoz, R. P. et al. (2015). *The Astrophysical Journal* 813(1), page L15. ISSN: 2041-8205. doi: 10.1088/2041-8205/813/1/L15.
- Navarro, J. F., Frenk, C. S., and White, S. D. M. (1996). *The Astrophysical Journal* 462, page 563. ISSN: 0004-637X. doi: 10.1086/177173.
- Ness, M. et al. (2013). *Monthly Notices of the Royal Astronomical Society* 432(3), pages 2092–2103. ISSN: 0035-8711. doi: 10.1093/mnras/stt533.
- Nguyen, D. D. et al. (2019). *The Astrophysical Journal* 872(1), page 104. ISSN: 0004-637X. doi: 10.3847/1538-4357/aafe7a.
- Nitschai, M. S., Cappellari, M., and Neumayer, N. (2020). *Monthly Notices of the Royal Astronomical Society*, staa1128. ISSN: 0035-8711, 1365-2966. doi: 10.1093/mnras/staa1128.
- Noguchi, M. (1998). *Nature* 392(6673), pages 253–256. ISSN: 1476-4687. doi: 10.1038/32596.
- Nordström, B. et al. (2004). *Astronomy & Astrophysics* 418(3), pages 989–1019. ISSN: 0004-6361, 1432-0746. doi: 10.1051/0004-6361:20035959.
- Oh, S. et al. (2018). *The Astrophysical Journal Supplement Series* 237(1), page 14. ISSN: 0067-0049. doi: 10.3847/1538-4365/aacd47.
- Oser, L. et al. (2010). *The Astrophysical Journal* 725(2), pages 2312–2323. ISSN: 0004-637X. doi: 10.1088/0004-637X/725/2/2312.
- Owers, M. S. et al. (2019). *The Astrophysical Journal* 873(1), page 52. ISSN: 0004-637X. doi: 10.3847/1538-4357/ab0201.
- Pascale, R. et al. (2018). *Monthly Notices of the Royal Astronomical Society* 480(1), pages 927–946. ISSN: 0035-8711. doi: 10.1093/mnras/sty1860.
- Peng, Y.-j. et al. (2010). *The Astrophysical Journal* 721(1), page 193. ISSN: 0004-637X. doi: 10.1088/0004-637X/721/1/193.
- Peng, Y.-j. et al. (2012). *The Astrophysical Journal* 757(1), page 4. ISSN: 0004-637X. doi: 10.1088/0004-637X/757/1/4.
- Perez, F. and Granger, B. E. (2007). *Computing in Science Engineering* 9(3), pages 21–29. ISSN: 1558-366X. doi: 10.1109/MCSE.2007.53.
- Pietrinferni, A. et al. (2004). *The Astrophysical Journal* 612(1), page 168. ISSN: 0004-637X. doi: 10.1086/422498.
- Pillepich, A. et al. (2019). *Monthly Notices of the Royal Astronomical Society* 490(3), pages 3196–3233. ISSN: 0035-8711. doi: 10.1093/mnras/stz2338.

- Pinna, F. et al. (2019a). *Astronomy & Astrophysics* 625, A95. issn: 0004-6361, 1432-0746. doi: 10.1051/0004-6361/201935154.
- Pinna, F. et al. (2019b). *Astronomy & Astrophysics* 623, A19. issn: 0004-6361, 1432-0746. doi: 10.1051/0004-6361/201833193.
- Pipino, A. et al. (2014). *The Astrophysical Journal* 797(2), page 127. issn: 0004-637X. doi: 10.1088/0004-637X/797/2/127.
- Poci, A., Cappellari, M., and McDermid, R. M. (2017). *Monthly Notices of the Royal Astronomical Society* 467(2), pages 1397–1413. issn: 0035-8711. doi: 10.1093/mnras/stx101.
- Poci, A. et al. (2019). *Monthly Notices of the Royal Astronomical Society* 487(3), pages 3776–3796. issn: 0035-8711. doi: 10.1093/mnras/stz1154.
- Poggianti, B. M. et al. (2006). *The Astrophysical Journal* 642(1), page 188. issn: 0004-637X. doi: 10.1086/500666.
- Postman, M. and Geller, M. J. (1984). *The Astrophysical Journal* 281, pages 95–99. issn: 0004-637X. doi: 10.1086/162078.
- Pota, V. et al. (2018). *Monthly Notices of the Royal Astronomical Society* 481(2), pages 1744–1756. issn: 0035-8711. doi: 10.1093/mnras/sty2149.
- Pulsoni, C. et al. (2018). *Astronomy & Astrophysics* 618, A94. issn: 0004-6361, 1432-0746. doi: 10.1051/0004-6361/201732473.
- Querejeta, M. et al. (2015). *Astronomy & Astrophysics* 579, page L2. issn: 0004-6361, 1432-0746. doi: 10.1051/0004-6361/201526354.
- Rizzo, F., Fraternali, F., and Iorio, G. (2018). *Monthly Notices of the Royal Astronomical Society* 476(2), pages 2137–2167. issn: 0035-8711, 1365-2966. doi: 10.1093/mnras/sty347.
- Rocha-Pinto, H. J. et al. (2004). *Astronomy & Astrophysics* 423(2), pages 517–535.
- Ryden, B. S., Lauer, T. R., and Postman, M. (1993). *The Astrophysical Journal* 410, pages 515–519. doi: 10.1086/172769.
- Saha, K., Tseng, Y.-H., and Taam, R. E. (2010). *The Astrophysical Journal* 721(2), pages 1878–1890. issn: 0004-637X. doi: 10.1088/0004-637X/721/2/1878.
- Salpeter, E. E. (1955). *Astrophysical Journal*, vol. 121, p.161 121, page 161. doi: 10.1086/145971.
- Sarzi, M. et al. (2018). *Monthly Notices of the Royal Astronomical Society* 478(3), pages 4084–4100. issn: 0035-8711. doi: 10.1093/mnras/sty1092.
- Schaefer, A. L. et al. (2019). *The Astrophysical Journal* 884(2), page 156. issn: 0004-637X. doi: 10.3847/1538-4357/ab43ca.
- Schreiber, N. M. F. et al. (2009). *The Astrophysical Journal* 706(2), pages 1364–1428. issn: 0004-637X. doi: 10.1088/0004-637X/706/2/1364.
- Schreiber, N. M. F. et al. (2014). *The Astrophysical Journal* 787(1), page 38. issn: 0004-637X. doi: 10.1088/0004-637X/787/1/38.
- Schwarzschild, M. (1979). *Astrophysical Journal, Part 1*, vol. 232, Aug. 15, 1979, p. 236-247. 232, pages 236–247. doi: 10.1086/157282.
- Scott, N. et al. (2020). *Monthly Notices of the Royal Astronomical Society* 497(2), pages 1571–1582. issn: 0035-8711. doi: 10.1093/mnras/staa2042.
- Seabold, S. and Perktold, J. (2010). *Python in Science Conference*. Austin, Texas, pages 92–96. doi: 10.25080/Majora-92bf1922-011.
- Seabroke, G. M. and Gilmore, G. (2007). *Monthly Notices of the Royal Astronomical Society* 380(4), pages 1348–1368. issn: 0035-8711. doi: 10.1111/j.1365-2966.2007.12210.x.
- Seidel, M. K. et al. (2015). *Monthly Notices of the Royal Astronomical Society* 446(3), pages 2837–2860. issn: 0035-8711. doi: 10.1093/mnras/stu2295.

- Serra, P. and Trager, S. C. (2007). *Monthly Notices of the Royal Astronomical Society* 374(3), pages 769–774. issn: 0035-8711. doi: 10.1111/j.1365-2966.2006.11188.x.
- Shao, S., Cautun, M., and Frenk, C. S. (2019). *Monthly Notices of the Royal Astronomical Society* 488(1), pages 1166–1179. issn: 0035-8711. doi: 10.1093/mnras/stz1741.
- Sharma, S. et al. (2014). *The Astrophysical Journal* 793(1), page 51. issn: 0004-637X. doi: 10.1088/0004-637X/793/1/51.
- Silverman, B. W. (1986). *Monographs on Statistics and Applied Probability*, London: Chapman and Hall, 1986. URL: <http://adsabs.harvard.edu/abs/1986desd.book.....S>.
- Smith, R. J., Lucey, J. R., and Carter, D. (2012). *Monthly Notices of the Royal Astronomical Society, Volume 426, Issue 4, pp. 2994-3007*. 426, pages 2994–3007. doi: 10.1111/j.1365-2966.2012.21922.x.
- Spavone, M. et al. (2020). *Astronomy & Astrophysics* 639, A14. issn: 0004-6361, 1432-0746. doi: 10.1051/0004-6361/202038015.
- Tacconi, L. J. et al. (2013). *The Astrophysical Journal* 768(1), page 74. issn: 0004-637X. doi: 10.1088/0004-637X/768/1/74.
- Tapia, T. et al. (2017). *Astronomy & Astrophysics* 604, A105. issn: 0004-6361, 1432-0746. doi: 10.1051/0004-6361/201628821.
- Taranu, D. S. et al. (2017). *The Astrophysical Journal* 850(1), page 70. issn: 0004-637X. doi: 10.3847/1538-4357/aa9221.
- Thomas, D. et al. (2005). *The Astrophysical Journal, Volume 621, Issue 2, pp. 673-694*. 621, pages 673–694. doi: 10.1086/426932.
- Thomas, J. et al. (2011). *Monthly Notices of the Royal Astronomical Society, Volume 415, Issue 1, pp. 545-562*. 415, pages 545–562. doi: 10.1111/j.1365-2966.2011.18725.x.
- Toomre, A. and Toomre, J. (1972). *The Astrophysical Journal* 178, pages 623–666. doi: 10.1086/151823.
- Tortora, C. et al. (2011). *Monthly Notices of the Royal Astronomical Society* 418(3), pages 1557–1564. issn: 0035-8711. doi: 10.1111/j.1365-2966.2011.19438.x.
- Tous, J. L., Solanes, J. M., and Perea, J. D. (2020). *Monthly Notices of the Royal Astronomical Society* 495(4), pages 4135–4157. issn: 0035-8711, 1365-2966. doi: 10.1093/mnras/staa1408.
- Turner, O. J. et al. (2017). *Monthly Notices of the Royal Astronomical Society* 471(2), pages 1280–1320. issn: 0035-8711. doi: 10.1093/mnras/stx1366.
- Valluri, M., Merritt, D., and Emsellem, E. (2004). *The Astrophysical Journal* 602(1), page 66. issn: 0004-637X. doi: 10.1086/380896.
- van de Ven, G., De Zeeuw, P. T., and Van Den Bosch, R. C. E. (2008). *Monthly Notices of the Royal Astronomical Society* 385(2), pages 614–646. issn: 0035-8711. doi: 10.1111/j.1365-2966.2008.12873.x.
- van den Bosch, R. C. E. et al. (2008). *Monthly Notices of the Royal Astronomical Society* 385(2), pages 647–666. issn: 0035-8711. doi: 10.1111/j.1365-2966.2008.12874.x.
- van den Bosch, R. C. E. et al. (2015). *The Astrophysical Journal Supplement Series* 218(1), page 10. issn: 0067-0049. doi: 10.1088/0067-0049/218/1/10.
- van der Marel, R. P. et al. (1998). *The Astrophysical Journal* 493(2), page 613. issn: 0004-637X. doi: 10.1086/305147.
- van der Wel, A. (2008). *The Astrophysical Journal* 675(1), pages L13–L16. issn: 1538-4357. doi: 10.1086/529432.
- Vasiliev, E. (2013). *Monthly Notices of the Royal Astronomical Society* 434(4), pages 3174–3195. issn: 0035-8711. doi: 10.1093/mnras/stt1235.

- Vasiliev, E. (2019). *Monthly Notices of the Royal Astronomical Society* 482(2), pages 1525–1544. issn: 0035-8711. doi: 10.1093/mnras/sty2672.
- Vasiliev, E. and Valluri, M. (2020). *The Astrophysical Journal* 889(1), page 39. issn: 1538-4357. doi: 10.3847/1538-4357/ab5fe0.
- Vazdekis, A. et al. (2010). *Monthly Notices of the Royal Astronomical Society*. issn: 00358711, 13652966. doi: 10.1111/j.1365-2966.2010.16407.x.
- Vazdekis, A. et al. (2016). *Monthly Notices of the Royal Astronomical Society* 463(4), pages 3409–3436. issn: 0035-8711, 1365-2966. doi: 10.1093/mnras/stw2231.
- Venhola, A. et al. (2018). *Astronomy & Astrophysics* 620, A165. issn: 0004-6361, 1432-0746. doi: 10.1051/0004-6361/201833933.
- Verolme, E. K. and de Zeeuw, P. T. (2002). *Monthly Notices of the Royal Astronomical Society* 331(4), pages 959–968. issn: 0035-8711, 1365-2966. doi: 10.1046/j.1365-8711.2002.05244.x.
- Virtanen, P. et al. (2020). *Nature Methods* 17(3), pages 261–272. issn: 1548-7105. doi: 10.1038/s41592-019-0686-2.
- Wang, H. et al. (2018a). *The Astrophysical Journal* 852(1), page 31. issn: 0004-637X. doi: 10.3847/1538-4357/aa9e01.
- Wang, Y. et al. (2018b). *The Astrophysical Journal* 868(2), page 130. issn: 0004-637X. doi: 10.3847/1538-4357/aae52e.
- Wang, Y. et al. (2020). *Monthly Notices of the Royal Astronomical Society* 491(4), pages 5188–5215. issn: 0035-8711, 1365-2966. doi: 10.1093/mnras/stz3348.
- Watkins, L. L. et al. (2013). *Monthly Notices of the Royal Astronomical Society* 436(3), pages 2598–2615. issn: 0035-8711. doi: 10.1093/mnras/stt1756.
- Wegner, G. A. et al. (2012). *The Astronomical Journal* 144(3), page 78. issn: 1538-3881. doi: 10.1088/0004-6256/144/3/78.
- Weijmans, A.-M. et al. (2014). *Monthly Notices of the Royal Astronomical Society* 444(4), pages 3340–3356. issn: 0035-8711. doi: 10.1093/mnras/stu1603.
- Whitaker, K. E. et al. (2014). *The Astrophysical Journal* 795(2), page 104. issn: 0004-637X. doi: 10.1088/0004-637X/795/2/104.
- Wielen, R. (1977). *Astronomy and Astrophysics* 60, pages 263–275. issn: 0004-6361. url: <http://adsabs.harvard.edu/abs/1977A%26A....60..263W>.
- Wilkins, S. M. et al. (2013). *Monthly Notices of the Royal Astronomical Society* 431(1), pages 430–439. issn: 0035-8711. doi: 10.1093/mnras/stt192.
- Wisnioski, E. et al. (2015). *The Astrophysical Journal* 799(2), page 209. issn: 0004-637X. doi: 10.1088/0004-637X/799/2/209.
- Yu, J. and Liu, C. (2018). *Monthly Notices of the Royal Astronomical Society* 475(1), pages 1093–1103. issn: 0035-8711. doi: 10.1093/mnras/stx3204.
- Zabel, N. et al. (2019). *Monthly Notices of the Royal Astronomical Society* 483(2), pages 2251–2268. issn: 0035-8711. doi: 10.1093/mnras/sty3234.
- Zhao, Y. (2012). *Astrophysics and Space Science* 337(2), pages 719–728. issn: 1572-946X. doi: 10.1007/s10509-011-0875-7.
- Zhu, L. et al. (2016a). *Monthly Notices of the Royal Astronomical Society* 463(1), pages 1117–1135. issn: 0035-8711. doi: 10.1093/mnras/stw2081.
- Zhu, L. et al. (2016b). *Monthly Notices of the Royal Astronomical Society* 462(4), pages 4001–4017. issn: 0035-8711. doi: 10.1093/mnras/stw1931.
- Zhu, L. et al. (2018a). *Monthly Notices of the Royal Astronomical Society* 473(3), pages 3000–3018. issn: 0035-8711. doi: 10.1093/mnras/stx2409.

- Zhu, L. et al. (2018b). *Nature Astronomy* 2(3), pages 233–238. ISSN: 2397-3366. doi: 10.1038/s41550-017-0348-1.
- Zhu, L. et al. (2020). *Monthly Notices of the Royal Astronomical Society* 496(2), pages 1579–1597. ISSN: 0035-8711. doi: 10.1093/mnras/staa1584.

# Appendices

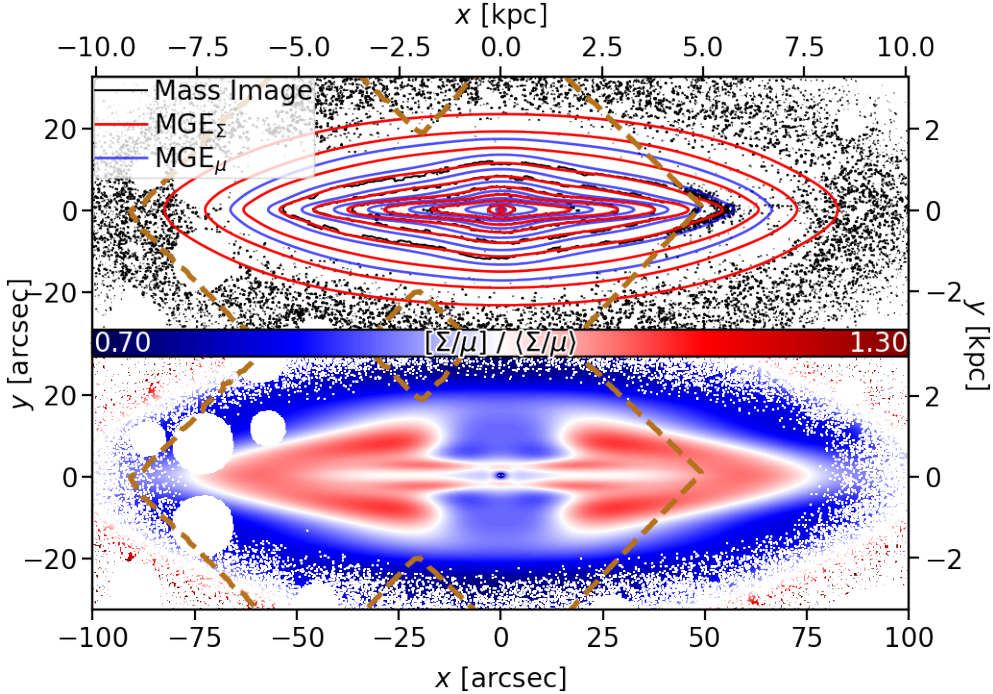


FIGURE 3.A.1: Mass-density MGE for FCC 153. *Top:* Contours of the projected mass density (black), the mass density  $MGE_{\Sigma}$  (red), and the surface brightness  $MGE_{\mu}$  (blue). *Bottom:* The ratio between the mass and surface-brightness models, showing the structural differences. This panel is normalised by the average  $M_{\star}/L$  such that values of 1.0 (white) are consistent with the assumption of a spatially-constant  $M_{\star}/L$ , and any deviations are percentages in stellar mass. The outline of the MUSE mosaic is shown in dashed brown.

## Appendix 3.A Mass Density MGE

Here we present the fits to the scaled mass ‘images’ described in § 3.3.1, in Figures 3.A.1 to 3.A.3, and the results themselves in Tables 3.A.1 to 3.A.3, for FCC 153, FCC 170, and FCC 177, respectively. The MGE in this work have their major-axis offsets  $\psi$  fixed to zero, which generates axisymmetric (in projection) mass models. This section illustrates a number of key aspects of this process. Firstly, it can be seen from the upper panels of Figures 3.A.1 to 3.A.3 that the transition from spectroscopically-derived to photometric-derived  $M_{\star}/L_R$  is seamless, albeit with higher noise in the photometry. Conversely, systematic over- and under-estimations of  $M_{\star}/L_R$  from the photometry would present as discontinuous shifts to larger and smaller radii, respectively, of a given contour at the transition between photometry and spectroscopy. Since there is no such discontinuity in these results, it indicates that the photometrically-derived  $M_{\star}/L_R$  values are quantitatively consistent with those derived from spectroscopy. Secondly, the lower panels clearly highlight the shape differences between the luminosity and mass surface densities. This is a direct result of the resolved structures in stellar populations, which are subsequently taken into account in the dynamical models by this approach.

## Appendix 3.B Dynamical Modelling

This section presents additional details of the Schwarzschild models and measured data products. The best-fit parameters of the Schwarzschild models are given in Tab. 3.B.1, while

$\Sigma$ [ $M_\odot/\text{pc}^2$ ]	$\sigma$ [arcsec]	$q$
68,049.68	0.278	0.52524
4,478.66	1.439	0.59253
2,013.16	4.619	0.51940
357.27	6.725	0.81297
904.26	14.553	0.15344
4,127.99	18.123	0.06621
582.02	26.947	0.15240
300.95	31.695	0.29016
12.17	74.105	0.53099

TABLE 3.A.1:  $\text{MGE}_\Sigma$  for FCC 153. The columns represent, from left to right, the projected mass surface density, the width (peak location), and axis ratio, respectively.

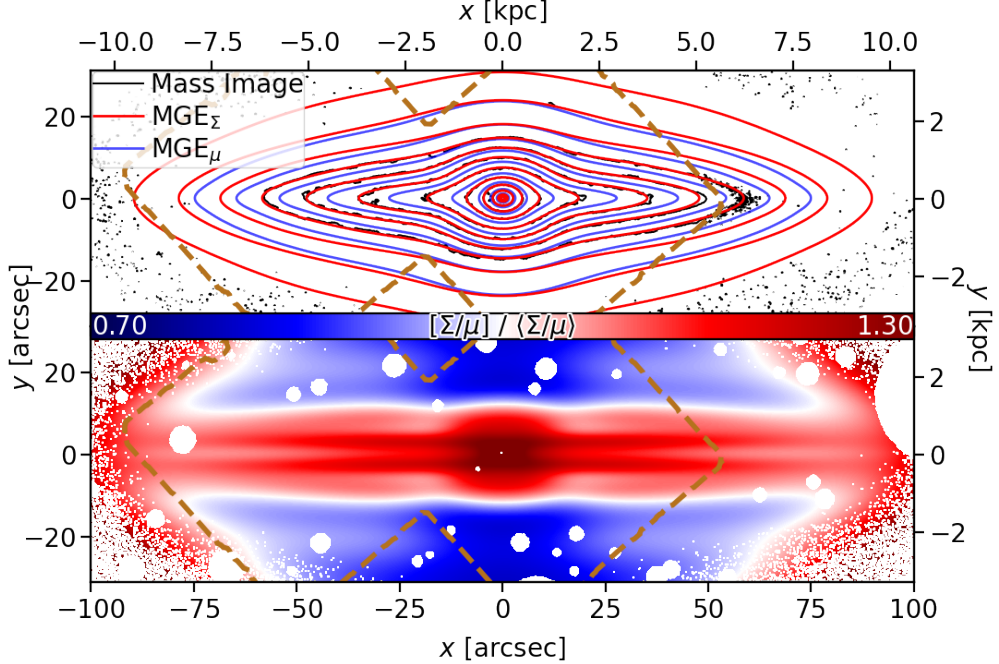


FIGURE 3.A.2: Same as Tab. 3.A.1, but for FCC 170.

$\Sigma$ [ $M_\odot/\text{pc}^2$ ]	$\sigma$ [arcsec]	$q$
177,222.31	0.358	0.73304
44,814.95	1.198	0.74880
17,514.47	2.819	0.75675
5,956.28	6.776	0.76166
127.74	12.580	0.99900
2,229.11	23.103	0.10200
1,113.45	29.559	0.18741
170.86	38.541	0.33380
18.98	68.965	0.71089
3.06	88.782	0.20664
1.81	88.782	0.99900

TABLE 3.A.2: Same as Tab. 3.A.1, but for FCC 170.

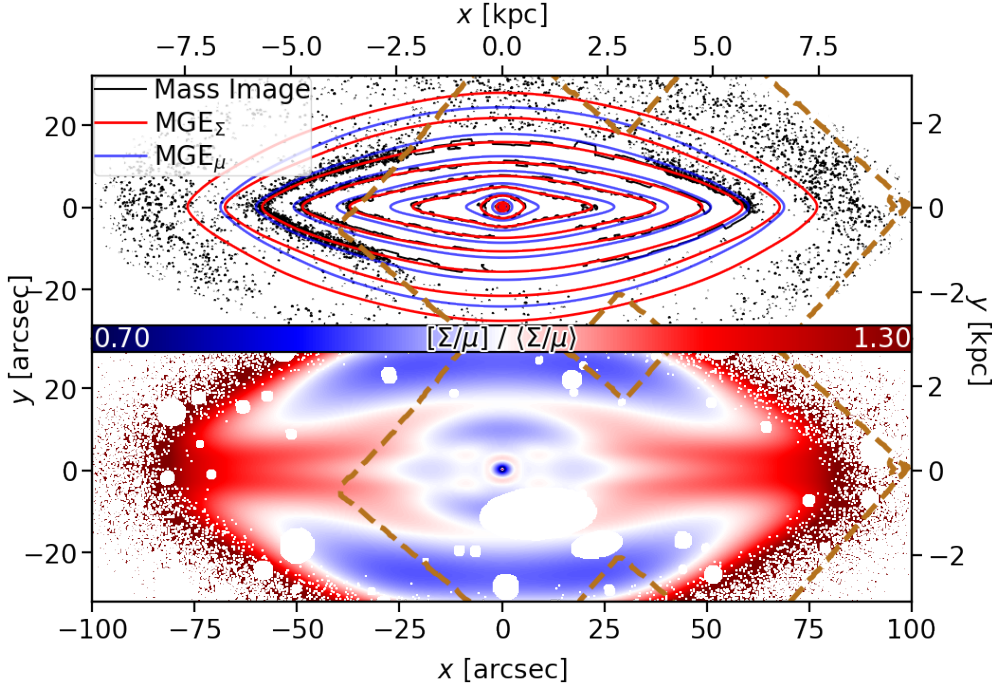


FIGURE 3.A.3: Same as Fig. 3.A.1, but for FCC 177.

their parameter-space distributions are shown in Figures 3.B.1 to 3.B.3. The measured (un-symmetrised) kinematics and stellar populations are presented in Figures 3.B.4 to 3.B.6.

It can be seen that FCC 170 exhibits the highest degree of intrinsic triaxiality, with the lowest  $p$ , though the triaxiality is small in all cases. The intrinsic shapes recovered by our models are in good agreement with, for instance, those of the oblate galaxies of Jin et al. (2019). Interestingly, the dynamical model of the field S0 NGC 3115 (Poci et al., 2019) has larger intrinsic triaxiality than the three cluster S0 galaxies studied here, but this is likely a consequence of its higher stellar mass, and the more violent assembly history inferred for that galaxy.

$\Sigma$ [ $M_\odot/\text{pc}^2$ ]	$\sigma$ [arcsec]	$q$
61,581.78	0.231	0.79514
1,601.36	1.497	0.80274
915.55	3.190	0.72995
315.87	9.467	0.45654
13.62	20.762	0.99701
363.99	22.622	0.07590
463.00	25.577	0.17350
174.70	29.337	0.35693
8.21	50.489	0.68817
7.51	64.291	0.23789

TABLE 3.A.3: Same as Tab. 3.A.1, but for FCC 177.

Galaxy	$\log_{10}(M_\bullet [\text{M}_\odot])^*$	$q$	$p$	$u^*$	$C_{\text{DM}}$	$\log_{10}(f_{\text{DM}})$	$\Upsilon$
FCC 153	6.03	0.0580	0.9980	0.9999	7.00	4.00	0.355
FCC 170	7.40	0.0600	0.9920	0.9999	2.50	2.70	0.530
FCC 177	5.52	0.0700	0.9999	0.9999	2.00	5.00	0.365

TABLE 3.B.1: Best-fit parameters for the Schwarzschild models. Columns marked with \* are fixed to the values given here.

## Appendix 3.C Validation on Mock Data

A crucial test to conduct for the modelling procedure used in this work is to determine the accuracy and precision with which it can recover known properties. To this end, we conducted tests on mock data of realistic galaxies from the Auriga simulation suite (Grand et al., 2017). In Zhu et al. (2020), this Schwarzschild code is used to fit the mock kinematic data of sub-halos from Auriga, at various projected inclinations. Here we take the dynamical models and apply the procedure described in §§ 3.3.3 and 3.3.4 in order to fit stellar populations in exactly the manner that is applied to the Fornax3D data. We then measure the diagnostics that inform the main scientific conclusions of this work, and compare directly to the underlying intrinsic distributions from the simulations. We conduct this analysis on Auriga halos 5 and 6, projected to an inclination of  $\theta = 80^\circ$

The stellar-population fits are shown in Fig. 3.C.1, where the ‘true’ maps are generated simply by projecting all the particles along each LOS. We also ran 100 Monte Carlo simulation fits to these maps as is done in the main text, however in this case the outputs are less informative because the ‘errors’ on the mock maps were generated artificially. The distributions of  $t - Z$  are presented in Fig. 3.C.2. We note here that the ‘true’ distributions are smoother due to the  $\sim 10^5$  particles that are used to generate them, in contrast to the  $\sim 10^2$  dynamical components which constitute the ‘model’ distributions. Kernel Density Estimates (KDE) were computed from these data to compare the marginalised distributions. Owing to the difference in the size of the data sets between the dynamical models and simulations, we derived the optimal bandwidth for the KDE of each data-set using a data-driven approach which minimises the variance and also takes into account each sample size (Silverman, 1986). This exercise has shown that not only can the models fit the projected maps, but also that our implementation recovers the underlying stellar-population distributions.

The main results from this work are derived from the assembly histories in Figures 3.10 to 3.12, and the AVR in Fig. 3.13. Comparing simulations to data in general can introduce inconsistencies in many ways, and so for clarity we describe the procedure for testing the recovery of the assembly histories on simulations, and the steps taken to mitigate potential inconsistencies. Firstly, the Cartesian coordinates of the simulation data are binned to the same spherical polar grid of the corresponding Schwarzschild model. The simulation kinematics,  $V_x, V_y, V_z$ , are then converted to cylindrical coordinates, in line with how the outputs from the Schwarzschild model are analysed. From here, the  $\sigma_z$  measurements on the simulation data proceed in an identical fashion as for the Schwarzschild model. Moreover, the distributions from the simulations are constructed using exactly the particles that lie within the mock FOV, by construction. Conversely, the Schwarzschild models (and indeed real observations) typically have contributions from orbits which reside (on average) outside the FOV, which are not present in the simulation. This means that any measurement on these data would be probing different physical regions between the two data sets. To remedy this inconsistency, the results from the Schwarzschild models do not include orbits with

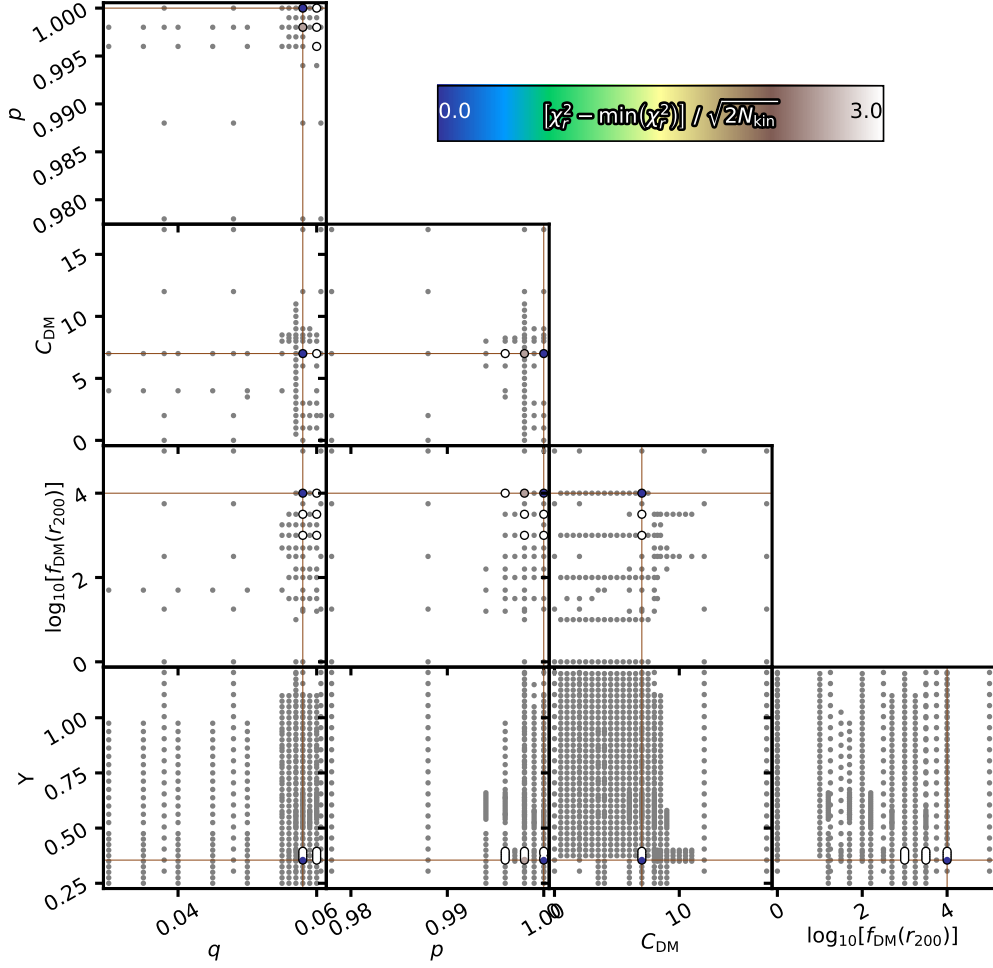


FIGURE 3.B.1: Optimisation over the 5D parameter-space for FCC 153. The grey points indicate the exploration of the parameter-space with the smaller orbit sampling, while the coloured points show the  $\chi^2_r$  of the models with the high orbit sampling (see § 3.3.2). The best-fit parameters are indicated by the brown lines.

time-averaged radii outside the FOV. This is only the case for the mock tests where strictly-consistent comparisons are sought. Our main results in Figures 3.10 to 3.12 include the full model.

The recovery of the assembly histories is presented in Fig. 3.C.3. It can be seen that the radial profiles of  $\sigma_z$  from the simulations often extend to larger radii than the corresponding profiles from the Schwarzschild model. This is due to the fact that each particle in the simulation contributes to its profile, while for the Schwarzschild model orbits are required to have spent some time in a particular region before being included. A single particle (or very few) in the simulations of a given  $t - [\text{Z}/\text{H}]$  component may give the impression of having a larger extent compared to the Schwarzschild model, while actually contributing negligible mass. Therefore we emphasise that it is the common radial regions for each pair of profiles, and the overall spatial distribution of particles/orbits for each panel, that provides the best indication of the model's recovery as this is where the vast majority of the mass resides. In this regime, there is clearly point-to-point variation between the intrinsic and recovered radial profiles of velocity dispersion, which are noisy for some components. The agreement is worse for decreasing mass, which is expected. Nevertheless, it can be seen that the general trends are accurately recovered by the model, in particular the relative dynamics

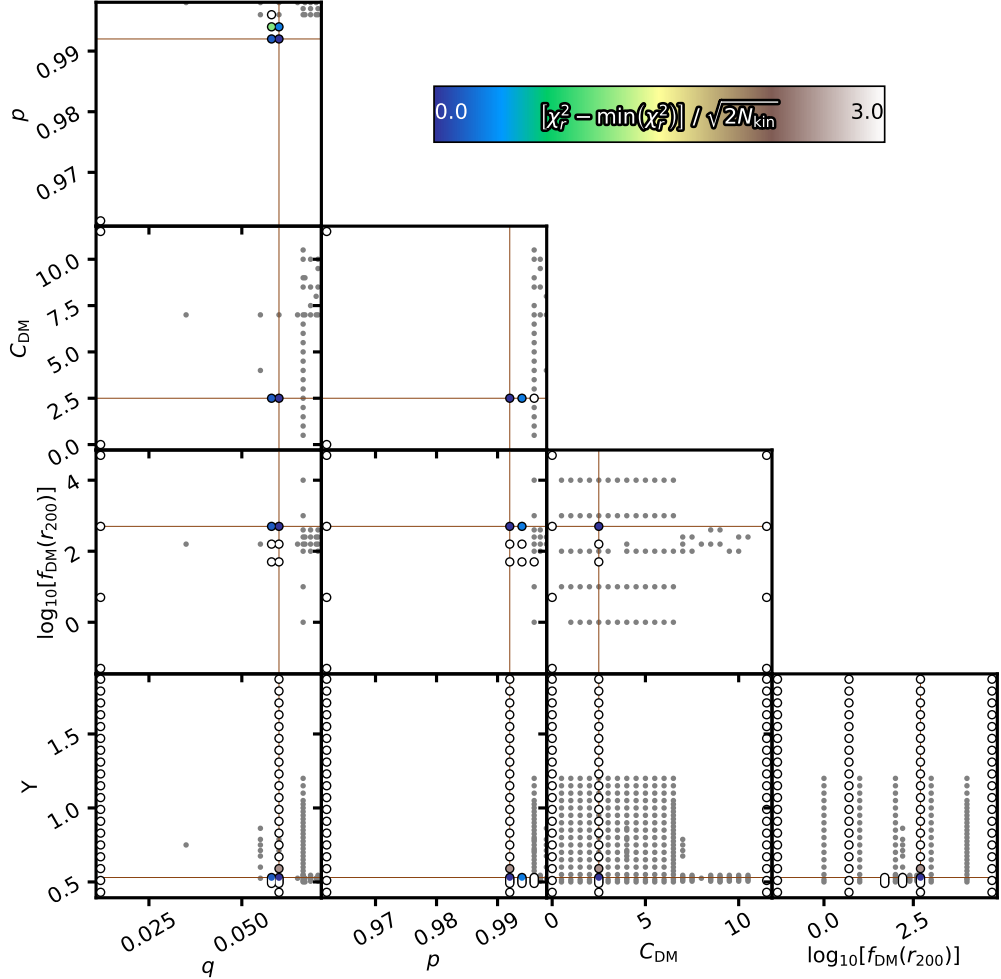


FIGURE 3.B.2: Same as Fig. 3.B.1, but for FCC 170.

between the different stellar populations. The absolute quantitative agreement between the model and simulations is also good, though in some cases there appears to be additional discretisation effects in the model producing sharply-varying profiles in the low-mass panels, which is likely due to the binning in circularity space combined with the binning in the  $t - Z$  space. Reassuringly, the 2D distributions are also well-matched by the model. Some mass is re-distributed to different bins compared to the simulations, which are typically the compact spheroidal structures. Such ‘boundary’ effects are inevitable when imposing discrete binning on the data, as those components with values close to these boundaries may straddle one way or the other. The Monte Carlo simulations show similar behaviour, and in this way the shaded regions account for these boundary effects. Finally, the recovery of the AVR are shown in Fig. 3.C.4. Once again, we see good qualitative and quantitative agreement.

We conclude that the model is sufficiently robust to be able to draw strong inferences about real galaxies. With regards to the main conclusions of this work, the relative behaviour of the chemo-dynamical populations is recovered well, where the model stellar AVR for both Auriga halos are consistent to within  $\sim 10 \text{ km s}^{-1}$  of their intrinsic values. We highlight that we believe this is an upper limit on account of our real data having higher spatial resolution, the corresponding models having higher orbit sampling, and all galaxies studied here having  $\theta > 80^\circ$  (where more edge-on projections are more reliable; Zhu et al., 2020), which all work in favour of improving the reliability of this technique further. We are therefore confident

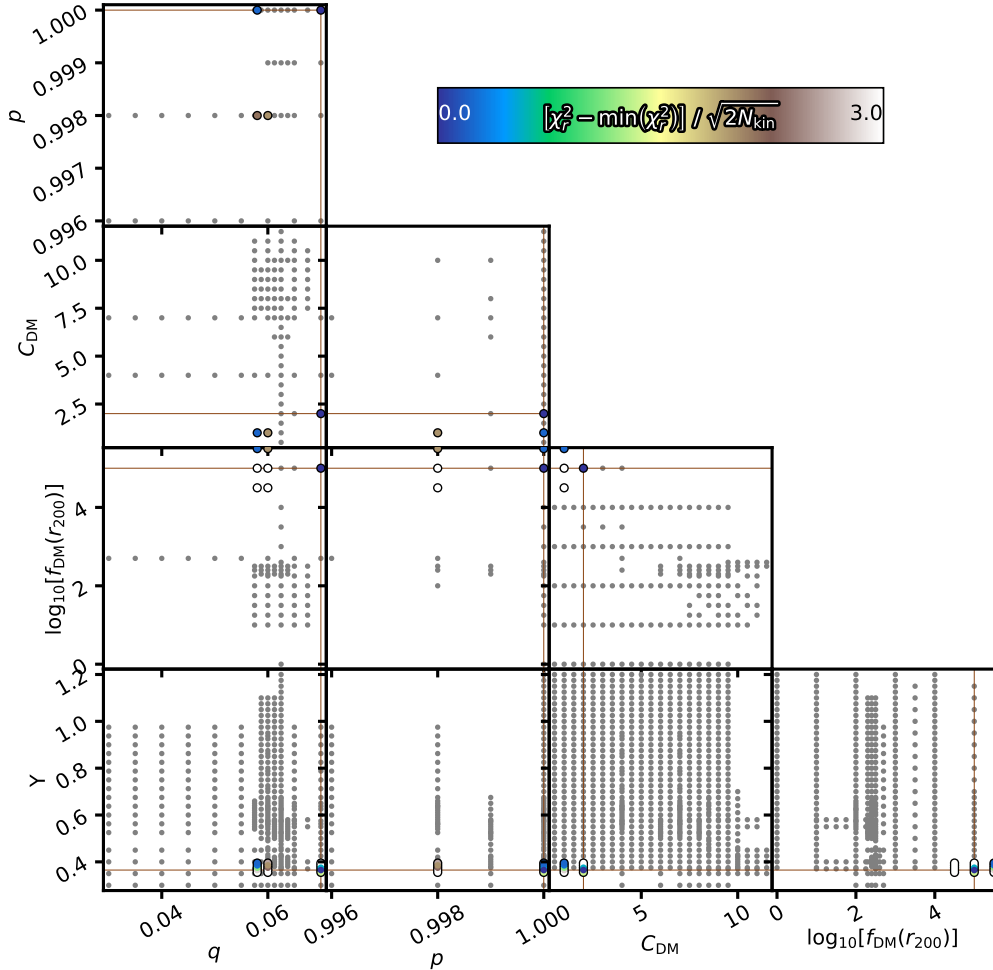


FIGURE 3.B.3: Same as Fig. 3.B.1, but for FCC 177.

that this method is able to recover not only projected average quantities like the 2D stellar-population maps of Fig. 3.C.1, but also quantitatively recover the underlying chemo-dynamic distributions, and that our main conclusions are robust against systematic effects.

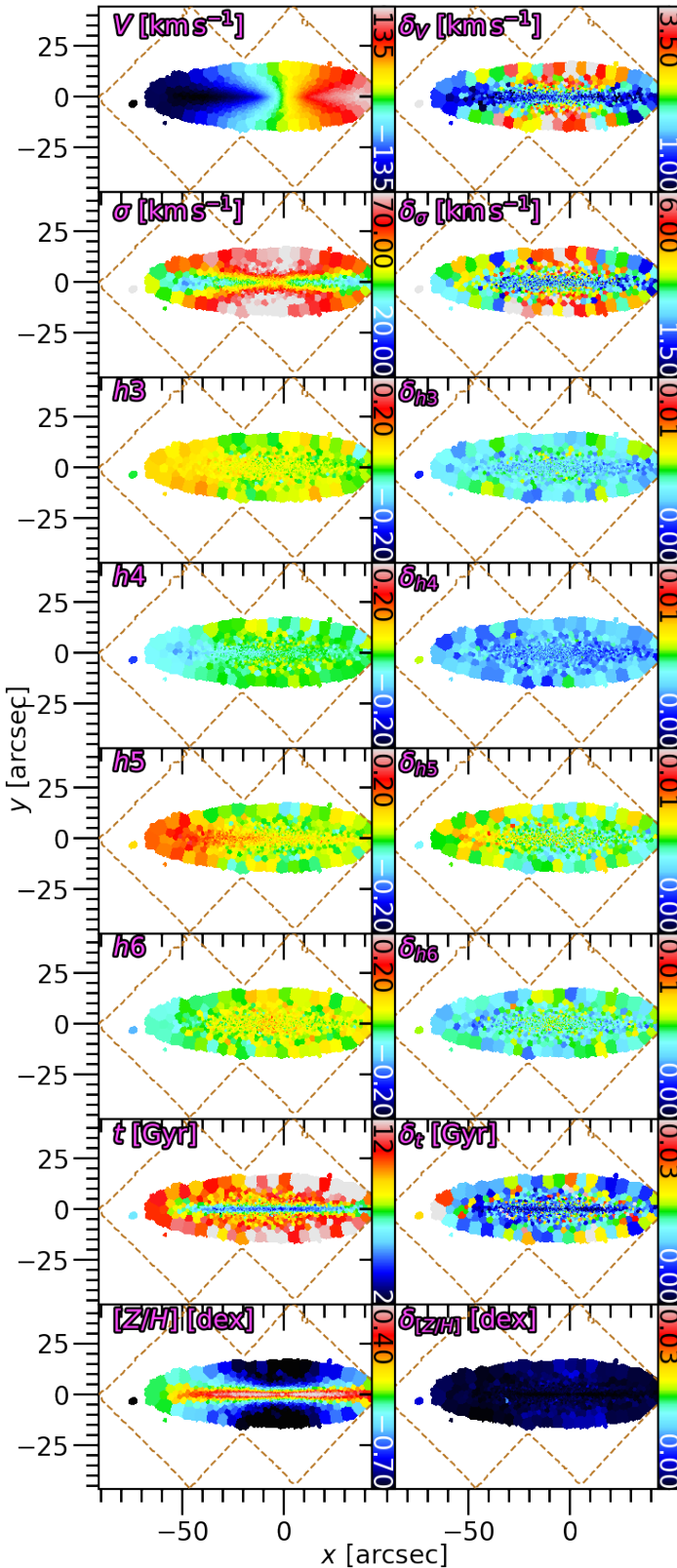


FIGURE 3.B.4: Un-symmetrised kinematics extracted for FCC 153 (*left*), and associated errors computed through Monte Carlo simulations (*right*). The outline of the MUSE mosaic is shown in dashed brown.

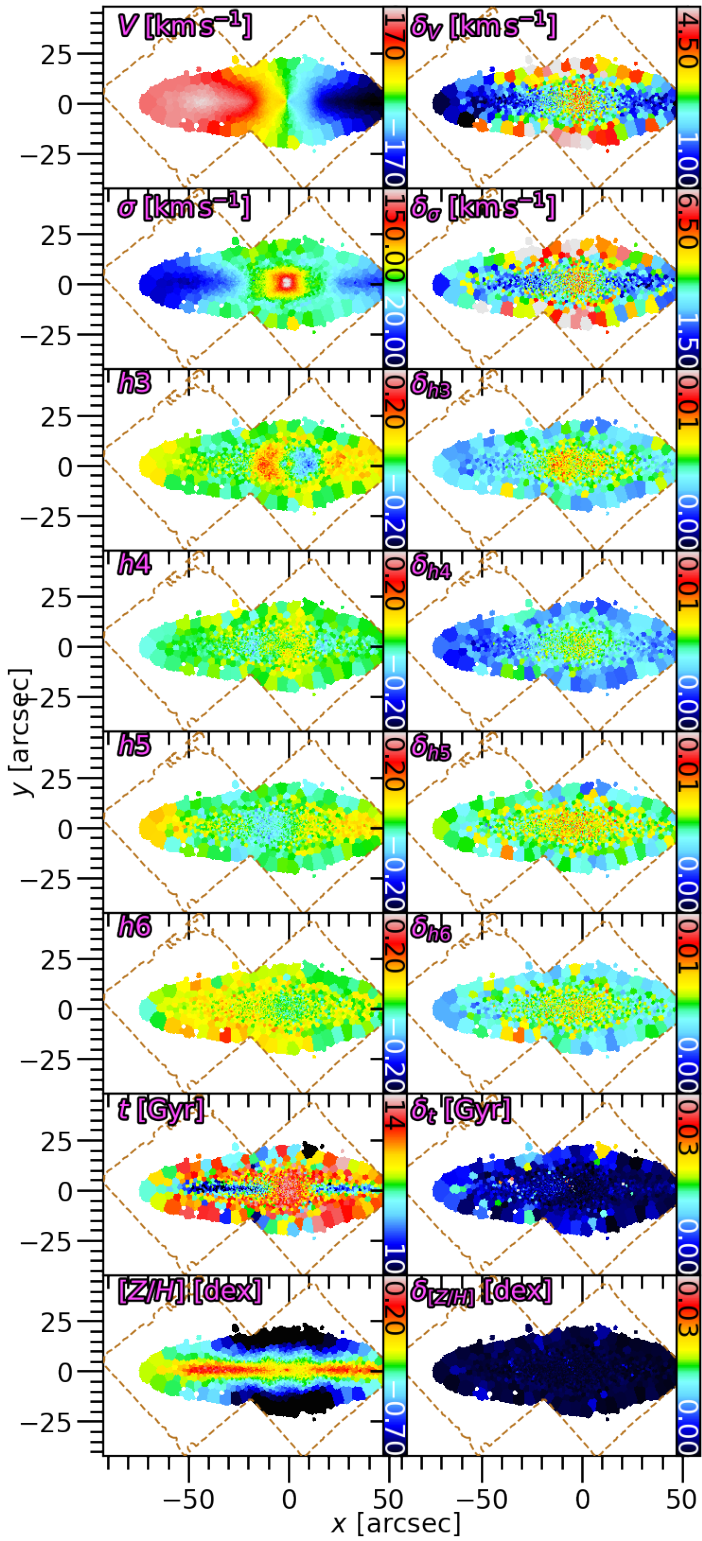


FIGURE 3.B.5: Same as Fig. 3.B.4, but for FCC 170.

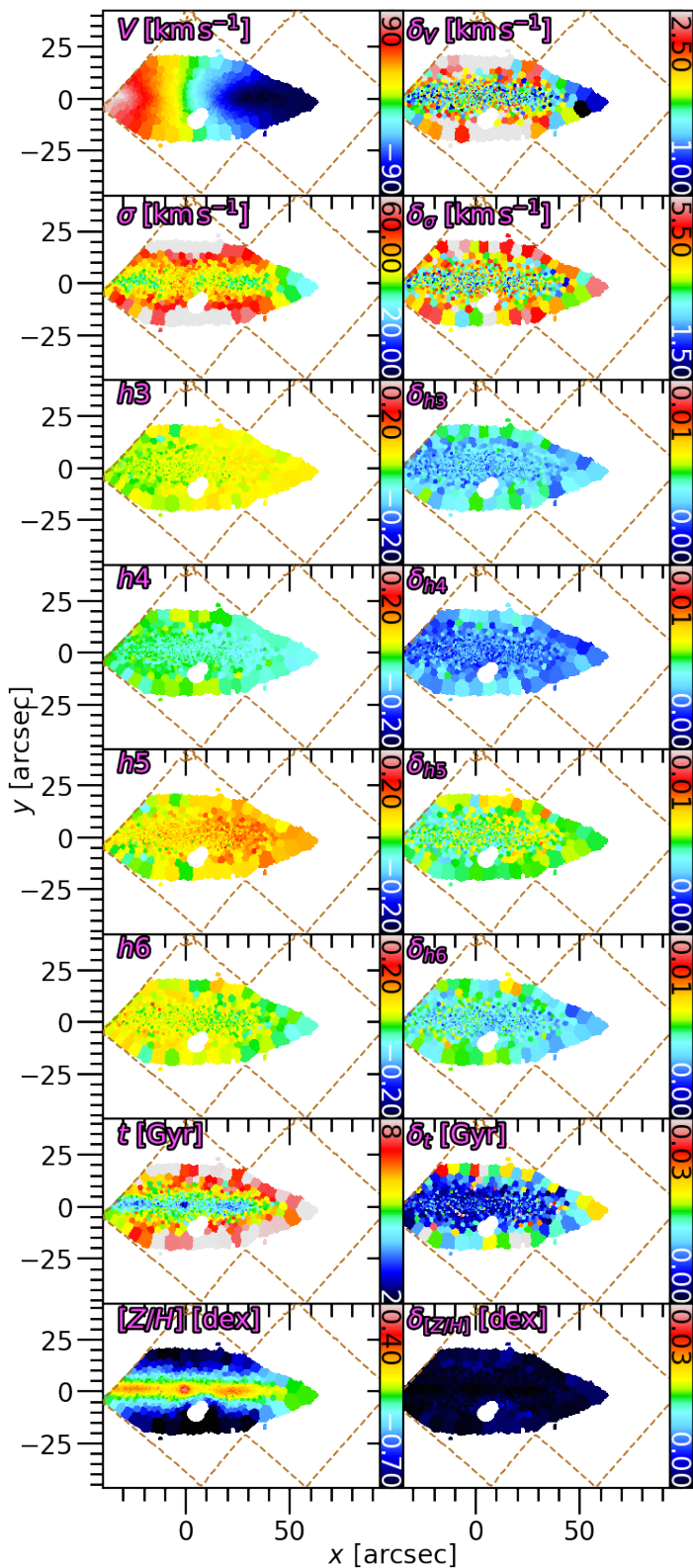


FIGURE 3.B.6: Same as Fig. 3.B.4, but for FCC 177.

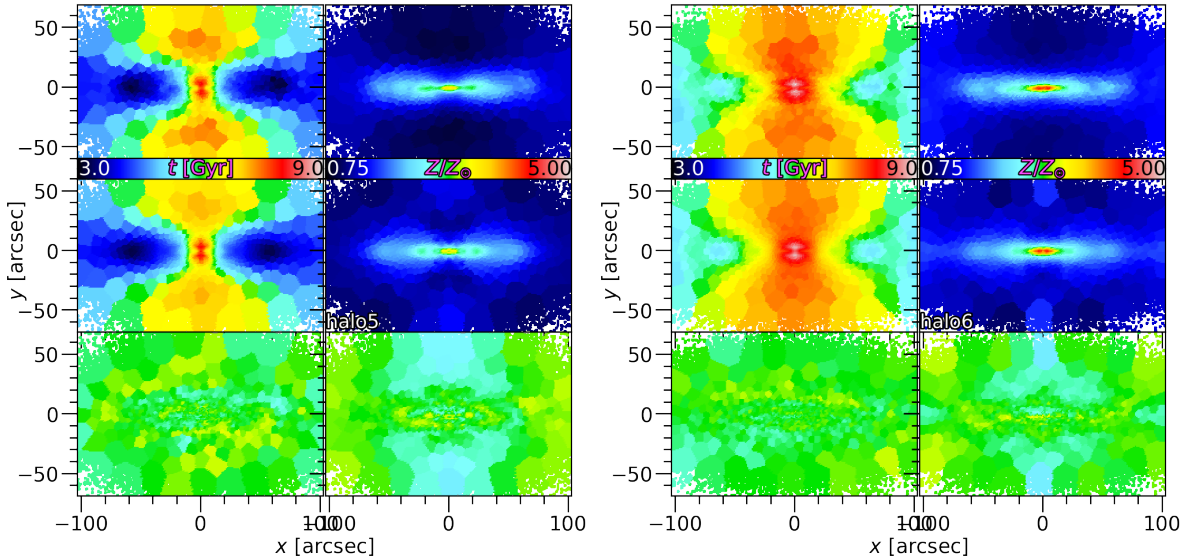


FIGURE 3.C.1: Stellar-population Schwarzschild model fits to the mock data. Mean stellar age (*left*) and metallicity (*right*) are shown for Auriga halos 5 (*top*) and 6 (*bottom*). From top to bottom, the rows represent the true means, models fits, and residuals.

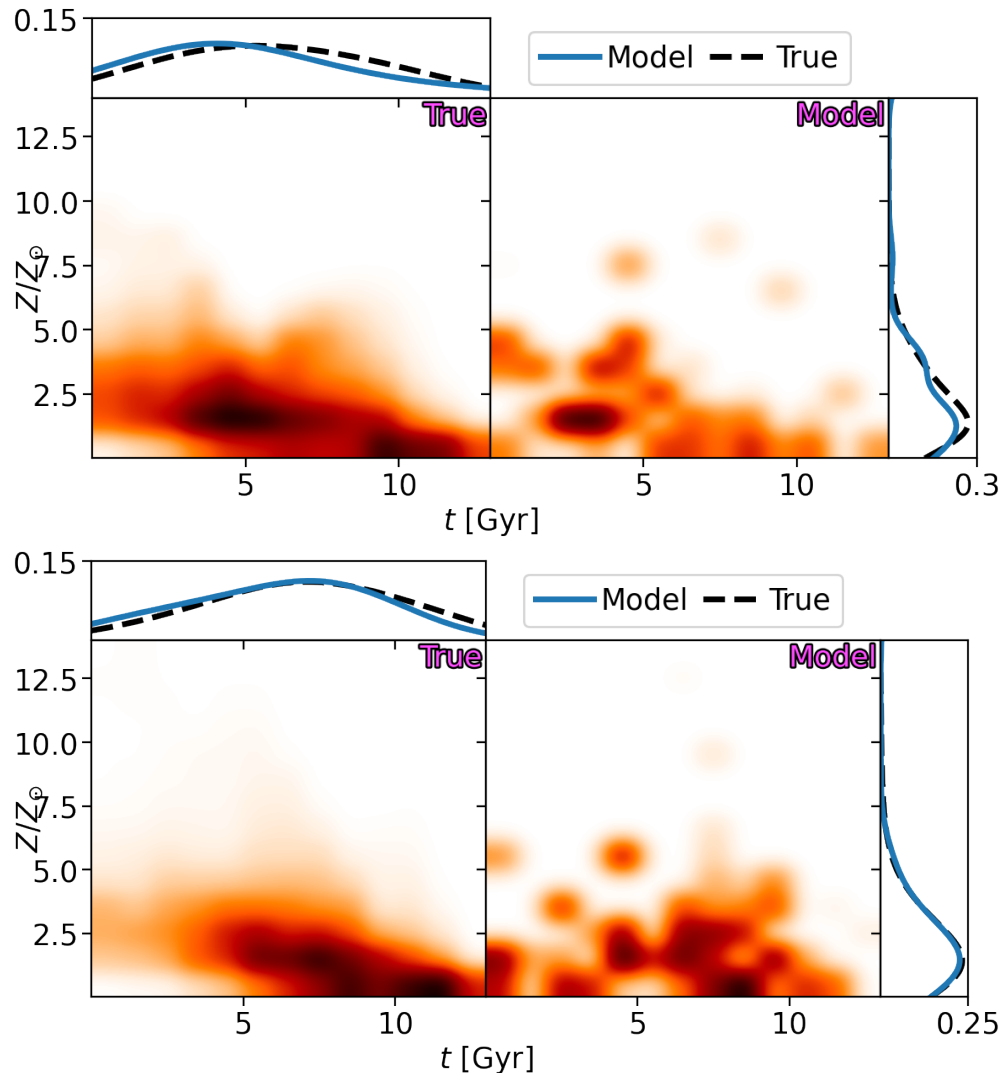


FIGURE 3.C.2: Intrinsic  $t - Z$  distribution (*left*) and that retrieved from our model (*right*) for halos 5 (*top*) and 6 (*bottom*). The 1D distributions are also shown for each simulation, as kernel density estimates of the underlying data. The intrinsic distributions are black dashed curves, and the model distributions are the blue solid curves.

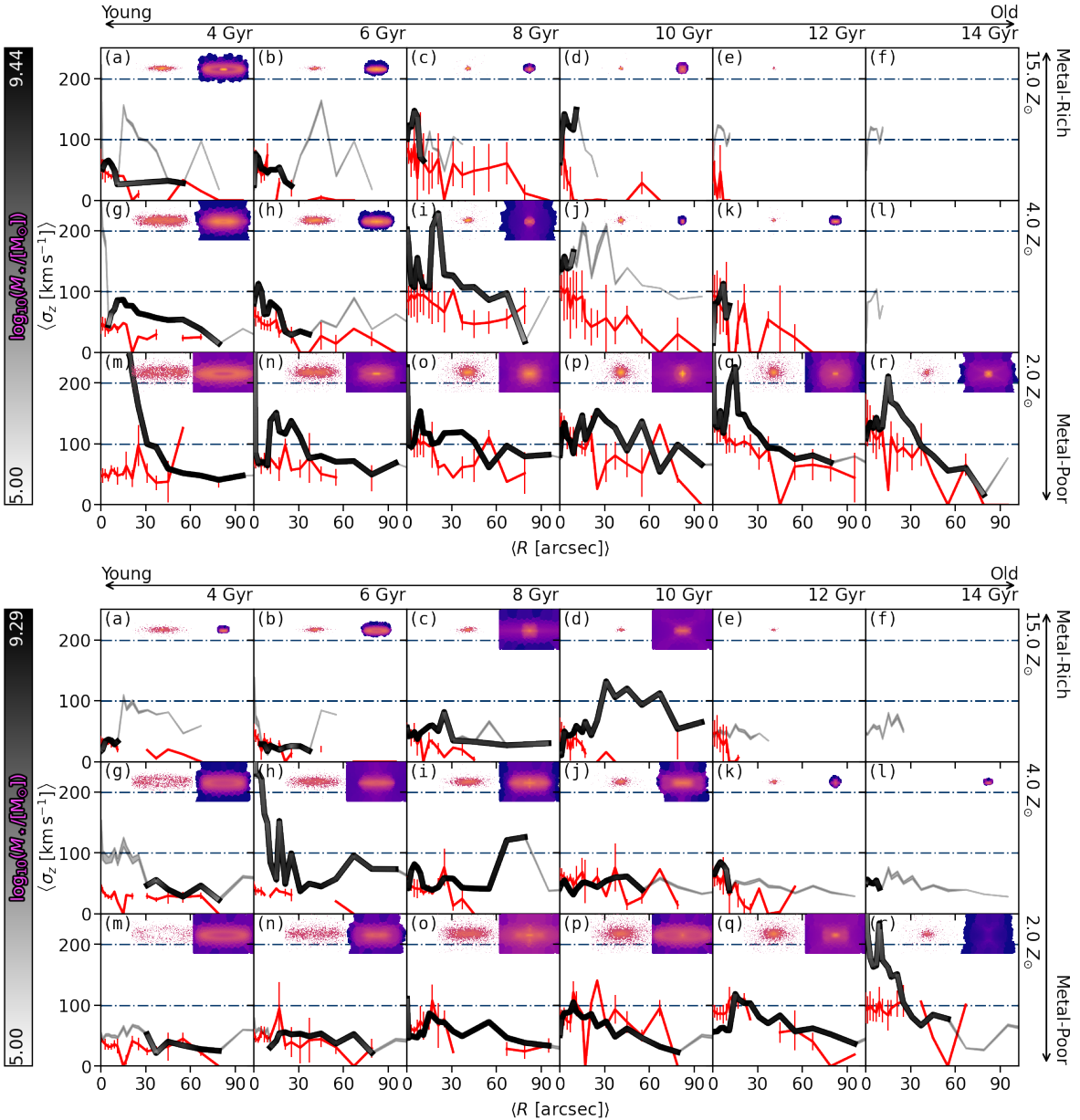


FIGURE 3.C.3: Similar to Fig. 3.10, showing the assembly history for halo 5 (top) and halo 6 (bottom). In addition to the  $\sigma_z$  radial profile (black/white line) and surface brightness distribution (upper right) from the Schwarzschild model, the shaded regions correspond to the variations derived from 100 Monte Carlo fits to the stellar population maps. Each panel also contains the intrinsic  $\sigma_z$  radial profile (red line) and surface brightness distribution (upper left) from the simulations.

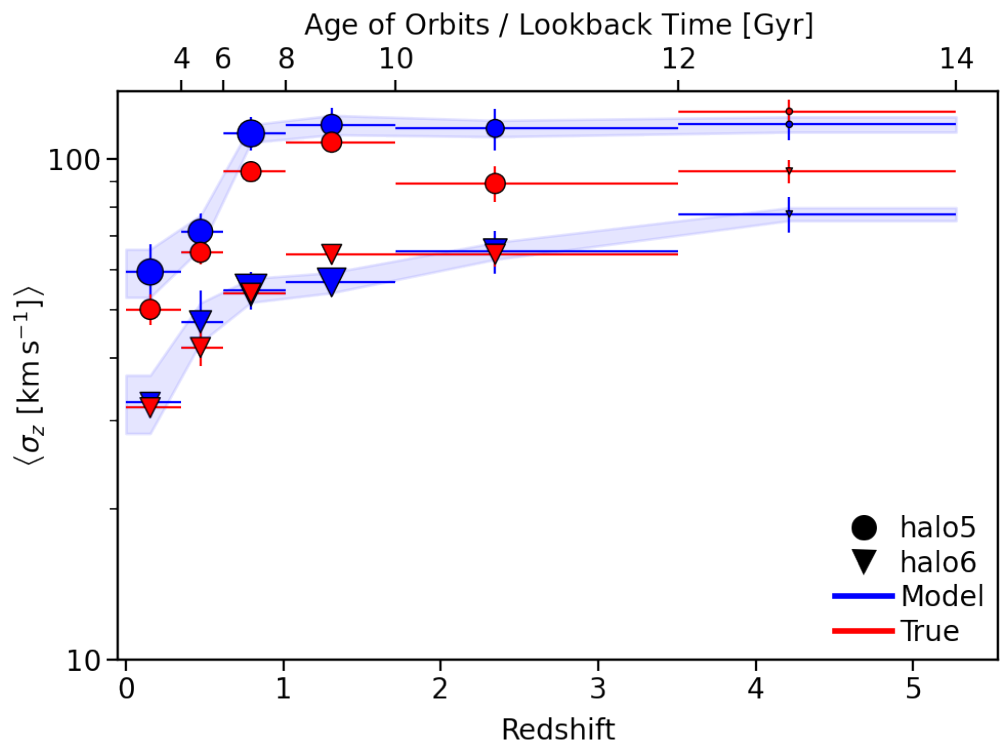


FIGURE 3.C.4: Similar to Fig. 3.13, showing the recovered (blue) and intrinsic (red) AVR for halos 5 and 6.



---

## CHAPTER 4

---

# AN ORBITAL MODEL OF THE LOCAL STELLAR INITIAL MASS FUNCTION IN NEARBY GALAXIES

### 4.1 Introduction

The stellar Initial Mass Function (IMF) is of paramount importance to many fields of astrophysics. Describing the probability distribution function of a local star-formation episode as a function of stellar mass (though see § 1.3.1), the IMF has a fundamental role in studies of star formation on GMC scales, galaxy formation, and has cosmological implications where the assembly of structure in the Universe depends on a (potentially redshift-dependent) IMF. The IMF has direct implications for chemical yields from stellar evolution and broader chemical evolution on galactic scales, so an accurate IMF is critical to test models of those processes.

Despite its importance for extragalactic measurements such as those presented in this thesis, the vast majority of work on external galaxies is under the assumption of a constant IMF; between galaxies, within galaxies, or both. This is primarily driven by technical limitations associated with the difficulties of *measuring* the IMF – especially for external galaxies – as described in § 1.3.1. Yet indirect methods have provided mounting evidence of variations of the IMF between individual galaxies, and typically with some dependence on integrated galactic properties such as the velocity dispersion (Treu et al., 2010; Cappellari et al., 2012; La Barbera et al., 2013; Spinelli et al., 2014; Tortora et al., 2014; Posacki et al., 2015; Li et al., 2017; Rosani et al., 2018),  $\alpha$ -element enrichment (McDermid et al., 2014), or total metal enrichment (Martín-Navarro et al., 2015a).

With increasingly modern data and measurement techniques, it is also becoming increasingly clear that variations of the IMF are local and correlate with local galactic properties. Interestingly the current generation of instrumentation is beginning to close the divide between the galactic and stellar IMF spatial scales, and this divide will only continue to close with subsequent generations of instrumentation. This is beginning to be exploited already by improved analysis techniques. Using spatially-resolved data, gravity-sensitive spectral features – which provide constraints on the relative abundance of low-mass stars, which in turn is related to the slope of the IMF – are observed to vary with galacto-centric radius, becoming relatively dwarf-rich at low radius (Martín-Navarro et al., 2015b,c). In a similar analysis, Parikh et al. (2018) find radial trends consistent with Martín-Navarro et al. (2015b,c) as well as an additional stellar mass dependence where more massive galaxies are consistent with a relatively dwarf-rich IMF (a factor of 1.5 times higher mass compared to a Kroupa, 2001 IMF) in their central regions. They find, however, that using only the Wing-Ford

FeH gravity-sensitive absorption feature produces the inverse radial behaviour, highlighting the observational difficulties associated with constraining the IMF. Similar radial behaviour – increasing dwarf abundance towards the galaxy centre – is also found in the study of Sarzi et al. (2018) using high-quality data of the nearby massive galaxy NGC 4486 (M 87;  $D \sim 16.4$  Mpc). Using molecular gas as a high-spatial-resolution tracer of the gravitational potential (dynamical mass) of the central regions of a sample of nearby galaxies, Davis and McDermid (2017) find that the discrepancy between dynamical and stellar masses (see § 1.3.1) can correlate positively, negatively, or not at all with galacto-centric radius. They also report no correlations with other galactic properties, global or local. van Dokkum et al. (2017) applied a similar technique to six high-mass galaxies and found that generally this discrepancy increases towards the galaxy centres, once again interpreted as a more dwarf-rich IMF there (up to  $\sim 2.5$  times higher mass compared to a Kroupa, 2001 IMF).

The emphasis in recent times has been on the development of statistically-robust methods, most commonly those exploiting Bayes theorem (originally proposed by Thomas Bayes in 1763; published posthumously in Bayes, 1958). This was motivated by the large number of free parameters of increasingly-complex models, as well as characterising potential correlations between them. This has been the case broadly across astronomy, but in the specific case of the IMF has had a number of distinct applications. These include `a1f` (Conroy and Dokkum, 2012; Conroy et al., 2013, 2017), `PyStaff` (Vaughan et al., 2018), and “Full-Index Fitting” (`FIF`; Martín-Navarro et al., 2019). This additional statistical constraining power comes with a marked increase in computational cost, so most of these techniques are restricted to coarse radial bins rather than taking advantage of the truly spatially-resolved IFU data (though see below).

While this transition from global to local correlations of the IMF represents a dramatic improvement in extragalactic IMF studies, the physical cause of these correlations remains elusive. Radial correlations of the IMF in particular can be driven by any number of underlying properties which also happen to correlate with radius. One such example is the purported impact of the stellar velocity dispersion on the IMF. Massive galaxies (the focus of most extragalactic IMF studies) typically exhibit radially-declining profiles of velocity dispersion, and so radial profiles of IMF variation may be driven by the velocity dispersion. One recent case study found that in a galaxy with a radially-*increasing* profile of velocity dispersion, the IMF remains relatively dwarf-rich in the centre (Barbosa et al., 2021). However this galaxy is the central galaxy of the Hydra I cluster, and so separate dynamical processes may have affected its velocity dispersion either independently or after the IMF was set. As such, it remains unclear if the IMF varies fundamentally with velocity dispersion and/or stellar mass.

Evidently these measurements require detailed modelling across the parameter-space of galactic properties in order to uncover drivers of this variation. We are in an ideal position to test exactly this; by extending our existing methodology, using the orbital-population model developed throughout Chapters 2 and 3, we can build a self-consistent dynamical model which connects local (spatially-resolved) dynamics, stellar populations, and IMF. By re-producing the measured IMF maps using our orbital dynamical model, we aim to investigate, for the first time, correlations of the local intrinsic kinematics with the local IMF. We utilise the `FIF` measurements for this work.

## 4.2 Full-Index Fitting

Exploiting the parallel advances in computing technologies and observational instrumentation, Martín-Navarro et al. (2019) present measurements which are sensitive to the relative fraction of low-mass stars. It is sufficiently computationally-efficient such that this measurement can be made for each spectrum in an optical IFU data-cube, and the IMF can therefore be investigated in a truly spatially-resolved manner (not just radially).

The IMF in this instance is assumed to be a power-law in stellar mass for high masses ( $m_\star \geq 0.6 M_\odot$ ), has a gradient of zero at low masses ( $m_\star \leq 0.2 M_\odot$ ), and a continuous transition between these two masses. This follows the functional form originally proposed by Vazdekis et al. (1996). Population synthesis models are generated using this IMF, and the observed spectra are then confronted with these models in order to make the measurements. Unlike conventional full-spectral fitting techniques, FIF isolates specific regions of a spectrum which contain IMF-sensitive information. In practise, this amounts to narrow band-passes surrounding key absorption features. While this is analogous to classic index-based measurements – which measure the integrated depth of specific absorption features – FIF differs in this regard by treating each spectral pixel along these absorption features as independent data-points. This is in fact more analogous to full-spectral fitting, without including the continuum regions between absorption features of the spectra.

Specifically, the Fe5270, Fe5335, Mg b5177, aTiO, TiO<sub>1</sub>, and TiO<sub>2</sub> absorption features are modelled simultaneously to constrain the mean stellar age, metallicity, elemental abundances [ $\alpha/\text{Fe}$ ], and the high-mass power-law IMF slope  $\Gamma_b$ . The IMF is subsequently re-parametrised in order to emphasise the changes in the stellar populations that are still directly observable in the present day. The specific parametrisation utilised by FIF, and in this work, is defined as

$$\xi = \frac{\int_{0.2}^{0.5} \Phi [\log(m)] dm}{\int_{0.2}^{1.0} \Phi [\log(m)] dm} \quad (4.1)$$

$$= \frac{\int_{0.2}^{0.5} m \cdot X(m) dm}{\int_{0.2}^{1.0} m \cdot X(m) dm} \quad (4.2)$$

where  $\Phi [\log(m)]$  in Eq. (4.1) is the IMF in logarithmic mass units and  $X(m)$  in Eq. (4.2) is the IMF in linear mass units. We define here

$$m_{0.5} = \int_{0.2}^{0.5} m \cdot X(m) dm \quad \text{and } (4.3)$$

$$m_{1.0} = \int_{0.2}^{1.0} m \cdot X(m) dm \quad (4.4)$$

such that

$$\xi = m_{0.5}/m_{1.0}.$$

$\xi$  represents the ratio of low- to intermediate-mass stars. These mass ranges are expected to contribute to the observed spectrum, unlike higher-mass stars which are likely to be non-luminous neutron stars or black-holes in the present-day. As presented in Martín-Navarro et al. (2019), literature IMF formalisms from Salpeter (1955), Kroupa (2002), and Chabrier (2003) have  $\xi$  values of 0.6370, 0.5194, and 0.4607, respectively. Larger values of  $\xi$  represent greater relative contributions from low-mass stars, producing more dwarf-rich populations.

The greater computational efficiency of FIF is achieved by excluding regions of the spectrum outside of specific absorption features. This does in fact reduce its ability to constrain the variations in different regions of the spectrum, and the continuum itself may also contain useful information. To circumvent this issue, an initial fit is performed on the full spectrum using a (non-Bayesian) quadratic solver – namely, pPXF – which provides a prior to the Bayesian fit for ages, metallicities, and abundances. Additionally, of the absorption features listed above, only  $[\text{Mg}/\text{Fe}]$  constrains the  $[\alpha/\text{Fe}]$  abundances. The variations of other individual elemental abundances are coupled to the variations of the  $[\text{Mg}/\text{Fe}]$ , further improving the efficiency at the cost of reduced generality. Finally, like existing index-based approaches, the depth of a given absorption feature measured by FIF can depend on the somewhat ambiguous definition of the continuum level on either side of it. With these caveats in mind, we describe below a method for fitting the 2D IMF maps from FIF in an orbital-based dynamical model.

FIF data for the three galaxies explored here are taken from Martín-Navarro et al. (subm). Owing to the subtle effects of varying IMF on the observational data, IMF maps are measured on re-binned data-cubes achieving a  $S/N$  of 250. While this means that the FOV is reduced with respect to that for age and metallicity, we aim to re-measure the IMF on the same spatial binning in future work, once we verify that it can be robustly measured at lower  $S/N$ .

### 4.3 The IMF in Orbital-Population Dynamical Models

The novel method presented in Chapters 2 and 3 have allowed the detailed analysis of a galaxy’s assembly history through the intrinsic properties it provides. It exploits the straightforward principle that the observed data result from the integrated contributions of many distinct populations of stars. This idea relies on the data itself representing a physical quantity which combines linearly. This is not the case for the IMF. Considering the high-mass slope  $\Gamma_b$ , for instance, the  $\Gamma_b$  of a composite stellar population depends non-linearly on the  $\Gamma_b^i$  of each constituent population  $i$ . The same holds true for  $\xi$ ; although it is effectively a mass fraction, both integrands in Eq. (4.2) depend on the  $\Gamma_b^i$  of a given population. This means that distinct populations through a given LOS will have distinct mass integrals  $m_{0.5}^i$  and  $m_{1.0}^i$ , and subsequently that individual  $\xi^i$  can not be linearly combined.

We thus seek a parametrisation which is both sensitive to changes in the IMF and which can be also be cast in terms of a linear combination of orbital properties. For this, we consider the mass of an orbital component integrated within a finite range of stellar mass. Since the observed spectra constrain  $\Gamma_b$  (via the FIF approach), this mass integral can be evaluated for the observed galaxy, providing maps of stellar mass integrated within the same mass bounds. This observed mass map can be fitted as a linear combination of the (kinematically-derived) orbital components. For a single range of integrated mass, this fit alone does not constrain the shape of the IMF (taken as the dwarf-to-giant ratio). However, fitting for two different mass ranges – such as those given in Eq. (4.2) – then taking the ratio between them, allows us to derive a value equivalent to the observational  $\xi$  parameter via the orbital model.

From a dynamical model such as those presented in Chapters 2 and 3, the relative contribution (luminosity weight) from each population  $i$  through the LOS in a given spatial bin is known. There exists then a set of  $m_{0.5}^i$  and  $m_{1.0}^i$  that, when linearly combined with the pre-determined luminosity weights, reproduces the measured maps of  $m_{0.5}$  and  $m_{1.0}$ ,

respectively. This framework is described in Eq. (4.5).

$$\begin{pmatrix} \tilde{\omega}_1^1 & \tilde{\omega}_1^2 & \cdots & \tilde{\omega}_1^{N_{\text{comp}}} \\ \tilde{\omega}_2^1 & \tilde{\omega}_2^2 & \cdots & \tilde{\omega}_2^{N_{\text{comp}}} \\ \vdots & \vdots & \ddots & \vdots \\ \tilde{\omega}_{N_{\text{aper}}}^1 & \tilde{\omega}_{N_{\text{aper}}}^2 & \cdots & \tilde{\omega}_{N_{\text{aper}}}^{N_{\text{comp}}} \end{pmatrix} \cdot \begin{pmatrix} m^1 \\ m^2 \\ \vdots \\ m^{N_{\text{comp}}} \end{pmatrix} = \begin{pmatrix} m'_1 \\ m'_2 \\ \vdots \\ m'_{N_{\text{aper}}} \end{pmatrix} \quad (4.5)$$

The  $\tilde{\omega}$  represent the luminosity weights for each dynamical component (from left to right), in each spatial aperture (from top to bottom). The  $m^i$  represent the mass of each dynamical component  $i \in [1, N_{\text{comp}}]$ , and the  $m'_j$  represent the integrated mass in each spatial aperture  $j \in [1, N_{\text{aper}}]$ . The  $m'_j$  are the values of the mass maps computed from Equations (4.3) and (4.4) using the  $\Gamma_b$  measurements from FIF. We solve Eq. (4.5) by inversion, first substituting  $m_{0.5}$  for  $m'_j$  to derive a set of  $m_{0.5}^i$ , then again (independently) substituting  $m_{1.0}$  to derive a set of  $m_{1.0}^i$ . The outcome of this process is that each dynamical component has a fitted  $m_{0.5}$  and  $m_{1.0}$  which is constrained by, and consistent with, the outputs of FIF.

Solving Eq. (4.5), which consists of a straight-forward linear matrix inversion, is done with a Bounded-Value Least Squares (BVLS) fit using the `lsq_linear` implementation within the SciPy ecosystem (Virtanen et al., 2020). Mathematically, the system described in Eq. (4.5) is only strictly fully constrained when  $N_{\text{comp.}} = N_{\text{aper}}$ . We are in the regime where  $N_{\text{comp.}} < N_{\text{aper}}$ , and so this system is formally *under-constrained*. In this regime, multiple sets of solutions (that is, underlying distributions) can reproduce the observed (average) maps equally well, leading to degeneracies. To minimise the impact of this, we apply linear regularisation to the solution weights, as described in detail in § 2.B. The regularisation, in the case where two solutions fit the data equally well, will favour the solution which has the smoothest distribution in weight-space; in our case, in the  $\lambda_z - R$  plane. In physical terms, orbits with similar angular momentum ( $\lambda_z$ ) and (cylindrical) radius will preferentially be given similar values of  $m_{0.5}$  and  $m_{1.0}$  if such a solution is otherwise indistinguishable from one which varies more rapidly. Setting up the fitting in this way allows the integration over all dynamical components through the LOS to be done in a physically-meaningful (rigorously linear) way for each mass quantity separately. Then, in order to compare to the observed  $\xi$ , we simply take the ratio of the two model mass maps,  $m_{0.5}$  and  $m_{1.0}$ .

## 4.4 Results

### 4.4.1 Fits to Observational Data

The results of the fits to the IMF parametrisations are presented in Figures 4.1 to 4.3, for FCC 153, FCC 170, and FCC 177, respectively. The  $\xi$  panels from our models are not fits of the observed  $\xi$  maps directly, but rather those inferred by the direct fitting of  $m_{0.5}$  and  $m_{1.0}$  maps separately. Reassuringly, the models are still able to re-produce the observed  $\xi$  maps in detail. The structures in the  $\xi$  maps do not necessarily follow those in any single stellar-population property. In FCC 153,  $\xi$  is noticeably elevated along the young, metal-rich disk. There is a minor central peak, but FCC 153 has a small (if any) central pressure-supported component, so a dramatic change in this region is not necessarily expected. In FCC 170, the IMF is seen to be dwarf-rich both in the relatively young disk and in the more metal-rich, old central component. Clearly, then, the IMF in FCC 170 traces neither age nor metallicity directly. Finally, in FCC 177, the IMF shows similar structure as the metallicity such that

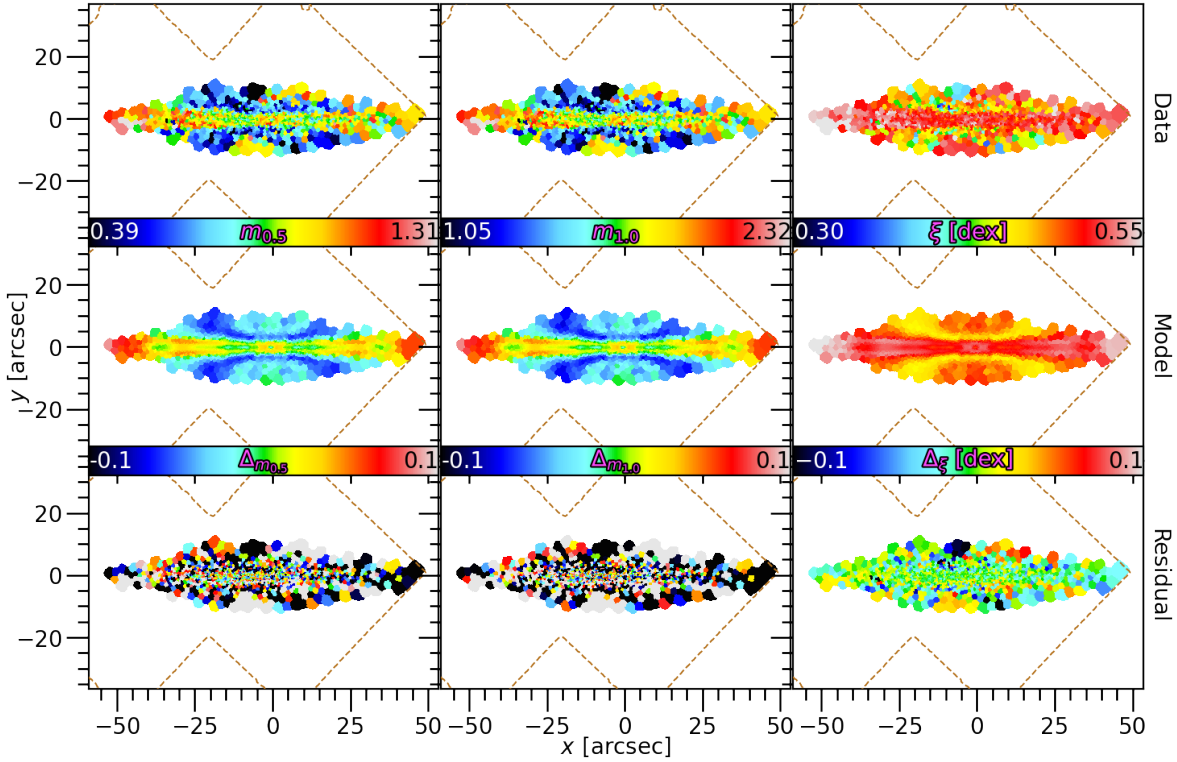


FIGURE 4.1: The IMF parametrisations  $m_{0.5}$  (left),  $m_{1.0}$  (middle), and  $\xi$  (right) for FCC 153. The rows show the data (top), model (middle), and residual (bottom). The outline of the MUSE mosaic is shown in dashed brown. Maps of  $\xi$  are presented on a common colour scale across all galaxies for comparison.

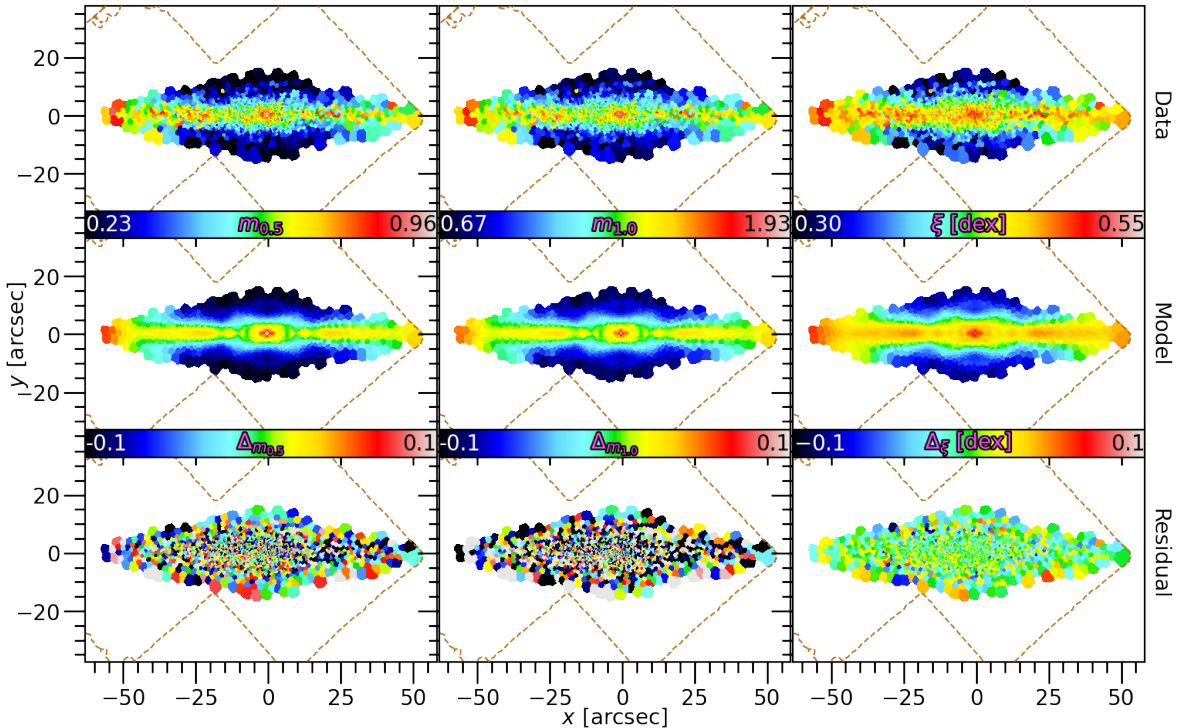


FIGURE 4.2: As Fig. 4.1, but for FCC 170.

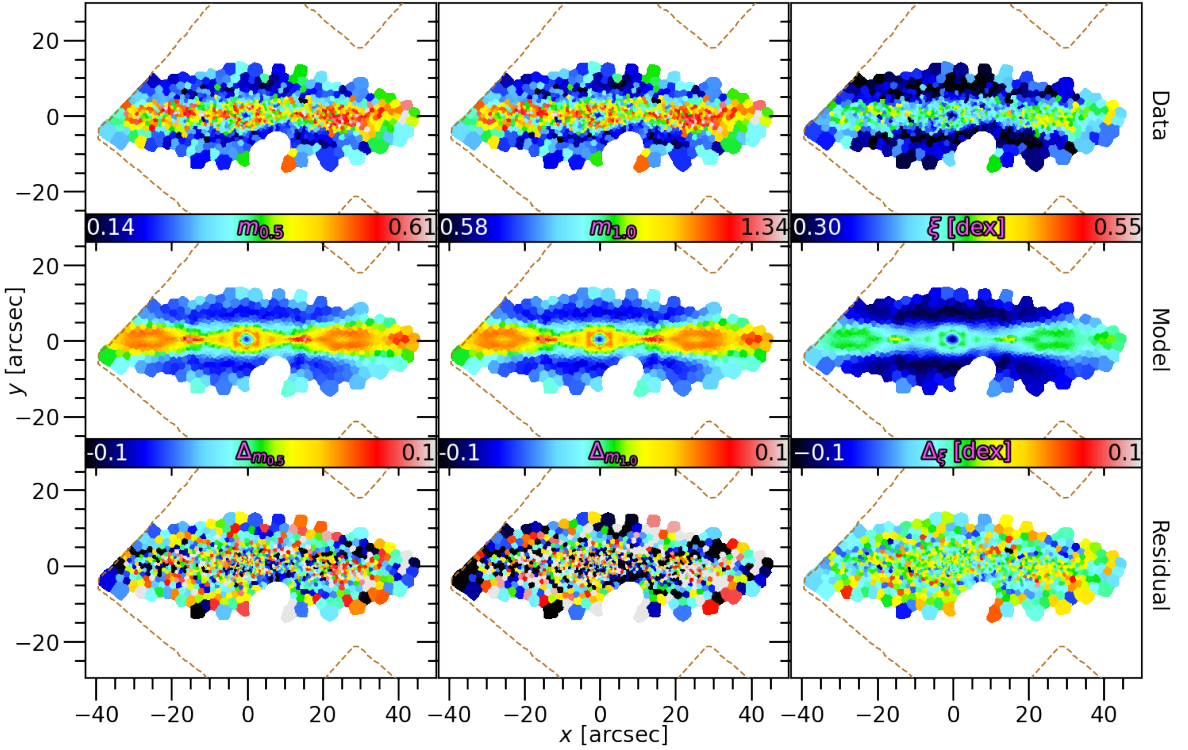


FIGURE 4.3: As Fig. 4.1, but for FCC 177.

$\xi$  is elevated along the disk and in a spheroidal-like central component. The exception is the very central region, embedded within the spheroid. This region appears to have a relatively high abundance of intermediate-mass stars (lower  $\xi$ ). This feature is mirrored by significantly younger ages and lower  $M_\star/L$  in this region, indicating a sudden shift in the time and conditions of that star-formation episode. However this region may be influenced by the young metal-rich nuclear star cluster in this galaxy (Fahrion et al., in prep.).

#### 4.4.2 The IMF in the Circularity Plane

As with the stellar age and metallicity, this technique allows us to investigate the distribution of IMF throughout each galaxy, and crucially investigate correlations with intrinsic dynamical properties. In Fig. 4.4, we re-project the circularity phase-space as a function of  $\xi$ . This is done by computing the luminosity-weighted circularity phase-space of  $m_{0.5}$  and  $m_{1.0}$  individually, then taking the ratio of the two projections. The transparency indicates the orbital weighting derived from the original Schwarzschild model, as illustrated in Figures 3.4 to 3.6. In these projections, regions with low transparency do not contribute significantly to the models/maps, irrespective of the integrated value of  $\xi$  (colour) in that region.

These projections clearly illustrate the variations of  $\xi$  between galaxies. They also show that the dwarf-rich (high  $\xi$ ) populations exists in the orbits with high angular momentum. Conversely, the dynamically-warm regions always exhibit relatively less dwarf-rich populations within each galaxy. These differences may be related to the origin of the stars in each component, discussed further in § 4.5.

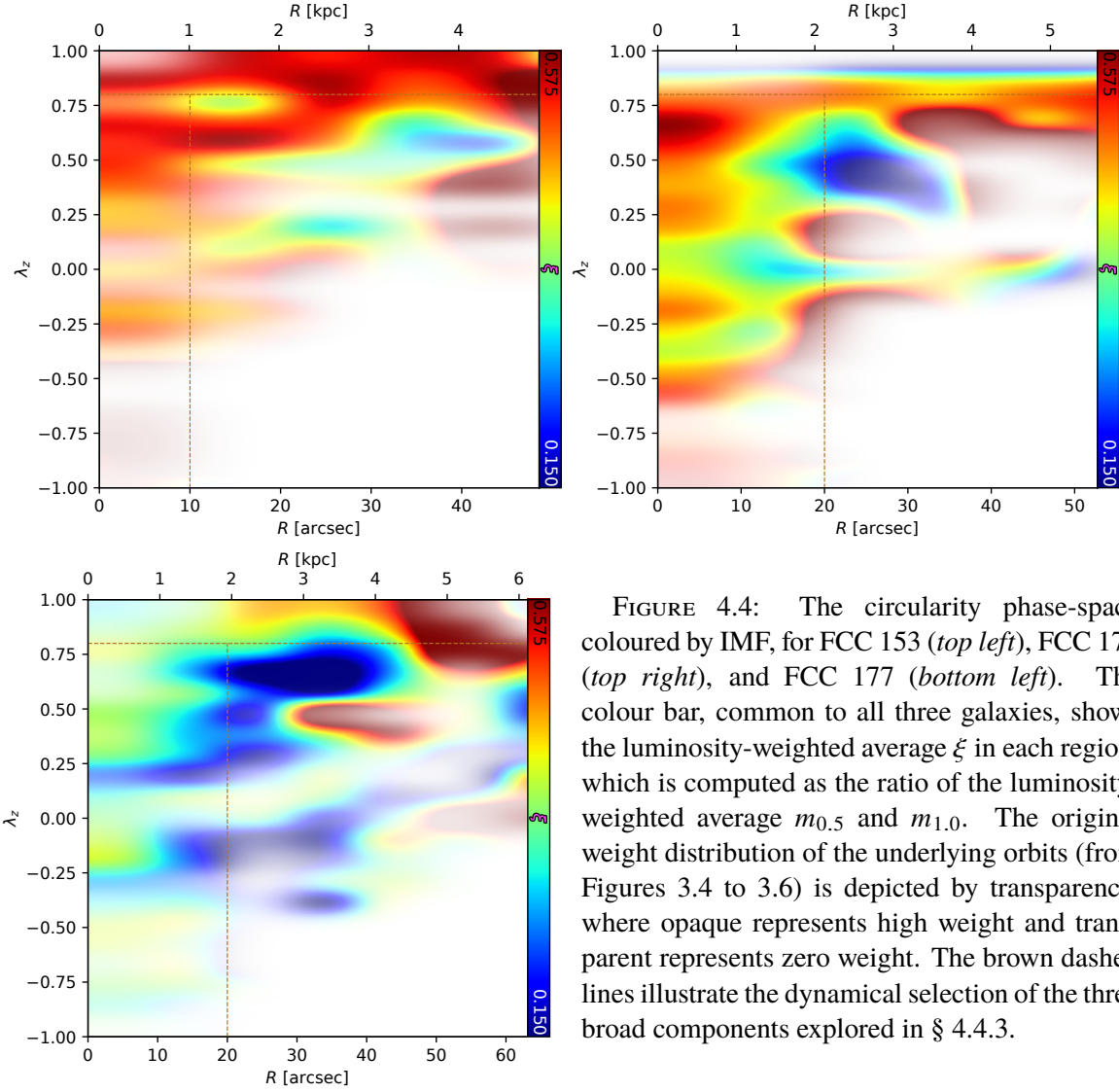


FIGURE 4.4: The circularity phase-space coloured by IMF, for FCC 153 (top left), FCC 170 (top right), and FCC 177 (bottom left). The colour bar, common to all three galaxies, shows the luminosity-weighted average  $\xi$  in each region, which is computed as the ratio of the luminosity-weighted average  $m_{0.5}$  and  $m_{1.0}$ . The original weight distribution of the underlying orbits (from Figures 3.4 to 3.6) is depicted by transparency, where opaque represents high weight and transparent represents zero weight. The brown dashed lines illustrate the dynamical selection of the three broad components explored in § 4.4.3.

#### 4.4.3 The IMF of Principle Galactic Orbital Components

As shown in Fig. 4.4, we separate the different dynamical populations to quantify the conclusions from the previous section. To do this, we define a rotationally-supported ‘disk’ as having  $\lambda_z \geq 0.8$ . A single radial cut is applied to the remaining orbits with  $\lambda_z < 0.8$  in order to isolate the central pressure-supported spheroid. This radius is derived from the original circularity space (Figures 3.4 to 3.6) by approximately identifying the natural ridge in the weight distribution. For FCC 153, this is  $10''$  (1.0 kpc), while for FCC 170 and FCC 177, this is  $20''$  (2.1 kpc and 1.9 kpc, respectively), reflecting the different proportions of dynamically-hot orbits within each galaxy. We refer to the resulting inner and outer components as ‘hot’ and ‘warm’, respectively. We can then investigate these components and their IMF distributions by projecting each subset of orbits onto the sky. These are shown in Figures 4.5 to 4.7.

Corroborating the conclusions from § 4.4.2, these figures show that dynamically-cold components of all three galaxies exhibit relatively dwarf-rich populations, while the central pressure-supported regions show similar (though somewhat lower) dwarf-richness. Conversely, the dynamically-warm orbits – which dominate the off-plane regions, as seen in the  $\tilde{\omega}$  panels of Figures 4.5 to 4.7 – exhibit relatively low  $\xi$  in all three galaxies, implying different

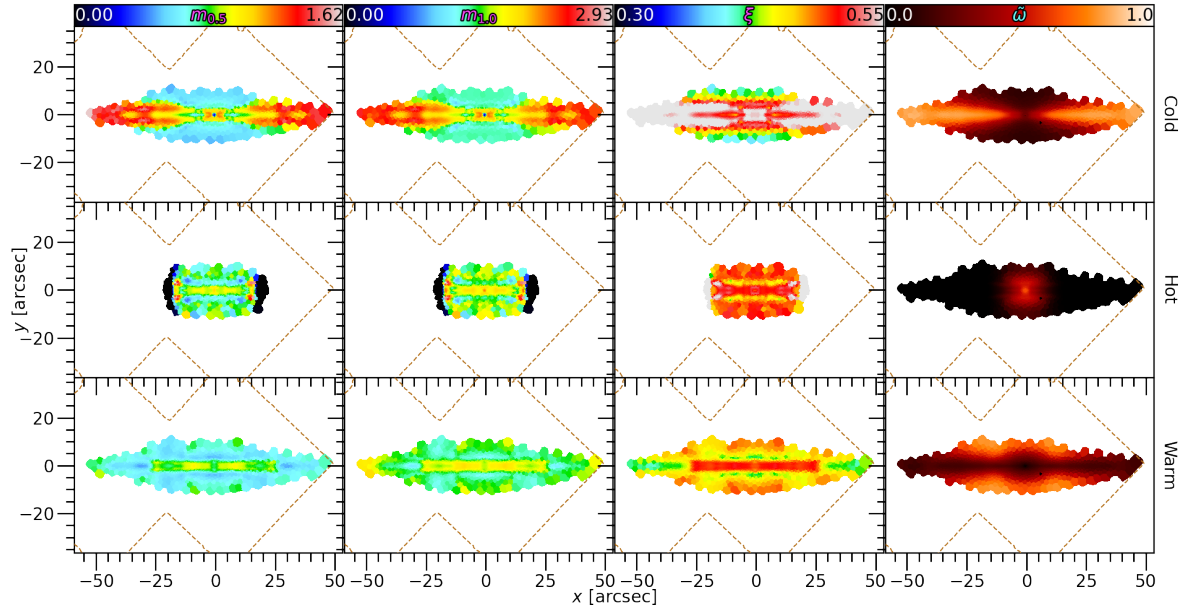


FIGURE 4.5: The spatial distribution of the IMF parametrisations in FCC 153 for the ‘disk’ (top), ‘bulge’ (middle), and ‘warm’ (bottom) components. The outline of the MUSE mosaic is shown in dashed brown. From left to right are the projected maps of  $m_{0.5}$ ,  $m_{1.0}$ , and  $\xi$ , as well as the fractional weight for all orbits in a given component ( $\tilde{\omega}$ ). Each component is necessarily re-normalised, but this means that the relative contribution to the same spatial region between the three rows is not captured. This is instead shown explicitly in the  $\tilde{\omega}$  panels, such that the values of the mass integrals and  $\xi$  for a given component contribute most to the observed maps (Fig. 4.1) in the regions where the respective weight is high. FCC 153 exhibits elevated  $\xi$  (increasing dwarf-richness) in the high-angular-momentum component concentrated in a disk-like geometry (but not exactly in the disk plane).

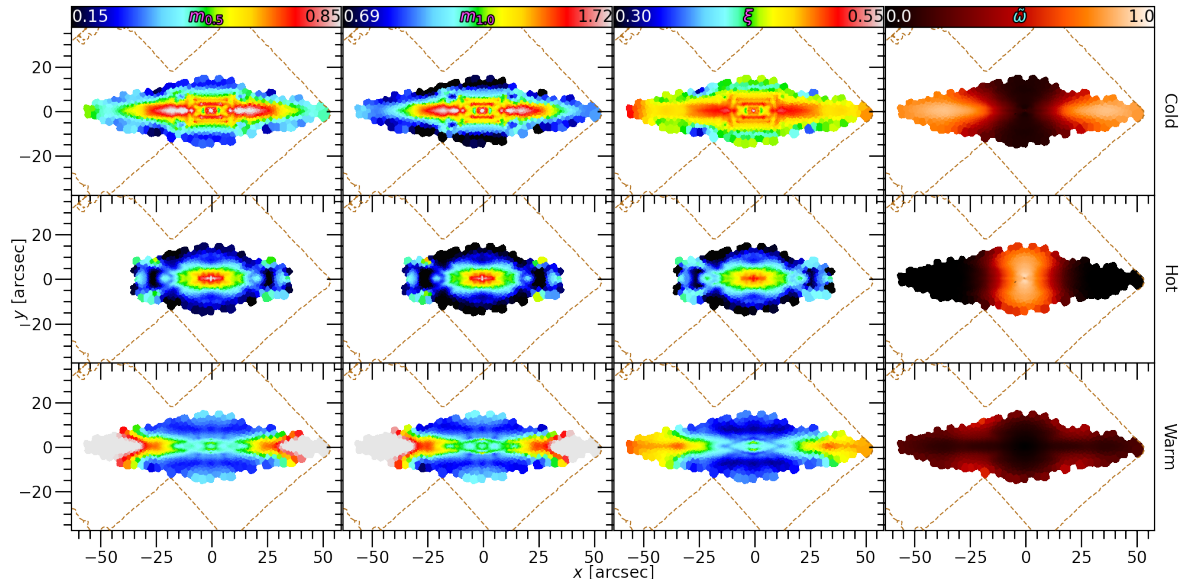


FIGURE 4.6: As Fig. 4.5, but for FCC 170. Like FCC 153, but to a lesser degree, FCC 170 exhibits increased  $\xi$  in the high-angular-momentum component in a disk-like geometry (except for the central region). Even the ‘warm’ component exhibits elevated  $\xi$  along the disk plane at larger radii.

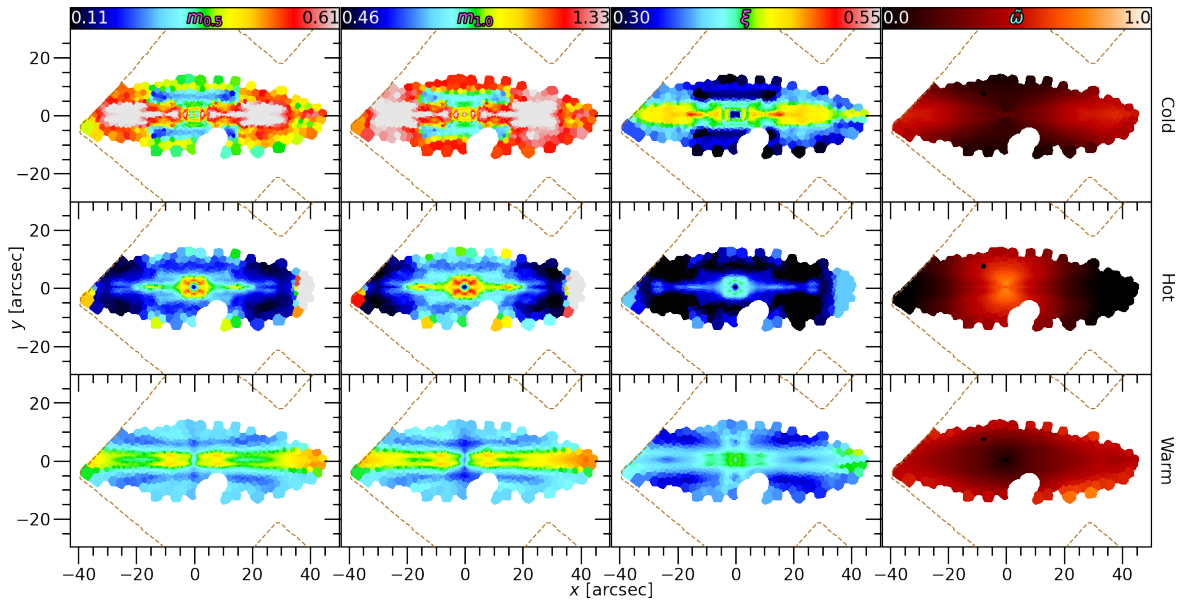


FIGURE 4.7: As Fig. 4.5, but for FCC 177. As with the other projections, FCC 177 exhibits globally lower values of  $\xi$ , yet a peak still exists in the ‘disk’ component.

star formation conditions.

To compare the components and galaxies quantitatively, we show average quantities in Fig. 4.8. These are computed as the average value of the orbits which satisfy the respective selection criteria of each component, weighted by the luminosity-weight of each orbit from the original Schwarzschild model fit. Furthermore, to avoid being driven by unconstrained orbits, the averages of each quantity are computed for only those orbits constrained by spectroscopic measurements – that is, within the maximum spectroscopic extent  $R_{\max}$ . Like in Chapters 2 and 3, we approximate the uncertainty of these average values by fitting random realisations of the IMF maps many times. To this end, we assume a conservative global uncertainty on  $\Gamma_b$  (which is the free parameter of the FIF fit) of 0.5 dex. After randomly generating new  $\Gamma_b$  values for every Voronoi bin within this uncertainty, the maps of  $m_{0.5}$  and  $m_{1.0}$  are re-computed and re-fit. The result of this process is shown in Fig. 4.8 as the shaded regions around each data point. This process does not characterise the systematic uncertainty, but doing so would require a robust statistical treatment of the free parameters of the Schwarzschild model, which is at present not feasible due to the sampling method of those parameters. Nevertheless, the small variation between these realisations – the narrow shaded area – can be understood as the result of the clear structural signatures in the observed maps, which require orbits with particular properties to be assigned particular values of  $\xi$  in order to reproduce them. We subsequently expect this result hold up against future improvements to this method (discussed in § 4.5.2).

Fig. 4.8 shows that the cold and central hot components of galaxies support an approximately equal concentration of dwarf stars which is proportionally higher compared to the extended warm components. Qualitatively, this trend was seen already from Figures 4.5 to 4.7. Between the three galaxies in Fig. 4.8, there is no trend with their present-day stellar mass, projected cluster-centric distance, or suspected time of in-fall into the cluster.

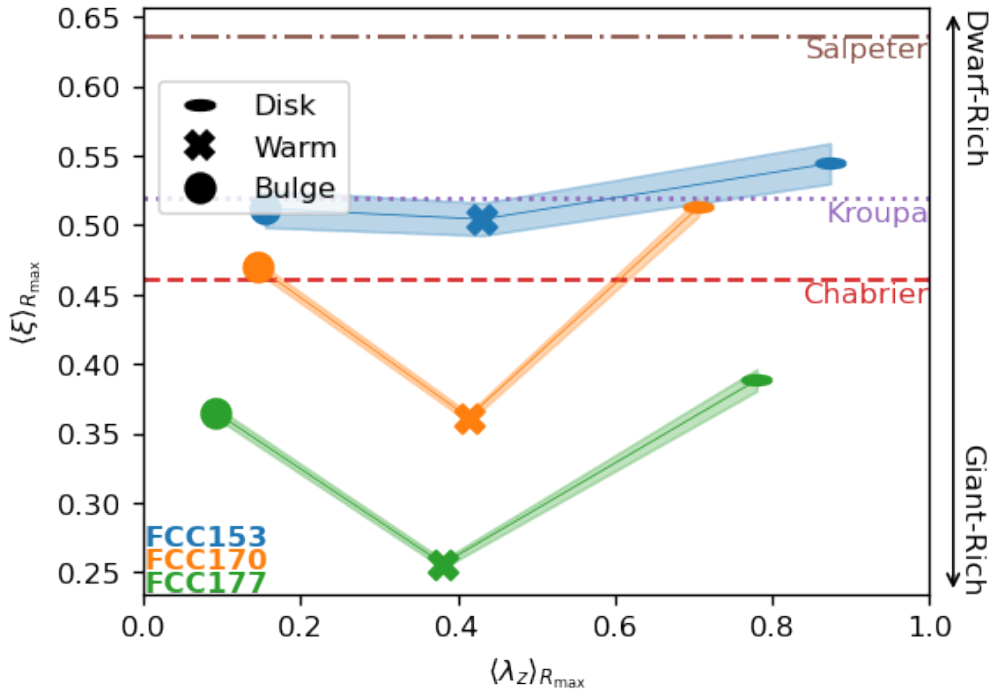


FIGURE 4.8: The luminosity-weighted average IMF as a function of the luminosity-weighted average orbital circularity for the three dynamical components (*symbols*, defined in text) of the three Fornax3D galaxies. Horizontal lines mark literature IMF values for reference. Only those orbits with time-averaged radii within the spectroscopic data are included during the averaging. The dynamically-cold components exhibit comparable richness of dwarf stars to the hot central spheroids, which are more dwarf-rich compared to the extended warm component.

## 4.5 Discussion

### 4.5.1 The Local Variations of the Galactic IMF

As seen from the results in § 4.4, there appears to be no clear correlations of the IMF with other galactic properties. We find strong evidence, however, that the disk and hot components share a common IMF. This is somewhat unexpected from literature studies of IMF variations. There, the interpretation is usually that the ‘extreme’ conditions present in the central regions of massive elliptical galaxies is what gives rise to these IMF variations (Sonnenfeld et al., 2012; van Dokkum and Conroy, 2012; Wegner et al., 2012; Dutton et al., 2013b; Spiniello et al., 2014; Martín-Navarro et al., 2015a; Smith et al., 2015). Although there is not much previous work in which the IMF is explored across galaxy components, Dutton et al. (2013a) and Brewer et al. (2014) find that bulges favour dwarf-rich IMF. They find that disks are more degenerate to measure in projection, but are consistent with ‘standard’ MW-like IMF such as Kroupa (relatively lower contribution from low-mass stars compared to the bulge of the same galaxy).

We instead look to properties defining the conditions in which the stars actually formed, since present-day structural components do not necessarily capture evolutionary changes experienced by the galaxy. In Chapter 3, one tentative conclusion was that FCC 170 and FCC 153 have accreted a similar amount of stellar mass,  $\log_{10}(M_{\text{acc}}/\text{M}_\odot) \sim 9$ , while for FCC 177 it is approximately 1 dex lower. Specifically, for FCC 170 it is claimed to have been brought in by a higher number of lower-mass satellites in order to explain the lower metallicity, compared to fewer higher-mass satellites for FCC 153. If this is the case, we may

posit that the galaxy mass *at the time of star formation* could impact the IMF of the resulting stars. For FCC 177, being overall lower mass, this explains the global shift to less dwarf-rich populations, while the suspected lower-mass satellites which were eventually accreted onto FCC 170 explains the offset of its warm component with respect to FCC 153. This would subsequently imply that the formation of high-mass stars ( $\gtrsim 1 M_{\odot}$ ) preferentially occurs in low-mass galaxies, which may or may not later be deposited into the outskirts of more massive galaxies. A physical explanation for this could be that increased turbulence of the interstellar medium produces fragmentation at lower cloud mass, producing more dwarf-rich populations (Chabrier et al., 2014).

The results of the literature works mentioned above on massive elliptical galaxies are usually interpreted as the conditions in the centres of galaxies specifically facilitating the over-abundance of low-mass stars. However, by definition, these elliptical galaxies do not have any significant disk structure. The IMF, therefore, can only be studied radially, typically how variations present in spheroidal systems. Those galaxies also have the largest accretion fractions on average (Oser et al., 2010; Lackner et al., 2012; Rodriguez-Gomez et al., 2016). Therefore, taken in the context of the results of this work, it's plausible that the central regions of those massive ellipticals are dwarf-rich because they likely formed *in situ*, while the exteriors are less dwarf-rich because they were accreted from lower-mass systems. This leads to a shift in the interpretation of local galactic IMF variations from being caused by the ‘extreme’ conditions at the centres of massive elliptical galaxies, to being determined by the origins of the stars themselves, likely depending on the mass of the system in which they were formed. In present-day galaxies, IMF variations are, in this scenario, explained simply by the mixing of *in-situ* and *ex-situ* populations whereby the stars formed in a variety of host masses.

#### 4.5.2 Further Developments

One implication of Fig. 4.8 is that the greatest internal variations of IMF are in the ‘warm’ components. These components reside in the diffuse outer regions, where there is limited coverage by the IFU data. Larger radial coverage of these galaxies will strengthen the results of this work, as the fraction of accreted material is expected to be higher at larger radius (for instance, Karademir et al., 2019). As mentioned above, we aim to mitigate this in the future by measuring the IMF maps on the same spatial binning as the rest of the data products. Further extending the IFU mosaic with additional (though necessarily deeper) observations, in particular along the minor axis, would also improve coverage of this important *ex-situ* material.

Broadly, our results indicate that both local and global galactic properties influence the IMF. In addition to the age–velocity-dispersion trends measured for these galaxies presented in Chapter 3, we have found further independent evidence that the present-day orbits of stars retain information about their respective star-formation conditions, in this case encoded in their IMF. Larger samples of galaxies are certainly needed for more robust conclusions. If indeed the galaxy mass (total or stellar) at the time of star formation is what determines the IMF, a targeted sample of so-called ‘relic’ galaxies (Beasley et al., 2018) spanning a range of stellar mass to which we apply our methodology could in principle provide the necessary test of this hypothesis. Incidentally, such a sample is currently being compiled (Spiniello et al., 2021), however without sufficient spatial resolution to conduct the orbital analysis developed here. Targeted follow-up using adaptive-optics assisted IFU such as the MUSE narrow-field mode (Leibundgut et al., 2019), and/or the up-coming MAVIS and HARMONI instruments would

provide the necessary data. Independently, a sample in field environments mass-matched to the Fornax galaxies studied here would also be ideal to probe any potential effects from the cluster environment which may be present in the current results.

This implementation has enabled the first direct comparison between the local orbital structure and stellar IMF for external galaxies. Our developments in fact pre-date the means to strictly verify them, as no current cosmological simulations can model the complexity of variable IMF – though this is beginning to change with one recent instance which includes preliminary IMF treatments (Barber et al., 2018). While isolated simulations have been performed incorporating non-universal IMF (Bekki, 2013), testing our methodology on these simulations would only assess its accuracy in numerically recovering known input quantities – which has already been shown in § 3.C. Thus, a more physically-motivated investigation of how accurately genuine IMF variations can be recovered will require the advent of more sophisticated models for star-formation in future cosmological simulations.

There also remain a few specific areas in which we are developing improvements. Firstly, we aim to measure the IMF on spatial bins fully consistent with the underlying kinematics used to constrain the dynamical model. This will not only ensure that the kinematic mapping to IMF is as consistent as possible, but will also extend the IMF measurements to larger galactocentric distances. Secondly, the stellar age and metallicity maps used in the preceding chapters are derived under the assumption of a fixed Kroupa (2002) IMF, and so the  $M_\star/L$  maps used to generate the projected mass density for the dynamical models are under the same assumption. In this chapter we use the dynamical models directly from Chapter 3, while at the same time fitting the map of varying IMF. The differences between the dynamical models with and without variable-IMF  $M_\star/L$  measurements will be small, since age and metallicity variations *are* already taken into account. Granted the increased freedom within FIF, and the potential degeneracies when measuring different stellar population properties from spectra, the measurements may be shifted with respect to those derived from pPXF which does not have the freedom to vary as many parameters. We measure differences between the two approaches of  $< 2$  Gyr and  $< 0.15$  dex for the age and metallicity, respectively, which is comparable to their measurement uncertainty from either approach individually. Therefore, not only is this magnitude of variation captured by the error estimates presented in each chapter (which are computed based on each parameter’s measurement uncertainty), but the framework presented here for the fitting of IMF within the dynamical model remains agnostic to the specific source of the data. Nevertheless, accounting for all sources of variations simultaneously and self-consistently is in principle possible. Incorporation of such  $M_\star/L$  maps from FIF will subsequently allow for even more robust characterisation of projected stellar mass densities from light distributions, leading to more robust and self-consistent dynamical models. The methodology presented in this chapter remains nonetheless robust and powerful, and as we have shown, represents a major milestone in the measuring and modelling of IMF variations in external galaxies.

The technique devised here is modular, in that it is insensitive to how the data are generated. As computational resources become less of a limitation, more complex extraction techniques – which are at present restricted to individual spectra – can be used to generate the necessary data products for this work. For example, BAYES-LOSVD (Falcón-Barroso and Martig, 2021) measures the LOSVDs from observed spectra within a Bayesian framework without using a Gauss-Hermite parametrisation. This will allow the modelling of more kinematically-complex systems, and the robust determination of observational uncertainties. Additionally, techniques such as ALF and PySTAFF could be used to generate IMF maps using alternative functional forms, and with different assumptions about the complex relations

between various chemical abundances. Crucially, all of these data can be switched ‘in place’ into the methodology developed throughout this thesis.

# Bibliography

- Barber, C., Crain, R. A., and Schaye, J. (2018). *Monthly Notices of the Royal Astronomical Society* 479(4), pages 5448–5473. issn: 0035-8711. doi: 10.1093/mnras/sty1826.
- Barbosa, C. E. et al. (2021). *Astronomy & Astrophysics* 645, page L1. issn: 0004-6361, 1432-0746. doi: 10.1051/0004-6361/202039810.
- Bayes, T. (1958). *Biometrika* 45(3-4), pages 296–315. issn: 0006-3444. doi: 10.1093/biomet/45.3-4.296.
- Beasley, M. A. et al. (2018). *Nature* 555(7697), pages 483–486. issn: 1476-4687. doi: 10.1038/nature25756.
- Bekki, K. (2013). *Monthly Notices of the Royal Astronomical Society* 436(3), pages 2254–2275. issn: 0035-8711. doi: 10.1093/mnras/stt1735.
- Brewer, B. J. et al. (2014). *Monthly Notices of the Royal Astronomical Society* 437(2), pages 1950–1961. issn: 0035-8711. doi: 10.1093/mnras/stt2026.
- Cappellari, M. et al. (2012). *Nature, Volume 484, Issue 7395, pp. 485-488 (2012)*. 484, pages 485–488. doi: 10.1038/nature10972.
- Chabrier, G. (2003). *Publications of the Astronomical Society of the Pacific* 115(809), page 763. issn: 1538-3873. doi: 10.1086/376392.
- Chabrier, G., Hennebelle, P., and Charlot, S. (2014). *The Astrophysical Journal* 796(2), page 75. issn: 0004-637X. doi: 10.1088/0004-637X/796/2/75.
- Conroy, C. and Dokkum, P. van (2012). *The Astrophysical Journal* 747(1), page 69. issn: 0004-637X. doi: 10.1088/0004-637X/747/1/69.
- Conroy, C., Dokkum, P. G. van, and Villaume, A. (2017). *The Astrophysical Journal* 837(2), page 166. issn: 0004-637X. doi: 10.3847/1538-4357/aa6190.
- Conroy, C., Graves, G. J., and Dokkum, P. G. van (2013). *The Astrophysical Journal* 780(1), page 33. issn: 0004-637X. doi: 10.1088/0004-637X/780/1/33.
- Davis, T. A. and McDermid, R. M. (2017). *Monthly Notices of the Royal Astronomical Society* 464(1), pages 453–468. issn: 0035-8711. doi: 10.1093/mnras/stw2366.
- Dutton, A. A. et al. (2013a). *Monthly Notices of the Royal Astronomical Society* 428(4), pages 3183–3195. issn: 0035-8711. doi: 10.1093/mnras/sts262.
- Dutton, A. A. et al. (2013b). *Monthly Notices of the Royal Astronomical Society* 432(3), pages 2496–2511. issn: 0035-8711. doi: 10.1093/mnras/stt608.
- Falcón-Barroso, J. and Martig, M. (2021). *Astronomy & Astrophysics* 646, A31. issn: 0004-6361, 1432-0746. doi: 10.1051/0004-6361/202039624.
- Karademir, G. S. et al. (2019). *Monthly Notices of the Royal Astronomical Society* 487(1), pages 318–332. issn: 0035-8711. doi: 10.1093/mnras/stz1251.
- Kroupa, P. (2001). *Monthly Notices of the Royal Astronomical Society* 322(2), pages 231–246. issn: 0035-8711. doi: 10.1046/j.1365-8711.2001.04022.x.
- Kroupa, P. (2002). *Science* 295(5552), pages 82–91. issn: 0036-8075, 1095-9203. doi: 10.1126/science.1067524.

- La Barbera, F. et al. (2013). *Monthly Notices of the Royal Astronomical Society* 433(4), pages 3017–3047. issn: 0035-8711. doi: 10.1093/mnras/stt943.
- Lackner, C. N. et al. (2012). *Monthly Notices of the Royal Astronomical Society* 425(1), pages 641–656. issn: 0035-8711. doi: 10.1111/j.1365-2966.2012.21525.x.
- Leibundgut, B. et al. (2019). *The Messenger* 176, pages 16–19. issn: 0722-6691. doi: 10.18727/0722-6691/5136.
- Li, H. et al. (2017). *The Astrophysical Journal* 838(2), page 77. issn: 0004-637X. doi: 10.3847/1538-4357/aa662a.
- Martín-Navarro, I. et al. (2019). *Astronomy & Astrophysics* 626, A124. issn: 0004-6361, 1432-0746. doi: 10.1051/0004-6361/201935360.
- Martín-Navarro, I. et al. (2015a). *The Astrophysical Journal* 806(2), page L31. issn: 2041-8205. doi: 10.1088/2041-8205/806/2/L31.
- Martín-Navarro, I. et al. (2015b). *Monthly Notices of the Royal Astronomical Society* 447(2), pages 1033–1048. issn: 0035-8711. doi: 10.1093/mnras/stu2480.
- Martín-Navarro, I. et al. (2015c). *Monthly Notices of the Royal Astronomical Society* 451(1), pages 1081–1089. issn: 0035-8711. doi: 10.1093/mnras/stv1022.
- McDermid, R. M. et al. (2014). *The Astrophysical Journal* 792(2), page L37. issn: 2041-8205. doi: 10.1088/2041-8205/792/2/L37.
- Oser, L. et al. (2010). *The Astrophysical Journal* 725(2), pages 2312–2323. issn: 0004-637X. doi: 10.1088/0004-637X/725/2/2312.
- Parikh, T. et al. (2018). *Monthly Notices of the Royal Astronomical Society* 477(3), pages 3954–3982. issn: 0035-8711. doi: 10.1093/mnras/sty785.
- Posacki, S. et al. (2015). *Monthly Notices of the Royal Astronomical Society* 446(1), pages 493–509. issn: 0035-8711. doi: 10.1093/mnras/stu2098.
- Rodriguez-Gomez, V. et al. (2016). *Monthly Notices of the Royal Astronomical Society* 458(3), pages 2371–2390. issn: 0035-8711. doi: 10.1093/mnras/stw456.
- Rosani, G. et al. (2018). *Monthly Notices of the Royal Astronomical Society* 476(4), pages 5233–5252. issn: 0035-8711. doi: 10.1093/mnras/sty528.
- Salpeter, E. E. (1955). *Astrophysical Journal*, vol. 121, p.161 121, page 161. doi: 10.1086/145971.
- Sarzi, M. et al. (2018). *Monthly Notices of the Royal Astronomical Society* 478(3), pages 4084–4100. issn: 0035-8711. doi: 10.1093/mnras/sty1092.
- Smith, R. J. et al. (2015). *Monthly Notices of the Royal Astronomical Society: Letters* 454(1), pages L71–L75. issn: 1745-3925. doi: 10.1093/mnrasl/slv132.
- Sonnenfeld, A. et al. (2012). *The Astrophysical Journal* 752(2), page 163. issn: 0004-637X. doi: 10.1088/0004-637X/752/2/163.
- Spinelli, C. et al. (2021). *Astronomy & Astrophysics* 646, A28. issn: 0004-6361, 1432-0746. doi: 10.1051/0004-6361/202038936.
- Spinelli, C. et al. (2014). *Monthly Notices of the Royal Astronomical Society* 438(2), pages 1483–1499. issn: 0035-8711. doi: 10.1093/mnras/stt2282.
- Tortora, C. et al. (2014). *Monthly Notices of the Royal Astronomical Society, Volume 445, Issue 1, p.115-127* 445, pages 115–127. doi: 10.1093/mnras/stu1616.
- Treu, T. et al. (2010). *The Astrophysical Journal, Volume 709, Issue 2, pp. 1195-1202* (2010). 709, pages 1195–1202. doi: 10.1088/0004-637X/709/2/1195.
- van Dokkum, P. et al. (2017). *The Astrophysical Journal* 841(2), page 68. issn: 1538-4357. doi: 10.3847/1538-4357/aa7135.
- van Dokkum, P. G. and Conroy, C. (2012). *The Astrophysical Journal* 760(1), page 70. issn: 0004-637X, 1538-4357. doi: 10.1088/0004-637X/760/1/70.

- Vaughan, S. P. et al. (2018). *Monthly Notices of the Royal Astronomical Society* 479(2), pages 2443–2456. issn: 0035-8711. doi: 10.1093/mnras/sty1434.
- Vazdekis, A. et al. (1996). *The Astrophysical Journal Supplement Series* 106, page 307. issn: 0067-0049, 1538-4365. doi: 10.1086/192340.
- Virtanen, P. et al. (2020). *Nature Methods* 17(3), pages 261–272. issn: 1548-7105. doi: 10.1038/s41592-019-0686-2.
- Wegner, G. A. et al. (2012). *The Astronomical Journal* 144(3), page 78. issn: 1538-3881. doi: 10.1088/0004-6256/144/3/78.



---

## CHAPTER 5

---

# CONCLUSION

### 5.1 Findings of this Thesis

This work has presented a method of self-consistently modelling the measured stellar kinematics and populations of external galaxies. By exploiting an orbit-based model, not only could all of the stellar properties be re-produced in projection, but the galaxies could also be decomposed based on a variety of intrinsic (deprojected) properties. This allowed for the formulation of diagnostic plots that illuminate major events in the assembly histories of these galaxies. This work has been able to empirically measure intrinsic correlations for external galaxies, such as that between the vertical velocity dispersion and age of the stars. This correlation can serve as the bridge between the local and distant Universe, since it can be measured directly for resolved systems, and approximated from gas dynamics at high redshift. Our technique is one of very few which can measure this correlation for unresolved systems outside of the Local Group. This correlation shows that the local conditions within star-formation sites leave a lasting dynamical imprint on the created stars. Moreover, for the specific galaxies studied here, we concluded that subsequent dynamical evolution has played a minor role. We have uncovered an intriguing correlation between the stellar metallicity and the vertical velocity dispersion, such that more metal-rich stars are dynamically cooler. This correlation is significant at fixed stellar age, implying a fundamental connection between the intrinsic metallicity and velocity dispersion. More broadly, this result places constraints on the local conditions of star formation within external galaxies. In this case, we proposed that higher metal content naturally leads to more efficient dynamical cooling prior to the onset of star formation. This correlation is especially intriguing because of the deficiency of literature studies, even among the Milky Way community, with only one other recent work observing a strikingly similar metallicity–velocity-dispersion relation (**sharma2020**). That work proposes instead that this correlation could be due in part to radial migration. More broadly, it can be concluded that, despite the differences between the present-day properties of the MW and the galaxy sample of this thesis, the consistency between the recovered correlations implies that galactic disks form in similar conditions, and that the formation of the MW disk is not unique or specifically tuned. Finally, we presented the detailed, chronological assembly histories of four lenticular galaxies in low- and high-density environments. Although the statistics are low, these results are still remarkably informative of galaxy formation processes. We were able to exclude (for our sample) specific formation pathways of S0 galaxies that are proposed in the literature. We accurately measured the stellar masses, stellar mass profiles, and intrinsic three-dimensional shapes and velocity ellipsoids, each of which are difficult to achieve with other techniques.

By incorporating a new approach for measuring stellar population properties from integrated spectra (Full Index Fitting), we were able to analyse – for the first time – any intrinsic connections between orbital properties and the galactic IMF. The results indicate that the properties of the galaxy in which stars formed dominates the impact on the IMF. Specifically, the stars we determined to have formed in-situ share a common IMF, whether they are in the classical ‘bulge’ or ‘disk’ regions in the present day. Conversely, the stars most likely to be accreted exhibit a distinct IMF, which is markedly less dwarf-rich compared to the in-situ component of their respective hosts. This is further supported by the differences of the ‘in-situ’ IMF between the galaxies in our sample. Overall, this implies that the global properties of galaxies determine the conditions of star formation locally, and casts a different interpretation on existing literature results.

Key innovations introduced in this work were crucial in achieving our robust results. The assumption of a spatially-constant  $M_\star/L$  in the vast majority of dynamical models is a key example of a common assumption which is being gradually invalidated by the quality of modern observational data. The kinematic data used to constrain dynamical models are dominated by the brightest population of stars at every spatial region. This does not necessarily imply that those populations which dominate the observed data also dominate the mass for that same spatial region, on account of potential spatial variations in the stellar age and metallicity, and the IMF from which that population was drawn. Yet it is specifically this mass that is crucial for dynamical models, and so accounting for the variations in the stellar-population properties is therefore necessary. Justifiably, early long-slit data could not constrain such variations, and therefore dynamical models with spatially-constant  $M_\star/L$  were equally consistent with the data. Early IFU implementations did not justify – indeed, allow – for the incorporation of the full structural variations in the stellar populations, but did allow for the computation of the mass density taking into account azimuthally-averaged radial variations (Mitzkus et al., 2017; Li et al., 2017; Poci et al., 2017). Finally, the undeniable spatial structures seen in modern IFU data not only justify but necessitate the self-consistent inclusion of the measured spatial variations in the stellar populations (see, for instance, Fig. 2.3 and Figures 3.7 to 3.9). The methodology developed in § 2.4.1 and extended in § 3.3.1 is one of the first such implementations. It showed that the observed variations in stellar populations can have as much as a 30% impact on the inferred  $M_\star/L$  (and since the observed flux is fixed, this translates into mass density) in specific regions within galaxies with respect to the spatial average (see § 3.A). In the bright regions of galaxies, this discrepancy is larger than the average contribution from dark matter (Cappellari et al., 2006, 2013; Thomas et al., 2007, 2011). Thus, in order to derive accurate properties and correlations on local scales, it is precisely these spatial variations (not simply the offset magnitude) which are crucial.

The novel linear approach presented here, which serves to couple the stellar kinematics and populations, is the foundation of the new results of this work. Via the robust dynamical model, this approach allowed the exploration of *intrinsic* chemo-dynamical properties of external galaxies. This in turn enabled direct comparisons to results from the Milky-Way, rather than comparing proxy parameters between the resolved and unresolved galactic observations. Such comparisons are powerful because the information-rich studies of the Milky Way can be exploited to make inferences regarding the external galaxies being studied. But these comparisons are also profound because they aide in placing the Milky Way into context in its local environment, eventually illuminating just how unique (or not) the Milky Way truly is, thereby beginning to answer one of the most fundamental questions posed by astronomical and cultural communities. It can be argued, therefore, that a methodology such as this, which probes intrinsic galactic properties, works to diminish the privilege the Milky Way has held

on account of our position within it.

## 5.2 The Current State of Galaxy Evolution

The field of galaxy formation and evolution is a rapidly-progressing one. Our understanding of galaxies has evolved from monolithic-collapse-like objects which transform from disks to spheroids, into a much more refined analysis of various sub-regions within each galaxy and their distinct paths of formation and evolution coupled with their local environment throughout cosmic time. This is the result of the combination of incremental advances in empirical and theoretical results built upon the growing body of literature, and of the dramatically improved quality and quantity of observational data, whose accessibility is also growing. These compounding effects have paved the way to be able to study galaxies near and far in an astounding level of detail.

Despite the roughly parallel advances in the data and data analysis, it can be argued that the quality and quantity of observations have out-paced the community's ability to analyse them. For handling the quantity, fundamentally new (for astronomy) techniques are being developed, leveraging the advances in computational hardware and machine-learning algorithms from the information technology sector. The quality of current, and certainly upcoming, observational facilities implore the use of ever-more sophisticated methodologies. However, many current common practises were developed for data of significantly lower quality, whose assumptions are being exposed by modern data.

The goal of this work was to build an approach which would maximise the amount of information retrievable from these high-quality observations. It aimed to be as unbiased as possible by being driven directly by the data in every aspect. Utilising the most general models available (both the Schwarzschild orbit-based dynamical model and the non-parametric SFH from pPXF) ensured that we were not limited by the assumptions inherent to the methodology, while the quality of data provided the necessary constraining power to optimise these models.

Galaxy formation under this framework adds a layer of quantitative constraints on top of the qualitative picture proposed by earlier works. For instance, while the two-phase formation scenario supposes that mergers shape the histories of galaxies (on average), our methodology has been able to place constraints on *when* these mergers must have occurred (if they occurred at all) based on specific chemo-dynamical properties in individual galaxies. Furthermore, while the galaxy population on average is consistent with the two-phase formation scenario, measuring the assembly histories of individual galaxies in a high level of detail will remain crucial for a number of reasons: (i) the assembly histories measured in our work provide benchmarks for other approaches which aim to measure average properties of the galaxy population (ii) galaxies outlying from the population must be analysed individually, requiring techniques which do not assume a *de facto* two-phase assembly history (iii) even for those galaxies which have integrated properties that are consistent with the broader galaxy population, diversity in their assembly histories still exists (the Milky Way, for instance; Kruijssen et al., 2019).

## 5.3 The Future of Galaxy Formation Models

The dramatic rise in data volume has driven galaxy formation models (like many others in astronomy) to more statistical (probabilistic) methods of analysis. The next generation of galaxy formation models will not fit data of every individual galaxy, as once was the

case, but rather make population-averaged predictions based on some machine-learning algorithm trained on a pre-existing data-set. These algorithms in practise amount to a dramatic dimensionality reduction, allowing data-sets which are intractable by conventional means to be analysed. Emerging use-cases of this are the identification of structure within phase-spaces of observables, such as with the large array of data coming from Milky Way surveys (Ostdiek et al., 2020; Ciucă et al., 2021; del Pino et al., 2021). Recent applications in extragalactic studies, primarily using trained neural networks, include: learning the SFH of spectra without fitting each spectrum individually (Lovell et al., 2019); evolutionary and structural analyses based on photometry alone (Pearson et al., 2019; Cai et al., 2020; Ghosh et al., 2020; Kalvankar et al., 2020); the identification and formation of bars in galaxies from photometry (Cavanagh and Bekki, 2020); identifying and studying strong lenses (Li et al., 2020; Schuldt et al., 2021); identifying and characterising low-surface brightness galaxies (Tanoglidis et al., 2020); connecting galaxies to their DM haloes (Moster et al., 2020); identifying the merger stage of a galaxy using single-epoch photometry (Bottrell et al., 2019); directly ‘extracting’ a dynamical model of emission-line kinematics (Dawson et al., 2021). Another approach makes use of ‘bundling’ algorithms in order to reduce the dimensionality of the parameter-space. Examples include Principle Component Analysis (PCA), which finds the abstract linear combination of parameters containing the most variation in the data (and are therefore the most significant), the non-linear analogue of PCA known as variational auto-encoders, and Gaussian Mixture Models. These techniques have been applied to spectral-fitting to efficiently extract population parameters from a large number of spectra (Pace et al., 2019; Alsing et al., 2020; Feeney et al., 2020; Portillo et al., 2020) and/or the ‘classification’ of spectral features (Tous et al., 2020).

These analysis techniques are being refined in anticipation of the next generation of observational facilities, such as the Extremely Large Telescope (ELT; Ramsay et al., 2020) and the Large Synoptic Survey Telescope (LSST; Ivezić et al., 2019). With much larger primary mirrors capable of observing fainter objects in less time and higher resolution instrumentation, these facilities will be able to dramatically extend the volume of the Universe which is accessible to resolved analyses. This will provide avenues to further verify many of the methodologies discussed in this work for recovering the properties of unresolved populations. In addition, the archaeological aspect of this work – inferring the properties of galaxies in the past based on those in the present – will also be experimentally verifiable, as these facilities will allow such analyses to be carried out directly at higher redshift (corresponding to larger lookback times and earlier stages of evolution). The gains in spatial resolution are beneficial even for nearby targets (which may already have existing data) such as those presented in this work. While the quality of existing data is already high, the physical spatial resolution of upcoming facilities (in the regime of parsecs rather than hundreds of parsecs) will enable the investigation of currently unresolved processes such as the spheres-of-influence of their central SMBH. Providing dynamical measurements of  $M_\bullet$  with higher accuracy and for larger samples of galaxies will allow the mechanisms by which black holes form, grow, and affect their hosts, to be studied in detail.

As argued in this work and discussed in § 5.2, significant variation in assembly histories can exist even among galaxies which meet population averages, such as the two-phase scenario of formation or the many scaling relations between galactic observables. This means that even with the development of sophisticated *statistical* frameworks such as the dimensionality-reduction and/or machine-learning approaches described above, there will remain a need in parallel to model individual galaxies in a high level of detail, similarly to what is presented throughout this thesis. Our technique has been shown to be able to robustly determine the

underlying distributions of stellar populations by fitting just the projected averages, analogous to what standard dynamical models achieve with kinematics. This is not to be expected *a priori*, but shows that the coherent spatial structures throughout the maps coupled to the underlying mathematical framework produces a physical model. Yet even the 2D maps of average quantities still reduce the amount of information accessible to the model. Both the stellar kinematics and populations are derived by first fitting entire spectra, then reducing this fit to some small number of quantities. Modern techniques can derive the underlying *distributions* of populations which give rise to the observed average with remarkable accuracy, even for unresolved systems (Boecker et al., 2020). Yet these too effectively reduce the amount of information. Ideally, models which directly fit the data-cube would have access to all information that is fundamentally observable. The ability to construct such a model in a physically-meaningful way (not just numerically) which can be compared directly to the observed data-cube is the penultimate galaxy formation technique. Such a model will be able to tie intrinsic physical properties to observable features in the (projected) data-cube. This will not only provide maximally-informative results for those individual galaxies, but such a connection will also be crucial to calibrate many of the machine-learning algorithms.

A number of attempts have been made to model the spectra of galaxies directly. Many of these approaches conduct bulge/disk decompositions on the spectra (Tabor et al., 2017; Johnston et al., 2018; Rizzo et al., 2018; Méndez-Abreu et al., 2019), analogous to those on the rotational-velocity radial profiles and photometric images. In fact, these techniques often utilise the photometric decompositions to inform the spectral decompositions, or otherwise require *a priori* assumptions on the kinematics of each component. It is possible, however, to use a more physical model such as the Schwarzschild technique, in order to avoid these assumptions. Thus, to maximise the usable information content from current and future observations, and for analysis techniques to match the quality of observational data, galaxy models should and likely will evolve into modelling the full data-cube. Through the continued development of these advanced techniques, in parallel with the rapid advancement of observing facilities and theoretical galaxy formation simulations with which to confront them, the study of galaxy formation and evolution moves ever closer to understanding the significance of galaxies, the Milky Way, and those within it.



# Bibliography

- Alsing, J. et al. (2020). *The Astrophysical Journal Supplement Series* 249(1), page 5. issn: 0067-0049. doi: 10.3847/1538-4365/ab917f.
- Boecker, A. et al. (2020). *The Astrophysical Journal* 896(1), page 13. issn: 0004-637X. doi: 10.3847/1538-4357/ab919d.
- Bottrell, C. et al. (2019). *Monthly Notices of the Royal Astronomical Society* 490(4), pages 5390–5413. issn: 0035-8711. doi: 10.1093/mnras/stz2934.
- Cai, Z.-Y., Zotti, G. D., and Bonato, M. (2020). *The Astrophysical Journal* 891(1), page 74. issn: 0004-637X. doi: 10.3847/1538-4357/ab7231.
- Cappellari, M. et al. (2006). *Monthly Notices of the Royal Astronomical Society, Volume 366, Issue 4, pp. 1126-1150.* 366, pages 1126–1150. doi: 10.1111/j.1365-2966.2005.09981.x.
- Cappellari, M. et al. (2013). *Monthly Notices of the Royal Astronomical Society, Volume 432, Issue 3, p.1709-1741* 432(3), pages 1709–1741. issn: 0035-8711. doi: 10.1093/mnras/stt562.
- Cavanagh, M. K. and Bekki, K. (2020). *Astronomy & Astrophysics* 641, A77. issn: 0004-6361, 1432-0746. doi: 10.1051/0004-6361/202037963.
- Ciucă, I. et al. (2021). *Monthly Notices of the Royal Astronomical Society* 503(2), pages 2814–2824. issn: 0035-8711. doi: 10.1093/mnras/stab639.
- Dawson, J. M. et al. (2021). *Monthly Notices of the Royal Astronomical Society* 503(1), pages 574–585. issn: 0035-8711, 1365-2966. doi: 10.1093/mnras/stab427. arXiv: 2102.05520.
- del Pino, A. et al. (2021). *The Astrophysical Journal* 908(2), page 244. issn: 0004-637X. doi: 10.3847/1538-4357/abd5bf.
- Feeney, S. M., Wandelt, B. D., and Ness, M. K. (2020). *Monthly Notices of the Royal Astronomical Society*, staa3586. issn: 0035-8711, 1365-2966. doi: 10.1093/mnras/staa3586. arXiv: 1912.09498.
- Ghosh, A. et al. (2020). *The Astrophysical Journal* 895(2), page 112. issn: 0004-637X. doi: 10.3847/1538-4357/ab8a47.
- Ivezić, Ž. et al. (2019). *The Astrophysical Journal* 873(2), page 111. issn: 0004-637X. doi: 10.3847/1538-4357/ab042c.
- Johnston, E. J., Merrifield, M., and Aragón-Salamanca, A. (2018). *Monthly Notices of the Royal Astronomical Society* 478(3), pages 4255–4267. issn: 0035-8711. doi: 10.1093/mnras/sty1342.
- Kalvankar, S., Pandit, H., and Parwate, P. (2020). *arXiv e-prints* 2008, arXiv:2008.13611. URL: <http://adsabs.harvard.edu/abs/2020arXiv200813611K>.
- Kruijssen, J. M. D. et al. (2019). *Monthly Notices of the Royal Astronomical Society* 486, pages 3180–3202. issn: 0035-8711. doi: 10.1093/mnras/sty1609.
- Li, H. et al. (2017). *The Astrophysical Journal* 838(2), page 77. issn: 0004-637X. doi: 10.3847/1538-4357/aa662a.

- Li, Z.-Z. et al. (2020). *The Astrophysical Journal* 894(1), page 10. issn: 0004-637X. doi: 10.3847/1538-4357/ab84f0.
- Lovell, C. C. et al. (2019). *Monthly Notices of the Royal Astronomical Society* 490(4), pages 5503–5520. issn: 0035-8711. doi: 10.1093/mnras/stz2851.
- Méndez-Abreu, J., Sánchez, S. F., and de Lorenzo-Cáceres, A. (2019). *Monthly Notices of the Royal Astronomical Society* 484(3), pages 4298–4314. issn: 0035-8711. doi: 10.1093/mnras/stz276.
- Mitzkus, M., Cappellari, M., and Walcher, C. J. (2017). *Monthly Notices of the Royal Astronomical Society* 464(4), pages 4789–4806. issn: 0035-8711. doi: 10.1093/mnras/stw2677.
- Moster, B. P. et al. (2020). *arXiv e-prints* 2005, arXiv:2005.12276. url: <http://adsabs.harvard.edu/abs/2020arXiv200512276M>.
- Ostdiek, B. et al. (2020). *Astronomy & Astrophysics* 636, A75. issn: 0004-6361, 1432-0746. doi: 10.1051/0004-6361/201936866.
- Pace, Z. J. et al. (2019). *The Astrophysical Journal* 883(1), page 82. issn: 0004-637X. doi: 10.3847/1538-4357/ab3723.
- Pearson, W. J. et al. (2019). *Astronomy & Astrophysics* 626, A49. issn: 0004-6361, 1432-0746. doi: 10.1051/0004-6361/201935355.
- Poci, A., Cappellari, M., and McDermid, R. M. (2017). *Monthly Notices of the Royal Astronomical Society* 467(2), pages 1397–1413. issn: 0035-8711. doi: 10.1093/mnras/stx101.
- Portillo, S. K. N. et al. (2020). *The Astronomical Journal* 160(1), page 45. issn: 1538-3881. doi: 10.3847/1538-3881/ab9644.
- Ramsay, S. et al. (2020). *Advances in Optical Astronomical Instrumentation 2019*. Volume 11203. International Society for Optics and Photonics, page 1120303. doi: 10.1117/12.2541400.
- Rizzo, F., Fraternali, F., and Iorio, G. (2018). *Monthly Notices of the Royal Astronomical Society* 476(2), pages 2137–2167. issn: 0035-8711, 1365-2966. doi: 10.1093/mnras/sty347.
- Schuldt, S. et al. (2021). *Astronomy & Astrophysics* 646, A126. issn: 0004-6361, 1432-0746. doi: 10.1051/0004-6361/202039574.
- Tabor, M. et al. (2017). *Monthly Notices of the Royal Astronomical Society, Volume 466, Issue 2, p.2024-2033* 466, pages 2024–2033. doi: 10.1093/mnras/stw3183.
- Tanoglidis, D., Ćiprijanović, A., and Drlica-Wagner, A. (2020). *arXiv:2011.12437 [astro-ph]*. arXiv: 2011.12437 [astro-ph]. url: <http://arxiv.org/abs/2011.12437>.
- Thomas, J. et al. (2007). *Monthly Notices of the Royal Astronomical Society* 382(2), pages 657–684. issn: 0035-8711. doi: 10.1111/j.1365-2966.2007.12434.x.
- Thomas, J. et al. (2011). *Monthly Notices of the Royal Astronomical Society, Volume 415, Issue 1, pp. 545-562* 415, pages 545–562. doi: 10.1111/j.1365-2966.2011.18725.x.
- Tous, J. L., Solanes, J. M., and Perea, J. D. (2020). *Monthly Notices of the Royal Astronomical Society* 495(4), pages 4135–4157. issn: 0035-8711, 1365-2966. doi: 10.1093/mnras/staa1408.